



**BRNO UNIVERSITY OF TECHNOLOGY**

VYSOKÉ UČENÍ TECHNICKÉ V BRNĚ

**FACULTY OF CIVIL ENGINEERING**

FAKULTA STAVEBNÍ

**INSTITUTE OF STRUCTURAL MECHANICS**

ÚSTAV STAVEBNÍ MECHANIKY

**FRACTURE AND FATIGUE PARAMETERS  
OF ADVANCED BUILDING MATERIALS  
WITH BRITTLE MATRIX**

LOMOVÉ A ÚNAVOVÉ PARAMETRY POKROČILÝCH STAVEBNÍCH MATERIÁLŮ  
S KŘEHKOU MATRICÍ

**HABILITATION THESIS**

HABILITAČNÍ PRÁCE

**AUTHOR**  
AUTOR PRÁCE

Ing. HANA ŠIMONOVÁ, Ph.D.

**BRNO 2023**

Copyright © 2023 Hana Šimonová  
Institute of Structural Mechanics  
Faculty of Civil Engineering  
Brno University of Technology

## **ABSTRACT**

The habilitation thesis summarizes the results and knowledge obtained by solving many partial tasks within the framework of research projects solved at the Faculty of Civil Engineering, the Brno University of Technology in which the author has been involved. The main emphasis is put on the experimental determination of mechanical fracture and fatigue characteristics of various types of commonly used but also newly developed building composites with the brittle matrix. This habilitation thesis is constituted through a series of published articles on selected topics. To sum up, this thesis consists of nine journal papers and two conference proceeding papers.

## **KEYWORDS**

Fracture, fatigue, experiment, quasi-brittle, composite, test configuration, fracture model.

## **ABSTRAKT**

Předložená habilitační práce shrnuje výsledky a poznatky získané řešením celé řady dílčích úkolů v rámci výzkumných projektů řešených na Fakultě stavební Vysokého učení technického v Brně, do nichž byla autorka práce zapojena. Hlavní důraz je v práci kladen na vyhodnocení statických a únavových lomových experimentů těles z různých typů běžně používaných ale i nově vyvíjených kompozitů s křehkou maticí. Tato habilitační práce je tvořena sérií publikovaných článků na vybraná témata. V souhrnu se tato práce skládá z devíti článků publikovaných ve vědeckých časopisech a dvou příspěvků uveřejněných ve sbornících mezinárodních konferencí.

## **KLÍČOVÁ SLOVA**

Lom, únava, experiment, kvazikřehký, kompozit, zkušební konfigurace, lomový model.

ŠIMONOVÁ, Hana. *Fracture and fatigue parameters of advanced building materials with brittle matrix*. Brno, 2023, 182 p. Habilitation thesis. Brno University of Technology, Faculty of Civil Engineering, Institute of Structural Mechanics.

## **DECLARATION OF AUTHORSHIP OF THE HABILITATION THESIS**

I declare that this habilitation thesis titled *Fracture and fatigue parameters of advanced building materials with brittle matrix* is my own work. I have indicated the presence of cited or paraphrased materials and provided references for all sources which are listed in the comprehensive bibliography at the end of the thesis.

Brno, 7<sup>th</sup> February 2023

.....  
Ing. Hana Šimonová, Ph.D.

## ACKNOWLEDGEMENT

First of all, I would like to express my gratitude to all my colleagues from the Institute of Structural Mechanics, Institute of Building Testing and Institute of Chemistry with whose I have had the opportunity to cooperate on different research tasks. It brought me a lot of new experiences and knowledge.

In particular, I am very grateful to my colleagues: Assoc. Prof. Barbara Kucharczyková, Assoc. Prof. Petr Daněk, Assoc. Prof. Pavel Schmid, Prof. Pavla Rovnaníková, Assoc. Prof. Pavel Rovnaník, Dr. Vlastimil Bílek, Jr., Prof. Zbyněk Keršner, Dr. Lucie Malíková, Dr. Petr Miarka, and Prof. David Lehký.

I would like also thank to the management of the Institute of Structural Mechanics for creating suitable conditions for the research of the selected topic.

My heartfelt gratitude goes to my immediate family. I sincerely thank my partner Jan, brother Ondřej and my parents.

The work is a collection of outcomes of several research projects. The financial support was provided by the *Czech Science Foundation* under project numbers:

**18-12289Y** "Advanced characterization of cracks propagation in composites based on alkali activated matrix";

**19-22708S** "New approaches to predicting air-entrained concrete durability by means of determination of pore size distribution and freeze-thaw resistance";

**19-09491S** "Multilevel determination of fracture–mechanical parameters for simulation of concrete structures (MUFRRAS)";

**16-00567S** "Alkali-activated aluminosilicate composites with enhanced electrical conductivity";

**16-18702S** "AMIRI – Aggregate-Matrix-Interface Related Issues in silicate-based composites";

**14-04522S** "Investigation of processes at the formation of solid structure in the silicon oxide-Portland cement system in a relation to the properties of binder";

**13-09518S** "Effect of carbon nanotubes on enhancement of the fracture behaviour of alkali activated aluminosilicate materials (NANOFRRAM)";

and the *Ministry of Education, Youth and Sports of the Czech Republic* under project numbers:

**LO1408** "AdMaS UP – Advanced Building Materials, Structures and Technologies";

**8J18AT009** "Fracture initiation and fracture of quasi-brittle building materials (FlnFraM)";

**8X17060** "Fiber reinforced alkali activated composites (properties and selected durability aspects)".

---

**CONTENTS**

<b>INTRODUCTION .....</b>	<b>9</b>
<b>PART I.....</b>	<b>11</b>
<b>I.1 MATERIAL UNDER STUDY .....</b>	<b>13</b>
<b>I.2 FRACTURE TESTS OF QUASI-BRITTLE MATERIALS .....</b>	<b>15</b>
<b>I.2.1 SPECIMENS AND FRACTURE TESTS CONFIGURATIONS.....</b>	<b>15</b>
<b>I.2.2 TESTING MACHINES AND DETAILS OF FRACTURE TEST COURSE.....</b>	<b>18</b>
<b>I.2.3 ADJUSTMENT OF RECORDED DATA .....</b>	<b>20</b>
<b>I.2.4 DETERMINATION OF MECHANICAL FRACTURE PARAMETERS .....</b>	<b>22</b>
<b>I.3 FATIGUE FRACTURE TESTS .....</b>	<b>26</b>
<b>I.3.1 CYCLIC FRACTURE TESTS IN 3PB TEST CONFIGURATION .....</b>	<b>26</b>
<b>I.3.2 EXPERIMENTAL DETERMINATION OF WÖHLER CURVE .....</b>	<b>27</b>
<b>I.3.3 CORRECTION PROCEDURE OF WÖHLER CURVE PARAMETERS .....</b>	<b>28</b>
<b>PART II .....</b>	<b>31</b>
<b>II.1 FRACTURE AND FATIGUE BEHAVIOUR OF FINE-GRAINED COMPOSITE BASED ON SODIUM HYDROXIDE-ACTIVATED SLAG .....</b>	<b>33</b>
<b>II.2 FRACTURE RESPONSE OF ALKALI-ACTIVATED SLAG MORTARS WITH DISPERSED REINFORCEMENT .....</b>	<b>67</b>
<b>II.3 FRACTURE RESPONSE OF SELECTED CONCRETE SPECIMENS.....</b>	<b>91</b>
<b>II.4 MECHANICAL FRACTURE PARAMETERS AS INPUTS OF MATERIALS MODELS FOR NUMERICAL MODELLING OF FRACTURE RESPONSE.....</b>	<b>131</b>
<b>II.5 FRACTURE BEHAVIOUR OF SELECTED QUASI-BRITTLE COMPOSITES CONTAINING DIFFERENT KINDS OF WASTE MATERIALS.....</b>	<b>151</b>

**CONCLUDING REMARKS..... 173**  
**REFERENCES ..... 175**  
**LIST OF ABBREVIATIONS AND SYMBOLS ..... 181**

## **INTRODUCTION**

The author of this thesis was engaged in different research tasks connected with experimental fracture mechanics of quasi-brittle materials within the framework of research projects solved at the Faculty of Civil Engineering, the Brno University of Technology. Therefore, it was decided to create this habilitation thesis through a series of published articles which represents an apposite way for the presentation of the obtained results. The main emphasis is put on the experimental determination of mechanical fracture and fatigue characteristics of various types of commonly used but also newly developed building composites with the brittle matrix.

The work is divided into two parts. Part I describes investigated materials, used fracture and fatigue test configurations, processing of experimentally obtained data, and determination of mechanical fracture and fatigue parameters. Part II is constituted through a series of published articles which are divided into five different research topics. To sum up, this thesis consists of nine journal papers and two conference proceeding papers.



# **Part I**



## I.1 MATERIAL UNDER STUDY

Many materials used in civil engineering including concrete as the main representative of this group may be classified as quasi-brittle material, showing the so-called tensile softening, i.e. gradual decrease of transmitting stress in the significant area ahead of the crack/notch tip (fracture process zone FPZ). Studying the mechanical response of specimens made of such composites under static and dynamic/fatigue loading is complicated due to their highly nonlinear nature. Numerical tools for modelling both elastic (elastic-plastic) behaviour and also fracture processes are commonly used to predict or assess this response. Such tools – often based on the finite element method [1] or physical discretization of the continuum [2] – usually exploit a type of nonlinear fracture model that simulates the cohesive nature of the cracking of quasi-brittle material [3–5]. The parameters of this fracture model are determined from records of fracture tests; this is carried out either using evaluation methods built on the principle of the used non-linear fracture model, e.g. the work-of-fracture method [6] or the size effect method [7], or using inverse analysis with the possible application of advanced identification methods [8–10]. The fracture models for quasi-brittle composites are most often based on the standardized geometry of specimens with stress concentrators; the three-point bending test [4] or wedge splitting test [11, 12] are typically used.

Assessment of the fracture behaviour of quasi-brittle materials is usually performed for notched specimens/structures subjected to the mode I of loading. The investigations of the fracture phenomena in other modes of loading and/or their combination (mixed modes of loading) are studied rather rarely even though the real structures made of quasi-brittle materials in civil engineering applications are usually loaded in a mixed-mode manner. It should be also emphasized that many structures are often subjected not only to static but also to repetitive cyclic loads of high-stress amplitude. Examples of such cyclic loads include automotive and train traffic, machine vibration, and wind action. The processes occurring within the quasi-brittle material structure and leading to its degradation under cyclic loading are more complicated in comparison to those affecting metals [13]. That is the reason why knowledge of the behaviour of quasi-brittle materials, not only under static or quasi-static conditions but also under cyclic conditions, is very important for the complex description of crack propagation in such materials. However, fracture and fatigue tests of quasi-brittle materials and structures are expensive and time-consuming, and for this reason, numerical modelling [14, 15] can represent a powerful tool for the prediction of the damage process and fatigue life of such materials under different service conditions. For the effective and correct use of a numerical (material) model, it is often necessary to tune its parameters using data obtained from experimental measurements. The correct evaluation of such data is becoming a prerequisite for the correct use of numerical models in practice.

Although Portland cement and its blends are and in the near future will be the most common binders in practical applications of civil engineering around the world because of their availability, versatility, and tradition, there are increasing efforts to search for some alternative binders. Nowadays, an important factor in the development of new building materials is their environmental credentials. The rational management of natural resources and the use of waste

materials are becoming more and more important [16]. Great emphasis is placed on environmental protection through reductions of CO<sub>2</sub> emissions of which a large amount is produced by cement industries. There are two feasible ways how to reduce the CO<sub>2</sub> emissions in the production of the above-mentioned building materials. The first one is the application of secondary raw materials as supplementary cementitious materials [17]. The other way is using the alkali-activated binder (AAB), this type of material is even more effective in reducing CO<sub>2</sub> emissions and energy consumption [18, 19]. Another option is to reduce raw materials consumption in the concrete mixture by substitution of natural aggregates with recycled aggregates [20–24].

The same as cement-based concrete, materials based on AABs belong to materials with the quasi-brittle response, i.e. low energy absorption capacity under tensile load. Different types of steel or synthetic fibres [25–27] are added to overcome this problem and improve the material's resistance to crack propagation. The environmentally guided trend of research leads to the use of a sustainable alternative to steel and synthetic materials. Naturally available fibres produced from different types of plants (e.g. hemp, flax) grown locally make renewable, biodegradable and relatively cheap alternatives [28, 29].

Knowledge of the mechanical and primarily fracture parameters of composites with a brittle matrix is essential for the quantification of their resistance to crack initiation and growth, as well as for the specification of material model parameters employed for the simulation of the quasi-brittle behaviour of structures or their parts made from this type of composite. Therefore, this habilitation thesis is presented the typical fracture tests and their evaluation using selected fracture models for the characterisation of quasi-brittle materials. Attention was paid to the static and fatigue fracture tests of different types of typical and alternative building materials which were mentioned above.

## I.2 FRACTURE TESTS OF QUASI-BRITTLE MATERIALS

The study of mechanical and primarily fracture properties of existing or newly developed composites with a brittle matrix is essential for the description of their fracture behaviour and quantification of resistance to crack propagation. Nevertheless, in many cases, the attention is still focused on the maximum strength of the material rather than analyzing the properties associated with resistance to crack formation and propagation. The main disadvantage of the fracture tests in context to the characterization using maximum strength values are especially time consumption (one test lasts at least 40 minutes), labour intensiveness, and also the process of evaluation which limits wider utilization in standard practice.

The determination of these parameters is based on standardized fracture experiments on specimens with stress concentrators. The typical fracture test configurations used by the author of this thesis and her colleagues are introduced in this chapter. At first, the type of used specimens and test configurations are introduced. Followed by the description of used testing machines and the details about carrying out fracture tests. A detailed description of experimental data processing and the evaluation of mechanical fracture parameters using selected fracture models are introduced.

### I.2.1 SPECIMENS AND FRACTURE TESTS CONFIGURATIONS

The most commonly used specimen shape for fracture tests is a standardized prism which is typically used for the determination of mechanical characteristics. The prisms with nominal dimensions  $40 \times 40 \times 160$  mm and  $100 \times 100 \times 400$  mm for composites with fine and coarse aggregate, respectively are usually used. The height of the ligament should be at least 5 times of maximum aggregate size.

The test specimen is provided with a stress concentrator (initial notch) before the test is performed. The central edge notch (Figure 1(a)) with a nominal depth of about 1/3 of the specimen's height is made by a diamond blade saw. The other type of notch shape is the Chevron notch (Figure 1(b)) which is typically used for fracture tests of ceramics, brittle metals or aluminium alloys [30]. The Chevron notch is also used for the determination of fracture parameters of rocks [31]. The core-drilled cylindrical specimens are usually used (Figure 1(c)). The cylindrical specimens can be beneficially used also for the characterization of materials of existing structures [32] when core drilling is used to obtain the material from the structure.

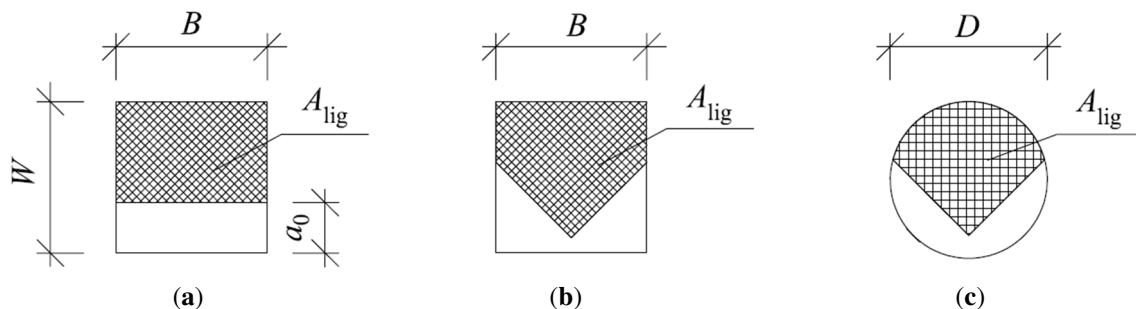


**Figure 1.** The shape of notch and area of ligament of prismatic/cylindrical test specimens: with edge notch (a), with Chevron notch (b) and (c).

All mentioned test specimens are typically tested in three-point bending (3PB) configuration, see Figure 2(a). The most common fracture test for the characterization of quasi-brittle materials is 3PB of the prismatic specimen with a straight-through notch. The main advantages of this configuration are the economy fabrication of both specimen and notch and the relative simplicity of the test procedure. The different types of specimens and notches tested in 3PB were investigated for example in [33].

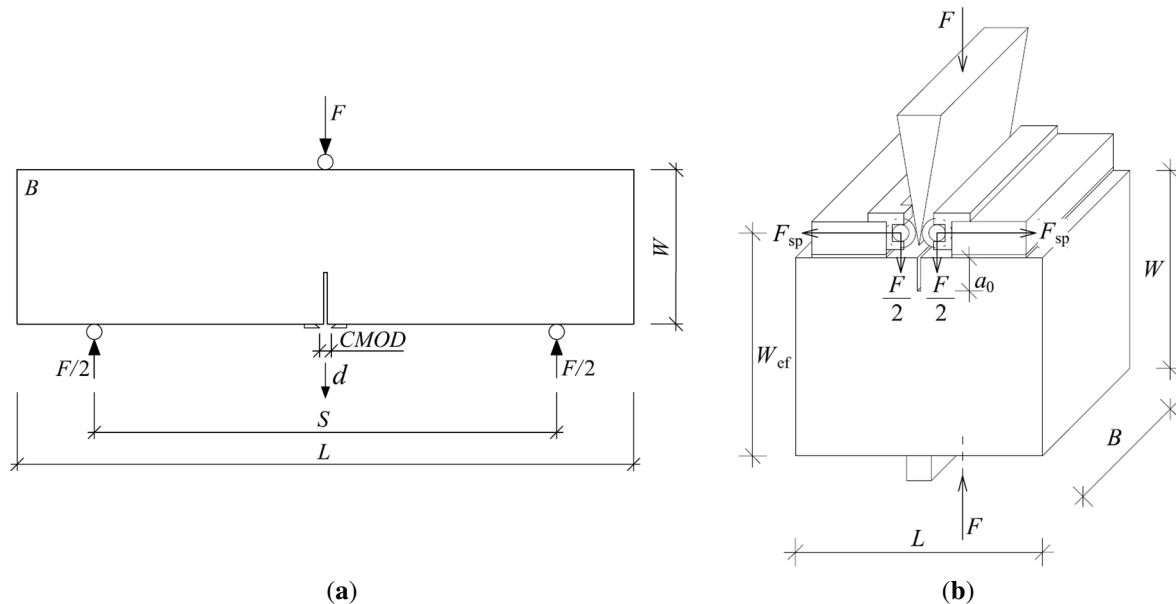


**Figure 2.** Three-point bending fracture test configuration of a beam specimen with a central edge notch (a); and a wedge-splitting test configuration (b).

The other fracture test configuration used for the characterization of quasi-brittle materials is a wedge-splitting test (WST), see Figure 2(b) [11, 12]. The specimens used for WST are very compact and require a smaller amount of material compared to the 3PB of the prismatic specimen with the straight-through notch. On the other hand, the carrying out of this type of test requires more complicated loading fixtures and the preparation of specimens itself is also much more complicated. For purpose of WST, different types of testing specimens with an initial notch are used. For placing the WST loading fixtures it is necessary to manufacture the rectangular groove on the top of the specimens which is made in different ways. One way is to cut out the groove with a diamond saw which is time-consuming and demanding. The other option is to put a prism with the required dimension of the groove in the mould before the specimens' casting [11]. Figure 3(a) introduced the standardized cubical specimens used for WST with a groove made in one of the above-described ways. The other possibility is to make the groove by gluing two plates on the top of the specimens (Figure 3(b)) [34]. Figure 3(c) introduces the cylindrical specimens which can be used for the characterization of materials drilled from existing structures. The specimens in the WST configuration are placed on one (see Figure 2(b)) or two linear supports. The second case can be found e.g. in [35] in which a detailed experimental campaign of concrete specimens of different sizes tested in 3PB and WST configurations is summarised.

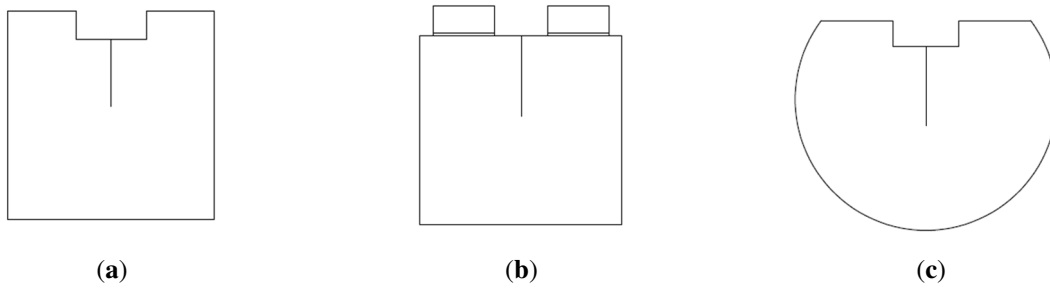


**Figure 3.** The scheme of test specimens used for WST: cubical specimen with precast or cut-out groove (a), cubical specimen with the groove made by gluing two plates on the top (b), and cylindrical specimen cut-out from the drilled core (c).

The 3PB with the central notch and WST represents the tensile mode I (crack opening) of loading [4, 36]. The investigations of the fracture phenomena in other modes of loading (in-plane shear mode II, out-of-plane shear mode III) and/or their combination (mixed modes of loading) are studied rather rarely even though the real structures made of quasi-brittle materials in civil engineering applications are usually loaded in a mixed-mode manner. For a description of the crack propagation under mixed-mode I/II conditions, various test configurations were used for testing the fracture parameters of rocks and cement-based composites. For this purpose, semi-circular disc specimens in 3PB [37–39], centrally cracked Brazilian disc [39, 40], and prismatic specimens in asymmetric three- [41, 42] or four-point [41, 43] bending configurations are mostly used. Selected semi-circular specimens with an inclined initial notch loaded in 3PB configuration (see Figure 4(a)) were designed for experimental verification of numerical simulations of crack propagation under mixed-mode I/II conditions within the implementation of project “Advanced characterization of cracks propagation in composites based on alkali activated matrix” [44]. The specimens were cast in special silicone moulds with a wooden frame (see Figure 4(b)), which were designed and made by the author of this thesis. The initial notches were made by a water jet cutter. The type of specimens was chosen also concerning the practical application to the in-situ structures when drilled cores are usually taken for verification of real mechanical characteristics from which this type of specimens can be also easily prepared.



**Figure 4.** Three-point bending fracture test configuration of a selected semi-circular disc specimen with an inclined initial notch (a); and a special mould (b).

## I.2.2 TESTING MACHINES AND DETAILS OF FRACTURE TEST COURSE

The stiffness of the testing machine is required to be adequate in comparison to the specimen's stiffness to enable stable fracture tests to be conducted without any interruption in the post-peak branch. Several mechanical testing machines which belong to facilities of the laboratories of the Institute of Building Testing FCE BUT are used for conducting the different configurations of fracture tests. In the past, the fracture tests were carried out using a Heckert FPZ 10/1 (Figure 5(a)) or Heckert FPZ 100/1 (Figure 5(b)) testing machines with the different loading range which was set individually according to the strength of tested materials.



**Figure 5.** The testing machines used for fracture tests: Heckert FPZ 10/1 (a), and Heckert FPZ 100/1 (b).

Nowadays, the stiff multi-purpose mechanical testing machine LabTest 6.250 with a loading range of 0–250 kN (Figure 6(a)) is the most often used or for the larger specimens the LabTest 6-1000.1.10 (Figure 6(b)) with the loading range of 0–1000 kN.



**Figure 6.** The testing machines used for fracture tests: LabTest 6.250 (a), and LabTest 6-1000.1.10 (b).

The loading process is in all cases governed by a constant increment of displacement of 0.02 mm/min during the whole course of testing. This loading procedure is slow enough for the whole post-peak behaviour of test specimens to be recorded. The inductive sensor with a measurement range of 0–2 mm is usually used for the measurement of the specimens' deflection in the 3PB configuration. The sensor is mounted into a special frame which is placed on the specimens (Figure 7(a)) or bedded on the upper surface of the specimens during the test (Figure 7(b)). The special frame in Figure 7(a) was designed by the author of this thesis. All frames are constructed to measure the deflection of twofold values in the middle of the span length.



**Figure 7.** Detail of the test measuring frame: placed on the specimen (a), bedded on the upper surface of specimen (b).

The strain gauge is used for the measurement of the crack mouth opening displacement (*CMOD*) in 3PB. It is mounted between two blades glued on the bottom surface of the specimens near the artificial notch ((Figure 8(a)). In the case of WST, the *CMOD* is measured using pairs of inductive sensors mounted in the special frame (Figure 8(b)).

The mentioned parameters together with loading force and time are continuously recorded by an HBM SPIDER 8 device or HBM Quantum X data-take with the frequency of 5 Hz.

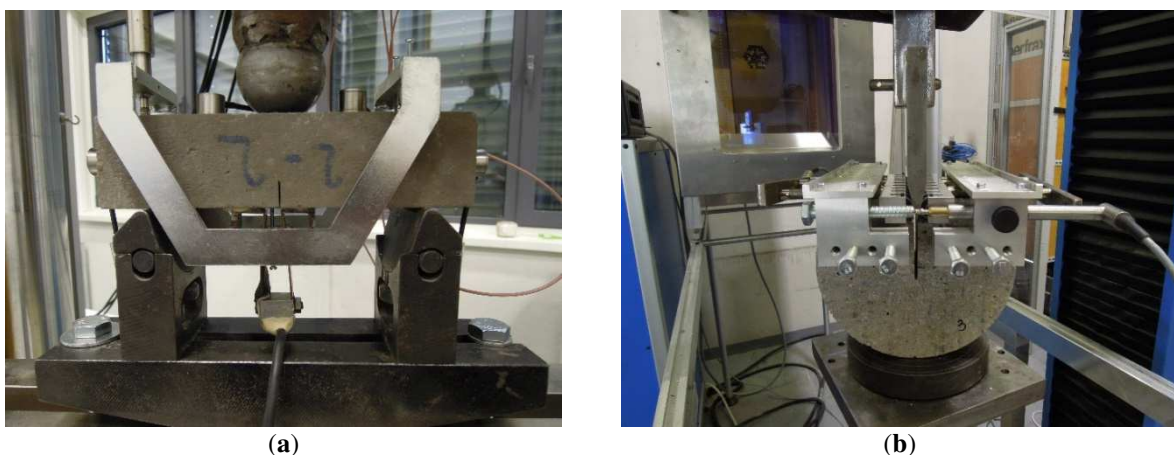


**Figure 8.** Detail of measuring the *CMOD*: 3PB test configuration (a), WST (b).

The advantage of the currently used testing machines is that a 2D video extensometer can be simultaneously used during the fracture test. During the loading process, the strains on the surfaces of the tested specimens are digitally measured using the system with one or two high-frequency cameras, see the example in Figure 9. This measurement system enables monitoring of the real-time crack development and provides high-quality images for further processing using e.g. digital image correlation (DIC). Obtained data could be later used for the analysis of the initiation and development of the FPZ or contactless measurement of deflection and/or *CMOD* if it is not possible to measure them directly.

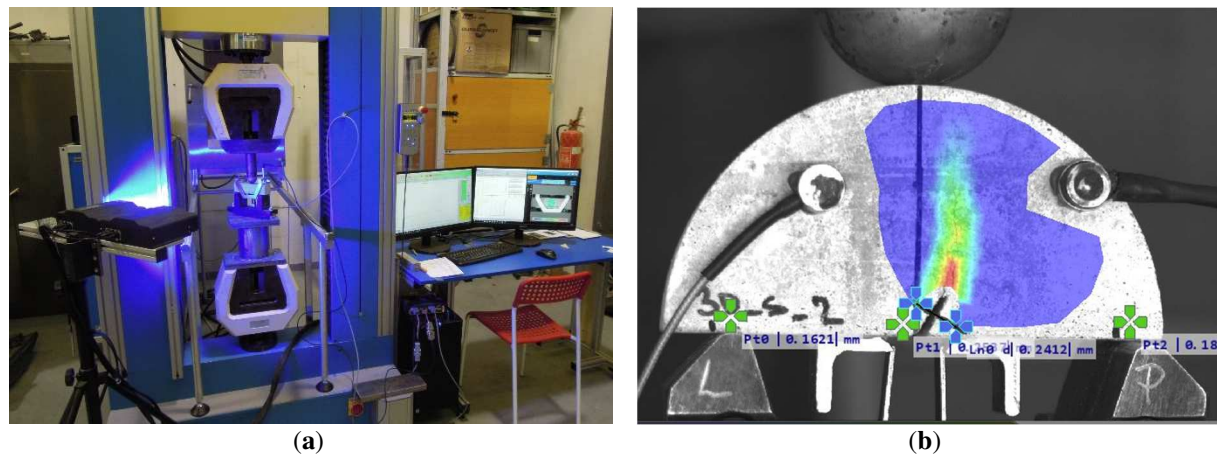


**Figure 9.** Arrangement of 2D video extensometer measurement (a), and example of crack propagation and measured surface strains (b) in selected 3PB test configurations.

### I.2.3 ADJUSTMENT OF RECORDED DATA

The outcome of each fracture test in 3PB configuration is a vertical force  $F$  vs.  $d$  diagram and  $F$  vs. *CMOD* diagram. The diagrams recorded during the tests are necessary to be processed to obtain the correct input values for consecutive diagram evaluations using the selected fracture models described below.

At the beginning of the specimen loading, small-sized deviations in the measured values of monitored parameters are often recorded. This effect is caused by small unevenness on the specimens' surface being crushed due to the pressure at the support and loading points. These phenomena usually occur over a short period at the beginning of the test, after which the recorded diagram proceeds with a linear part. It follows that it is appropriate to adjust the beginning part of the diagram to obtain the correct input values for the subsequent diagram evaluation. The adjustment of the recorded diagrams is performed in GTDiPS software [45], which is based on advanced transformation methods used for the processing of extensive point sequences. The processing of recorded data is described for the case of  $F-d$  diagram for illustration.

Figure 10(a) shows the recorded data from the fracture test. The loading during the fracture test is compressive and because of the setting of the testing machine, the recorded values of load are negative. As above-mentioned, the measured deflection is a twofold value of the midspan deflection which is necessary to know for further  $F-d$  diagram evaluation. Therefore, the first

step of recorded data adjustment consists of the change of the minus sign of recorded load values, the division of recorded deflection by two, and the elimination of duplicate points (Figure 10(b)).

The second step is shifting the origin of the coordinate system which consists of the removal of the initial part of the diagram ending at the point where is the maximum derivative, the approximation of the beginning part of the diagram by a straight line which is used to find the point of intersection with a horizontal axis, and the shifting of all points of the diagram equidistantly, thus making the point of intersection the new origin of the coordinate system (Figure 10(c)).

Figure 10(d) shows the final  $F-d$  diagram which is used for further determination of mechanical fracture parameters. The last step of adjustments consists of the smoothing of the diagram and the reduction of the number of points.

It is worth noticing that the same procedure is applied also to processing the recorded  $F-CMOD$  diagrams from 3PB tests and of course also to the other types of fracture test configurations.

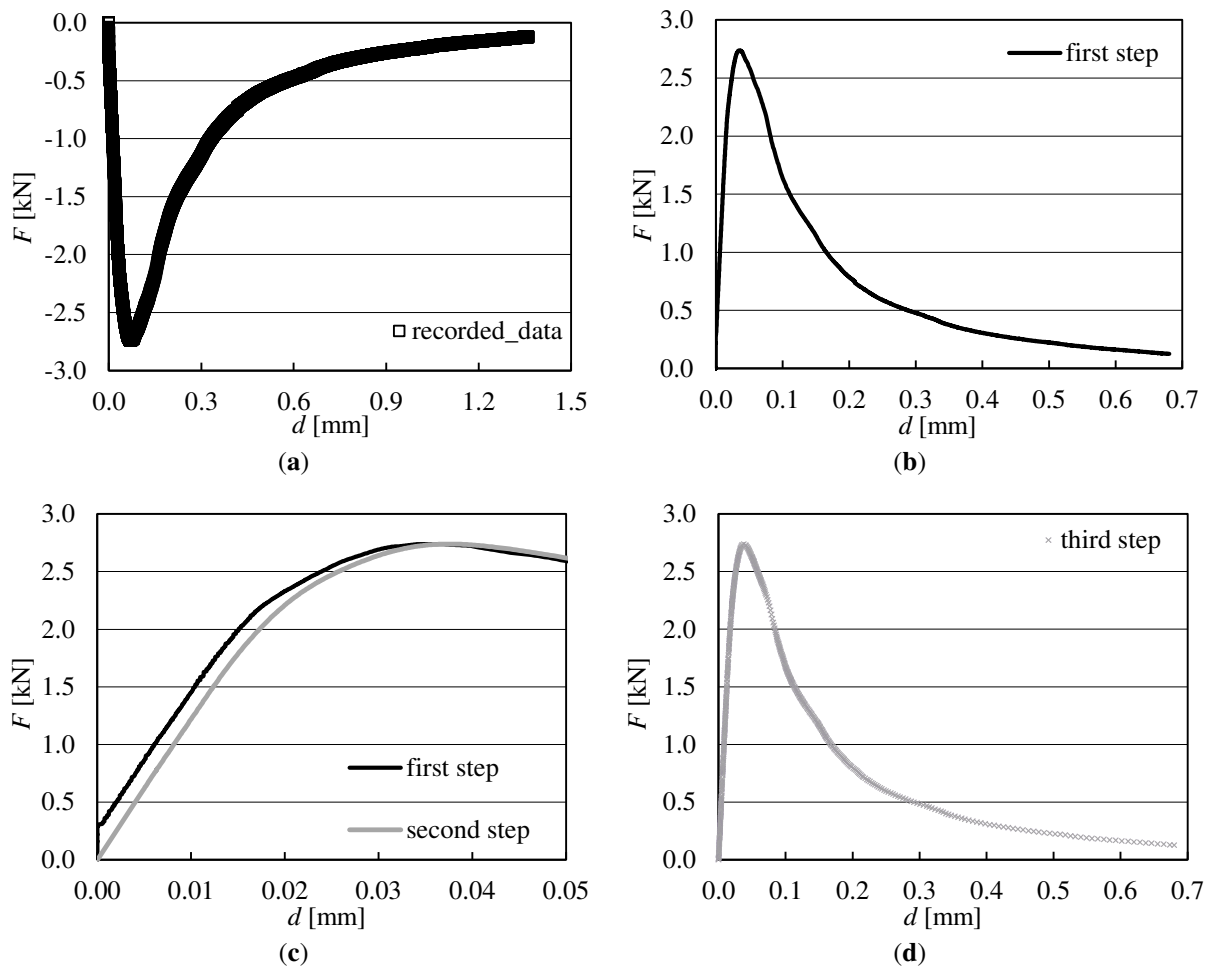


**Figure 10.** Detail of processing of  $F-d$  diagram: recorded data (a), data after the first step of adjustment (b), data after the second step of adjustment – detail of diagram until peak load (c), and data after the third step of adjustment – final diagram used for further evaluation (d).

## I.2.4 DETERMINATION OF MECHANICAL FRACTURE PARAMETERS

As above-mentioned, the most commonly used fracture test configuration is 3PB of the prismatic specimen with the edge notch. Therefore, the determination of mechanical fracture parameters from records of this type of test using the selected fracture models is described in this section.

The value of the static modulus of elasticity  $E$  is calculated from the initial part of the  $F-d$  diagrams according to [4] with modification by Stibor [46]:

$$E = \frac{F_i}{4Bd_i} \left( \frac{S}{W} \right)^3 \left[ 1 - 0.387 \frac{W}{S} + 12.13 \left( \frac{W}{S} \right)^{2.5} \right] + \frac{9}{2} \frac{F_i}{Bd_i} \left( \frac{S}{W} \right)^2 F_1(\alpha_0), \quad (1)$$

where  $F_i$  is the vertical force in the ascending linear part of the diagram,  $B$  is the specimen width,  $d_i$  is the midspan deflection corresponding to the force  $F_i$ ,  $W$  is the specimen height,  $S$  is the span length (see Figure 2(a)), and

$$F_1(\alpha_0) = \int_0^{\alpha_0} \alpha Y^2(\alpha) d\alpha, \quad (2)$$

where  $\alpha = a/W$  is relative crack length and then  $\alpha_0 = a_0/W$  is relative notch depth ( $a_0$  is the initial notch depth), and  $Y(\alpha)$  is the geometry function for the 3PB configuration proposed by Brown and Strawley [4]:

$$Y(\alpha) = 1.93 - 3.07\alpha + 14.53\alpha^2 - 25.11\alpha^3 + 25.80\alpha^4. \quad (3)$$

The fracture toughness value is determined based on the linear elastic fracture mechanics (LEFM) approach for brittle fracture. This parameter is related to the stress field near the tip of the crack. The fracture toughness value  $K_{Ic}$  is calculated using this formula [4]:

$$K_{Ic} = \frac{6M_{\max}}{BW^2} Y(\alpha_0) \sqrt{a_0}, \quad (4)$$

where  $M_{\max}$  is the bending moment due to the maximum load  $F_{\max}$  and self-weight.

Several adaptations of LEFM have been proposed to cover the nonlinear behaviour of the quasi-brittle materials. One of them is the effective crack model ECM [4], which includes the effect of the pre-peak nonlinear behaviour of a real quasi-brittle structure containing the initial notch through an equivalent elastic structure containing a notch of effective length  $a_e > a_0$ . The effective crack length  $a_e$  is calculated from the secant stiffness of the specimen corresponding to the maximum load  $F_{\max}$  and matching midspan deflection  $d_{F_{\max}}$ . The  $a_e$  for the prismatic specimen with a central edge notch tested in the 3PB configuration is determined according to [4] from the following relationship:

$$d_{F_{\max}} = \frac{F_{\max}}{4BE'} \left( \frac{S}{W} \right)^3 \left[ 1 + \frac{5qS}{8F_{\max}} + \left( \frac{W}{S} \right)^2 \left\{ 2.70 + 1.35 \frac{qS}{F_{\max}} \right\} - 0.84 \left( \frac{W}{S} \right)^3 \right] + \frac{9}{2} \frac{F_{\max}}{BE'} \left( 1 + \frac{qS}{2F_{\max}} \right) \left( \frac{S}{W} \right)^2 F_1(\alpha_e), \quad (5)$$

where  $E'$  is the static modulus of elasticity corresponding to secant stiffness, and  $q$  is the self-weight of the specimens per unit length.

Subsequently, the effective fracture toughness value  $K_{Ic}$  is calculated using a LEFM formula eq. (4) where  $\alpha_0$  is replaced by  $\alpha_e$ . Since the effective crack length  $a_e$  is in eq. (2) as the argument of integral, the problem is solved by an iterative method.

The complete  $F-d$  diagrams, including their post-peak parts, are employed to determine the work of fracture  $W_F$  value, which is given by the area under the diagram. In this case,  $W_F$  is calculated according to the Stibor [46], where the area under the measured diagram, the effect of the unmeasured part, and the self-weight of the specimen are considered. After that, the specific fracture energy  $G_F$  value is determined according to the RILEM recommendation [6] as the average energy given by dividing the total  $W_F$  by the projected fracture area  $A_{lig}$  (i.e. the area of the initially uncracked ligament):

$$G_F = \frac{W_F}{(W - a_0)B}. \quad (6)$$

The double- $K$  fracture ( $2K$ ) model [47] is used for the evaluation of the  $F-CMOD$  diagrams to determine selected fracture parameters. The parameters describing different phases of the fracture process are determined using this fracture model. The unstable fracture toughness  $K_{Ic}^{un}$  is defined as the critical stress intensity factor corresponding to the  $F_{max}$  and it represents the phase of unstable crack propagation. This parameter is similar to the effective fracture toughness  $K_{Ic}$  used in the ECM by Karihaloo [4]. The equivalent elastic crack length  $a_c$  is determined from the following equation [47]:

$$CMOD_{F_{max}} = \frac{6F_{max}Sa_c}{BW^2E}V(\alpha'_c), \quad (7)$$

where  $CMOD_{F_{max}}$  is  $CMOD$  corresponding to maximum load  $F_{max}$ , and

$$V(\alpha'_c) = 0.76 - 2.28\alpha'_c + 3.87\alpha'_c{}^2 - 2.04\alpha'_c{}^3 + \frac{0.66}{(1 - \alpha'_c)^2}, \quad (8)$$

where  $\alpha'_c = (a_c + H_0) / (W + H_0)$ ;  $H_0$  is the thickness of blades fixed on the bottom surface of the specimens between which the strain gauge is placed.

Once the equivalent elastic crack length  $a_c$  is known, the  $K_{Ic}^{un}$  is determined according to eq. (4) where  $\alpha$  is replaced with  $\alpha_c$ , and the geometry function is in this case [4]:

$$Y(\alpha_c) = \frac{1.99 - \alpha_c(1 - \alpha_c)(2.15 - 3.93\alpha_c + 2.70(\alpha_c)^2)}{(1 + 2\alpha_c)(1 - \alpha_c)^{3/2}}. \quad (9)$$

The important parameter for the nonlinear fracture mechanics calculations is the relation between the stress and crack opening displacement, see Figure 11.

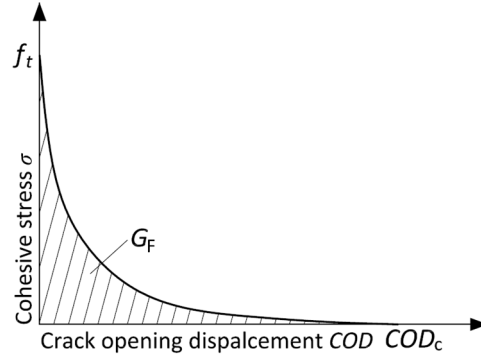


**Figure 11.** The parameters of softening function.

The fracture energy  $G_F$  is a derivative parameter of this relation, which represents the area under this curve (softening function). There are two ways how to obtain the parameters of the softening function. The first way is based on the experimental determination of the  $G_F$  from the uniaxial tensile strength test with deformation-controlled loading. The  $G_F$  is then calculated as the area under the  $\sigma$ – $COD$  diagram. However, it is quite complicated to perform such a test in a stable way for the specimen made of quasi-brittle material, i.e. to catch also the post-peak part of the diagram. Another way consists of the indirect method of determination of critical crack opening displacement  $COD_c$ . In this case, the  $G_F$ , tensile strength  $f_t$ , determined experimentally from the 3PB test and uniaxial tensile test, respectively, and the suitable shape of softening function are the input parameters [48]. Based on the author's previous studies it can be stated that the type of softening function (bilinear or nonlinear) had no significant effect on the calculated values of fracture parameters. The input parameters of the softening function are more important, especially the way of estimation of tensile strength. As above-mentioned, carrying out the uniaxial tensile test for quasi-brittle materials is quite complicated. Therefore, the compressive strength values are commonly used for the estimation of the tensile strength of the materials. However, it is more appropriate to determine the tensile strength by an inverse analysis, for example, based on the artificial neural network [49, 50]. The principle consists in the identification of the material parameters, which gives the corresponding  $F$ – $d$  diagrams response as obtained during real-time specimen loading. It is presumed that such strength is very close to the uniaxial tensile strength.

In the  $2K$  model, the softening function has to be also known to calculate cohesive toughness at critical condition  $K_{Ic}^c$ , which can be interpreted as an increase in the resistance to crack propagation caused by bridging of aggregate grains and other toughening mechanisms in the fracture process zone FPZ [47]. In the following part, the relations using the nonlinear softening function according to Hordijk [48] are introduced for illustration. The cohesive stress  $\sigma(CTOD_c)$  at the tip of an initial notch at the critical state can be then obtained from this softening function:

$$\sigma(CTOD_c) = f_t \left\{ \left[ 1 + \left( c_1 \frac{CTOD_c}{COD_c} \right)^3 \right] \exp \left( -c_2 \frac{CTOD_c}{COD_c} \right) - \frac{CTOD_c}{COD_c} (1 + c_1^3) \exp(-c_2) \right\}, \quad (10)$$

where  $CTOD_c$  is the critical crack tip opening displacement according to Jenq and Shah [51]:

$$CTOD_c = CMOD_{F_{\max}} \left( \left( 1 - \frac{a_0}{a_c} \right)^2 + (1.081 - 1.149\alpha_c) \left( \frac{a_0}{a_c} - \left( \frac{a_0}{a_c} \right)^2 \right) \right)^{\frac{1}{2}}, \quad (11)$$

and  $c_1$  and  $c_2$  are the material constants, which are taken from [47].  $COD_c$  is calculated using the value of fracture energy  $G_F$  determined using eq. (6) or by the inverse analysis [49, 50] according to this formula:

$$COD_c = \frac{5.136G_F}{f_t}. \quad (12)$$

Subsequently, the linear function for the calculation of cohesive stress  $\sigma(x)$  along the length of the equivalent elastic crack can be formulated:

$$\sigma(x) = \sigma(CTOD_c) + \frac{x - a_0}{a_c - a_0} (f_t - \sigma(CTOD_c)). \quad (13)$$

Once this relation is known, the cohesive fracture toughness  $K_{Ic}^c$  is determined as follows:

$$K_{Ic}^c = \int_{a_0/a_c}^1 2 \sqrt{\frac{a_c}{\pi}} \sigma(U) F(U, \alpha_c) dU, \quad (14)$$

where the substitution  $U = x/a_c$  is used and  $F(U, \alpha_c)$  is determined according to [52]:

$$F(U, \alpha_c) = \frac{3.52(1-U)}{(1-\alpha_c)^{3/2}} - \frac{4.35 - 5.28U}{(1-\alpha_c)^{1/2}} + \left( \frac{1.30 - 0.30U^3}{(1-U^2)^{1/2}} + 0.83 - 1.76U \right) [1 - (1-U)\alpha_c]. \quad (15)$$

The following formula based on the formerly obtained parameters is used to calculate the initial cracking toughness  $K_{Ic}^{ini}$ :

$$K_{Ic}^{ini} = K_{Ic}^{un} - K_{Ic}^c, \quad (16)$$

the  $K_{Ic}^{ini}$  represents the beginning of stable crack propagation.

At last, the load level  $F_{ini}$ , which expresses the load at the outset of stable crack propagation from the initial notch, is determined according to the relation:

$$F_{ini} = \frac{4 \cdot S_M \cdot K_{Ic}^{ini}}{S \cdot Y(\alpha_0) \cdot \sqrt{a_0}}, \quad (17)$$

where  $S_M$  is the section modulus (calculated as  $S_M = 1/6 \cdot B \cdot W^2$ ), and  $Y(\alpha_0)$  is the geometry function according to eq. (9) where  $\alpha_0$  is used instead of  $\alpha_c$ .

### **I.3 FATIGUE FRACTURE TESTS**

Many structures in civil engineering are often subjected not only to static but also to repetitive cyclic loads of high-stress amplitude. The phenomenon known as material fatigue, a process in which progressive and permanent internal damage occurs in materials subjected to repeated loading, is a serious problem also for quasi-brittle materials [13]. The processes are connected with the progressive growth of internal microcracks which on a macro level leads to changes in material properties. Therefore, for the complex description of damage processes in quasi-brittle materials is knowledge of fatigue behaviour very important.

Concrete and other quasi-brittle materials are highly heterogeneous materials and thus processes occurring within their structure and leading to their degradation under cyclic loading are more complicated in comparison to those affecting metals [13]. This is one reason why the understanding of fatigue failure in these materials is still lacking in comparison to that of ferrous materials, even though concrete is a widely used construction material.

As in the case of static tests, different loading arrangements have been used in fatigue testing, including compression [53], tension [54], and bending [55, 56] tests. The most common method of fatigue testing, by far, is using the bending tests, also the test specimens with an initial stress concentrator are used [57, 58].

As in the case of static fracture tests, the author's attention is paid to the evaluation of the cyclic 3PB test and the determining fatigue characteristics of composites with the brittle matrix. The cyclic tests are much more time-consuming compared to static ones. Therefore, to achieve a relevant evaluation of experiments, it is necessary in the case of quasi-brittle materials to consider also the ageing of specimens. A correction procedure of the measured data based on static compressive strength measurements covering the time interval of performing the fatigue tests was suggested and checked. The procedure is applied to Wöhler curves obtained from cyclic 3PB tests of beam specimens with a central edge notch.

#### **I.3.1 CYCLIC FRACTURE TESTS IN 3PB TEST CONFIGURATION**

The most commonly used specimen shape for cyclic tests is also a standardized prism which is typically used for the determination of mechanical characteristics. The prisms with nominal dimensions  $40 \times 40 \times 160$  mm and  $100 \times 100 \times 400$  mm for composites with fine and coarse aggregate, respectively are usually used. The specimens are before testing provided with the central edge notch (see ligament in Figure 1(a)) with a nominal depth of about 1/10 of the specimen's height which is made by a diamond blade saw.

The fatigue experiments are typically carried out using servo-hydraulic testing machines. Figure 12(a) introduces an example of such a testing machine the Zwick/Roell Amsler HC25 with a loading range of 0–25 kN, which belongs to laboratories of the Institute of Physics of Materials (IPM), Czech Academy of Sciences (CAS). The author of this thesis cooperates with colleagues from IPM, CAS in conducting and evaluating of fatigue tests of specimens made of different quasi-brittle materials over a long period. The typical arrangement of a 3PB cyclic fracture test configuration is shown in Figure 12(b).

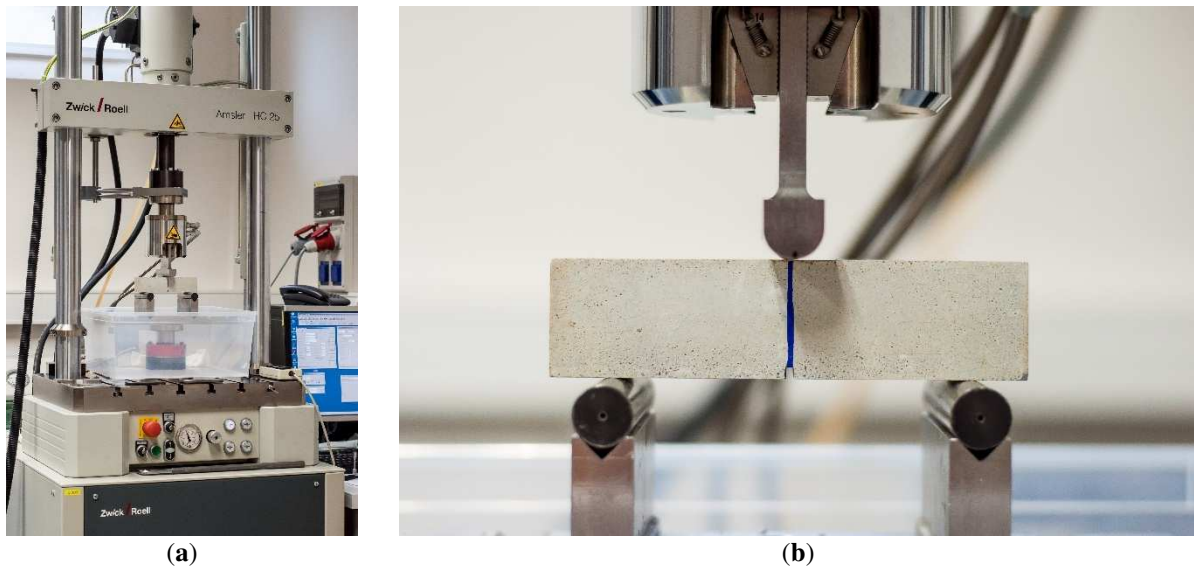


**Figure 12.** The testing machine used for cyclic/fatigue fracture test (a), the arrangement of cyclic test in 3PB configuration (b).

In practice, the structures are subjected to random fatigue loading. This process of loading is very difficult to model in laboratory conditions, therefore there is an effort to simplify the course of loading. The most frequent way is the replacement of the random loading by sinusoidal load, which is also used in experiments described here. The cyclic loading process is governed by a force; the force amplitude is controlled. The stress ratio  $R = F_{Fmin}/F_{Fmax} = 0.1$ , where  $F_{Fmin}$  and  $F_{Fmax}$  refer to the minimum and maximum load of a sinusoidal wave in each cycle. The load frequency is set to 10 Hz to cover all fatigue regions in a reasonable time. The number of cycles  $N$  at failure is recorded for each specimen.

The fatigue loading is traditionally divided into two categories [59] i.e. low-cycle and high-cycle loading. Low-cycle loading involves the application of a few load cycles at high-stress levels. On the other hand, high-cycle loading is characterized by a large number of cycles at lower stress levels. In this chapter, attention is paid to high-cycle fatigue. Therefore, the upper limit to the number of cycles  $N$  to be applied is selected as 2 million cycles. The test is finished when the failure of the specimen occurred or the upper limit of loading cycles is reached, whichever occurred first.

### I.3.2 EXPERIMENTAL DETERMINATION OF WÖHLER CURVE

Various approaches have been used to assess the fatigue life of structural members in recent years. The generally accepted approach in engineering practice is based on empirically derived  $S_F-N$  diagrams known as Wöhler curves (applied stress during the load cycle  $S_F$  vs. the number of cycles to failure  $N$ ), see Figure 13.  $S_F-N$  test data are usually displayed in a semi-logarithmic plot, where its course is approximated by slanting and horizontal lines. The parameters of the  $S_F-N$  curve are determined only for test specimens that are broken during the cyclic test (circles in Figure 13), the specimens which withstand 2 million cycles are not taken into consideration (run-outs – circles with arrows in Figure 13). With respect to the time demand of cyclic tests, the fatigue limit is determined as the highest stress level at which three test specimens withstand

2 million cycles. However, this fatigue limit is not finite, and fatigue failure can occur with more load cycles.

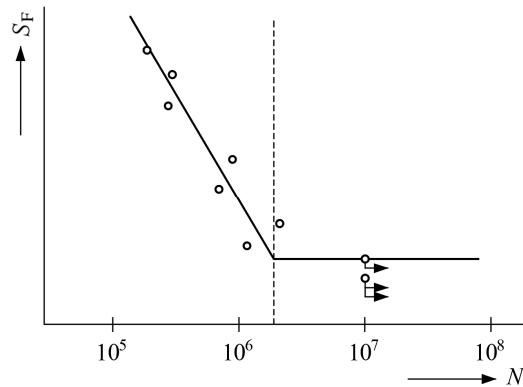


**Figure 13.** Typical  $S_F-N$  (Wöhler) curve according to [60].

The  $S_F-N$  curve can be constructed covering different stress levels depending on the used load for its determination, i.e. using the maximum load of a sinusoidal wave  $F_{Fmax}$ , the load amplitude  $F_a = (F_{Fmax} - F_{Fmin}) / 2$  or the load range  $\Delta F = F_{Fmax} - F_{Fmin}$ .

Fatigue tests of quasi-brittle materials are characterized by a relatively large scattering of the measured number of cycles at individual stress levels, therefore for an appropriate determination of the Wöhler curve, several specimens have to be tested at each stress level. The first stress level is equal to effective flexural strength. Then stress level is reduced gradually by approximately 10 % and the specimen is loaded with cyclic load until its failure or when the fatigue limit is reached. A minimum of 8–12 specimens of tested material is necessary to determine the Wöhler curve. For a more accurate determination of its parameters, or for its statistical evaluation, 15–20 specimens are needed.

There are several mathematical descriptions of the Wöhler curve, one of them is Basquin’s power law [61]:

$$S_F = a \cdot N^b \quad (18)$$

where  $a$  and  $b$  are material constants.

### I.3.3 CORRECTION PROCEDURE OF WÖHLER CURVE PARAMETERS

Theoretically, all test specimens are broken after the same number of cycles for one particular stress level. However, the fatigue behaviour of heterogeneous quasi-brittle materials is distant from an optimal case and the results show variability. On that account, it is necessary to determine not only the analytical expression of the corresponding  $S_F-N$  curve but also the close-fitting of regression, such as the coefficient of determination  $R^2$ . The variability is connected also with the time demand of cyclic tests which leads to the different ages and thus materials characteristics of the individual specimen during the cyclic tests. The suggested correction procedure allows a more accurate determination of the fatigue parameters corresponding to the age of the specimen when the cyclic test is performed.

The measured stress levels of the  $S_F-N$  curve are divided by coefficients determined from the approximation curve of relative compressive strength values to obtain correct values of fatigue characteristics corresponding to the age of the specimen at which a particular cyclic test is performed. The measured data are standardized to a particular age of specimens by this procedure. Compressive strength is chosen because it is the most commonly determined mechanical parameter of quasi-brittle composites and it is used as an input parameter in the structural design. The compressive strength test is also less time-consuming in comparison with the static fracture test. Nevertheless, the presented procedure can be used with any other mechanical or fracture parameter [62].

The measured values of compressive strength are divided by the average value at the chosen specimen's age. In the example presented below in Figure 14, the compressive strength values at the specimen's age of 28 days are chosen. The compressive strength at the age of 28 days is usually used as a reference value in the design of cement-based composites. However, in the case of composites based on alkali-activated binder (AAB) the mechanical fracture parameters significantly changes during the specimen's ageing also after 90 days so different reference age of specimens can be chosen based on the investigated material. By this procedure, the relative compressive strength values for all investigated ages of specimens are obtained. These values are then approximated by the selected function. The modified form of the function according to Abdel-Jawad [63] is presented here:

$$rf_c = c \cdot (1 - e^{-m \cdot t^n}) \quad (19)$$

where  $t$  is the specimen's age in days,  $rf_c$  is the dimensionless relative compressive strength,  $c$  is the coefficient corresponding with an asymptote of the approximation curve, in other words, the ratio of the theoretical value of the compressive strength at Infinitum to the value of compressive strength at the chosen specimen's age, and  $m$ ,  $n$  are the coefficients corresponding with the size of the time-dependent change of compressive strength, which is generally dependent on the compositions of the used mixture. The approximation is performed using the GTDiPS software [45]. The procedure is based on the nonlinear least-square method provided by genetic algorithms which are implemented in this open-source Java GA package [45].

The above-described procedure can be applied also by using simple approximation (regression) curves which cover only the interval in which fatigue tests are performed [62]. For example, the power, logarithmic or polynomial trendline is possible to use, which is part of MS EXCEL software.

For illustration, the approximation curve and its coefficients according to eq. (19) for relative compressive strength values related to the mean value of this parameter at the specimen's age of 28 days of C30/37 strength class concrete is displayed in Figure 14(a). In this case, the cyclic tests of concrete specimens were performed between the age of 30 to 150 days. From Figure 14(a) is evident that the compressive strength value increased in this interval by about 25 %. The results of cyclic fracture tests of specimens in 3PB configuration at different load levels are summarized in Figure 14(b) in the form of the Wöhler curve (eq. (18)). The coefficient of determination  $R^2$  of the  $S_F-N$  curve determined directly from the measured values is relatively low for this type of

concrete. In addition to the measured data, the standardized data using the coefficients obtained from the advanced approximation curve of the relative compressive strength values (Figure 14(a)) are also plotted, including the analytical expression of the  $S_F-N$  and  $R^2$ . This procedure led to a significant increase in the value of the dimensionless coefficient of determination  $R^2$  from 0.38 to 0.70. The obtained results can be considered as evidence of the efficacy of the described correction procedure.

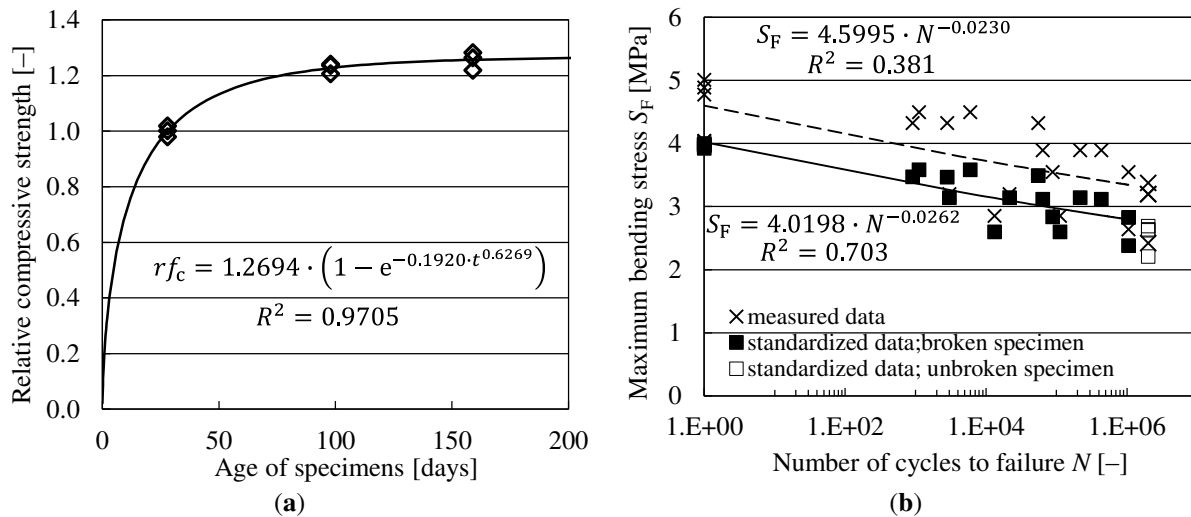


**Figure 14.** The approximation curve for relative compressive strength values related to the specimen's age of 28 days (a), the example of  $S_F-N$  curve plotted for measured and standardized data at the specimen's age of 28 days; the horizontal axis is plotted in logarithmic scale (b).

# **Part II**



## **II.1 FRACTURE AND FATIGUE BEHAVIOUR OF FINE-GRAINED COMPOSITE BASED ON SODIUM HYDROXIDE-ACTIVATED SLAG**

The articles present the main results obtained within the implementation of junior research grant project No. 18-12289Y; “Advanced characterization of crack propagation in composites based on alkali activated matrix“ supported by Czech Science Foundation. The author of this thesis was the principal investigator of this project. Final evaluation – outstanding project results (of international importance) and the project was among the nominated for the GACR President’s awards for 2021.

### **II.1.1**

Šimonová, H., Kucharczyková, B., Bílek, V., Malíková, L., Miarka, P., Lipowczan, M. Mechanical Fracture and Fatigue Characteristics of Fine-Grained Composite Based on Sodium Hydroxide-Activated Slag Cured under High Relative Humidity. *Applied Sciences*. 2021, vol. 11, Article No. 259. <https://doi.org/10.3390/app11010259> (Q3–Engineering, multidisciplinary; 3 citations without self-citations of all authors according to WoS)

#### *II.1.1 Description*

The obtained results presented in the article are valuable primarily because the material parameters are monitored from a long-term point of view, and a complex set of material characteristics was collected as well. The attention was also focused on the fracture and fatigue parameters that are not commonly investigated. These parameters give more comprehensive information about material behaviour and could be utilized in the effective design of newly develop quasi-brittle materials with the alternative binder to commonly used Portland cement.

#### *II.1.1 Role of the author – the percentage of contribution: 30 %*

Hana Šimonová is the main author of this article responsible for the concept, the methodology and the evaluation of performed fracture and fatigue experiments of the presented research. Furthermore, she prepared the original draft of the article which was later reviewed in cooperation with other co-authors.

### **II.1.2**

Malíková, L., Miarka, P., Kucharczyková, B., Šimonová, H. Williams expansion utilized for assessment of crack behaviour under mixed-mode loading in alkali-activated fine-grained composite. *Fatigue Fract Eng Mater Struct*. 2021, Vol. 44, Iss. 5, pp. 1151–1161. <https://doi.org/10.1111/ffe.13418>. (Q2–Engineering, mechanical; 2 citations without self-citations of all authors according to WoS)

#### *II.1.2 Description*

The article concerns an experimental and extensive numerical study on the crack deflection angle in a semi-circular disc made of an alkali-activated fine-grained composite under mixed-mode conditions. The results presented in the previous article (II.1.1) were used as valuable input parameters of material models used for numerical simulations of crack propagation in semi-circular specimens loaded under mixed-mode I/II conditions. Recommendations regarding the necessity of the multi-parameter fracture mechanics approach based on the mutual comparison of experimental and numerical data obtained on specimens made of AAB-based

composite can be transferred to any other similar type of quasi-brittle material loaded under mixed-mode I+II.

II.1.2 *Role of the author – the percentage of contribution: 20 %*

Hana Šimonová is a co-author of this paper responsible for the preparation and evaluation of fracture tests of semi-circular discs made of an alkali-activated fine-grained composite. Furthermore, she prepared the original draft of the article's parts describing the material and fracture tests.

Article

# Mechanical Fracture and Fatigue Characteristics of Fine-Grained Composite Based on Sodium Hydroxide-Activated Slag Cured under High Relative Humidity

Hana Šimonová <sup>1,\*</sup> , Barbara Kucharczyková <sup>1</sup> , Vlastimil Bílek <sup>2</sup> , Lucie Malíková <sup>1</sup> , Petr Miarka <sup>1</sup>   
and Martin Lipowczan <sup>1</sup> 

<sup>1</sup> Faculty of Civil Engineering, Brno University of Technology, Veveří 331/95, 602 00 Brno, Czech Republic; barbara.kucharczykova@vutbr.cz (B.K.); malikova.l@fce.vutbr.cz (L.M.); petr.miarka@vut.cz (P.M.); lipowczan.m@fce.vutbr.cz (M.L.)

<sup>2</sup> Faculty of Chemistry, Brno University of Technology, Purkyňova 464/118, 612 00 Brno, Czech Republic; bilek@fch.vut.cz

\* Correspondence: simonova.h@vutbr.cz; Tel.: +420-541-147-381

**Abstract:** A typical example of an alternative binder to commonly used Portland cement is alkali-activated binders that have high potential as a part of a toolkit for sustainable construction materials. One group of these materials is alkali-activated slag. There is a lack of information about its long-term properties. In addition, its mechanical properties are characterized most often in terms of compressive strength; however, it is not sensitive enough to sufficiently cover the changes in microstructure such as microcracking, and thus, it poses a potential risk for practical utilization. Consequently, the present study deals with the determination of long-term mechanical fracture and fatigue parameters of the fine-grained composites based on this interesting binder. The mechanical fracture parameters are primarily obtained through the direct evaluation of fracture test data via the effective crack model, the work-of-fracture method, the double-*K* fracture model, and complemented by parameter identification using the inverse analysis. The outcome of cyclic/fatigue fracture tests is represented by a Wöhler curve. The results presented in this article represent the complex information about material behavior and valuable input parameters for material models used for numerical simulations of crack propagation in this quasi-brittle material.

**Keywords:** fracture; fatigue; experiment; slag; alkali activation; fine-grained composite



**Citation:** Šimonová, H.; Kucharczyková, B.; Bílek, V.; Malíková, L.; Miarka, P.; Lipowczan, M. Mechanical Fracture and Fatigue Characteristics of Fine-Grained Composite Based on Sodium Hydroxide-Activated Slag Cured under High Relative Humidity. *Appl. Sci.* **2021**, *11*, 259. <https://doi.org/10.3390/app11010259>

Received: 1 December 2020

Accepted: 25 December 2020

Published: 29 December 2020

**Publisher's Note:** MDPI stays neutral with regard to jurisdictional claims in published maps and institutional affiliations.



**Copyright:** © 2020 by the authors. Licensee MDPI, Basel, Switzerland. This article is an open access article distributed under the terms and conditions of the Creative Commons Attribution (CC BY) license (<https://creativecommons.org/licenses/by/4.0/>).

## 1. Introduction

Although Portland cement and its blends are and in the near future will be the most common binders in practical applications around the world because of their availability, versatility, and tradition, there are increasing efforts to search for some alternative binders. A typical example is alkali-activated binders that have high potential as a part of a toolkit for sustainable construction materials, especially in applications where resistance to elevated temperatures or aggressive environments is required [1]. One group of alkali-activated materials is alkali-activated slag (AAS), which sets and hardens rapidly even at room temperatures and reaches high strengths [2]. On the other hand, AAS suffers from extensive shrinkage accompanied by cracking and was found to be very brittle [3]. There is a lack of information about the long-term properties, fracture characteristics, or fatigue of AAS. In addition, its behavior is characterized most often in terms of its compressive strength; however, this is not sensitive enough to sufficiently cover the changes in microstructure such as microcracking, and thus, it poses a potential risk for practical utilization. Consequently, the present study deals with the determination of long-term mechanical fracture and fatigue parameters of the fine-grained composites based on this interesting binder. To record and evaluate the formation of cracks and their further propagation during the

mechanical fracture tests, it is necessary to design an AAS material with acceptable material characteristics (sufficient compressive and tensile strength, and appropriate value of modulus of elasticity) together with a low potential of cracking. This is rather a challenge in the case of AAS materials for in situ applications with curing under ambient conditions. It was proven that their composition is sensitive to curing conditions, and different behavior can be expected for the different type and dosage of activator. Our own experiment is presented as an example. Two AAS materials of a similar composition containing different activators were produced and cured under wet conditions with relative humidity (RH)  $\geq 95\%$  to observe cracking tendency. Despite the high relative humidity during curing, opened cracks appeared in the case of AAS material activated by waterglass (see Figure 1).

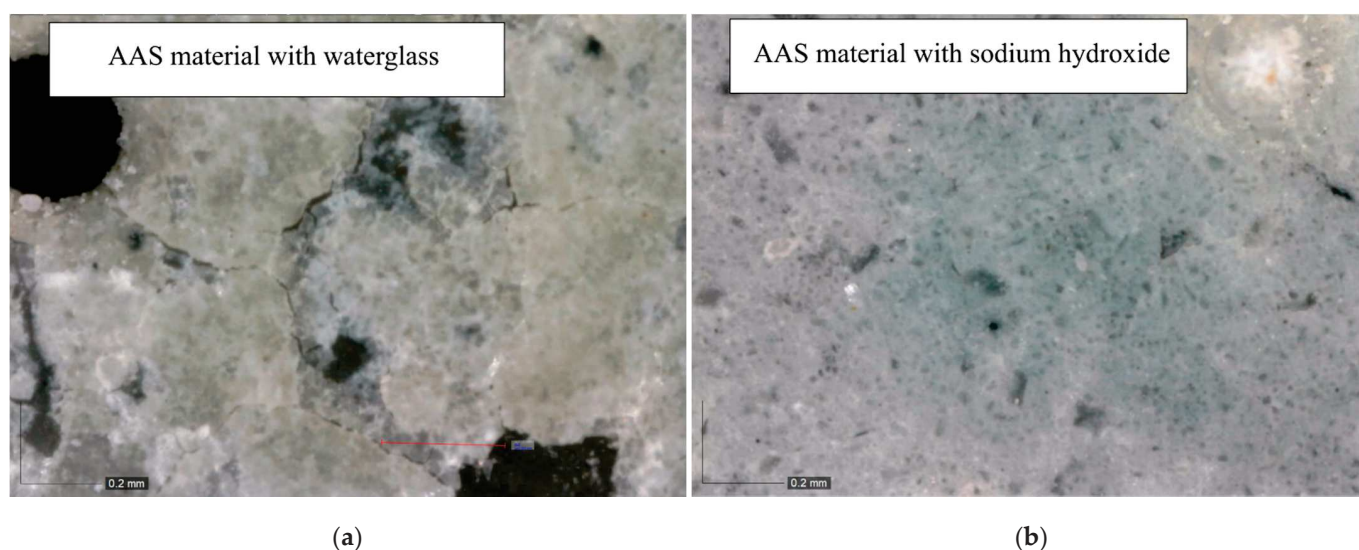


**Figure 1.** The surface of the alkali-activated slag (AAS) materials with a different activator (waterglass (a) and sodium hydroxide (b)) cured in relative humidity (RH)  $\geq 95\%$  (240 $\times$  magnification).

Assessment of the fracture behavior of quasi-brittle materials is performed for notched specimens/structures subjected to mode I of loading. The investigations of the fracture phenomena such as the relation of the fracture process zone (FPZ) extent to the size/geometry/boundary effect, etc., in other modes of loading and/or their combination (mixed-modes of loading) are studied rather rarely despite the fact that the real structures made of quasi-brittle materials in civil engineering applications are usually loaded in a mixed-mode manner. It should also be emphasized that many structures are often subjected not only to static but also to repetitive cyclic loads of high-stress amplitude. Examples of such cyclic loads include automotive and train traffic, machine vibration, and wind action. The processes occurring within the quasi-brittle material structure and leading to its degradation under cyclic loading are more complicated in comparison to those affecting metals [4]. That is the reason why knowledge of the behavior of quasi-brittle materials, not only under static or quasi-static conditions but also under cyclic conditions, is very important for the complex description of crack propagation in such materials. However, fatigue tests of quasi-brittle materials and structures are expensive, and for this reason, numerical modeling [5,6] can represent an effective tool for the prediction of the damage process and fatigue life of such materials under different service conditions. For the effective and correct use of a numerical (material) model, it is often necessary to tune its parameters using data obtained from experimental measurements. The correct evaluation of such data is becoming a prerequisite for the correct use of numerical models in practice.

Therefore, this research area was covered by the currently solved research project “Advanced characterization of cracks propagation in composites based on alkali-activated matrix”. An extensive numerical and experimental analysis of the fracture behavior of

selected composites with an alkali-activated matrix subjected to static (also in the mixed-mode) and cyclic/fatigue loading was performed. For a description of the crack propagation under mixed-mode I/II conditions, various test configurations were designed based on the literature search of test specimens used for testing the fracture parameters of rocks and cement-based composites. For this purpose, semi-circular disc specimens in three-point bending [7–11], centrally cracked Brazilian discs [10,12,13], and prismatic-specimens in asymmetric three- [14,15] or four-point [14,16] bending configurations are mostly used. Semi-circular discs were chosen for the present study. The type of specimens was chosen with respect to the practical application to the in situ structures when drilled cores are usually taken for the verification of real mechanical characteristics. Selected semi-circular specimens with an inclined initial notch were loaded in a three-point bending configuration (SCB) for the purpose of experimental verification of numerical simulations of crack propagation under mixed-mode I/II condition; see the selected configuration in Figure 2a. Note that numerical simulation was performed prior to the experimental verification to suggest different geometrical configurations with various mixed-mode I/II conditions (to cover as wide a range of mixed-mode levels as possible) and to design the experiment. The detailed information can be found in a separate article, which is currently under consideration for publication [17].

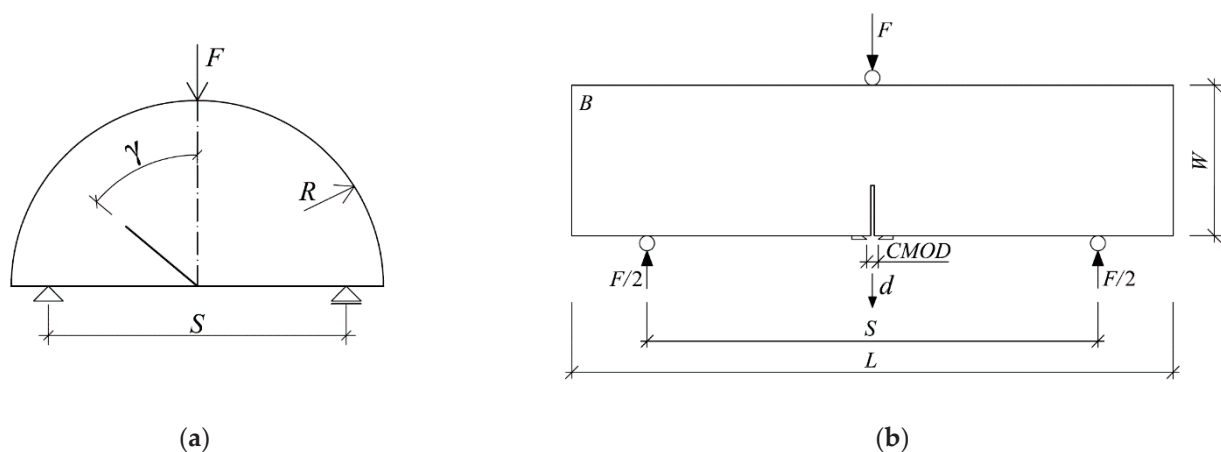


**Figure 2.** Three-point bending fracture test configuration of a selected semi-circular disc specimen with an inclined initial notch (a); and a beam specimen with a central edge notch (b).

The numerical modeling of the fracture initiation and propagation in quasi-brittle materials has been developed for several decades. Impressive results have been achieved with continuous models (usually with the help of the finite element method (FEM)) enhanced by non-linear constitutive relations where, after reaching the tensile strength, the stress decreases gradually with the crack opening. If the model does not contain information about material meso-structure directly, spurious sensitivity of the results to mesh discretization appears [18]. Such mesh dependency must be eliminated with help of a localization limiter (crack band model, non-local model, gradient model). The continuous models are typically studied on simple experiments such as a three-point bending test, but they achieved excellent results also in cases of complex mixed-mode configurations [19]. When some of the models described above shall be applied, several important mechanical fracture parameters need to be determined/known. One of the fundamental fracture parameters is the fracture energy representing cracking resistance and fracture toughness. To be able to estimate the FPZ size and shape, the necessary parameters (such as tensile strength, fracture energy, stress–strain diagram, etc.), methods, and approaches have to be known.

Commonly used standard test specimens (prisms with nominal dimensions of  $40 \times 40 \times 160 \text{ mm}^3$ ) were manufactured and tested under typical configurations to obtain the basic physical, mechanical, fracture, and fatigue characteristics essential for numeri-

cal simulations. The test specimens were provided with an initial notch before the test, and subsequently, static and cyclic/fatigue fracture tests were performed in a three-point bending configuration; see Figure 2b.

The outcome of each static fracture test is a vertical force vs. midspan deflection and vertical force vs. crack mouth opening displacement diagram. The mechanical fracture parameters are primarily obtained through the direct evaluation of fracture test data via the effective crack model [20], the work-of-fracture method [21], and the double-K fracture model [22]. The vertical force vs. midspan deflection diagrams are also used to obtain mechanical fracture parameters indirectly—based on a combination of fracture testing and inverse analysis [23]. The inverse analysis has several advantages, such as its ability to identify parameters whose direct testing and evaluation are difficult or even impossible. The representative of such parameters is the tensile strength. The outcome of cyclic/fatigue fracture tests is represented by a Wöhler curve [4].

For the present study, sodium hydroxide was used as an alkaline activator to produce appropriate test specimens with low potential of cracking. It was experimentally verified by authors (see Figure 1) and confirmed by other researchers that such AAS material reaches sufficiently high strengths together with noticeably lower shrinkage [24,25], and thus, the risk of cracking before the test is reduced. The complex information about the material included the mechanical, fracture, and fatigue characteristics of AAS fine-grained composite used as the input values for a numerical simulation are presented herein. The standard test specimens with nominal dimensions of  $40 \times 40 \times 160 \text{ mm}^3$  were manufactured and tested under typical configurations. Non-traditional curing conditions of ambient temperature and high relative humidity (RH)  $\geq 95\%$  for a long period was chosen to prevent the cracking of the material before fracture and fatigue tests. In practical applications of investigated material, these non-traditional curing conditions can be found in the design of precast elements rather than in situ applications.

## 2. Materials and Methods

### 2.1. Materials and Specimens

A fine-grained composite that used sodium hydroxide-activated slag as a binder and CEN siliceous sand with a maximum grain size of 2 mm (meeting requirements of EN 196-1) in the dose three times higher than the slag weight was produced. Granulated blast furnace slag with a predominant amount of glassy phase ground to the Blaine fineness of  $400 \text{ m}^2/\text{kg}$  was used. It was alkali-activated using sodium hydroxide solution in the dose corresponding to 6%  $\text{Na}_2\text{O}$  of the slag weight. The water-to-slag ratio including water from an activator as well as extra-added water was 0.45. In addition, 1% of lignosulfonate-based plasticizer was used.

The mixing was carried out using a Hobart mixer. First, slag was mixed with liquid components, and then, the sand was gradually added. The total mixing time was 10 min. Then, the fresh mortar was cast into the molds and sealed with stretch polyethylene (PE) foil to prevent moisture loss (Figure 3a). After 24 h, the specimens were demolded and stored under laboratory conditions with the temperature of  $21 \pm 2 \text{ }^\circ\text{C}$  in a closed box with RH  $> 95\%$  (Figure 3b) up to the date the particular tests were performed. There was an exception in the curing conditions for the specimens intended for shrinkage measurement. To observe the cracking tendency under dry-air curing conditions, the specimens were not protected from drying during the whole time of aging (including the first 24 h after molding) and stored in an air-conditioned laboratory with a temperature of  $21 \pm 2 \text{ }^\circ\text{C}$  and RH of  $55 \pm 10\%$ . In this experiment, it is considered as the most critical curing with the risk of cracking.

In total, 72 prismatic specimens with nominal dimensions of  $40 \times 40 \times 160 \text{ mm}^3$  were manufactured for the experiment. The test specimens were manufactured in three batches. The fracture tests of prismatic specimens were performed at the age of 40, 160, and 530 days. The cyclic/fatigue fracture tests were performed between the age of 140 to 160 days. Shrinkage process and the development of dynamic modulus of elasticity were

measured in regular intervals to record the increase in these parameters during the whole duration of the experiment.



**Figure 3.** Manufactured test specimens covered with a stretch PE foil (a); test specimens after demolding prepared to storage in a closed box with RH > 95% (b).

### 2.2. Shrinkage Measurement

Prismatic specimens with dimensions of  $40 \times 40 \times 160 \text{ mm}^3$  equipped with stainless steel markers embedded into the ends of specimens were used for shrinkage measurement. The measurement set contained three test specimens. The measurement started immediately after demolding of the specimens at the age of 24 h and continued at regular intervals until the time when the length changes and mass losses were stabilized. The changes in length were measured using the measurement gauge equipped with the digital probe with a resolution of 0.001 mm. Simultaneously, the mass of each specimen was recorded using the scale with a resolution of 0.1 g. The specimens were stored in an air-conditioned laboratory with a temperature of  $(21 \pm 2) \text{ }^\circ\text{C}$  and RH of  $(55 \pm 10)\%$  during the whole time of measurement.

### 2.3. Dynamic Modulus of Elasticity and Rigidity, and Dynamic Poisson's Ratio

A non-destructive test based on the resonance method was employed to monitor the development of the dynamic modulus of elasticity  $E_{rL}$  and dynamic Poisson's ratio  $\mu_r$  of investigated material during aging. The specimens were stored at laboratory conditions with a temperature of  $21 \pm 2 \text{ }^\circ\text{C}$  in a closed box with RH > 95% (Figure 3b) during the whole time of measurement. The natural frequency of longitudinal and torsional vibrations was measured on the specimens with dimensions of  $40 \times 40 \times 160 \text{ mm}^3$  using a Handyscope HS4 oscilloscope equipped with an acoustic sensor. For more details about the principle of measurement, refer to [26]. The absolute values of  $E_{rL}$  and  $\mu_r$  were calculated in compliance with the ASTM C215-19 [27] as:

$$E_{rL} = 4 \left( \frac{L}{WB} \right) m f_L^2 \quad (1)$$

where  $E_{rL}$  is the dynamic modulus of elasticity,  $L$  is the length of specimens,  $W$  and  $B$  are cross-section dimensions (see Figure 2b),  $m$  is the mass of specimens, and  $f_L$  is the fundamental longitudinal frequency.

$$\mu_r = \left( \frac{E_{rL}}{2 \cdot G_r} \right) - 1 \quad (2)$$

where  $\mu_r$  is the dimensionless dynamic Poisson's ratio,  $E_{rL}$  is the dynamic modulus of elasticity, and  $G_r$  is the dynamic modulus of rigidity, which was calculated as:

$$G_r = 4 \left( \frac{LR}{WB} \right) m f_t^2 \quad (3)$$

where  $R$  is the shape factor (1.183 for a square cross-section prism), and  $f_t$  is the fundamental torsional frequency.

#### 2.4. Static Fracture Tests

As mentioned above, three-point bending (3PB) tests were carried out to determine the selected mechanical fracture characteristics of the investigated composite with alkali-activated slag matrix. The above-mentioned prismatic specimens were provided with an initial notch one day before fracture tests were performed. The central edge notch with a nominal depth of about 1/3 of the specimen's height was made by a diamond blade saw. The span length was set to 120 mm. The specimens were tested at different ages of their hardening, namely at the age of 40, 160, and 530 days. Fracture tests were conducted using the stiff multi-purpose mechanical testing machine LabTest 6.250 with the load range of 0–250 kN. An arrangement of a static 3 PB fracture test is shown in Figure 4a. The loading process was governed by a constant increment of displacement of 0.02 mm/min during the whole course of testing. The vertical displacement (midspan deflection)  $d$  was measured using the inductive sensor mounted in a special measurement frame placed on the specimens (see Figure 4b). Crack mouth opening displacement (CMOD) was measured using a strain gauge mounted between blades fixed on the bottom surface of the test specimens, close to the initial notch (see Figure 4b).



**Figure 4.** Arrangement of static fracture test (a), fracture test configuration in three-point bending (3PB) (b) including the measurement frame (1), and the sensors for measuring the midspan deflection (2) and the crack mouth opening displacement (3).

The outcome of each test is a vertical force  $F$  vs.  $d$  diagram and  $F$  vs.  $CMOD$  diagram. The diagrams recorded during the tests were processed to obtain the correct input values for consecutive diagram evaluations using the selected fracture models described below. In this case, the modification of diagrams covered the elimination of duplicate points, the shifting of the origin of the coordinate system, the smoothing of the diagram, and the reduction of the number of points. The processing of recorded diagrams was performed in GTDiPS software [28], which is based on advanced transformation methods used for the processing of extensive point sequences. The  $F-d$  and  $F-CMOD$  diagrams after the above-mentioned corrections for investigated ages of specimens are introduced in Figure 5.

Note that in the case of  $F$ – $CMOD$  diagrams, only their part until a peak load is used for consecutive evaluation. Therefore, only the details of these parts are introduced in Figure 5d–f.

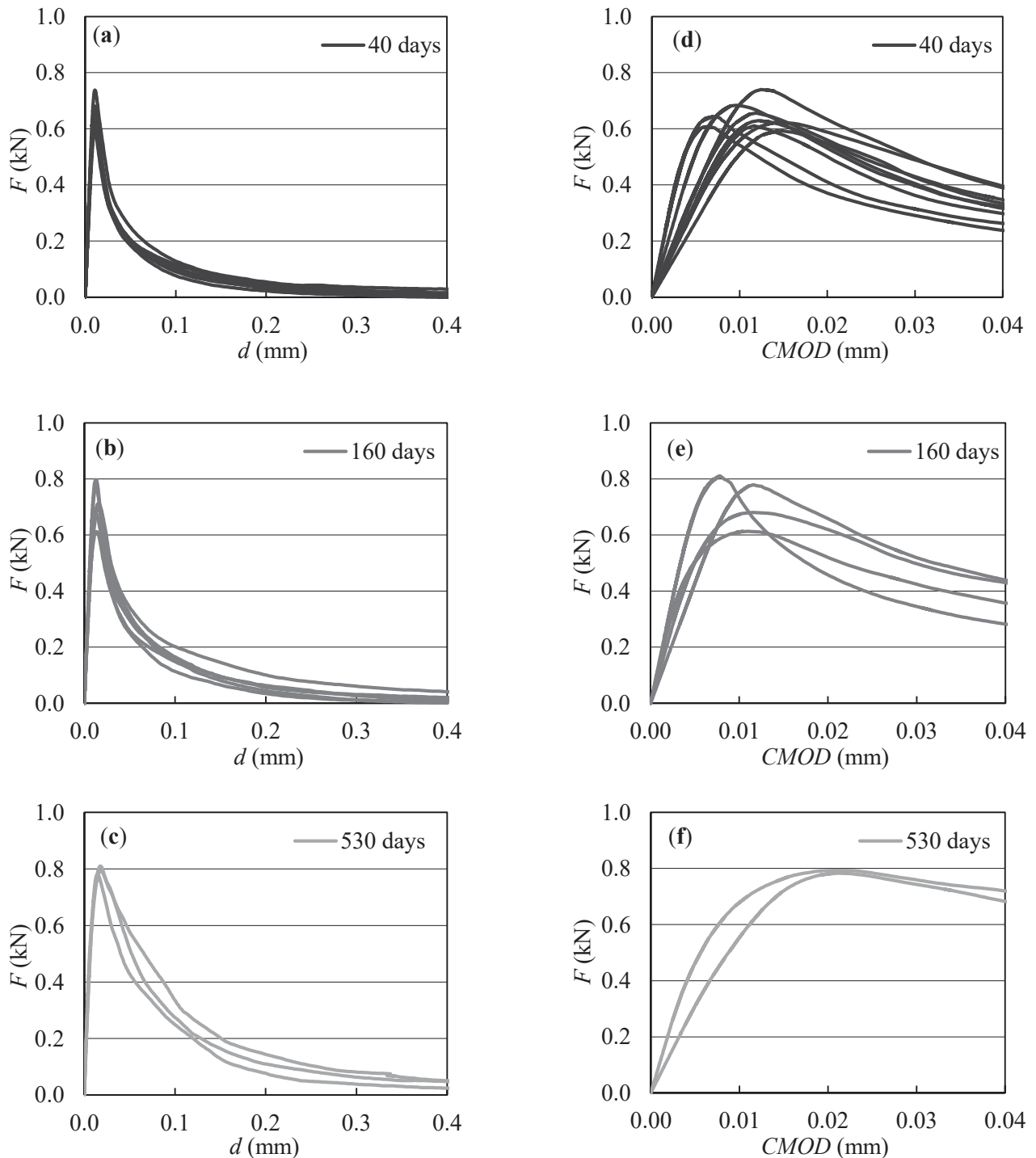


**Figure 5.**  $F$ – $d$  diagrams (a–c) and  $F$ – $CMOD$  diagrams (d–f) from 3PB fracture test for investigated ages of specimens: 40, 160 and 530 days, respectively.

#### 2.4.1. Direct Evaluation of Mechanical Fracture Parameters from $F-d$ Diagrams

The value of static modulus of elasticity was calculated from the initial part of the recorded  $F-d$  diagrams according to Stibor [29]:

$$E = \frac{F_i}{4Bd_i} \left( \frac{S}{W} \right)^3 \left[ 1 - 0.387 \frac{W}{S} + 12.13 \left( \frac{W}{S} \right)^{2.5} \right] + \frac{9}{2} \frac{F_i}{Bd_i} \left( \frac{S}{W} \right)^2 F_1(\alpha_0) \quad (4)$$

where  $F_i$  is the vertical force in the ascending linear part of the diagram,  $B$  is the specimen width,  $d_i$  is the midspan deflection corresponding to the force  $F_i$ ,  $W$  is the specimen height,  $S$  is the span length (see Figure 2b), and

$$F_1(\alpha_0) = \int_0^{\alpha_0} xY^2(x)dx \quad (5)$$

where  $\alpha_0 = a_0/W$  is the relative notch depth ( $a_0$  is the initial notch depth), and  $Y(x)$  is the geometry function for the 3PB configuration proposed by Brown and Strawley [20]:

$$Y(\alpha_0) = 1.93 - 3.07\alpha_0 + 14.53\alpha_0^2 - 25.11\alpha_0^3 + 25.80\alpha_0^4. \quad (6)$$

Several adaptations of linear elastic fracture mechanics (LEFM) have been proposed to consider the non-linear behavior of quasi-brittle materials in an approximate manner. One representative is an effective crack model (ECM) [20], which includes the effect of pre-peak nonlinear behavior of a real quasi-brittle structure containing initial notch through an equivalent elastic structure containing a notch of effective length  $a_e > a_0$ . The effective crack length  $a_e$  is calculated from the secant stiffness of the specimen corresponding to the peak load  $F_{\max}$  and matching midspan deflection  $d_{F_{\max}}$ . The  $a_e$  for the prismatic specimen with a central edge notch tested in the 3 PB configuration was determined according to [20]:

$$d_{F_{\max}} = \frac{F_{\max}}{4BE} \left( \frac{S}{W} \right)^3 \left[ 1 + \frac{5qS}{8F_{\max}} + \left( \frac{W}{S} \right)^2 \left\{ 2.70 + 1.35 \frac{qS}{F_{\max}} \right\} - 0.84 \left( \frac{W}{S} \right)^3 \right] + \frac{9}{2} \frac{F_{\max}}{BE} \left( 1 + \frac{qS}{2F_{\max}} \right) \left( \frac{S}{W} \right)^2 F_1(\alpha_e), \quad (7)$$

where  $q$  is the self-weight of the specimens per unit length.

Subsequently, the effective fracture toughness value  $K_{I_{ce}}$  was calculated using a LEFM formula according to Karihaloo [20]:

$$K_{I_{ce}} = \frac{6M_{\max}S}{BW^2} Y(\alpha_e) \sqrt{a_e}, \quad (8)$$

where  $Y(\alpha_e)$  is the geometry function (6) with  $\alpha_e = a_e/W$  [20], and  $M_{\max}$  is the bending moment due to the maximum applied vertical force  $F_{\max}$  and self-weight of the specimen.

According to the RILEM recommendation [21], the specific fracture energy  $G_f$  is the average energy given by dividing the total work of fracture by the projected fracture area (i.e., the area of the initially uncracked ligament). Therefore, for a specimen of depth  $W$  and initial notch length  $a_0$ , the fracture energy  $G_f$  is given by:

$$G_f = \frac{1}{(W - a_0)B} \left( \int Fdd + m_q d_{\max} \right), \quad (9)$$

where  $m_q$  is the specimen weight,  $d$  is the midspan deflection, and  $d_{\max}$  is the maximum vertical deflection at failure.

Note that the informative compressive strength  $f_c$  was determined according to ČSN EN 196-1 [30] on the fragments remaining after the fracture experiments had been conducted. The maximum vertical force  $F_{\max}$  recorded during the fracture test was used for calculation of the informative flexural strength:

$$f_f = \frac{3F_{\max}S}{2B(W - a_0)^2}. \quad (10)$$

#### 2.4.2. Identification of Mechanical Fracture Parameters from $F-d$ Diagrams

The artificial neural network-based inverse analysis method was employed to identify selected mechanical fracture parameters from  $F-d$  diagrams recorded during 3PB static fracture tests. The inverse procedure proposed by Novák and Lehký [23] transforms fracture test response data into the desired mechanical fracture parameters. This procedure is based on a comparison of the experimentally recorded  $F-d$  diagrams with the results obtained by simulating the 3PB test numerically. The artificial neural network (ANN) is used here as a substitute model of an unknown inverse function between input mechanical fracture parameters and corresponding response parameters.

The dataset intended for training the ANN was prepared numerically using a finite element method (FEM) model. The simulations represent a static 3PB fracture test (see Figure 2b) with random realizations of material parameters. The random values of material parameters were generated using the stratified sampling method and by performing an inverse transformation of the distribution function to reflect the probability distribution of the parameter. In this case, the ATENA FEM program (Červenka et al. [31]) was used for the numerical simulation of the 3PB fracture test. The 3D NonLinear Cementitious 2 material model was selected to govern the gradual evolution of localized damage.

The used identification system comprises of an ensemble of ANNs. Three-dimensional space is defined by three mechanical fracture parameters—modulus of elasticity  $E_{ID}$ , tensile strength  $f_{t,ID}$ , and specific fracture energy  $G_{f,ID}$ . The whole space is divided into several subspaces because of the various materials properties of fine-grained composites with different binders. Each subspace covers a single robust ANN trained for a limited range of parameters. A suitable subspace for the particular analyzed specimen is selected automatically, and the relevant ANN is activated based on an initial analysis of the fracture test response data. The above-mentioned mechanical fracture parameters are calculated by simulating the ANN with obtained response parameters. For more details on ANN-based identification and utilization of the ANN ensemble, see [32,33].

#### 2.4.3. Direct Evaluation of Mechanical Fracture Parameters from $F-CMOD$ Diagrams

The double- $K$  fracture (2K) model [22] was used for the evaluation of the  $F-CMOD$  diagrams to determine selected fracture parameters. The parameters describing different phases of the fracture process were determined using this fracture model. The unstable fracture toughness  $K_{Ic}^{un}$  is defined as the critical stress intensity factor corresponding to the maximum load, and it represents the phase of unstable crack propagation. This parameter is similar to effective fracture toughness (Equation (8)) used in the effective crack model by Karihaloo [20]. The equivalent elastic crack length  $a_c$  was determined from the following equation [22]:

$$CMOD_{F_{\max}} = \frac{6F_{\max}Sa_c}{BW^2E}V(\alpha_c) \quad (11)$$

where  $CMOD_{F_{\max}}$  is  $CMOD$  corresponding to peak load  $F_{\max}$ , and

$$V(\alpha_c) = 0.76 - 2.28\alpha_c + 3.87\alpha_c^2 - 2.04\alpha_c^3 \frac{0.66}{(1 - \alpha_c)^2} \quad (12)$$

where  $\alpha_c = (a_c + H_0)/(W + H_0)$ ;  $H_0$  is the thickness of blades fixed on the bottom surface of the specimens between which the strain gauge was placed.

When the equivalent elastic crack length  $a_c$  is known, the  $K_{Ic}^{un}$  was determined according to Equation (8), when the  $a_c$  is substitute by  $a_e$  and geometry function was in this case [20]:

$$Y(\alpha_c) = \frac{1.99 - \alpha_c(1 - \alpha_c)(2.15 - 3.93\alpha_c + 2.70\alpha_c^2)}{(1 + 2\alpha_c)(1 - \alpha_c)^{3/2}}, \quad (13)$$

where  $\alpha_c = a_c/W$ .

The cohesive softening function has to be known to calculate cohesive fracture toughness  $K_{Ic}^c$ , which can be interpreted as an increase in the resistance to crack propagation caused by the bridging of aggregate grains and other toughening mechanisms in the FPZ. This function describes the relationship between the cohesive stress and effective crack opening displacement. Based on the author’s previous studies, it can be stated that the type of softening function (bilinear or non-linear) had no significant effect on the calculated values of fracture parameters. The input parameters of the softening function are more important, especially the way of estimation of tensile strength. Commonly, the compressive strength values are used for the estimation of the tensile strength of the materials. It is more appropriate to determine the tensile strength directly from the tensile test performed in the configuration similar to the loading of the real structural element. Therefore, the tensile strength  $f_{t,ID}$  was identified from the measured  $F-d$  diagrams (see Section 2.4.2). In this study, the results obtained using the non-linear softening function according to Hordijk [34] are presented. Then, the cohesive stress  $\sigma(CTOD_c)$  at the tip of an initial notch at the critical state can be obtained from this softening function:

$$\sigma(CTOD_c) = f_t \left\{ \left[ 1 + \left( c_1 \frac{CTOD_c}{COD_c} \right)^3 \right] \exp \left( -c_2 \frac{CTOD_c}{COD_c} \right) - \frac{CTOD_c}{COD_c} (1 + c_1^3) \exp(-c_2) \right\} \tag{14}$$

where  $f_t$  is the tensile strength,  $CTOD_c$  is the critical crack tip opening displacement according to Jenq and Shah [35]:

$$CTOD_c = CMOD_c \left( \left( 1 - \frac{a_0}{a_c} \right)^2 + \left( 1.081 - 1.149 \frac{a_c}{W} \right) \left( \frac{a_0}{a_c} - \left( \frac{a_0}{a_c} \right)^2 \right) \right)^{\frac{1}{2}} \tag{15}$$

$COD_c$  is the critical crack opening displacement, and  $c_1$  and  $c_2$  are the material constants, which were taken from [36]. In this paper,  $COD_c$  is calculated using a value of fracture energy  $G_f$  determined using Equation (9) according to this formula [22]:

$$COD_c = \frac{5.136G_f}{f_{t,ID}} \tag{16}$$

Subsequently, the linear function for the calculation of cohesive stress  $\sigma(x)$  along the length of the effective crack can be formulated [22]:

$$\sigma(x) = \sigma(CTOD_c) + \frac{x - a_0}{a_c - a_0} (f_t - \sigma(CTOD_c)) \tag{17}$$

When this relation is known, the cohesive fracture toughness  $K_{Ic}^c$  is determined as follows [37]:

$$K_{Ic}^c = \int_{a_0/a_c}^1 2 \sqrt{\frac{a_c}{\pi}} \sigma(U) F(U, \alpha) dU \tag{18}$$

where the substitution  $U = x/a_c$  is used and  $F(U, \alpha)$  is determined according to [37]

$$F(U, \alpha) = \frac{3.52(1 - U)}{(1 - \alpha)^{3/2}} - \frac{4.35 - 5.28U}{(1 - \alpha)^{1/2}} + \left( \frac{1.30 - 0.30U^{3/2}}{(1 - U^2)^{1/2}} + 0.83 - 1.76U \right) [1 - (1 - U)\alpha] \tag{19}$$

where  $\alpha = a_c/W$ .

The following formula based on the formerly obtained parameters was used to calculate the initial cracking toughness  $K_{Ic}^{ini}$ :

$$K_{Ic}^{ini} = K_{Ic}^{un} - K_{Ic}^c \tag{20}$$

where  $K_{Ic}^{ini}$  represents the phase of stable crack propagation.

At last, the load level  $F_{ini}$  expressing the load at the outset of stable crack propagation from the initial notch was determined according to this relation:

$$F_{ini} = \frac{4 \cdot S_M \cdot K_{Ic}^{ini}}{S \cdot Y(\alpha_0) \cdot \sqrt{a_0}} \quad (21)$$

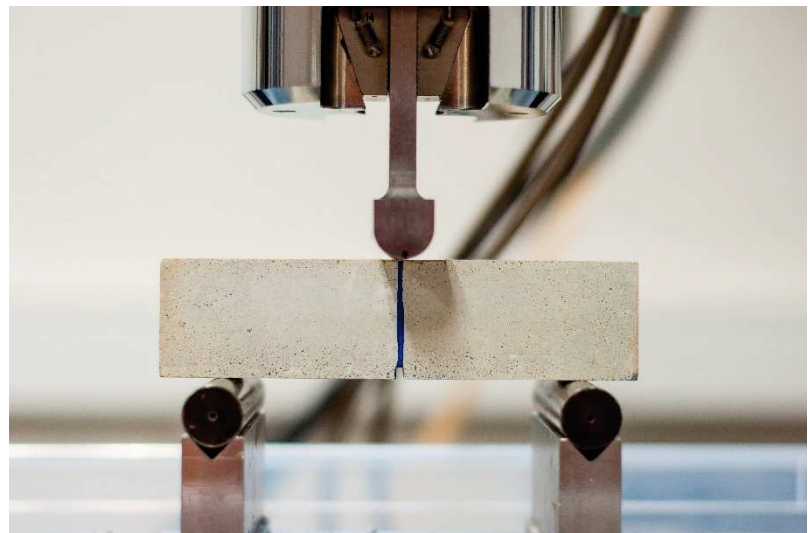
where  $S_M$  is the section modulus (calculated as  $S_M = 1/6 \cdot B \cdot W^2$ ),  $S$  is the span length, and  $Y(\alpha_0)$  is the geometry function (Equation (13)); where  $\alpha_0 = a_0/W$  is used instead of  $\alpha_c$ .

### 2.5. Cyclic/Fatigue Fracture Tests

The 3PB tests were also carried out to determine the basic fatigue characteristics of the investigated composite with an alkali-activated slag matrix. The central edge notch with a nominal depth of about 1/10 of the specimen's height was made by a diamond blade saw. The span length was set to 120 mm. The specimens were tested at different ages of their hardening, namely between the age of 140 and 160 days. The cyclic fracture tests were conducted using the servo-hydraulic testing machine Zwick/Roell Amsler HC25 with the load range of 0–25 kN (Figure 6a). An arrangement of a 3PB cyclic fracture test configuration is shown in Figure 6b. The loading process was governed by a force; the force amplitude was controlled. The stress ratio  $R = F_{Fmin}/F_{Fmax} = 0.1$ , where  $F_{Fmin}$  and  $F_{Fmax}$  refer to the minimum and maximum load of a sinusoidal wave in each cycle. The load frequency was set to 10 Hz. The number of cycles before failure was recorded for each specimen. The specimens were loaded in the range of high-cycle fatigue from  $10^3$  to  $10^6$  number of cycles. Therefore, the upper limit to the number of cycles  $N$  to be applied was selected as 2 million cycles. The test was finished when the failure of the specimen occurred or the upper limit of loading cycles was reached, whichever occurred first.



(a)



(b)

**Figure 6.** The testing machine used for cyclic/fatigue fracture test (a); the arrangement of test (b).

The results of the cyclic fracture test are presented in the form of an empirically derived  $S_F-N$  curve, which is known as the Wöhler curve [4]:

$$S_F = a \cdot N^b \quad (22)$$

where  $S_F$  is the maximum stress in 3 PB,  $N$  is the number of cycles, and  $a$  and  $b$  are material constants. The maximum stress  $S_F$  is calculated as follows:

$$S_F = \frac{3F_{Fmax}S}{2B(W - a_0)^2} \tag{23}$$

The parameters of the  $S_F-N$  curve are determined only for test specimens that were broken during the cyclic test, and the specimens that withstand 2 million cycles are not taken into consideration. The fatigue limit was determined as the highest stress level at which three test specimens withstand 2 million cycles.

### 3. Results and Discussion

The results of performed experiments that involved determining physical, mechanical, and mechanical fracture parameters are displayed in Figures 7 and 8. The mean values accompanied by the sample standard deviations (error bars) are shown for all investigated characteristics. Although the test specimens were produced in three different batches, the variability of results is low, which proves the possibility to produce the composite with reproducible properties. As a result of the non-traditional curing conditions of ambient temperature and high RH  $\geq 95\%$  for a long period, the results of strength, fracture, and fatigue characteristics are hard to compare with other AAS or ordinary Portland cement (OPC) materials. For this reason, the results are partially compared in terms of materials of similar composition cured under different conditions.

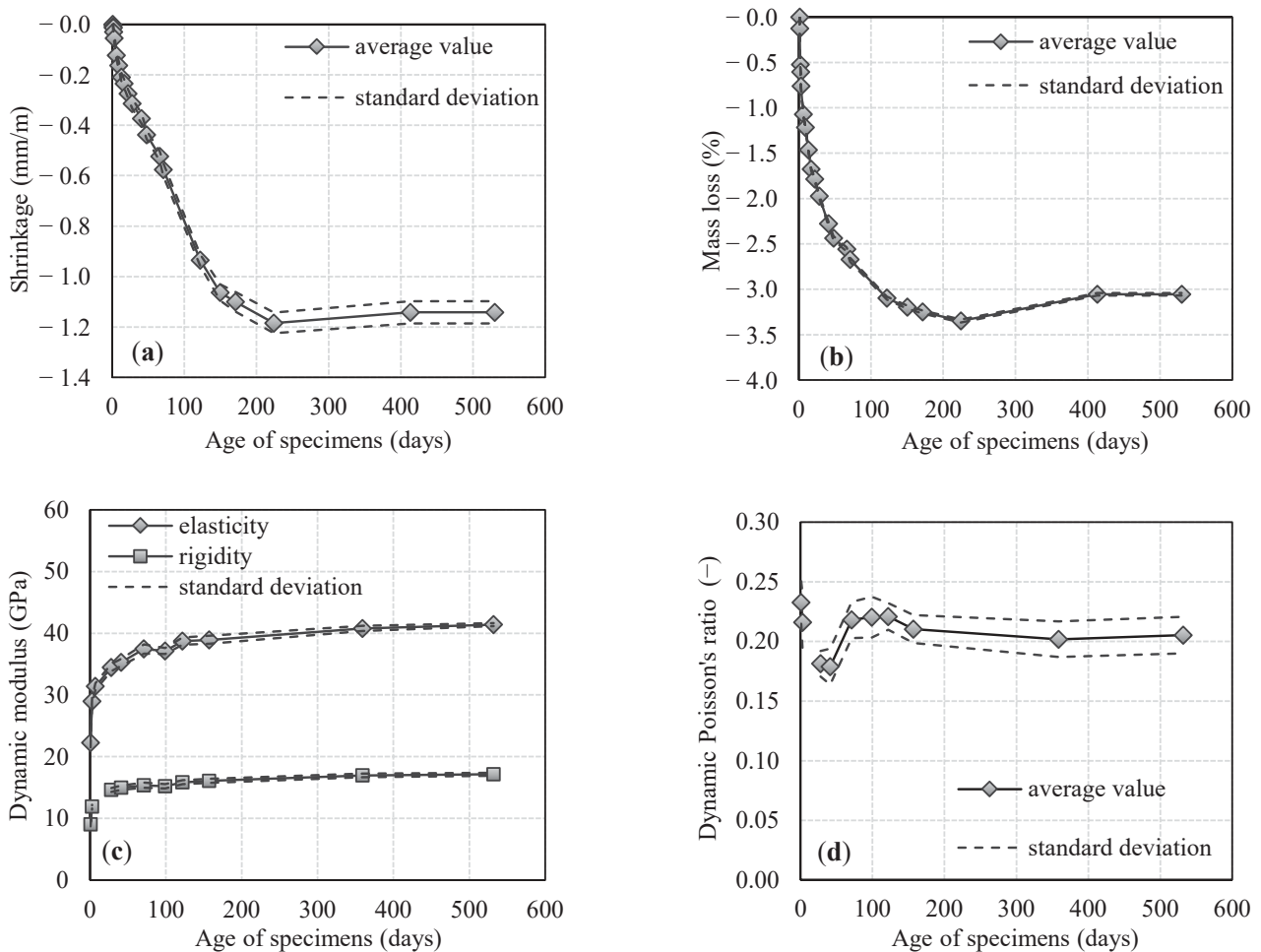


**Figure 7.** The mean values of shrinkage (a), mass loss (b) at RH of  $(55 \pm 10)\%$ , dynamic modulus of elasticity and rigidity (c), and dynamic Poisson’s ratio (d) at RH  $\geq 95\%$  of the investigated alkali-activated slag (AAS) composite during the specimen’s aging.

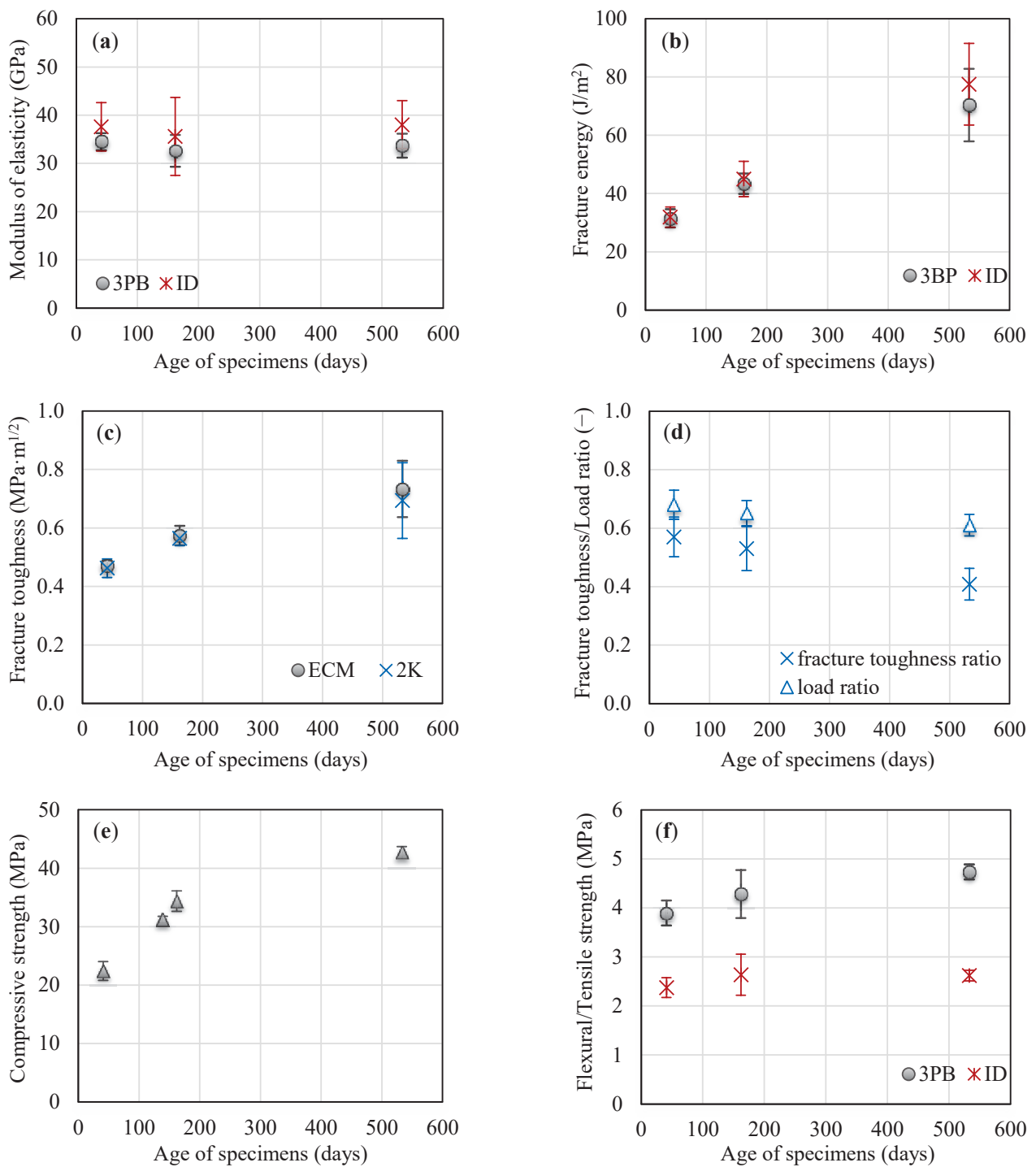


**Figure 8.** The mean values of modulus of elasticity (a), fracture energy (b), fracture toughness (c), fracture toughness/load ratio (d), compressive strength (e), and flexural/tensile strength (f) of the investigated AAS composite during the specimen’s aging (3PB—direct evaluation of particular parameter from fracture test, ID—identification of particular parameter, ECM—effective crack model, 2K—double-K fracture model).

### 3.1. Basic Physical and Mechanical Parameters

The shrinkage measurement was performed in regular intervals on the three same specimens during the whole period of the specimen’s aging. The results are presented in Figure 7a. The steady-state value of shrinkage of 1.2 mm/m was recorded at the age of about 200 days. The trend of the shrinkage process is similar to the shrinkage process in

OPC materials [38,39]. The difference is observed in time when the shrinkage stabilizes, which is two times later than in the OPC of similar composition cured under the same conditions. The absolute value of shrinkage of the investigated AAS composite at the age of 90 days is about two times higher in comparison with an OPC material with a similar water to binder ( $w/b$ ) ratio and the same sand to binder ( $s/b$ ) ratio cured under the same conditions [39]. On the other hand, the shrinkage is about six times lower in comparison with an AAS composite activated by waterglass with the similar  $w/b$  ratio, the same  $s/b$  ratio, and a higher activator dose stored under the same curing conditions [40].

The values of the dynamic modulus of elasticity are determined using the resonance method. At least three specimens are used to determine this parameter for a particular age of specimens. The value of the dynamic modulus of elasticity is about 40 GPa at the specimen's age of 530 days (see Figure 7c). The significant increase of this parameter is observed during the first 40 days of hardening when it achieves 35 GPa, but the follow-up increase with the specimen's age is not so high. A similar trend of development of the parameter value during hardening is also observed in the case of dynamic modulus of rigidity, which is about 17 GPa at the specimen's age of 530 days (see Figure 7c).

The dynamic modulus of elasticity and rigidity of the investigated AAS composite at the age of 530 days are about 1.5 and 1.8 times higher, respectively, in comparison with an AAS composite activated by waterglass with a similar  $w/b$  ratio and the same  $s/b$  ratio [41]. Nevertheless, the AAS composite activated by waterglass was stored at a lower RH of about 60%, i.e., under more severe conditions with the risk of microcracking and limited hydration process. The dynamic modulus of elasticity and rigidity of the investigated AAS composite at the age of 28 days is about 20% lower in comparison with OPC materials with a  $w/b$  ratio of 0.40 and the same  $s/b$  ratio, cured under the same conditions.

The Poisson's ratio was around 0.21 during the whole time of aging (see Figure 7d). A higher fluctuation was observed during the first 70 days when the dynamic modulus of elasticity and rigidity exhibited a steep increase. All dynamic characteristics gradually stabilized after this age. The absolute value of Poisson's ratio is similar to OPC materials of similar composition cured under the same conditions.

### 3.2. Mechanical Fracture Parameters

The mechanical fracture parameters determined during the specimen's hardening based on direct evaluation of records of fracture test in the form of the  $F-d$  and  $F-CMOD$  diagrams are presented in this section (Figure 8). These results are supplemented by parameters determined based on identification using an ensemble of ANNs. The number of specimens taken into the account for parameters evaluation is evident from Figure 5 where only the correctly recorded diagrams are presented. The results obtained by direct evaluation and identification are marked as 3PB and ID, respectively.

The value of modulus of elasticity determined by direct evaluation is about 33.5 GPa and is the same during the whole period of hardening (see Figure 8a) when the variability of the results is taken into account. The modulus of elasticity determined by identification is about 3 GPa higher for all investigated ages of specimens. The variability of results is higher for values determined by the method of identification. The modulus of elasticity of the investigated AAS composite at the age of 90 days is slightly higher in comparison with the OPC material with a similar  $w/b$  ratio and the same sand  $s/b$  ratio [39]. The modulus of elasticity at the age of 530 days is more than two times higher in comparison with the AAS composite activated by waterglass [42]. Nevertheless, the AAS composite activated by waterglass was stored at a lower RH of about 60%, i.e., in more severe conditions with the risk of microcracking and limited hydration process.

The fracture energy value gradually increases during the whole period of hardening (see Figure 8b). The highest value of about 70 J/m<sup>2</sup> is observed at the specimen's age of 530 days, which reaches more than 200% and 60% higher values in comparison with value at the age of 40 and 160 days, respectively. The same trend of development of this parameter during the hardening is observed for both the direct evaluation and identification. In the

case of the AAS composite, the stability loss during the loading did not occur; therefore, the post-peak parts of  $F-d$  diagrams are taken into consideration when the fracture energy is calculated, unlike the OPC material with a similar  $w/b$  ratio and the same  $s/b$  ratio [39].

The fracture toughness value gradually increases during the whole period of hardening (see Figure 8c). The same values were obtained for both used fracture models. The highest value of about  $0.73 \text{ MPa}\cdot\text{m}^{1/2}$  is observed at the specimen's age of 530 days, which reaches about 56% and 28% higher values in comparison with value at the age of 40 and 160 days, respectively. A similar value of fracture toughness is observed for the AAS composite activated by a combination of sodium carbonate and hydroxide [42]; however, only the value at the age of 28 days is presented in this literature. The fracture toughness of the investigated AAS composite at the age of 90 days is about 30% lower in comparison with the OPC material with a similar  $w/b$  ratio and the same  $s/b$  ratio [39]. Nevertheless, both composites were stored at a lower RH of about 55–60%.

The resistance to stable crack propagation is represented by fracture toughness ratio: the initial cracking toughness  $K_{Ic}^{ini}$  to unstable fracture toughness  $K_{Ic}^{un}$  ratio. The fracture toughness ratio gradually decreases during the period of composite hardening (see Figure 8d). A similar trend is also observed for load ratio, which represents the ratio of load  $F_{ini}$  at the outset of stable crack propagation to the maximum load  $F_{max}$ . A little bit lower fracture toughness ratio value is observed for the AAS composite activated by a combination of sodium carbonate and hydroxide stored at a lower RH of about 60% [43].

The compressive strength value gradually increases during the whole period of hardening (see Figure 8e). The value at the age of 530 days about 43 MPa is almost twofold in comparison with the value at the age of 40 days. The compressive strength of the investigated AAS composite at the age of 90 days is comparable with the OPC materials with a similar  $w/b$  ratio and the same  $s/b$  ratio stored at lower RH [39] and slightly lower than for the AAS composite with the similar  $w/b$  and  $s/b$  ratio and the same activator dose stored at a lower RH of about 65% [24]. It is necessary to emphasize that the 28 days' compressive strength of AAS with sodium hydroxide is about 70% lower than in the case of OPC materials of similar composition cured under  $RH \geq 95\%$ . While OPC materials show a significant increase in strength during the first 28 days, which makes it possible to use the 28 days' compressive strength for reliable structural design, in the case of AAS materials, the increase in strength is much slower and takes a longer time. It is evident from Figure 8e that in the case of the investigated AAS composite, the steep increase in compressive strength is observed up to the age of about a half-year. It is necessary to respect this fact during structural design where the long-term characteristics should be considered for effective and reliable design.

The flexural strength also gradually increases during the whole period of hardening (see Figure 8f); however, the increase is not so significant as in the case of compressive strength. The value at the age of 530 days about 4.7 MPa is about 20% higher in comparison with the value at the age of 40 days. A similar trend is also observed for tensile strength obtained by identification, but the values are equal to about 60% of the flexural strength. The flexural strength of the investigated AAS composite at the age of 90 days is slightly lower in comparison with the AAS composite with a similar  $w/b$  and  $s/b$  ratio and same activator dose stored at a lower RH of about 65% [24]. The same ratio of flexural to compressive strength of about 0.13 was observed [24].

### 3.3. Fatigue Characteristics

The results of cyclic fracture tests of specimens in 3PB at different load levels are summarized in Figure 9a in the form of a Wöhler curve (Equation (22)) where the maximum normal stress  $S_F$  (in Figure 9 marked as  $y$ ) applied during experiments is plotted against the logarithm of the number of cycles to failure  $N$  (in Figure 9 marked as  $x$ ). Theoretically, all test specimens are broken after the same number of cycles for one particular stress level. However, the fatigue behavior of a heterogeneous material such as the investigated AAS composite is distant from an optimal case, and the results show variability. It is also

connected with the different ages of specimens during the cyclic tests. In this case, the specimens were tested between the age of 140 and 160 days. It is evident that mechanical fracture parameters of the investigated AAS composite significantly change during the specimen's aging (see Figure 8), even after 160 days of hardening.

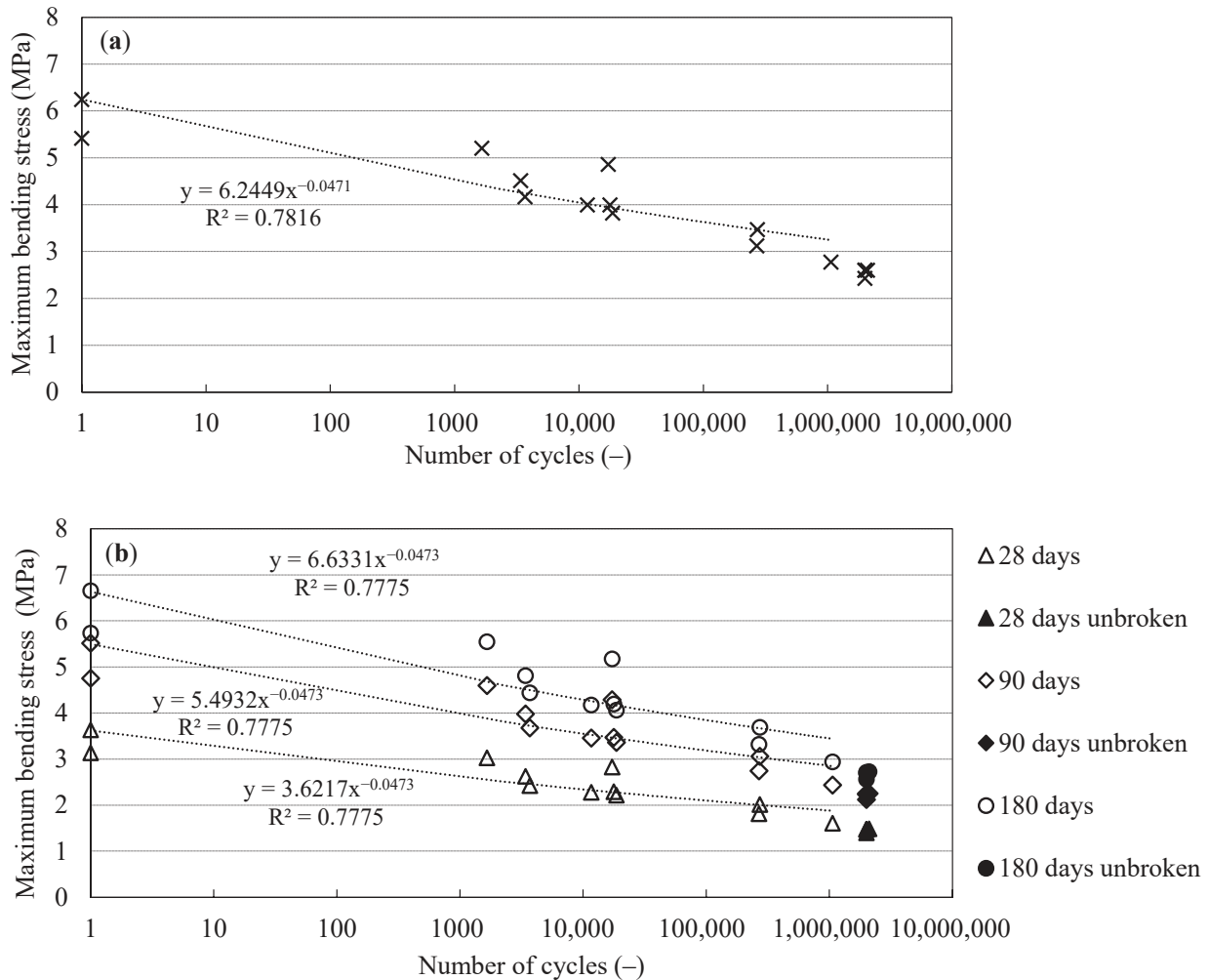


**Figure 9.** The  $S_F-N$  curve for the investigated AAS composite plotted for measured data (a), the  $S_F-N$  curve plotted for standardized data at the specimen's age 28, 90, and 180 days (b); the horizontal axis is plotted in logarithmic scale.

Therefore, the measured data are divided by coefficients determined from the approximation curve of relative compressive strength values to obtain correct values of fatigue characteristics corresponding to the age of specimens at which a particular cyclic test is performed. The measured data are standardized to a particular age of specimens by this procedure. In this case, the compressive strength is chosen because it is the most commonly determined mechanical parameter of quasi-brittle composites, and it is used as an input parameter in the structural design. The compressive strength test is also less time-consuming in comparison with the static fracture test. Nevertheless, the presented procedure can be used with any other mechanical or fracture parameter.

The measured values of compressive strength are divided by the average value at the chosen specimen's age. In this case, the compressive strength values at the specimen's age of 28, 90, and 180 days are chosen. The compressive strength at the age of 28 days is usually used as a reference value in the design of cement-based composites. The other two ages of specimens are chosen because the mechanical fracture parameters of the investigated AAS composite significantly change during the specimen's aging. By this procedure, the relative

compressive strength values for all investigated ages of specimens are obtained. Then, these values are approximated by the selected function:

$$y = a \cdot (1 - e^{-b \cdot x^c}), \quad (24)$$

where  $x$  is the specimen's age in days,  $y$  is the dimensionless relative compressive strength,  $a$  is the coefficient corresponding with an asymptote to the approximation curve, in other words, the ratio of the theoretical value of the compressive strength at infinitum to the value of compressive strength at the specimen's age of 28, 90, or 180 days, and  $b$ ,  $c$  are the coefficients corresponding with the size of the time-dependent change of compressive strength, which is generally dependent on the compositions of the used mixture. The approximation is performed using the GTDiPS software [28]. The procedure is based on the non-linear least-square method provided by genetic algorithms, which are implemented in this open-source Java GA package [28]. The approximation curves and coefficients  $a$ ,  $b$ , and  $c$  for relative compressive strength values related to the specimen's age of 28, 90, and 180 days are displayed in Figure 10.

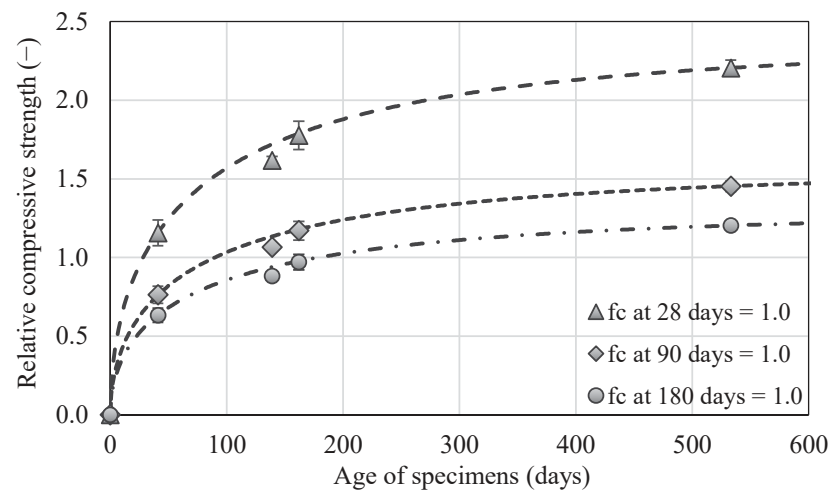


**Figure 10.** The approximation curves for relative compressive strength values related to the specimen's age of 28, 90, and 180 days, respectively.

The Wöhler curves for standardized data are introduced in Figure 9b. In addition, the fatigue limit was determined as the highest stress level at which three test specimens withstand 2 million cycles, and it is equal to 1.48, 2.24, and 2.71 MPa for data standardized using relative compressive strength values related to the specimen's age of 28, 90, and 180 days (see Figure 9b). The fatigue parameters of quasi-brittle materials are not commonly determined, although many structures made of these materials are often subjected not only to static but also to repetitive cyclic loads. If only the measured data without the effect of the particular age of specimens during the cyclic test are compared, then it might seem from Figure 9a that the investigated AAS composite has slightly better fatigue behavior than the OPC material with the same  $s/b$  and  $w/b$  ratios stored in the water [44]. In fact, the OPC material has slightly better fatigue behavior when the age of specimens is taken into the account and standardized data to the age of 28 days are compared with Figure 9b. The fatigue limit is about 0.5 MPa higher in the case of the OPC material [44].

#### 4. Conclusions

The main aim of the present research is to investigate the long-term mechanical, fracture, and fatigue behavior of a fine-grained composite based on sodium hydroxide-activated slag under  $RH \geq 95\%$ . The structures made of quasi-brittle materials are usually loaded in a mixed-mode manner in civil engineering applications; therefore, the attention in the performed experimental campaign was focused also on this issue. The results presented

in this article were used as valuable input parameters of material models used for numerical simulations of crack propagation in the semi-circular specimens loaded under mixed-mode I/II conditions. The results of numerical simulations were used for the verification of experimentally obtained data and were presented in a separate article [17].

The obtained results can be used in the design of quasi-brittle materials with the alternative binder to commonly used Portland cement. The presented results are valuable primarily because the parameters are monitored from a long-term point of view, and the complex set of material characteristics was collected as well. The attention was also focused on the fracture and fatigue parameters that are not commonly investigated. These parameters give more comprehensive information about material behavior and could be utilized in the effective design of newly developing materials. Although the test specimens were produced in three different batches, the variability of results is low, which proves the possibility to produce the composite with reproducible properties.

In addition, a substantial long-term increase in mechanical fracture parameters such as fracture energy, fracture toughness, or compressive strength proves that AAS hydration considerably proceeds even within the years. Therefore, the identification of these parameters only at relatively early stages, such as after 28 days, can lead to underestimation of their full potential. It simultaneously amplifies the role of appropriate numerical simulations as an alternative to the long-term testing.

**Author Contributions:** Conceptualization, H.Š., B.K., V.B. and L.M.; methodology, H.Š., B.K. and V.B.; software, M.L.; validation, P.M., and L.M.; formal analysis, H.Š. and B.K.; investigation, H.Š. and B.K.; resources, H.Š., B.K. and V.B.; data curation, H.Š., B.K. and M.L.; writing—original draft preparation, H.Š., B.K. and V.B.; writing—review and editing, L.M., P.M. and M.L.; visualization, H.Š.; supervision, H.Š. and L.M.; project administration, H.Š.; funding acquisition, H.Š. and L.M. All authors have read and agreed to the published version of the manuscript.

**Funding:** This research was funded by the Czech Science Foundation, grant number 18-12289Y.

**Institutional Review Board Statement:** Not applicable.

**Informed Consent Statement:** Not applicable.

**Data Availability Statement:** Data are available on request from the corresponding author.

**Conflicts of Interest:** The authors declare no conflict of interest.

## References

1. Provis, J.L. Alkali-activated materials. *Cem. Concr. Res.* **2018**, *114*, 40–48. [[CrossRef](#)]
2. Gao, X.; Yu, Q.; Brouwers, H. Assessing the porosity and shrinkage of alkali activated slag-fly ash composites designed applying a packing model. *Constr. Build. Mater.* **2016**, *119*, 175–184. [[CrossRef](#)]
3. Kumarappa, D.B.; Peethamparan, S. Stress-strain characteristics and brittleness index of alkali-activated slag and class C fly ash mortars. *J. Build. Eng.* **2020**, *32*, 101595. [[CrossRef](#)]
4. Lee, M.; Barr, B. An overview of the fatigue behaviour of plain and fibre reinforced concrete. *Cem. Concr. Compos.* **2004**, *26*, 299–305. [[CrossRef](#)]
5. Dobromil, P.; Jan, C.; Radomir, P. Material model for finite element modelling of fatigue crack growth in concrete. *Procedia Eng.* **2010**, *2*, 203–212. [[CrossRef](#)]
6. Toumi, A.; Bascoul, A.; Turatsinze, A. Modeling of fatigue crack growth in concrete subjected to mode I crack opening. In Proceedings of the 4th International Conference on Fracture Mechanics of Concrete Structures, Cachan, France, 28 May–1 June 2001; de Borst, R., Mazars, J., Pijaudier-Cabot, G., van Mier, J.G.M., Eds.; CRC Press: Cambridge, UK, 2001; pp. 637–640.
7. Xie, Y.; Cao, P.; Jin, J.; Wang, M. Mixed mode fracture analysis of semi-circular bend (SCB) specimen: A numerical study based on extended finite element method. *Comput. Geotech.* **2017**, *82*, 157–172. [[CrossRef](#)]
8. Kuruppu, M.D.; Chong, K.P. Fracture toughness testing of brittle materials using semi-circular bend (SCB) specimen. *Eng. Fract. Mech.* **2012**, *91*, 133–150. [[CrossRef](#)]
9. Razmi, A.; Mirsayar, M. On the mixed mode I/II fracture properties of jute fiber-reinforced concrete. *Constr. Build. Mater.* **2017**, *148*, 512–520. [[CrossRef](#)]
10. Erarslan, N. Analysing mixed mode (I–II) fracturing of concrete discs including chevron and straight-through notch cracks. *Int. J. Solids Struct.* **2019**, *167*, 79–92. [[CrossRef](#)]
11. Mirsayar, M.; Razmi, A.; Aliha, M.R.M.; Berto, F. EMTSN criterion for evaluating mixed mode I/II crack propagation in rock materials. *Eng. Fract. Mech.* **2018**, *190*, 186–197. [[CrossRef](#)]

12. Xing, Y.; Huang, B.; Ning, E.; Zhao, L.; Jin, F. Quasi-static loading rate effects on fracture process zone development of mixed-mode (I-II) fractures in rock-like materials. *Eng. Fract. Mech.* **2020**, *240*, 107365. [CrossRef]
13. Seitzl, S.; Pokorný, P.; Bilek, V. The mixed-mode fracture resistance of C 50/60 and its suitability for use in precast elements as determined by the Brazilian disc test and three-point bending specimens. *Theor. Appl. Fract. Mech.* **2018**, *97*, 108–119. [CrossRef]
14. Alanazi, N.; Susmel, L. Estimating Static/Dynamic Strength of Notched Unreinforced Concrete under Mixed-Mode I/II Loading. *Eng. Fract. Mech.* **2020**, 107329. [CrossRef]
15. Ruiz, G.; De La Rosa, A.; Almeida, L.; Poveda, E.; Zhang, X.; Tarifa, M.; Wu, Z.; Yu, R.C. Dynamic mixed-mode fracture in SCC reinforced with steel fibers: An experimental study. *Int. J. Impact Eng.* **2019**, *129*, 101–111. [CrossRef]
16. Aliha, M.; Mousavi, S.; Ghoreishi, S. Fracture load prediction under mixed mode I + II using a stress based method for brittle materials tested with the asymmetric four-point bend specimen. *Theor. Appl. Fract. Mech.* **2019**, *103*, 102249. [CrossRef]
17. Malíková, L.; Miarka, P.; Kucharczyková, B.; Šimonová, H. Williams expansion utilized for assessment of crack behaviour under mixed-mode loading in alkali-activated fine-grained composite. *Fatigue Fract. Eng. Mater. Struct.* **2021**. under review.
18. Bažant, Z.P.; Planas, J. *Fracture and Size Effect in Concrete and other Quasibrittle Materials*; Informa UK Limited: London, UK, 2019.
19. Jirásek, M.; Grassl, P. Evaluation of directional mesh bias in concrete fracture simulations using continuum damage models. *Eng. Fract. Mech.* **2008**, *75*, 1921–1943. [CrossRef]
20. Karihaloo, B.L. *Fracture Mechanics and Structural Concrete*, 1st ed.; Longman Scientific & Technical: Harlow, UK, 1995; 330p.
21. RILEM Determination of the fracture energy of mortar and concrete by means of three-point bend tests on notched beams. *Mater. Struct.* **1985**, *18*, 287–290. [CrossRef]
22. Kumar, S.; Barai, S.V. *Concrete Fracture Models and Applications*, 1st ed.; Springer: Berlin, Germany, 2011; p. 262.
23. Novák, D.; Lehký, D. ANN inverse analysis based on stochastic small-sample training set simulation. *Eng. Appl. Artif. Intell.* **2006**, *19*, 731–740. [CrossRef]
24. Atis, C.D.; Bilim, C.; Çelik, Ö.; Karahan, O. Influence of activator on the strength and drying shrinkage of alkali-activated slag mortar. *Constr. Build. Mater.* **2009**, *23*, 548–555. [CrossRef]
25. Bakharev, T.; Sanjayan, J.G.; Cheng, Y.-B. Alkali activation of Australian slag cements. *Cem. Concr. Res.* **1999**, *29*, 113–120. [CrossRef]
26. Kocáb, D.; Zitt, P.; Danek, P.; Cenek, M.; Alexa, M.; Hanus, P. The influence of specimen size on the dynamic properties of lightweight concrete determined by the resonance method. *IOP Conf. Ser. Mater. Sci. Eng.* **2019**, 583. [CrossRef]
27. ASTM International. *ASTM C215-19: Standard Test Method for Fundamental Transverse, Longitudinal, and Torsional Resonant Frequencies of Concrete Specimens*; ASTM International: West Conshohocken, PA, USA, 2020.
28. Frantík, P.; Mašek, J. GTDIIPS Software. 2015. Available online: <http://gtdips.kitnarf.cz/> (accessed on 1 October 2020).
29. Stibor, M. Fracture Parameters of Quasi-Brittle Materials and Their Determination. Bachelor's Thesis, Brno University of Technology, Brno, Czech Republic, 2004. (In Czech).
30. ÚNMZ. *ČSN EN 196-1 Methods of Testing Cement—Part 1: Determination of Strength*; ÚNMZ: Prague, Czech Republic, 2016.
31. Červenka, V.; Jendele, L.; Červenka, J. *ATENA Program Documentation—Part 1: Theory*; Cervenka Consulting Ltd.: Prague, Czech Republic, 2016.
32. Lehy, D. A neural network ensemble for the identification of mechanical fracture parameters of Fine-grained Brittle Matrix Composites. In *FraMCoS-X 10th International Conference on Fracture Mechanics of Concrete and Concrete Structures*; Pijaudie-Cabot, G., Grassl, P., La Bordiere, C., Eds.; IA-FraMCoS: Bayonne, France, 2019; pp. 1–9. [CrossRef]
33. Lehký, D.; Lipowczan, M.; Šimonová, H.; Keršner, Z. A hybrid artificial neural network-based identification system for fine-grained brittle matrix composites. *Comput. Concr.* **2021**. under review.
34. Hordijk, D.A. Local Approach to Fatigue of Concrete. Ph.D. Thesis, Technische Universiteit Delft, Delft, The Netherlands, 1991.
35. Jenq, Y.; Shah, S.P. Two Parameter Fracture Model for Concrete. *J. Eng. Mech.* **1985**, *111*, 1227–1241. [CrossRef]
36. Reinhardt, H.W.; Cornelissen, H.A.W.; Hordijk, D.A. Tensile Tests and Failure Analysis of Concrete. *J. Struct. Eng.* **1986**, *112*, 2462–2477. [CrossRef]
37. Xu, S.; Reinhardt, H.W. Determination of double-K criterion for crack propagation in quasibrittle fracture, Part II: Analytical evaluating and practical measuring methods for three-point bending notched beams. *Int. J. Fract.* **1999**, *98*, 151–177. [CrossRef]
38. Kucharczyková, B.; Topolář, L.; Daněk, P.; Kocáb, D.; Misák, P. Comprehensive Testing Techniques for the Measurement of Shrinkage and Structural Changes of Fine-Grained Cement-Based Composites during Ageing. *Adv. Mater. Sci. Eng.* **2017**, *2017*, 1–10. [CrossRef]
39. Kucharczyková, B.; Šimonová, H.; Misák, P.; Keršner, Z. Development of shrinkage and fracture parameters in selected fine-grained cement-based composites. In *MATEC Web of Conferences: Dynamics of Civil Engineering and Transport Structures and Wind Engineering—DYN-WIND'2017*; Melcer, J., Kotrasová, K., Eds.; EDP Sciences—Web of Conferences: Les Ulis, France, 2017; Volume 107, pp. 1–7. [CrossRef]
40. Kucharczyková, B.; Bilek, V.; Kocáb, D.; Karel, O. Shrinkage of Fine-Grained Composites Based on Alkali-Activated Slag. *Key Eng. Mater.* **2018**, *761*, 7–10. [CrossRef]
41. Alexa, M.; Kocáb, D.; Kucharczyková, B.; Kotrla, J. The influence of a shrinkage reducing admixture on the long-term development of dynamic properties in alkali-activated slag. In *Acta Polytechnica CTU Proceedings*; Czech Technical University in Prague: Prague, Czech Republic, 2019; Volume 22, pp. 1–6. [CrossRef]

42. Šimonová, H.; Kucharczyková, B.; Lipowczan, M.; Lehký, D.; Bílek, V., Jr.; Kocáb, D. Identification of Mechanical Fracture Parameters of Alkali-activated Slag Based Composites during Specimens Ageing. *Trans. VŠB–Tech. Univ. Ostrav. Civ. Eng. Ser.* **2019**, *19*, 59–64. [[CrossRef](#)]
43. Akturk, B.; Akca, A.H.; Kizilkanat, A.B. Fracture response of fiber-reinforced sodium carbonate activated slag mortars. *Constr. Build. Mater.* **2020**, *241*, 118128. [[CrossRef](#)]
44. Seitzl, S.; Pokorný, P.; Šimonová, H.; Frantík, P.; Kersner, Z.; Domski, J.; Katzer, J. Change of Fatigue and Mechanical Fracture Properties of a Cement Composite due to Partial Replacement of Aggregate by Red Ceramic Waste. *Period. Polytech. Civ. Eng.* **2019**, *63*, 152–159. [[CrossRef](#)]

# Williams expansion utilized for assessment of crack behaviour under mixed-mode loading in alkali-activated fine-grained composite

Lucie Malíková<sup>1,2</sup>  | Petr Miarka<sup>1,2</sup>  | Barbara Kucharczyková<sup>3</sup>  |  
Hana Šimonová<sup>1</sup> 

<sup>1</sup>Faculty of Civil Engineering, Institute of Structural Mechanics, Brno University of Technology, Brno, Czech Republic

<sup>2</sup>Czech Academy of Sciences, Institute of Physics of Materials, Brno, Czech Republic

<sup>3</sup>Faculty of Civil Engineering, Institute of Building Testing, Brno University of Technology, Brno, Czech Republic

## Correspondence

Petr Miarka, Institute of Physics of Materials, Czech Academy of Sciences, Žitkova 22, 616 00 Brno, Czech Republic.  
Email: petr.miarka@vut.cz

## Funding information

Faculty of Civil Engineering, Brno University of Technology, Grant/Award Number: FAST-S-20-5896; Czech Science Foundation, Grant/Award Number: 18-12289Y

## Abstract

The paper concerns an experimental study on the crack deflection angle in a semi-circular disc made of an alkali-activated fine-grained composite under mixed-mode conditions. This study is supplemented by an extensive numerical analysis that calculates the crack deflection angles via generalized (multi-parameter) fracture criteria. It is proved that the use of higher-order terms of the Williams expansion for the approximation of the crack-tip stress field leads to more accurate results. The influence of various parameters on the crack deflection angle is discussed, and recommendations on their proper choice are presented. The conclusions help in describing the crack behaviour under mixed-mode conditions more accurately.

## KEYWORDS

alkali-activated concrete, mixed-mode loading, multi-parameter fracture criteria, Williams expansion

## 1 | INTRODUCTION

Besides binder, aggregate and water, concrete mixture can contain various additives that improve selected properties of the finished product. Up to the present day, the most common binder has always been Portland cement, or blends containing it. Unfortunately, its fabrication produces a high amount of CO<sub>2</sub> emissions, which have a negative impact on the environment.<sup>1</sup> As a consequence, a search is underway to identify environmentally friendly alternatives.<sup>2</sup> One possibility that is being tested is the use of geopolymers,<sup>3</sup> resulting from alkali reaction, which activates secondary raw or waste products. Several recent publications are devoted to the presentation of the basic properties of alkali-activated composites (AAC),<sup>4</sup> as well as to demonstrations/analyses of their practical

application.<sup>5</sup> AAC has also been suggested as an environmentally friendlier alternative to traditional cement-based composite in this current work. Before it can be utilized as a basic material in structures and the building industry, the mechanical properties of AAC need to be understood reliably, as well as its fracture behaviour.

Today, a special concept of linear elastic fracture mechanics is often applied to the assessment of crack behaviour in concrete specimens. The main reason is that concrete material exhibits quasi-brittle fracture that typically arises through fracture processes occurring in a larger region around the crack tip. Therefore, the classical (one-parameter) fracture mechanics idea fails, and new approaches are required, and are being searched for. In this work, a generalized/multi-parameter procedure is applied to estimate the initial crack deflection angle.

Using more terms of the Williams expansion (WE)<sup>6</sup> seems to be more suitable for the approximation of the crack-tip stress and displacement field.

It has been proved in several technical works<sup>7,8</sup> that the stress intensity factor as the first (singular) term of the WE is dominant, relevant and sufficient only for the assessment of a very specific type of fracture. In other cases, the higher-order terms of the WE are also of high importance.<sup>9–17</sup> In this work, multi-parameter fracture criteria are introduced (similarly to those in the literature<sup>8,18–24</sup>) in order to estimate the crack propagation angle under mixed-mode loading conditions. Additional proofs regarding the necessity of considering a longer part of the Williams power series can be found in previous studies,<sup>25–28</sup> where for instance the constraint and/or size effect is assessed.

In this paper, the multi-parameter form of well-known fracture criteria is applied for the determination of the crack deflection angle under mixed-mode conditions in a semi-circular disc under three-point bending. Particularly, the well-known Maximum Tangential Stress (MTS) criterion<sup>29</sup> and Minimum Strain Energy Density (SED) criterion<sup>30,31</sup> are generalized in order to provide better estimations of the crack path.

## 1.1 | Williams power expansion

The Williams power expansion<sup>6</sup> is utilized in this paper in order to approximate the crack-tip stress/displacement field. Higher-order terms (HOTs) of the WE will help to improve the accuracy of the following fracture criteria approach:

$$\sigma_{ij} = \sum_{n=1}^{\infty} \frac{n}{2} r^{\frac{n}{2}-1} f_{ij}(n, \theta) A_n + \sum_{m=1}^{\infty} \frac{m}{2} r^{\frac{m}{2}-1} g_{ij}(m, \theta) B_m, \quad (1)$$

$$u_i = \sum_{n=0}^{\infty} r^{\frac{n}{2}} f_i(n, \theta, E, \nu) A_n + \sum_{m=0}^{\infty} r^{\frac{m}{2}} g_i(m, \theta, E, \nu) B_m. \quad (2)$$

Whereas Equation 1 is derived for stress tensor components, Equation 2 holds for displacement vector components. Originally, both equations were derived for a homogeneous elastic isotropic cracked body subjected to arbitrary remote loading. The meaning of the individual symbols is as follows:

- $i, j$  represents the indexes of the stress tensor/displacement vector in the Cartesian  $(x, y)$  or polar  $(r, \theta)$  coordinate system whose centre is considered to lie at the crack tip;

- $f_{ij}, g_{ij}$  stand for known functions corresponding to loading mode I, II in the stress tensor expansion;
- $f_i, g_i$  stand for known functions corresponding to loading mode I, II in the displacement vector expansion;
- $n, m$  are indexes of the individual terms of the Williams expansion;
- $A_n, B_m$  represent unknown coefficients of the individual terms of the WE and must be determined numerically via some of the derived methods;
- note that the Williams series' are used in their truncated form within this work considering the total number of  $N$  and  $M$  of the higher-order terms for mode I and II, respectively.

In the following section, the method selected to calculate the coefficients of the HOTs of the WE is described.

## 1.2 | Determination of the WE coefficients

In the past, various approaches to calculating WE coefficients were suggested and tested, including the boundary collocation method,<sup>32</sup> the fractal finite element method,<sup>33</sup> the hybrid crack element method<sup>34</sup> and so forth. Unfortunately, all of these methods require difficult mathematical procedures and/or the utilization of special crack elements and/or complicated finite element (FE) formulations. Therefore, a relatively simple method was chosen for this work. The principle behind the over-deterministic method (ODM) consists in the application of the basic least-squares formulation. The pure definition of the crack-tip displacement field is utilized, see Equation 2. This means that classical numerical methods are combined with finite element simulations of the problem. The numerically generated displacements of a set of nodes around the crack tip are needed from the FE analysis. These values are then inserted into Equation 2 together with the polar coordinates of the corresponding nodes. The procedure must fulfil specific assumptions in order to be solvable. Thus, an over-determined system of equations is built and can be solved. The solution provides the coefficients of the HOTs of the WE which are needed for a better approximation of the crack-tip stress field further from the crack tip.

## 1.3 | Crack deflection angle estimation

The previous procedure allows the calculation of the HOTs of the WE, and subsequently the more accurate approximation of the crack-tip stress field. The crack-tip

stress tensor components are actually the main input for various fracture criteria. In this paper, the crack deflection angle under mixed-mode I/II conditions is investigated for a novel environmentally friendly alkali-activated slag-based material. Therefore, fracture criteria for the estimation of the further crack propagation angle are needed. Particularly, the most commonly used criteria known as Maximum Tangential Stress (MTS) and Strain Energy Density (SED) are employed in their classical (one-parameter) form as well as their multi-parameter (generalized) form. The advantages and disadvantages of all these principles are discussed in the section devoted to the presentation of the reached results.

### 1.3.1 | MTS criterion

The general principle behind the MTS criterion consists in the assumption that a crack propagates in the direction of the maximum tangential stress  $\sigma_{\theta\theta}$ . When only a singular term (stress intensity factor) of the Williams expansion is considered as the single-controlling parameter, an explicit form of the MTS criterion can be derived:

$$\gamma = 2\arctan \frac{-2K_{II}}{K_I + \sqrt{K_I^2 + 8K_{II}^2}}. \quad (3)$$

In Equation 3,  $K_I$  and  $K_{II}$  represent the mode I and II stress intensity factors.

Of course, Equation 3 can help in some specific tasks, but in this paper, its results are compared to the multi-parameter approach that proceeds from the general mathematical formulation of a search for the local maximum of a function:

$$\frac{\partial \sigma_{\theta\theta}}{\partial \theta} = 0 \text{ and } \frac{\partial^2 \sigma_{\theta\theta}}{\partial \theta^2} < 0. \quad (4)$$

In Equation 4,  $\sigma_{\theta\theta}$  represents the tangential stress that is expressed via the WE considering various numbers of its initial terms. Note that this approach results in one new phenomenon: because the stress tensor components are dependent on the radial distance at various powers in each term, the final crack deflection angle is also dependent on the distance from the crack tip where the criterion is applied. This distance must be properly chosen according to some recommended approaches based on the material structure dimensions and/or properties, see for instance the previous studies.<sup>35–37</sup>

### 1.3.2 | SED criterion

The minimum strain energy density criterion consists in the idea that the crack propagates in the direction where the strain energy density factor reaches its minimum, see, for example, the literature.<sup>30,31</sup> This condition can be mathematically written through the derivatives:

$$\frac{\partial \Sigma}{\partial \theta} = 0 \text{ and } \frac{\partial^2 \Sigma}{\partial \theta^2} > 0, \text{ where } \Sigma = \frac{1}{2\mu} \left[ \frac{\kappa+1}{8} (\sigma_{rr} + \sigma_{\theta\theta})^2 - \sigma_{rr}\sigma_{\theta\theta} + \sigma_{r\theta}^2 \right]. \quad (5)$$

In Equation 5,  $\Sigma$  represents the strain energy density factor whose value depends on the polar stress components, as is expressed above. The symbol  $\kappa$  stands for Kolosov's constant,  $\sigma_{rr}$  is radial stress,  $\sigma_{\theta\theta}$  tangential stress and  $\sigma_{r\theta}$  shear stress.

## 2 | SPECIMEN GEOMETRY AND MATERIAL PROPERTIES

### 2.1 | Semi-circular discs under three-point bending

The whole analysis has been performed on semi-circular discs with an inclined crack loaded under three-point bending (SCB). This geometry ensures mixed-mode conditions and crack deflection. In order to cover the various conditions and also experimental inaccuracies that can occur, geometries with an eccentric crack as well as with non-symmetrical supports were also considered both in the numerical simulations and in the experimental campaign, see Figure 1.

Most configurations have been tested for the case of an inclined crack in the centre of the specimen (Figure 1A). Particularly, specimens with the following dimensions were produced and tested in order to compare the results with the performed numerical simulations:

- the radius of the SCB specimen,  $R = 50$  mm;
- half-span between the supports,  $S = 40$  mm;
- the angle of the inclined crack,  $\beta = 30, 40$  and  $50^\circ$ ;
- crack length,  $a = 10$  and  $25$  mm (i.e. relative crack length,  $\alpha = 0.2$  and  $0.5$ ).

Thus, six basic configurations could be investigated. Moreover, four configurations were suggested for the case of SCB with an eccentric crack (Figure 1B):

- the radius of the SCB specimen,  $R = 50$  mm;

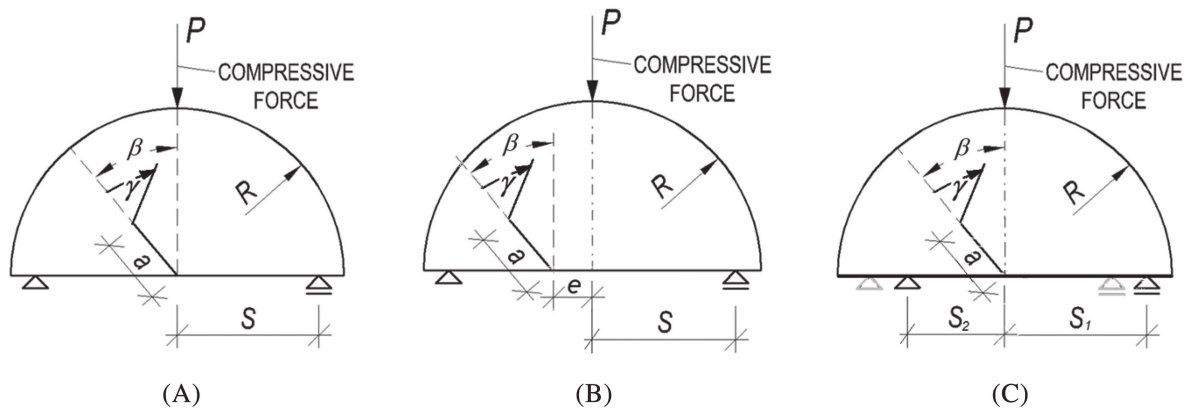


**FIGURE 1** Schema of the SCB specimen: (A) an inclined crack in the middle of the specimen; (B) an eccentric crack; (C) asymmetrical supports

- half-span between the supports,  $S = 40$  mm;
- the angle of the inclined crack,  $\beta = 40$  and  $50^\circ$ ;
- crack length,  $a = 10$  mm (i.e. relative crack length,  $\alpha = 0.2$ );
- crack eccentricity,  $e = 10$  and  $15$  mm.

The last case of an SCB specimen with asymmetric supports (Figure 1C) was tested in two different configurations:

- the radius of the SCB specimen,  $R = 50$  mm;
- span distances  $S_1 = 40$  mm,  $S_2 = 30$  mm and vice versa;
- the angle of the inclined crack,  $\beta = 50^\circ$ ;
- crack length,  $a = 10$  mm (i.e. relative crack length,  $\alpha = 0.2$ ).

Note that the particular geometrical configurations were chosen based on an extensive parametrical numerical study in order to cover the cases where the HOTs of the WE had the largest effect on the estimation of the crack deflection angle; this corresponds to a loading mode II that is as significant as possible. For each configuration, three real specimens were produced in order to have the option of employing statistics tools.

## 2.2 | Alkali-activated slag fine-grained composite

As stated in the introduction to this paper, efforts are being made to replace common concrete/fine-grained composites (made of Portland cement besides other things) with a more ecological material. As a contribution to these efforts, an alkali-activated slag fine-grained composite (AAFC) was prepared for this research. This material was produced by mixing ground granulated blast

furnace slag (Kotouč Štramberk, spol. s.r.o, Czech Republic - Blaine fineness  $400 \text{ m}^2/\text{kg}$ ) with standardized siliceous CEN sand with a maximum grain size of 2 mm. The aggregate/slag ratio (a/s) was 3:1, the water/slag ratio (w/s) was 0.45, and the dose of sodium hydroxide activator was 6% of  $\text{Na}_2\text{O}$  with respect to the slag weight. To maintain the appropriate workability of the mortar, lignosulfonate-based plasticiser was dosed in the amount of 1% by mass of slag.

The basic mechanical fracture properties of the AAFC were determined based on the results of experiments performed on prisms with the dimensions  $40 \text{ mm} \times 40 \text{ mm} \times 160 \text{ mm}$ . A static modulus of elasticity of 35 GPa was determined from the initial part of load versus displacement diagrams recorded during the fracture tests,<sup>38</sup> and a dynamic Poisson's ratio of 0.21 was determined using the resonant frequency method.<sup>39</sup> Note that at least these two values are necessary for the definition of the corresponding material model in FE simulations. The average experimentally determined compressive strength and bulk density values were about 34.5 MPa and  $2,250 \text{ kg/m}^3$ , respectively. The material characteristics were determined at the same age as when the fracture tests were performed in the mixed-mode configuration. Detailed information about the development of mechanical fracture and fatigue characteristics of AAFC during ageing is presented in a separate article.<sup>40</sup>

## 2.3 | Manufacturing of SCB specimens

The SCB specimens were cast in special silicon moulds with a wooden frame in order to prepare specimens with a diameter of 100 mm and a thickness of 20 mm. These specimens were stored directly in the moulds and wrapped in PE foil for 24 h. After demoulding, the specimens were cured in a closed chamber at a temperature of

$21 \pm 2^\circ\text{C}$  and  $\text{RH} > 95\%$  until the tests were performed. The initial notches were made by a water jet cutter close to the time of testing/just before testing. The fracture tests in various configurations were performed at a specimen age of 160 days.

## 2.4 | Fracture tests

During the fracture tests, the SCB specimens were subjected to quasi-static loading using a very stiff LabTest 6.250 multi-purpose mechanical testing machine with a load capacity of 250 kN. The loading process was controlled by a constant increment of displacement of 0.02 mm/min during the entire course of the test. The loading force ( $F$ ) and crack mouth opening displacement ( $CMOD$ ) were continuously recorded during the test with a frequency of 5 Hz. Simultaneously, a 2D video extensometer was engaged to monitor the surface strain during the fracture tests (see Figure 2). This measurement system enabled the monitoring of real-time crack development and provided the images needed for the measurement of the real crack inclination angle for particular test configurations. An example of an SCB specimen with an inclined crack during a three-point-bending test can be seen in Figure 2, from which the crack inclination angle  $\gamma$  was measured.

Several captured  $F - CMOD$  diagrams are shown in Figure 3 for various mode-mixity levels  $M^e$ , where the parameter  $M^e$  is defined by means of only the stress intensity factors  $K_I$  and  $K_{II}$  (as used in several works by other authors<sup>41,42</sup>). The mixity parameter can generally achieve values ranging between 0 (pure mode II) and 1 (pure mode I), and is defined as:

$$M^e = \frac{2}{\pi} \arctg \frac{K_I}{K_{II}}. \quad (6)$$

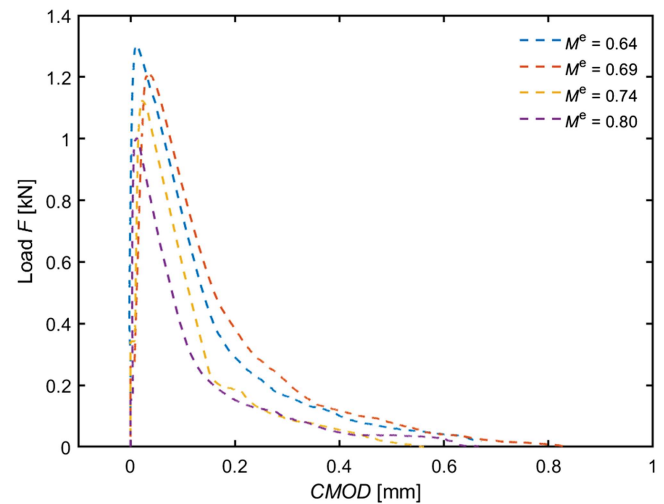


**FIGURE 3** Experimentally captured  $F - CMOD$  diagrams for various mode-mixity parameters  $M^e$  [Colour figure can be viewed at [wileyonlinelibrary.com](http://wileyonlinelibrary.com)]

The recorded  $F - CMOD$  diagrams show the same initial stiffness for various mode-mixity  $M^e$  levels and the same notch lengths  $\alpha$ . However, the maximum force  $F_{\max}$  decreases with increasing mode-mixity levels  $M^e$ . This difference in the measured values of the maximum force  $F_{\max}$  is connected to the mode II crack initiation, which consumes energy induced by the testing machine until the crack initiates. The higher the crack inclination angle, the higher the level of loading mode II. Generally, it holds that mode I crack propagation is the less energetically expensive fracture response of the material. When

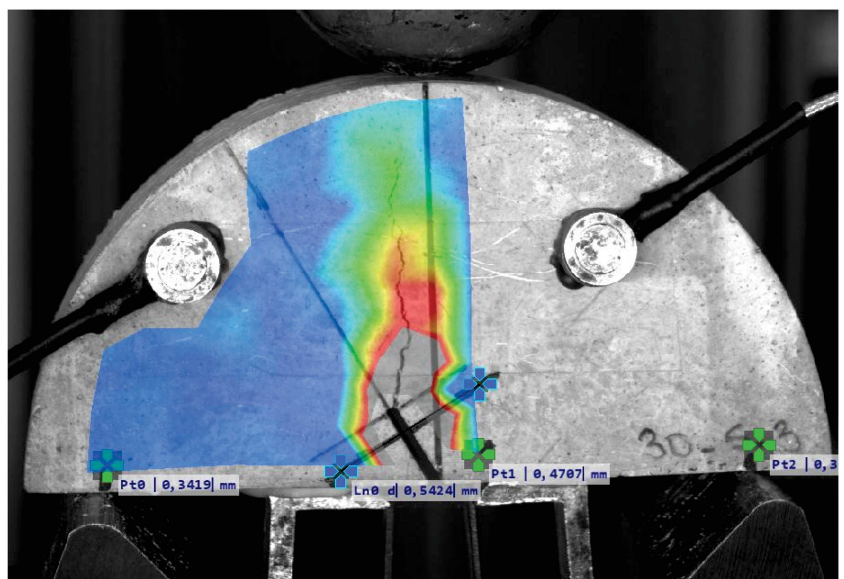


**FIGURE 2** Example of the experimental set-up for an SCB specimen with a centrally located inclined crack:  $\beta = 30^\circ$  and  $a = 10$  mm (i.e.  $\alpha = 0.2$ ) [Colour figure can be viewed at [wileyonlinelibrary.com](http://wileyonlinelibrary.com)]

the crack is oriented in another direction to the applied load, its initiation and propagation require a higher force to be applied. When a mode I crack starts to grow, it can be documented by a similar post-peak slope. The mode II dominance is documented in the measured and calculated values of crack initiation direction  $\gamma$ .

## 2.5 | Finite element model

Because the nodal displacements need to be known for the application of the ODM in the estimation of the HOTs of the WE, a two-dimensional (2D) numerical model of the SCB specimens used in the experimental campaign was created in ANSYS commercial FE software, see a selected configuration in Figure 4.

The FE model of the SCB specimen had the following parameters:

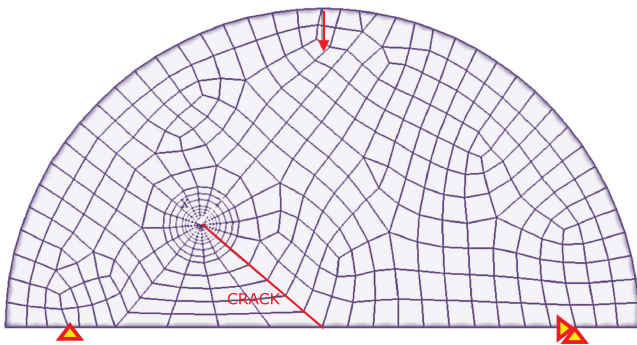


**FIGURE 4** FE mesh of an SCB specimen with a centrally located inclined crack with applied load and boundary conditions in ANSYS:  $\beta = 50^\circ$  and  $a = 25$  mm (i.e.  $\alpha = 0.5$ ) [Colour figure can be viewed at [wileyonlinelibrary.com](http://wileyonlinelibrary.com)]

- the quadrilateral 8-node elements PLANE183;
- mesh refinement around the crack tip by means of the KSCON command, ensuring stress singularity;
- a ring of nodes at a distance of 4 mm from the crack tip for obtaining the input data for the ODM process;
- plane stress conditions (based on the assumption that the results of the FE simulations are compared to experimentally obtained crack deflection angles observed optically at the specimen surface);
- the compressive loading force  $P = 1$  kN.

## 3 | RESULTS AND DISCUSSION

The previous sections provide the theoretical background and introduce the methods applied within this research. Now, the results obtained experimentally as well as via FE simulations will be presented and discussed. Particularly, the importance of the multi-parameter approach for the estimation of the crack deflection angle under mixed-mode loading conditions in an SCB specimen shall be investigated. Also, the fracture properties of the novel AAFC material shall be assessed. Note that the distance over which the initial crack propagation angle was experimentally investigated was estimated from the relation derived by Irwin for the extent of plastic deformation<sup>43</sup>:

$$r_c = \frac{1}{6\pi} \left( \frac{K_{IC}}{\sigma_t} \right)^2 = \frac{1}{6\pi} \left( \frac{0.57}{3.96} \right)^2 \quad (7)$$

$$= 1,1 \cdot 10^{-3} \text{ m} = \left( \frac{\text{MPam}^{1/2}}{\text{MPa}} \right)^2.$$

**TABLE 1** Values of the mixity parameter  $M^e$  for all the SCB configurations investigated, the parameters  $e$ ,  $S_1$ ,  $S_2$ ,  $\alpha$ ,  $\beta$  and  $\gamma$  are used in accordance with Figure 1

$e$ [mm]	$S_1$ [mm]	$S_2$ [mm]	$\alpha$ [-]	$\beta$ [deg]	$K_I/K_{II}$ [-]	$M^e$ [-]	$\gamma$ [°]	STD of $\gamma$ [°]
15	40	40	10	50	1.58	0.641	56.3	13.5
0	40	30	10	50	1.65	0.653	41.0	17.1
10	40	40	10	50	1.66	0.655	51.7	4.1
0	40	40	25	50	1.68	0.657	63.7	11.2
0	40	40	10	50	1.80	0.678	55.7	17.1
0	30	40	10	50	1.82	0.680	66.3	7.2
15	40	40	10	40	1.90	0.692	49.3	21.8
10	40	40	10	40	2.03	0.708	53.3	11.0
0	40	40	25	40	2.15	0.723	56.0	17.3
0	40	40	10	40	2.28	0.737	40.0	10.6
0	40	40	25	30	2.84	0.784	57.0	8.0
0	40	40	10	30	3.05	0.798	34.3	4.5

In Equation 7,  $K_{IC}$  stands for the effective fracture toughness for mode I evaluated on the AAFC material through the effective crack model,<sup>38</sup> and  $\sigma_t$  represents the flexural strength obtained from the three-point-bending test.

The dependences of the crack deflection angle are displayed as functions of the mixity parameter  $M^e$  (as it is defined by means of Equation 6) in the following part of the work. Therefore, the corresponding values of  $M^e$  for all the SCB configurations investigated are stated in Table 1. Note that an extensive numerical study was performed as a starting point in order to select ideal configurations for the experimental campaign. The geometrical configurations presented in the

paper satisfy the requirement for mode II levels which are as high as possible while taking into account the limitations on the preparation of SCB testing specimens (the sawing of the notch under a high inclination angle) and/or numerical simulations. The table also contains the mean values of the crack deflection angles  $\gamma$  obtained experimentally, and their standard deviations (STD).

Before proceeding to the presentation of the results, it should be noted that positive crack deflection angles represent the propagation of the crack towards the loading force. The plots include both the experimental as well as the numerical results for all the configurations mentioned above. Thus, 12 experimental points (each of them

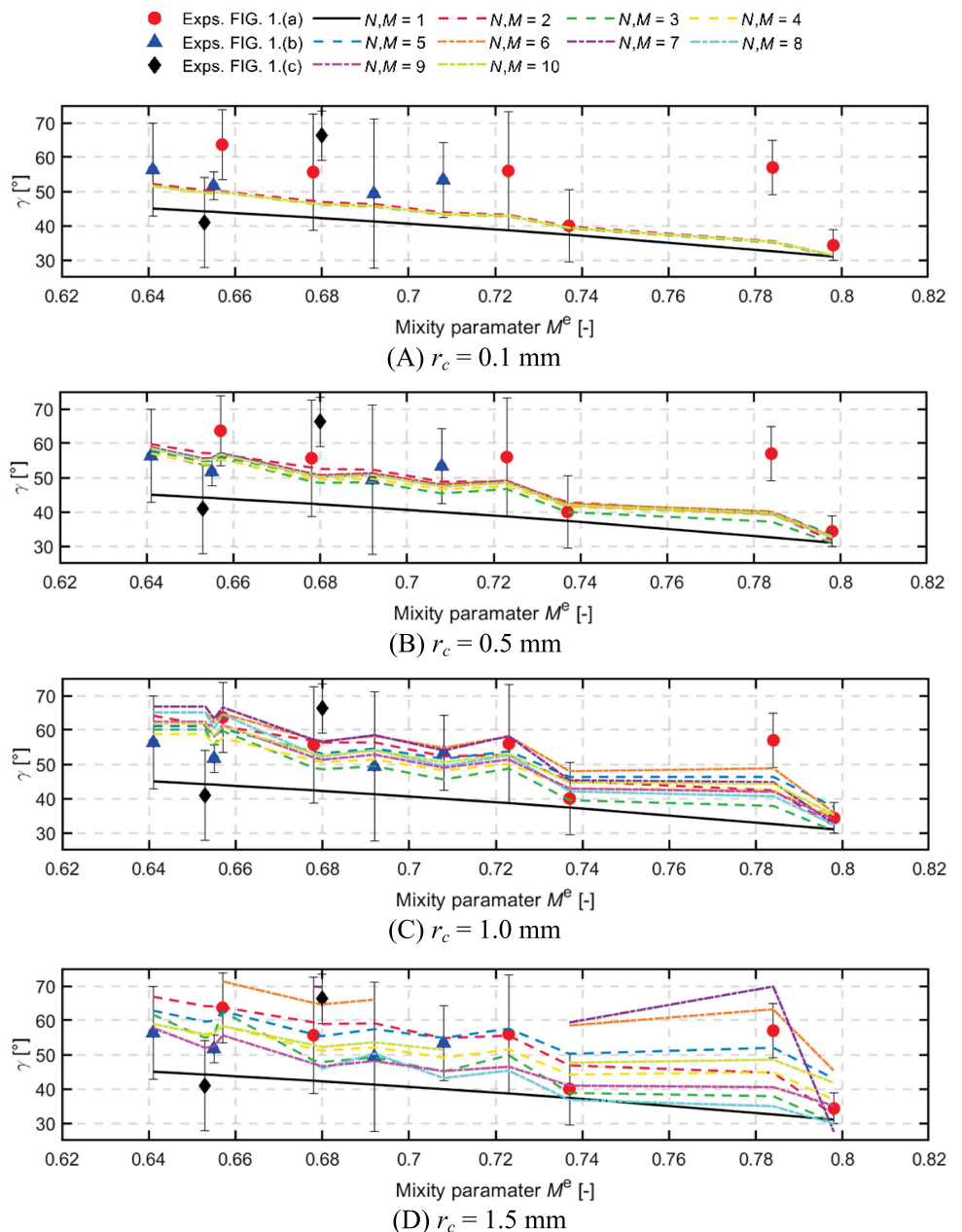


**FIGURE 5** Dependence of the initial kink angle  $\gamma$  on the mixity parameter  $M^e$  for selected SCB configurations: Experimental vs. numerical results obtained via the multi-parameter MTS criterion with various  $r_c$ : (a) 0.1 mm, (b) 0.5 mm, (c) 1.0 mm and (d) 1.5 mm [Colour figure can be viewed at [wileyonlinelibrary.com](http://wileyonlinelibrary.com)]

being the mean value of three fracture tests) are compared to curves obtained numerically via the multi-parameter fracture criterion considering 1, 2, ... 10 initial WE terms for stress approximation. This comparison is then made at four different critical distances  $r_c = 0.1, 0.5, 1.0$  and  $1.5$  mm. Figure 5 displays the results of the multi-parameter MTS criterion, while Figure 6 displays the results of the multi-parameter SED criterion.

From the results introduced in Figures 5 and 6 representing the comparison of the experimentally obtained crack deflection angles and the angles calculated numerically via generalized/multi-parameter fracture criteria (MTS and SED), the following conclusions can be made:

- the SED criterion gives generally lower crack deflection angle values than the MTS criterion (in their classical one-parameter as well as in their generalized multi-parameter form);
- the multi-parameter SED criterion is less sensitive to the choice of the critical distance as well as the choice of the number of the initial terms of the WE to be taken into account;
- the MTS criterion seems, therefore, more effective than SED with regard to experimentally obtained results;
- for both criteria, it holds that when they are applied at a small distance from the crack tip, the higher-order terms only have a very low (negligible) effect on the results;

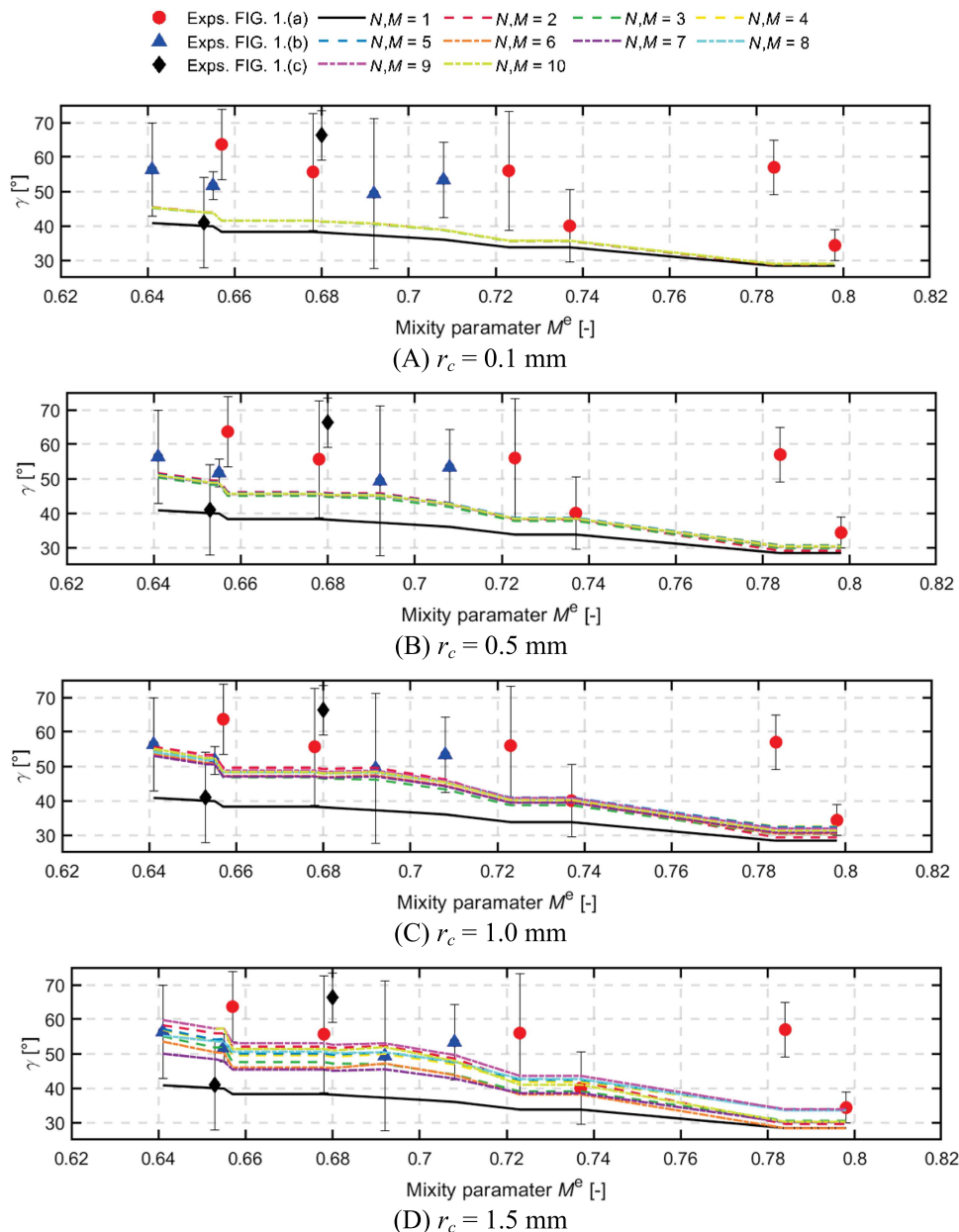


**FIGURE 6** Dependence of the initial kink angle  $\gamma$  on the mixity parameter  $M^e$  for selected SCB configurations: Experimental vs. numerical results obtained via the multi-parameter SED criterion with various  $r_c$ : (a) 0.1 mm, (b) 0.5 mm, (c) 1.0 mm and (d) 1.5 mm [Colour figure can be viewed at [wileyonlinelibrary.com](http://wileyonlinelibrary.com)]

- when larger critical distances are considered, the importance of considering a higher number of initial terms of the WE increases—this is evidence for the recommendation of multi-parameter fracture criteria when materials with a larger fracture process zone are being dealt with;
- ts oscillate when the number of initial terms of the WE increase, and it is not possible to observe a clear trend, that would enable a recommendation to be made on the proper choice of the number of WE terms;
- nevertheless, it is obvious that the classical one-parameter form of the fracture criteria tested is mostly very far from the experimental results, and that considering more terms of the WE helps to make the calculated crack deflection angles more accurate;
- when the results for different critical distances are compared, it could be stated that when about 1 mm is selected for parameter  $r_c$  (as is also calculated from Equation 6), numerical results (MTS and SED) are obtained that agree quite well with the experiment, at least for several configurations;
- whereas the SED criterion results match the experimental data better for an eccentric crack, the MTS criterion gives a better match for central crack configurations;
- note that all configurations investigated have  $K_I > K_{II}$ : it would therefore also be interesting to include configurations in which mode II prevails, which was not experiment-friendly in the case of the SCB specimen.

Note that it is supposed that the higher sensitivity of the generalized MTS criterion to considering a higher number of the Williams expansion terms can consist in the theoretical definition of the strain energy density factor (Equation 5). It is defined as a combination of the second powers of three different stress tensor components. Because the coefficients of the higher order terms of the Williams expansion decrease significantly with their order, their second power is an even lower value, and therefore their total influence on the strain energy density factor and crack deflection angle decreases.

## 4 | CONCLUSION

The paper deals with an analysis of the crack deflection angle on a semi-circular disc made of alkali-activated fine-grained composite with an inclined crack under mixed-mode conditions. Experimentally obtained results are compared to results from multi-parameter fracture criteria. Particularly, MTS and SED criteria are tested and the influence of various parameters (such as mixed-mode level, critical distance and number of the initial terms of

the WE) on the results are discussed. Based on the data presented, the MTS criterion seems to be more suitable when crack behaviour in this kind of (quasi-brittle) material is described. It is also shown that the choice of the proper radial distance for the application of the fracture criteria is necessary: in this case, a distance of about 1 mm is recommended together with a higher number of initial terms of the WE. Unfortunately, it is not possible to give a general recommendation regarding its value.

## ACKNOWLEDGEMENTS

Financial support from the Czech Science Foundation (project no. 18-12289Y) and from the Faculty of Civil Engineering, Brno University of Technology (project no. FAST-S-20-5896) is gratefully acknowledged.

## NOMENCLATURE

$\alpha$	relative crack length
$\beta$	notch inclination angle
$\gamma$	crack deflection angle
$\sigma_{ij}$	stress tensor
$\sigma_t$	flexural strength
2D	two-dimensional
$a$	crack length
AAC	alkali-activated composite
AAFC	alkali-activated slag fine-grained composite
CMOD	crack mouth opening displacement
$e$	crack eccentricity
FE	finite element
HOT	higher-order terms
$K_I$	stress intensity factor for mode I
$K_{IC}$	fracture toughness
$K_{II}$	stress intensity factor for mode II
$M_e$	mode mixity parameter
MTS	maximum tangential stress
$r_c$	critical distance
$S$	half span
SCB	semi-circular bend
SED	strain energy density
STD	standard deviation
WE	Williams' expansion

## ORCID

Lucie Malíková  <https://orcid.org/0000-0001-5868-5717>  
 Petr Miarka  <https://orcid.org/0000-0002-4103-8617>  
 Barbara Kucharčzyková  <https://orcid.org/0000-0002-7123-5099>  
 Hana Šimonová  <https://orcid.org/0000-0003-1537-6388>

## REFERENCES

1. Josa A, Aguado A, Cardim A, Byars E. Comparative analysis of the life cycle impact assessment of available cement inventories in the EU. *Cem Concr Res*. 2007;37(5):781-788.

2. Chen C, Habert G, Bouzidi Y, Jullien A. Environmental impact of cement production: detail of the different processes and cement plant variability evaluation. *J Clean Prod.* 2010;18(5):478-485.
3. Nikolic V, Komljenovic M, Džunuzovic N, Ivanovic T. The influence of mechanical activation of fly ash on the toxic metals immobilization by fly ash-based geopolymers. In: *Key Engineering Materials.* Vol.761 KEM. Baech Switzerland: Trans Tech Publications Ltd; 2018:3-6.
4. Bilek V, Hurta J, Done P, Zidek L. Development of alkali-activated concrete for structures—mechanical properties and durability. *Perspect Sci.* 2016;7:190-194.
5. Bilek V, Hurta J, Done P, Zidek L, Zajdlík T. Hybrid alkali activated concretes—conception and development for practical application. In: *Solid State Phenomena.* Vol.249 SSP. Baech Switzerland: Trans Tech Publications Ltd; 2016:3-7.
6. Williams ML. On the stress distribution at the base of a stationary crack. *J Appl Mech.* 1957;24:109-114.
7. Ayatollahi MR, Rashidi Moghaddam M, Razavi SMJ, Berto F. Geometry effects on fracture trajectory of PMMA samples under pure mode-I loading. *Eng Fract Mech.* 2016;163:449-461.
8. Smith DJ, Ayatollahi MR, Pavier MJ. The role of T-stress in brittle fracture for linear elastic materials under mixed-mode loading. *Fatigue Fract Eng Mater Struct.* 2001;24(2):137-150.
9. Ayatollahi MR, Zakeri M. T-stress effects on isochromatic fringe patterns in mode II. *Int J Fract.* 2007;143(2):189-194.
10. Aliha MR, Ayatollahi MR, Kharazi B. Mode II fracture assessment using ASFPB specimen. *Int J Fract.* 2009;159(2):241-246.
11. Berto F, Lazzarin P. Multiparametric full-field representations of the in-plane stress fields ahead of cracked components under mixed mode loading. *Int J Fatigue.* 2013;46:16-26.
12. Berto F, Lazzarin P, Kotousov A. On higher order terms and out-of-plane singular mode. *Mech Mater.* 2011;43(6):332-341.
13. Chen YZ. Closed form solution of T-stress in plane elasticity crack problems. *Int J Solids Struct.* 2002;37:1629-1637.
14. Christopher CJ, James MN, Patterson EA, Tee KF. Towards a new model of crack tip stress fields. *Int J Fract.* 2007;148(4):361-371.
15. Ramesh K, Gupta S, Kelkar AA. Evaluation of stress field parameters in fracture mechanics by photoelasticity-revisited. *Eng Fract Mech.* 1997;56(1):25-45.
16. Larsson SG, Carlsson AJ. Influence of non-singular stress terms and specimen geometry on small-scale yielding at crack tips in elastic-plastic materials. *J Mech Phys Solids.* 1973;21(4):263-277.
17. Fett T, Munz D. T-stress and crack path stability of DCDC specimens. *Int J Fract.* 2003;124(1/2):L165-L170.
18. Malíková L. Multi-parameter fracture criteria for the estimation of crack propagation direction applied to a mixed-mode geometry. *Eng Fract Mech.* 2015;143:32-46.
19. Hou C, Wang Z, Liang W, Li J. Determination of fracture parameters in center cracked circular discs of concrete under diametral loading: a numerical analysis and experimental results. *Theor Appl Fract Mech.* 2016;85:355-366.
20. Ayatollahi MR, Razavi SMJ, Yahya MY. Mixed mode fatigue crack initiation and growth in a CT specimen repaired by stop hole technique. *Eng Fract Mech.* 2015;145:115-127.
21. Mirsayar MM, Razmi A, Aliha MRM, Berto F. EMTSN criterion for evaluating mixed mode I/II crack propagation in rock materials. *Eng Fract Mech.* 2018;190:186-197.
22. Mirsayar MM, Berto F, Aliha MRM, Park P. Strain-based criteria for mixed-mode fracture of polycrystalline graphite. *Eng Fract Mech.* 2016;156:114-123.
23. Mirsayar MM, Park P. The role of T-stress on kinking angle of interface cracks. *Mater des.* 2015;80:12-19.
24. Ayatollahi MR, Rashidi Moghaddam M, Berto F. A generalized strain energy density criterion for mixed mode fracture analysis in brittle and quasi-brittle materials. *Theor Appl Fract Mech.* 2015;79:70-76.
25. Berto F, Lazzarin P. On higher order terms in the crack tip stress field. *Int J Fract.* 2010;161(2):221-226.
26. Karihaloo BL. Size effect in shallow and deep notched quasi-brittle structures. *Int J Fract.* 1999;95(1/4):379-390.
27. Karihaloo BL, Abdalla H, Xiao QZ. Coefficients of the crack tip asymptotic field for wedge splitting specimens. *Eng Fract Mech.* 2003;70(17):2407-2420.
28. Veselý V, Frantik P, Keršner Z. Cracked volume specified work of fracture. Proc Twelfth Int Conf Civil, Struct Environ Eng Comput 2009;91.
29. Erdogan F, Sih GC. On the crack extension in plates under plane loading and transverse shear. *J Basic Eng.* 1963;55:519-525.
30. Sih GC. Some basic problems in fracture mechanics and new concepts. *Eng Fract Mech.* 1973;5(2):365-377.
31. Sih GC. Strain energy density factor applied to mixed mode crack problems. *Int J Fract Mech.* 1974;10(3):305-321.
32. Xiao QZ, Karihaloo BL, Liu XY. Direct determination of SIF and higher order terms of mixed mode cracks by a hybrid crack element. *Int J Fract.* 2004;2:207-225.
33. Su RKL, Fok SL. Determination of coefficients of the crack tip asymptotic field by fractal hybrid finite elements. *Eng Fract Mech.* 2007;74(10):1649-1664.
34. Tong P, Pian TH, Lasry SJ. A hybrid-element approach to crack problems in plane elasticity. *Int J Numer Methods Eng.* 1973;7(3):297-308.
35. Seweryn A, Lukaszewicz A. Verification of brittle fracture criteria for elements with V-shaped notches. *Eng Fract Mech.* 2002;69(13):1487-1510.
36. Sih GC, Ho JW. Sharp notch fracture strength characterized by critical energy density. *J Theor Appl Fract Mech.* 1991;16(3):179-214.
37. Susmel L, Taylor D. The theory of critical distances to predict static strength of notched brittle components subjected to mixed-mode loading. *Eng Fract Mech.* 2008;75(3-4):534-550.
38. Karihaloo BL, Nallathambi P. An improved effective crack model for the determination of fracture toughness of concrete. *Cem Concr Res.* 1989;19(4):603-610.
39. ASTM C215–19 Standard Test Method for Fundamental Transverse, Longitudinal, and Torsional Resonant Frequencies of Concrete Specimens. Available at: <https://www.astm.org/Standards/C215>. Accessed December 1, 2020.
40. Šimonová H, Kucharczyková B, Bilek V, Malíková L, Miarka P, Lipowczan M. Mechanical fracture and fatigue characteristics of fine-grained composite based on sodium hydroxide-activated

- slag. *Appl Sci*. 2021;11(259):1-10. <https://www.mdpi.com/2076-3417/11/1/259/htm>
41. Aliha MRM, Ayatollahi MR. Analysis of fracture initiation angle in some cracked ceramics using the generalized maximum tangential stress criterion. *Int J Solids Struct*. 2012;49(13):1877-1883.
42. Li XH, Zheng XY, Yuan WJ, Cui XW, Xie YJ, Wang Y. Instability of cracks initiation from a mixed-mode crack tip with iso-stress intensity factors K I and K II. *Theor Appl Fract Mech*. 2018;96:262-271.
43. Anderson TL. *Fracture Mechanics: Fundamentals and Applications*. Florida: CRC Press LLC; 1995.

**How to cite this article:** Malíková L, Miarka P, Kucharczyková B, Šimonová H. Williams expansion utilized for assessment of crack behaviour under mixed-mode loading in alkali-activated fine-grained composite. *Fatigue Fract Eng Mater Struct*. 2021;44:1151-1161. <https://doi.org/10.1111/ffe.13418>



## II.2 FRACTURE RESPONSE OF ALKALI-ACTIVATED SLAG MORTARS WITH DISPERSED REINFORCEMENT

Just like materials based on Portland cement, composites based on AAB are quasi-brittle materials that show what is known as tensile softening. Different types of steel, synthetic or natural fibres are added to improve the material's resistance to crack propagation. The selected articles present results of the fracture behaviour of alkali-activated slag composites with steel microfibers and carbon nanotubes.

### II.2.1

Šimonová, H., Frantík, P., Keršner, Z., Schmid, P., Rovnaník, P. Components of the fracture response of alkali-activated slag composites with steel microfibers. *Applied Sciences*. 2019, Vol. 9, No. 9, article 1754. <https://doi.org/10.3390/app9091754> (Q2–Engineering, multidisciplinary; 2 citations without self-citations of all authors according to WoS)

#### II.2.1 Description

The main aim of the present work was to determine the fracture parameters of alkali-activated slag (AAS) composites with steel microfibers and quantify the contribution of the matrix of AAS composites to their fracture response. Five AAS composites were investigated. The obtained results can be used when designing alternative binders for Portland cement and also as relevant input data for material models for the realistic numerical modelling of the response of structures or their parts which are made from this type of composite.

#### II.2.1 Role of the author – the percentage of contribution: 35 %

Hana Šimonová is the main author of this article responsible for the methodology and the detailed data processing and evaluation of performed fracture experiments of the presented research. Furthermore, she prepared the original draft of the article which was later reviewed in cooperation with other co-authors.

### II.2.2

Rovnaník, P., Šimonová, H., Topolář, L., Bayer, P., Schmid, P., Keršner, Z. Carbon nanotube reinforced alkali-activated slag mortars. *Construction and Building Materials*. 2016, Vol. 119, pp. 223–229. ISSN 0950-0618. <http://dx.doi.org/10.1016/j.conbuildmat> (Q1–Engineering, civil; 23 citations according WoS)

#### II.2.2 Description

The main aim of this work was to apply multi-walled carbon nanotubes (MWCNTs) as a shrinkage-reducing admixture for AAS-based mortars. However, the MWCNTs exhibit extraordinary mechanical properties and thus they are promising nanomaterials for enhancing the mechanical fracture properties of building materials and their resistance to crack propagation. Therefore, the fracture properties of AAS composites with various amounts of MWCNTs as dispersed reinforcement have been investigated. It was shown that the addition of up to 0.2 % of MWCNTs improves the fracture properties of AAS. Although a higher content of MWCNTs reduces the total number of microcracks, it introduces too many imperfections to the AAS matrix and causes the composite to become more brittle, so fewer crack propagation events are needed before the complete fracture of the specimen.

II.2.2 *Role of the author – the percentage of contribution: 20 %*

Hana Šimonová is a co-author of this paper responsible for the preparation and detailed evaluation of fracture tests of specimens made of investigated composites. Furthermore, she prepared the original draft of the article's parts describing the fracture tests and their evaluation.

Article

# Components of the Fracture Response of Alkali-Activated Slag Composites with Steel Microfibers

Hana Šimonová \*, Petr Frantík, Zbyněk Keršner, Pavel Schmid and Pavel Rovnaník

Brno University of Technology, Faculty of Civil Engineering, Veveří 331/95, 602 00 Brno, Czech Republic; kitnarf@centrum.cz (P.F.); kersner.z@fce.vutbr.cz (Z.K.); pavel.schmid@vutbr.cz (P.S.); rovnanik.p@fce.vutbr.cz (P.R.)

\* Correspondence: simonova.h@vutbr.cz; Tel.: +420-541-147-381

Received: 4 April 2019; Accepted: 24 April 2019; Published: 27 April 2019



**Abstract:** Knowledge of the mechanical and primarily fracture parameters of composites with a brittle matrix is essential for the quantification of their resistance to crack initiation and growth, and also for the specification of material model parameters employed for the simulation of the quasi-brittle behavior of structures made from this type of composite. Therefore, the main target of this paper is to quantify the mechanical fracture parameters of alkali-activated slag composites with steel microfibers and the contribution of the matrix to their fracture response. The first alkali-activated slag composite was a reference version without fibers; the others incorporated steel microfibers amounting to 5, 10, 15 and 20% by weight of the slag. Prism specimens with an initial central edge notch were used to perform the three-point bending fracture tests. Load vs. displacement (deflection at midspan) and load vs. crack mouth opening displacement diagrams were recorded during the fracture tests. The obtained diagrams were employed as inputs for parameter identification, the aim of which was to transfer the fracture test response data to the desired material parameters. Values were also determined for fracture parameters using the effective crack model, work-of-fracture method and double-*K* fracture model. All investigated mechanical fracture parameters were improved by the addition of steel microfibers to the alkali-activated matrix. Based on the obtained results, the addition of 10 to 15% of microfibers by weight is optimal from the point of view of the enhancement of the fracture parameters of alkali-activated slag composite.

**Keywords:** alkali-activated slag; steel microfibers; fracture test; identification; work-of-fracture method; double-*K* model; crack propagation

## 1. Introduction

The global production of cement in 2018 was about 4.1 billion tons [1]. That immense volume of cement production is related to a very substantial impact on the environment: the carbon dioxide emissions produced by the cement industry contribute up to 8% of worldwide CO<sub>2</sub> emissions [2].

The majority of Portland cement (PC) is employed to produce concrete, mortars and plasters in the building industry. To decrease cement consumption, supplementary cementitious materials with good hydraulic cementitious properties (especially fly ash and ground granulated blast furnace slag) are often used as partial substitutes for PC in specific applications. They are also employed as constituent parts of blended cements [1]. The other possibility is to use alternative types of binder. Alkali-activated materials (AAM) are one example of the relatively new binders now being produced via the alkaline activation of different materials of geological origin or by-product materials that are rich in silicon and aluminum. The utilization of secondary raw materials (fly ashes, slags, etc.) or

other aluminosilicate materials during alkali activation leads to a decrease in cement consumption, resulting in the more efficient reduction of CO<sub>2</sub> emissions and energy consumption. Although the production of alkaline activators is connected with CO<sub>2</sub> emissions it is assumed that the global warming potential of alkali-activated composites is approximately 40–70% lower than that of ordinary PC-based composites [3,4]. AAMs also show good durability compared to Portland cement [5,6].

Just like materials based on Portland cement, AAMs are quasi-brittle materials that show what is known as tensile softening. The different types of steel, synthetic or natural fibers which are used in Portland cement-based materials [7–10] are added to improve the material's resistance to crack propagation. Knowledge of the mechanical and primarily fracture parameters of composites with a brittle matrix is essential for the quantification of their resistance to crack initiation and growth, as well as for the specification of material model parameters employed for the simulation of the quasi-brittle behavior of structures or their parts made from this type of composite. Studying the mechanical response of specimens made of such composites under static and dynamic/fatigue loading is complicated due to their highly nonlinear nature. Numerical tools for modeling both elastic (elastic-plastic) behavior, and also the fracture process, are commonly used to predict or assess this response. Such tools—often based on the finite element method [11] or physical discretization of the continuum [12]—usually exploit a type of nonlinear fracture model that simulates the cohesive nature of the cracking of quasi-brittle material [13–15]. The parameters of this fracture model are determined from records of fracture tests; this is carried out either using evaluation methods built on the principle of the used non-linear fracture model, e.g., the work-of-fracture method [16] or the size effect method [17], or using inverse analysis with the possible application of advanced identification methods [18–20]. The fracture models for quasi-brittle composites are most often based on the standardized geometry of specimens with stress concentrators; the three-point bending test [14] or wedge splitting test [21,22] are typically used.

As mentioned above, in order to perform the realistic numerical modeling of the response of quasi-brittle composite structures it is essential to determine the parameters of the used material models from experimental measurements. Unfortunately, the literature on the fracture properties of alkali-activated mortars which can be used as suitable inputs for material models is still fairly limited. Most of the published articles are only concerned with the determination of basic mechanical parameters, i.e., compressive and flexural strengths, or in some cases modulus of elasticity [23–30]. Only a few researchers' findings connected with the fracture behavior of this kind of material have been published. Goncalves et al. [31] presented a study about the crack growth resistance of fiber-reinforced alkali-activated fly ash concrete exposed to extreme conditions. Alomayri [32] investigated the effects of glass microfiber content on the mechanical properties of fly ash-based geopolymer. It was found that the optimal amount of glass microfibers is 2 mass% from the point of view of the enhancement of fracture toughness, compressive strength, Young's modulus and hardness. Ding et al. [33,34] examined the fracture properties of alkali-activated slag (AAS) and ordinary Portland cement (OPC) concrete and mortar. It was observed that the fracture energy value was lower in the case of AAS mortar, as compared to OPC mortar with the same compressive strength. Sarker et al. [35] investigated the effect of geopolymer binder on the fracture characteristics of concrete. The fracture energy of geopolymer determined by the work-of-fracture method was similar to that of the investigated OPC concrete. The critical stress intensity factor was higher in the case of geopolymer compared to OPC concrete with the same compressive strength. Ngyuen et al. [36] ascertained that the addition of polypropylene fibers to AAS mortar leads to an increase in fracture energy and fracture toughness compared to mortar without fibers.

Because of the lack of information about the fracture properties of composites with alkali-activated matrix which could be used as relevant inputs for the material model, the main aim of the present work is to determine the fracture parameters of alkali-activated slag composites with steel microfibers and quantify the contribution of the matrix of AAS composites to their fracture response. Five AAS composites were investigated. The first was a reference version without fibers; the others contain

steel microfibers amounting to 5, 10, 15 and 20% by weight of the slag. The AAS mixtures were cast into molds with dimensions of  $40 \times 40 \times 160$  mm so as to prepare prismatic specimens for use in fracture testing. The fracture characteristics were determined based on the results of three-point bending tests conducted on specimens which were provided with an initial central edge notch before testing. Load vs. displacement (deflection at midspan) and load vs. crack mouth opening displacement diagrams were recording during the fracture tests. Each diagram was processed in order to obtain the component that corresponds to the structural response of the matrix of the composite, which consists of AAS matrix and the steel microfibers reinforcing that matrix. The obtained diagrams were employed as inputs for parameter identification, the aim of which was to transfer the fracture test response data to the required material parameters. Values were also determined for the fracture parameters using the effective crack model [14], work-of-fracture method [16] and double-K fracture model [37].

## 2. Materials and Methods

### 2.1. Mixtures

The first alkali-activated slag composite was a reference version without fibers. Granulated blast furnace slag provided by Kotouč, s.r.o. (CZ) was chosen as a binder. The specific surface and mean grain size of the slag were  $383 \text{ m}^2/\text{kg}$  and  $15.5 \text{ }\mu\text{m}$ , respectively. Solid sodium silicate (Susil MP 2.0) fabricated by Vodní sklo, a.s. (CZ) was used to achieve the alkali activation of the slag. The alkaline activator has a molar  $\text{SiO}_2/\text{Na}_2\text{O}$  ratio equal to 2.0, and a  $\text{SiO}_2$  content of 52.4%. The fine-grained AAS composites were produced using quartz sand with a maximum grain size of 2.5 mm. Brass coated steel microfibers with an average length of 6 mm and a diameter of 0.175 mm supplied by KrampeHarex CZ s.r.o. were used as reinforcement (see Figure 1). The added steel microfibers amounted to 5, 10, 15 and 20% of the weight of the slag.



**Figure 1.** The used steel microfibers with an average length of 6 mm and a diameter of 0.175 mm.

The AAS mixtures used for casting the prismatic specimens were prepared according to the following previously optimized procedure. At first, solid alkaline activator was suspended in water in which it dissolved partially. Then, the slag and quartz sand were added to the activator and the mixture was stirred in the planetary mixer for about 5 min to provide a fresh slurry. The aggregate to slag ratio was equal to 3.0. Finally, steel microfibers were added to the mixture and further mixed for another 3 min so as to disperse them properly. The AAS mixture composition is presented in Table 1. The designation of individual mixtures is based on their steel microfiber content: SF00, SF05, SF10, SF15, and SF20. Mixture SF00 is a reference mix without steel microfibers.

The prepared fresh mixtures were cast into prismatic moulds of  $40 \times 40 \times 160$  mm in size. Three specimens were made from each mixture. After 24 h the hardened specimens were immersed in a water bath at  $20 \text{ }^\circ\text{C}$  for further 27 days. Before the fracture tests were performed, all specimens were pulled out of the water and allowed to dry spontaneously under ambient conditions for 24 h.

**Table 1.** Composition of alkali-activated slag mixtures.

Component	Unit	SF00	SF05	SF10	SF15	SF20
Slag	g	450	450	450	450	450
Sodium silicate	g	90	90	90	90	90
Aggregate	g	1350	1350	1350	1350	1350
Steel microfibers	g	–	22.5	45.0	67.5	90.0
Water	mL	190	190	190	195	195

## 2.2. Fracture Test Configuration

The determination of the mechanical fracture parameters of composites with brittle matrix is most often based on fracture tests conducted on specimens of standardized geometry with stress concentrators; the three-point bending test [14] or wedge splitting test [21,22] are typically used. In this case, the three-point bending configuration was chosen because of the availability of testing equipment. Standardized prism specimens with a nominal size of  $40 \times 40 \times 160$  mm, which are typically used for the determination of basic mechanical properties of mortars, were used for the fracture tests. An initial notch was cut by a diamond blade saw in the center of the prisms. The nominal depth was about 13 mm. The span length was 120 mm. The fracture tests were performed at the age of 29 days.

A very stiff mechanical testing machine (LabTest 6-1000.1.10, LaborTech s.r.o., Opava, Czech Republic) was used to perform the fracture tests. The stiffness of the testing machine is required to be adequate in comparison to the specimen's stiffness so as to enable stable fracture tests to be conducted without any interruption in the post-peak branch. The loading was conducted so that displacement occurred in constant increments, which were equal to 0.02 mm/min. This loading procedure is slow enough for the whole post-peak behavior of test specimens to be recorded.

The dependence between loading force and the deflection of the center of the prism specimen ( $F-d$  diagram), as well as crack mouth opening displacement ( $F-CMOD$  diagram), constituted the outputs of the performed fracture tests. The deflection and  $CMOD$  values were gauged using an inductive sensor placed above the support and by extensometer placed between blades fixed close to the initial notch, respectively (see Figures 2 and 3). The mentioned parameters together with time were continuously recorded by an HBM Quantum X data logger (HBM, Darmstadt, Germany); the frequency was 5 Hz.



**Figure 2.** The selected reference specimen after the fracture test was performed with crack propagation from initial notch; detail of blades fixed close to the initial notch used for measurement of  $CMOD$ .

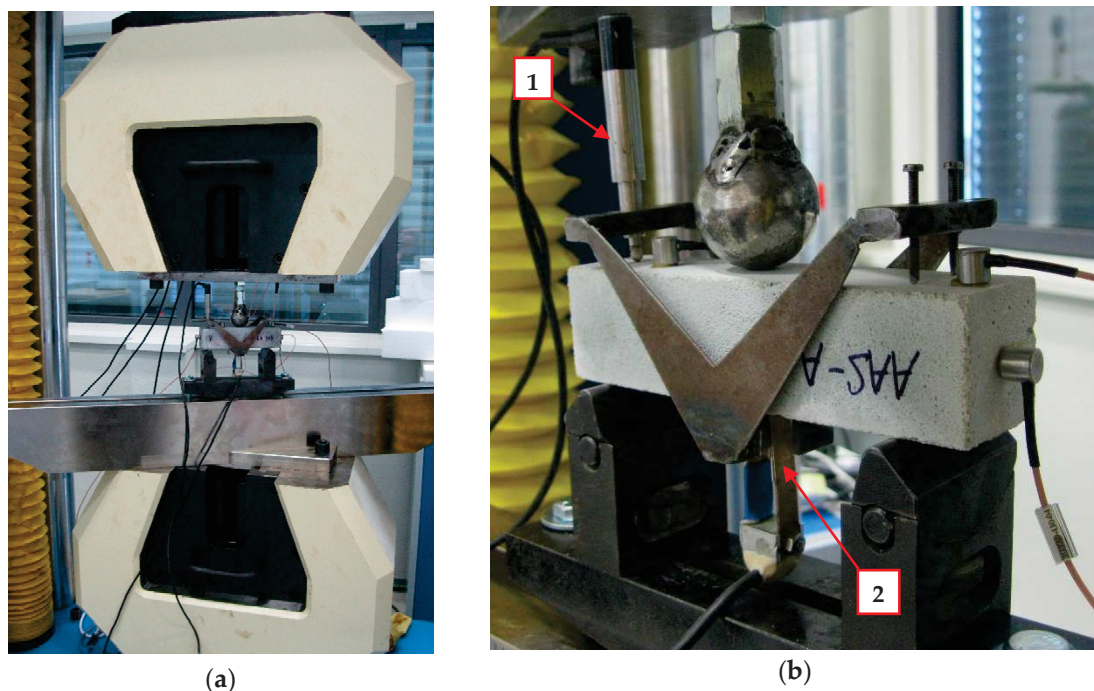


**Figure 3.** Fracture test configuration: (a) Overall view of the testing machine; (b) Detail of the positions of measuring sensors (1—deflection sensor fixed in the measurement frame, 2—extensometer).

### 2.3. Adjustment of Measured $F-d$ and $F-CMOD$ Diagrams

At the beginning of the specimen loading, small-sized deviations in the measured values of monitored parameters are often recorded. This effect is caused by small projections on the specimen's surface being crushed due to the pressure at the support and loading points. These phenomena usually occur over a short period at the beginning of the loading test, after which the measured diagram proceeds with a linear part. It follows that it is appropriate to adjust the beginning part of the diagram in order to obtain the correct input values for the subsequent evaluation of diagrams using the selected fracture model. The first step is to construct a straight best-fit line for the linear part of the diagram, after which the intersection of the line with the horizontal axis must be pinpointed. The second step consists in the shifting of all points of the diagram equidistantly, thus making the intersection the new origin of the coordinate system.

The adjustment of the recorded diagrams was performed in GTDiPS software (v3.01, developed by Petr Frantík and Jan Mašek, Brno University of Technology, Czech Republic) [38], which is based on advanced transformation methods used for the processing of extensive point sequences. The adjustment of diagrams in this case incorporated the erasing of duplicate points, the moving of the origin of the coordinate system, the smoothing of the diagram and the reduction of the number of points.

Thereafter, each diagram was processed to obtain the component that corresponds to the structural response of the matrix of the composite and the steel microfibers reinforcing that matrix. The individual steps of the decomposition procedure are as follows: first, the measured diagram of the steel microfiber-reinforced AAS composite specimen is plotted; then, the last part of this diagram (after the substantial drop in the curve) is assumed to be the result of the contribution of the steel microfibers only and the composite matrix is not expected to have an effect here. That last part is subjected to a straightforward linear regression analysis so that an approximation of the initial part of the diagram can also be obtained (a polynomial function is used here with extrapolation to the origin of the diagram space). Finally, the approximation is subtracted from the recorded diagram, which results in a simulated diagram corresponding to the plain AAS matrix for the next evaluation. A detailed illustration of the used procedure can be found in [39].

The above-described procedure was applied to all measured  $F-d$  and  $F-CMOD$  diagrams. For the purpose of illustration, Figure 4 shows corrected  $F-CMOD$  diagrams of AAS composites with various amounts of microfibers. The use of the  $F-d$  diagrams after the decomposition procedure is described in the following section.

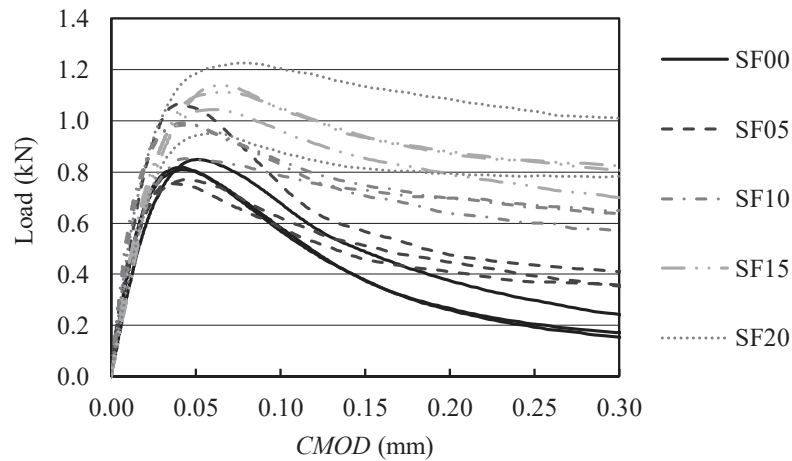


**Figure 4.**  $F-CMOD$  diagrams of alkali-activated slag (AAS) composites with various amounts of microfibers.

#### 2.4. Identification of Material Parameters

After the previously mentioned adjustment, the  $F-d$  diagrams were utilized as input data for parameter identification with the aim of transferring the fracture test response data to the desired material parameters. The FiCubS application [40] developed by co-author Petr Frantík was used for this purpose. The FiCubS application is used to simulate the performance of a fracture test in the three-point bending configuration on a fiber-reinforced composite prism with a notch.

Using symmetry, half of the specimen is modeled as an elastic body connected to the plane of symmetry by boundary conditions, which can be released and replaced by cohesive forces. The release of a particular condition occurs after the tensile strength of the material is overstepped. Cohesive forces are dependent on displacements of the released ligament area and on the identified cohesive function. The used cohesive function consists of two components: cohesion provided by the matrix and by fiber resistance. The matrix cohesive function is modeled by the Hordijk function [41]:

$$\sigma = f_t \left[ \left( 1 + \left( c_1 \frac{w}{w_c} \right)^3 \right) e^{(-c_2 \frac{w}{w_c})} - \frac{w}{w_c} (1 + c_1^3) e^{-c_2} \right] \quad (1)$$

where  $\sigma$  is cohesive stress,  $f_t$  is tensile strength,  $w$  is crack opening displacement,  $w_c$  is critical crack opening displacement, and  $c_1$  and  $c_2$  are material constants.

The fiber resistance is modeled by the proposed function:

$$\sigma = \sigma_{\max} \left( 1 - \frac{1}{w_{cf}} \left( w e^{p(w-w_{cf})} + (w_{cf} - w) e^{-kw} \right) \right) \quad (2)$$

where  $\sigma$  is the cohesive stress applied for displacement  $w$ ,  $\sigma_{\max}$  is the approximate maximum cohesive stress,  $w_{cf}$  is the displacement limit where cohesion disappears and  $k, p$  are parameters determining the initial and finite slope. Initial and finite slopes are given by:

$$\frac{\partial \sigma}{\partial w} \Big|_{w=0} = \frac{\sigma_{\max}}{w_{cf}} \left( 1 + kw_{cf} - e^{-pw_{cf}} \right) \quad (3)$$

$$\frac{\partial}{\partial w} \sigma \Big|^{w=w_{cf}} = \frac{\sigma_{\max}}{w_{cf}} \left( 1 - (pw_{cf} + 1)e^{kw_{cf}} \right) e^{-kw_{cf}} \tag{4}$$

The total fracture energy  $G$  represented by this function is given by the relation:

$$G = \sigma_{\max} \left( \frac{1}{w_{cf}} \left( \frac{1}{k^2} (1 - e^{-w_{cf}k}) + \frac{1}{p^2} (1 - e^{-w_{cf}p}) \right) - \frac{1}{k} - \frac{1}{p} + w_{cf} \right) \tag{5}$$

From the identified parameters of the model (seven independent values) it was necessary to determine the effective modulus of elasticity of the composite, the tensile strength of the composite, the fracture energy and the coefficient of transverse contraction.

To illustrate, Figure 5 shows  $F-d$  diagrams for selected specimens of AAS composite with various amounts of steel microfibers. The following diagrams are plotted in the graphs: a measured diagram of composite reinforced by microfibers (COMP); a simulated diagram corresponding to the plain AAS matrix (MTX); an identified diagram of AAS composite reinforced by microfibers (ID).

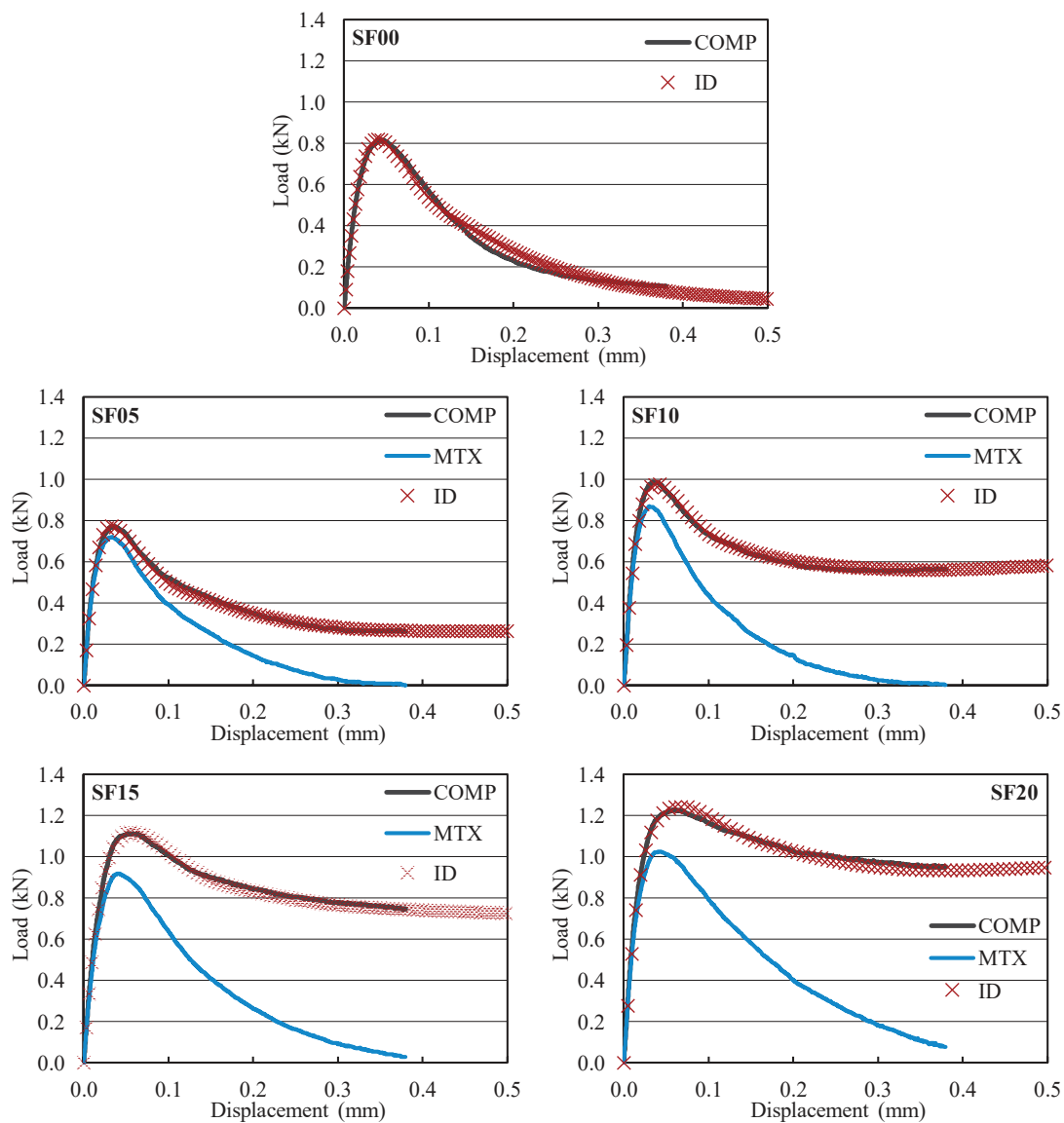


**Figure 5.**  $F-d$  diagrams for selected specimens of individual AAS composites with various amounts of steel microfibers: COMP—a measured diagram of composite reinforced by microfibers; MTX—a simulated diagram corresponding to the plain AAS matrix; ID—an identified diagram of composite reinforced by microfibers.

### 2.5. Evaluation of $F-d$ Diagrams

After the previously mentioned diagram adjustment, the ascending linear parts of the  $F-d$  diagrams were utilized to estimate the modulus of elasticity  $E_c$  values according to [14]:

$$E_c = \frac{F_i}{4Bd_i} \left(\frac{S}{D}\right)^3 \left[ 1 + \frac{5qS}{8F_i} + \left(\frac{D}{S}\right)^2 \left\{ 2.70 + 1.35 \frac{qS}{F_i} \right\} - 0.84 \left(\frac{D}{S}\right)^3 \right] + \frac{9}{2} \frac{F_i}{Bd_i} \left( 1 + \frac{qS}{2F_i} \right) \left(\frac{S}{D}\right)^2 F_1(\alpha_0) \tag{6}$$

where  $F_i$  is load in the ascending linear part of the diagram;  $d_i$  is deflection at midspan corresponding with load  $F_i$ ;  $B$  and  $D$  are the breadth and depth of the specimen, respectively;  $q$  is the self-weight of the specimen per unit length;  $S$  is length of the span and with  $\alpha_0 = a_0/D$ , and  $Y(x)$  is the geometry function for the three-point bending configuration [14] ( $a_0$  is the depth of the initial notch).

The effective fracture toughness  $K_{Ice}$  was determined based on the  $F-d$  diagrams using the effective crack model [14]. First, the effective crack length  $a_e$  corresponding with the maximum load  $F_{max}$  and matching deflection at midspan  $d_{Fmax}$  was calculated. From the effective crack concept, it follows that the  $a_e$  can be calculated from rearranged Equation (6) using  $F_{max}$  and  $d_{Fmax}$  instead of  $F_i$  and  $d_i$ . Subsequently, the effective fracture toughness values were calculated using a linear elastic fracture mechanics formula according to [14,42]:

$$K_{Ice} = \frac{3F_{max}S}{2BD^2} Y(\alpha_e) \sqrt{a_e} \tag{7}$$

where  $Y(\alpha_e)$  is the geometry function with  $\alpha_e = a_e/D$  [14].

The complete  $F-d$  diagrams, including their post-peak parts, were employed to determine the work of fracture  $W_F^*$ , which is given by the area under the  $F-d$  diagram. After that, the specific fracture energy values were determined according to the RILEM method [16,43]:

$$G_F^* = \frac{W_F^*}{B(D - a_0)} \tag{8}$$

### 2.6. Evaluation of $F-CMOD$ Diagrams

After the previously mentioned diagram adjustment, the double- $K$  fracture model was employed for subsequent evaluation of the  $F-CMOD$  diagrams. The benefit of the double- $K$  fracture model lies in its ability to predict the different phases that occur during crack propagation in quasi-brittle material: crack initiation and both stable and unstable crack propagation. The different phases of the fracture process in quasi-brittle material can be connected with two size-independent parameters: the initiation fracture toughness  $K_{Ic}^{ini}$  and unstable fracture toughness  $K_{Ic}^{un}$ . The determination of double- $K$  model parameters is based on an approach involving the action of cohesive forces on the faces of the fictitious (effective) crack increment combined with the stress intensity factor criterion (for details refer to (for example) Kumar and Barrai [37]).

In the instance of the present research, as the first step the unstable fracture toughness  $K_{Ic}^{un}$  was determined. In the second step, the cohesive fracture toughness  $K_{Ic}^c$  was determined. As the last step, the following formula based on the formerly obtained parameters was utilized to calculate the initiation fracture toughness  $K_{Ic}^{ini}$ :

$$K_{Ic}^{ini} = K_{Ic}^{un} - K_{Ic}^c \tag{9}$$

The exact procedure concerning the determination of cohesive and unstable fracture toughness values can be found in many published works, e.g., [37,44].

In general, the relation between the cohesive stress and the effective crack opening displacement is given by the cohesive stress function in the cohesive crack model. The cohesive stress at the tip of an initial notch at the critical state can be gained from the softening function. In this study, a non-linear

softening function (1) (as stipulated in Hordijk [41]) was used. The parameters of the softening function were considered to be as follows: the tensile strength  $f_t$  was considered based on identification described in Section 2.4, the fracture energy was determined according to Equation (8), and the material constants were considered according to [41] as being  $c_1 = 3$  and  $c_2 = 6.93$ .

Finally, the load  $F_{ini}$ , which expresses the load at the outset of stable crack propagation from the initial crack/notch, was determined according to this relation:

$$F_{ini} = \frac{4 \cdot W \cdot K_{Ic}^{ini}}{S \cdot F_1(\alpha_0) \cdot \sqrt{a_0}} \tag{10}$$

where  $W$  is the section modulus (calculated as  $W = 1/6 \cdot B \cdot D^2$ ),  $S$  is span length,  $F_1(\alpha_0)$  is the geometry function for a three-point bending configuration [14] and  $\alpha_0$  is the  $a_0/D$  ratio.

### 3. Results and Discussion

The average values (determined based on 3 independent measurements) and sample standard deviations (given by the error bars) of selected mechanical fracture parameters of AAS composites with different amounts of steel microfibers obtained from  $F-d$  and  $F-CMOD$  diagrams are summarized in the following figures. The values obtained for the monitored parameters using the above-described non-linear fracture models were determined for composite reinforced by microfibers (COMP) and for the plain AAS matrix (MTX) which results when the decomposition procedure is applied to the measured diagrams. Selected parameters were determined via the inverse analysis of  $F-d$  diagrams of AAS composites reinforced by microfibers (ID).

Compressive and tensile strength values gained for AAS composite with different amounts of steel microfibers are shown in Figure 6. The compressive strength was determined according ČSN EN 196-1 [45] from two parts of the prismatic specimens obtained after the fracture tests were finished. The reference AAS composite achieved a compressive strength equal to 65 MPa, which is comparable with values gained for alkali-activated slag [33] and fly ash-based composite [46] that have been published in the literature. The addition of steel microfibers did have a reinforcing effect: compressive strength gradually increased with the addition of microfibers amounting to 5 and 10% by weight. The highest mean value of 93 MPa was obtained for the composite with a 15% microfiber content. However, there is no significant difference between microfiber contents of 10 to 20%.

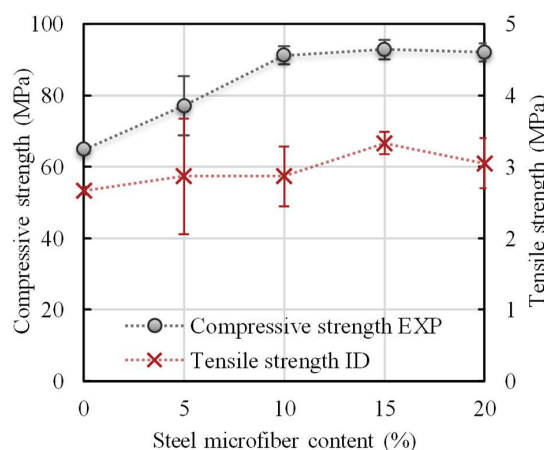


Figure 6. Compressive and tensile strength of AAS mortar with different amounts of steel microfibers.

The tensile strength value was obtained by identification from measured  $F-d$  diagrams. The tensile strength of the reference AAS composite was 2.7 MPa. As in the case of compressive strength, the highest mean value was obtained for the composite with a 15% microfiber content, the increase being about 25% in comparison with composite without fibers.

The modulus of elasticity of the reference AAS composite was 15.1 GPa (see Figure 7), which is comparable with values for alkali-activated slag-based composite published in the literature [33]. The modulus of elasticity increased with the addition of microfibers by about 30–40%. The highest mean value of 21.1 GPa was reached for the composite with a 5% microfiber content. However, the standard deviation for higher amounts of microfibers is so high that the modulus of elasticity can be considered to be almost the same. The higher standard deviation especially for 20% microfiber content is caused by heterogeneity of material when the uniform dispersion of fibers became more difficult to achieve. The same trend seen for the modulus of elasticity with the addition of microfibers was observed for the values obtained by identification. The identified values are about 5% higher. If only the contribution of plain AAS matrix is taken into consideration, then the modulus of elasticity is up to 5% lower in comparison with AAS composite containing steel microfibers.

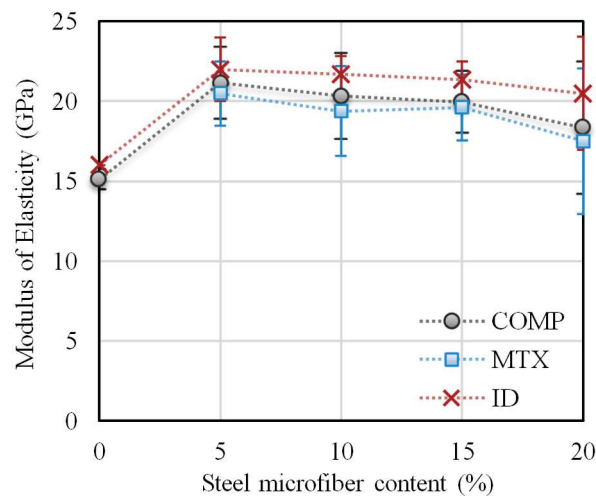


Figure 7. Modulus of elasticity of AAS mortar with different amounts of steel microfibers.

The fracture toughness values for AAS mortar with different amounts of steel microfibers determined by two different non-linear fracture models are presented in Figure 8a. Fracture toughness gradually increased with the addition of steel microfibers in both cases. The fracture toughness values obtained by both models are the same in the case of microfiber contents of 5–10%. The fracture toughness obtained by the double-K model is about 15% lower in the case of the reference composite and composites with a microfiber content of 15% and more. The fracture toughness of the reference AAS composite is comparable with values gained for alkali-activated slag-based composite with similar compressive strength that have been published in the literature [36].

If only the contribution of plain AAS matrix is taken into consideration, then the fracture toughness is about 95, 85, 80 and 70% of the fracture toughness of AAS composites containing steel microfibers SF05, SF10, SF15 and SF20, respectively (see Figure 8b). The same trend was also observed for fracture toughness determined by the double-K fracture model.

The fracture energy values gained for AAS mortar with various amounts of steel microfibers determined by the work-of-fracture method are presented in Figure 9. The specific fracture energy of the reference composite is 113 J/m<sup>2</sup>, and this gradually increases as the amount of steel microfibers rises. The fracture energy of the reference AAS composite is comparable with that of an AAS composite with similar compressive strength published in the literature [33]. The highest mean value was obtained for the composite with a 20% microfiber content. This is more than 2.5 times higher than the reference composite value. However, the standard deviation is so high that the value can be considered to be almost the same as for the composite with a 15% microfiber content. The same trend in fracture energy values with the addition of microfibers was observed for values gained via identification. The values obtained in this way are about 15–25% lower in comparison to those obtained via the work-of-fracture method. The sample standard deviation is significantly higher in the case of values determined by

identification. If only the contribution of plain AAS matrix is taken into consideration, the fracture energy ranges between 40–50% of that of AAS composite containing steel microfibers.

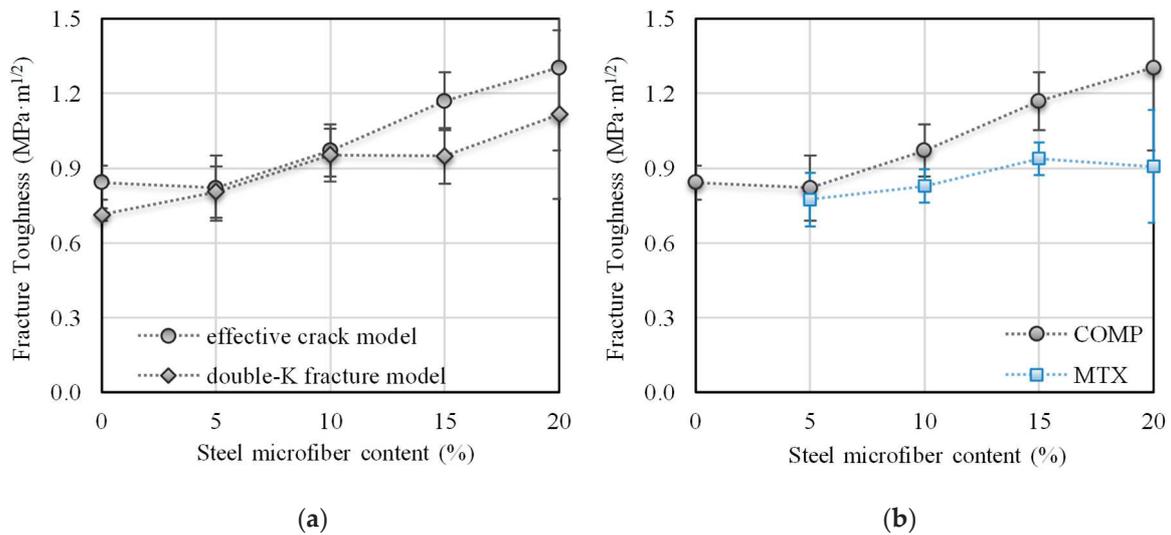


**Figure 8.** Fracture toughness of AAS mortar with different amounts of steel microfibers determined by: (a) Two different fracture models; (b) The effective crack model—contribution of plain AAS matrix.

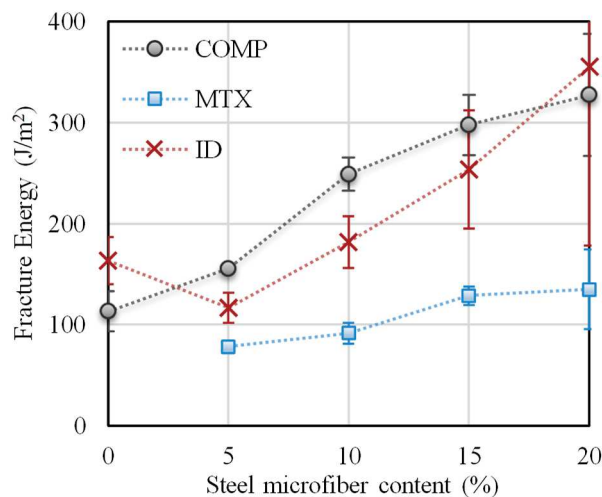


**Figure 9.** Fracture energy of AAS mortar with different amounts of steel microfibers.

The  $K_{Ic}^{ini}/K_{Ic}^{un}$  ratio (fracture toughness ratio, see Figure 10a), which expresses resistance to stable crack propagation, decreased by about 15% in the case of composite with a steel microfiber content of up to 10%. For composite with a higher steel microfiber content, the fracture toughness ratio is comparable with that of the reference composite.

The ratio between the load at the outset of stable crack propagation and the maximum load obtained during the test (load ratio, see Figure 10b) shows a trend analogous to that of the fracture toughness ratio. The addition of steel microfibers (5% by weight) caused a slight decrease in the load ratio. The load ratio for higher amounts of steel microfibers is comparable with that of the reference composite when standard deviation is taken into consideration.

From the obtained results it is obvious that the addition of steel microfibers has a positive effect on resistance to unstable crack propagation and the post-peak behavior of composite. However, resistance to stable crack propagation is rather negatively affected by the addition of steel microfibers, which can be attributed to the heterogeneity of the specimens which occurs when fibers are added. If only the

contribution of plain AAS matrix is taken into consideration, the resistance to stable crack propagation is about 10–15% higher than in the case of AAS composite with a steel microfiber content of more than 10%.

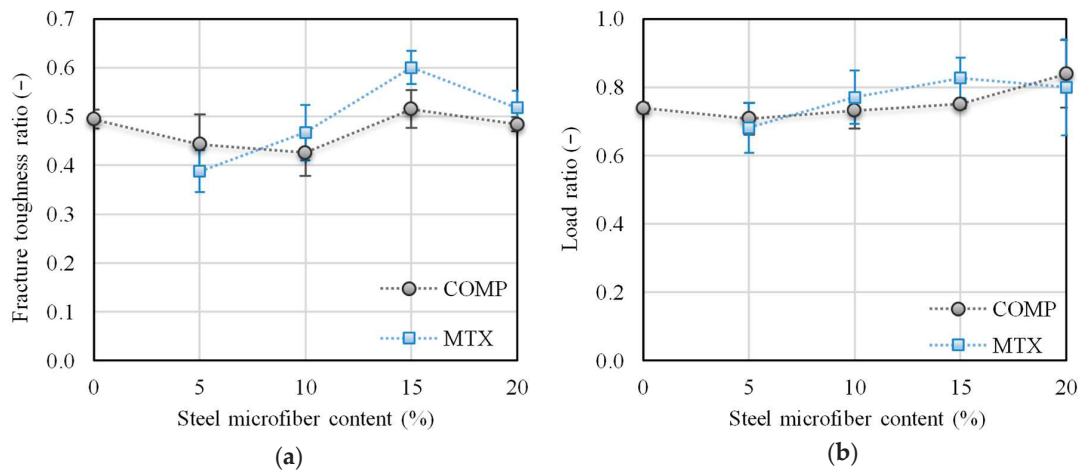


**Figure 10.** Fracture toughness ratio (a) and load ratio (b) of AAS mortar with different amounts of steel microfibers.

#### 4. Conclusions

Because of the lack of information concerning the fracture properties of composites with alkali-activated matrix which could be used as inputs for material models, the main aim of the present research was to assess the fracture parameters of alkali-activated slag composites with steel microfibers and quantify the contribution of the matrix of AAS composites to their fracture response. The following conclusions can be drawn based on the obtained experimental research results:

- The compressive strength value increased by up to 40% in the case of composite with a steel microfiber content of more than 10%;
- The modulus of elasticity increased with the addition of steel microfibers by about 30–40%. The highest mean value was obtained for the composite with a 5% content of steel microfibers by weight. If a comparison is made between AAS matrix alone and the composite including steel microfibers, it can be seen that the values are almost the same.

Generally, the addition of steel microfibers to AAS matrix should contribute to a lowering in the tendency to crack, and to an enhancement in the tensile properties of AAS based materials. The presented research results are in line with these suppositions:

- The addition of steel microfibers to the AAS matrix caused the resistance to unstable crack propagation expressed here by the fracture toughness to gradually increase by up to 50% for the composite with a 20% content of steel microfibers;
- The steel microfiber-reinforced AAS composites proved to have a much better load carrying capacity after the maximum load is reached in comparison with the reference composite;
- The addition of steel microfibers to the AAS matrix caused the fracture energy value to gradually increase by up to 2.5 times the reference composite value for the composite with a 20% content of steel microfibers; the energy absorption mechanism is related to the de-bonding and pull-out of microfibers that bridge cracks.

Based on the performed study, the addition of 10 to 15% by weight of microfibers to AAS composite is optimal from the point of view of the enhancement of the fracture properties of this composite. The obtained results can be used when designing alternative binders for Portland cement, as well as relevant input data for material models for the realistic numerical modeling of the response of structures or their parts which are made from this type of composite.

**Author Contributions:** Conceptualization, P.R.; methodology, H.S. and P.F.; software, P.F.; validation, P.R., P.F. and Z.K.; formal analysis, H.S. and P.F.; investigation, P.R., P.S. and H.S.; resources, P.R. and P.S.; data curation, H.S., P.F. and P.R.; writing—original draft preparation, H.S. and P.F.; writing—review and editing, P.R. and Z.K.; visualization, H.S.; supervision, P.R. and Z.K.; project administration, P.R.; funding acquisition, P.R.

**Funding:** This researcher was funded by the Czech Science Foundation, project No. 16-00567S, and the Ministry of Education, Youth and Sports of the Czech Republic under “National Sustainability Programme I” (project No. LO1408 AdMaS UP).

**Conflicts of Interest:** The authors declare no conflict of interest.

## References

1. U.S. Geological Survey. *Mineral Commodity Summaries 2019*; U.S. Geological Survey: Reston, VA, USA, 2019; 200p. [CrossRef]
2. Andrew, R.M. Global CO<sub>2</sub> emissions from cement production. *Earth Syst. Sci. Data* **2018**, *10*, 195–217. [CrossRef]
3. McLellan, B.C.; Williams, R.S.; Lay, J.; van Reissen, A.; Corder, G.D. Costs and carbon emissions for geopolymers in comparison to ordinary portland cement. *J. Clean. Prod.* **2011**, *19*, 1080–1090. [CrossRef]
4. Keun-Hyeok, Y.; Jin-Kyu, S.; Keun-Il, S. Assessment of CO<sub>2</sub> reduction of alkali-activated concrete. *J. Clean. Prod.* **2013**, *39*, 265–272. [CrossRef]
5. Provis, J.L.; van Deventer, J.S. (Eds.) *Alkali Activated Materials: State-of-the-Art Report RILEM TC 224-AAM*, 1st ed.; Springer: Dordrecht, The Netherlands, 2014; 388p. [CrossRef]
6. Shi, C.; Krivenko, P.V.; Roy, D. *Alkali-Activated Cements and Concretes*, 1st ed.; CRC Press: London, UK, 2003; 392p. [CrossRef]
7. Johnston, C.D. *Fiber-Reinforced Cements and Concretes*, 1st ed.; Taylor & Francis Group: London, UK, 2010; 261p.
8. Zanichelli, A.; Carpinteri, A.; Fortese, G.; Ronchei, C.; Scorza, D.; Vantadori, S. Contribution of date-palm fibres reinforcement to mortar fracture toughness. *Procedia Struct. Integr.* **2018**, *13*, 542–547. [CrossRef]
9. Smarzewski, P. Influence of basalt-polypropylene fibres on fracture properties of high performance concrete. *Compos. Struct.* **2019**, *209*, 23–33. [CrossRef]
10. Kizilkanat, A.B.; Kabay, N.; Akyüncü, V.; Chowdhury, S.; Akça, A.H. Mechanical properties and fracture behavior of basalt and glass fiber reinforced concrete: An experimental study. *Constr. Build. Mater.* **2015**, *100*, 218–224. [CrossRef]
11. Červenka, V.; Jendele, L.; Červenka, J. *ATENA Program Documentation—Part 1: Theory*; Červenka Consulting: Prague, Czech Republic, 2016.
12. Frantík, P. FyDiK Application. 2015. Available online: <http://fydik.kitnarf.cz/> (accessed on 1 April 2019).
13. Bažant, Z.P.; Planas, J. *Fracture and Size Effect in Concrete and other Quasibrittle Materials*, 1st ed.; CRC Press: Boca Raton, FL, USA, 1998; 640p.
14. Karihaloo, B.L. *Fracture Mechanics and Structural Concrete*, 1st ed.; Longman Scientific & Technical: Harlow, UK, 1995; 330p.
15. Shah, S.P.; Swartz, S.E.; Ouyang, C. *Fracture Mechanics of Structural Concrete: Applications of Fracture Mechanics to Concrete, Rock, and Other Quasi-Brittle Materials*, 1st ed.; John Wiley & Sons, Inc.: New York, NY, USA, 1995; 592p.
16. RILEM TC—50 FMC (Recommendation). Determination of the fracture energy of mortar and concrete by means of three-point bend tests on notched beams. *Mater. Struct.* **1985**, *18*, 287–290. [CrossRef]
17. RILEM TC—89 FMT (Recommendation). Size-effect method for determining fracture energy and process zone size of concrete. *Mater. Struct.* **1990**, *23*, 461–465. [CrossRef]
18. Frantík, P. CheCyId Application. 2017. Available online: <http://checyid.kitnarf.cz> (accessed on 1 April 2019).
19. Novák, D.; Lehký, D. ANN inverse analysis based on stochastic small-sample training set simulation. *Eng. Appl. Artif. Intell.* **2006**, *19*, 731–740. [CrossRef]
20. Lehký, D.; Novák, D.; Keršner, Z. FraMePID-3PB software for material parameter identification using fracture tests and inverse analysis. *Adv. Eng. Softw.* **2014**, *72*, 147–154. [CrossRef]
21. Brühwiler, E.; Wittmann, F.H. The wedge splitting test, a new method of performing stable fracture mechanics tests. *Eng. Fract. Mech.* **1990**, *35*, 117–125. [CrossRef]
22. Tschegg, E.K. New equipments for fracture tests on concrete. *Mater. Test.* **1991**, *33*, 338–342.
23. Bagheri, A.; Nazari, A.; Sanjayan, J.G. Fibre-reinforced boroaluminosilicate geopolymers: A comparative study. *Ceram. Int.* **2018**, *44*, 16599–16605. [CrossRef]

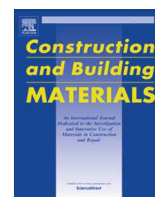
24. Nath, P.; Sarker, P.K. Flexural strength and elastic modulus of ambient-cured blended low-calcium fly ash geopolymer concrete. *Constr. Build. Mater.* **2017**, *130*, 22–31. [[CrossRef](#)]
25. Marjanović, N.; Komljenović, M.; Bašćarević, Z.; Nikolić, V.; Petrović, R. Physical–mechanical and microstructural properties of alkali-activated fly ash–blast furnace slag blends. *Ceram. Int.* **2015**, *41*, 1421–1435. [[CrossRef](#)]
26. Aydin, S.; Baradan, B. Effect of activator type and content on properties of alkali-activated slag mortars. *Compos. B Eng.* **2014**, *57*, 166–172. [[CrossRef](#)]
27. Rashad, A.M. A comprehensive overview about the influence of different additives on the properties of alkali-activated slag—A guide for Civil Engineer. *Constr. Build. Mater.* **2013**, *47*, 29–55. [[CrossRef](#)]
28. Aydin, S.; Baradan, B. The effect of fiber properties on high performance alkali-activated slag/silica fume mortars. *Compos. B Eng.* **2013**, *45*, 63–69. [[CrossRef](#)]
29. Natali, A.; Manzi, S.; Bignozzi, M.C. Novel fiber-reinforced composite materials based on sustainable geopolymer matrix. *Procedia Eng.* **2011**, *21*, 1124–1131. [[CrossRef](#)]
30. Puertas, F.; Amat, T.; Fernández-Jiménez, A.; Vázquez, T. Mechanical and durable behaviour of alkaline cement mortars reinforced with polypropylene fibres. *Cem. Concr. Res.* **2003**, *33*, 2031–2036. [[CrossRef](#)]
31. Goncalves, J.R.A.; Boluk, Y.; Bindiganavile, V. Crack growth resistance in fibre reinforced alkali-activated fly ash concrete exposed to extreme temperatures. *Mater. Struct.* **2018**, *51*, 42. [[CrossRef](#)]
32. Alomayri, T. The microstructural and mechanical properties of geopolymer composites containing glass microfibers. *Ceram. Int.* **2017**, *43*, 4576–4582. [[CrossRef](#)]
33. Ding, Y.; Dai, J.G.; Shi, C.J. Fracture properties of alkali-activated slag and ordinary Portland cement concrete and mortar. *Constr. Build. Mater.* **2018**, *165*, 310–320. [[CrossRef](#)]
34. Ding, Y.; Dai, J.G.; Shi, C.J. Mechanical properties of alkali-activated concrete: A state-of-the-art review. *Constr. Build. Mater.* **2016**, *127*, 68–79. [[CrossRef](#)]
35. Sarker, P.K.; Haque, R.; Ramgolam, K.V. Fracture behaviour of heat cured fly ash based geopolymer concrete. *Mater. Des.* **2013**, *44*, 580–586. [[CrossRef](#)]
36. Nguyen, H.; Carvelli, V.; Adesanya, E.; Kinnunen, P.; Illikajnen, M. High performance cementitious composite from alkali-activated ladle slag reinforced with polypropylene fibers. *Cem. Concr. Compos.* **2018**, *90*, 150–160. [[CrossRef](#)]
37. Kumar, S.; Barai, S.V. *Concrete Fracture Models and Applications*, 1st ed.; Springer: Berlin, Germany, 2011; 262p. [[CrossRef](#)]
38. Frantík, P.; Mašek, J. GTDiPS Software. 2015. Available online: <http://gtdips.kitnarf.cz/> (accessed on 24 August 2018).
39. Havlíková, I.; Frantík, P.; Schmid, P.; Šimonová, H.; Veselý, V.; Abdulrahman, A.; Keršner, Z. Components of Fracture Response of Steel Fibre Reinforced Concrete Specimens. *Appl. Mech. Mater.* **2016**, *827*, 287–291. [[CrossRef](#)]
40. Frantík, P. FiCubS Application. 2017. Available online: <http://ficubs.kitnarf.cz> (accessed on 2 October 2018).
41. Hordijk, D.A. Local Approach to Fatigue of Concrete. Ph.D. Thesis, Technische Universiteit Delft, Delft, The Netherlands, 1991.
42. Nallathambi, P.; Karihaloo, B.L. Determination of specimen-size independent fracture toughness of plain concrete. *Mag. Concr. Res.* **1986**, *38*, 67–76. [[CrossRef](#)]
43. Karihaloo, B.L.; Abdalla, H.M.; Imjai, T. A simple method for determining the true specific fracture energy of concrete. *Mag. Concr. Res.* **2003**, *55*, 471–481. [[CrossRef](#)]
44. Zhang, X.; Xu, S. A comparative study on five approaches to evaluate double-K fracture toughness parameters of concrete and size effect analysis. *Eng. Fract. Mech.* **2011**, *78*, 2115–2138. [[CrossRef](#)]
45. ČSN EN 196-1 *Methods of Testing Cement—Prat 1: Determination of Strength*; ÚNMZ: Prague, Czech Republic, 2016.
46. Al-mashhadani, M.M.; Canpolat, O.; Aygörmez, Y.; Uysal, M.; Erdem, S. Mechanical and microstructural characterization of fiber reinforced fly ash based geopolymer composites. *Constr. Build. Mater.* **2018**, *167*, 505–513. [[CrossRef](#)]





Contents lists available at ScienceDirect

# Construction and Building Materials

journal homepage: [www.elsevier.com/locate/conbuildmat](http://www.elsevier.com/locate/conbuildmat)

## Carbon nanotube reinforced alkali-activated slag mortars



Pavel Rovnaník\*, Hana Šimonová, Libor Topolář, Patrik Bayer, Pavel Schmid, Zbyněk Keršner

Brno University of Technology, Faculty of Civil Engineering, Veveří 331/95, Brno 602 00, Czech Republic

### HIGHLIGHTS

- Application of MWCNTs in alkali-activated slag binders is introduced.
- Dosage of MWCNTs has a significant effect on the mechanical fracture properties of AAS composites.
- Acoustic emission method was used to monitor the hardening process of AAS mortars.
- Optimum dosage to obtain the best performance lies around 0.10% of MWCNTs.

### ARTICLE INFO

#### Article history:

Received 12 November 2015  
 Received in revised form 27 April 2016  
 Accepted 4 May 2016

#### Keywords:

Alkali-activation  
 Slag  
 Carbon nanotubes  
 Fracture properties  
 Acoustic emission  
 Microstructure

### ABSTRACT

The paper reports on a study of the effect of multi-walled carbon nanotubes (MWCNTs) when used as dispersed reinforcement on the fracture properties and microstructure of alkali-activated slag mortars. The amount of MWCNTs added varied in the range of 0.05–1.0% of the mass of slag. Mechanical and fracture properties were determined using fracture tests carried out on  $40 \times 40 \times 160$  mm specimens with a central notch. The observed parameters were compressive strength, modulus of elasticity, effective fracture toughness and specific fracture energy. Specimen response during fracture tests was also monitored by means of acoustic emission, and this method was also used for the determination of cracking tendency due to autogenous and drying shrinkage occurring during the hardening process. It is shown that the addition of up to 0.2% of MWCNTs improves the fracture properties of alkali-activated slag. Although a higher dosage of MWCNTs reduced the number of microcracks observed by acoustic emission, the mechanical properties of the slag deteriorated due to the less effective dispersion of the MWCNTs and the formation of bundles.

© 2016 Elsevier Ltd. All rights reserved.

### 1. Introduction

The development of infrastructure leads to an increase in the demand for natural resources, which are limited, and the building industry in particular consumes a huge amount of raw materials for the production of building materials. Ordinary Portland Cement (OPC) will remain a key player in the future, although its production is energy demanding and contributes to the ongoing increase in global CO<sub>2</sub> emissions. There are two possible ways of reducing the negative impact of the building industry. One way is to utilize secondary raw materials as supplementary cementing materials, among which blast furnace slag is the most effective at reducing CO<sub>2</sub> footprint [1]. The other way is to utilize alkali-activated concrete. This type of material is even more effective in reducing CO<sub>2</sub> emissions and energy consumption. Different sources show

that the global warming potential of alkali-activated concrete is approximately 40–70% lower than that of OPC concrete [2–4].

One of the most common and intensively studied alkali-activated materials is alkali-activated slag (AAS). It is composed of finely ground granulated blast furnace slag and alkaline activator. Alkaline hydroxides, carbonates and especially silicates (water glass) are known to be the most effective activator for this type of material [5,6]. The mixture sets to form a very stable product and its properties depend on a number of factors such as the chemical and mineralogical composition of the slag, the type, composition and dosage of alkali activator, curing conditions, etc. The mechanical properties and application possibilities of AAS are very similar to those of OPC concrete. However, in contrast to OPC-based binders, AAS offers superior properties such as higher corrosion resistance against acid or sulphate attack [7–11] and also higher resistance to elevated temperatures and fire [12–16]. Its major disadvantage is increased shrinkage. This effect is caused by both autogenous and drying shrinkage and finally results in volume

\* Corresponding author.

E-mail address: [rovnanik.p@fce.vutbr.cz](mailto:rovnanik.p@fce.vutbr.cz) (P. Rovnaník).

contraction, micro-cracking and the deterioration of tensile and bending properties [5].

Autogenous shrinkage is a basic property of CSH gel, which is a predominant binding phase; however, due to its different character, the shrinkage that affects AAS is more severe than in the case of OPC. Autogenous shrinkage increases with the increasing amount of Na<sub>2</sub>O in the activator and it becomes more evident in the case of water glass activated materials as opposed to NaOH or Na<sub>2</sub>CO<sub>3</sub> activated ones [17]. Drying shrinkage is even more severe because it acts unevenly and causes cracking especially in the surface layer, which is then responsible for the deterioration of the mechanical properties and decreasing serviceability of the structure. It depends not only on the nature of the material itself, but also on exterior conditions such as curing temperature, relative humidity, drying rate, etc. Collins and Sanjayan [18] used a crack-detection microscope to examine the cracking of AAS concrete. When the concrete specimens were cured in a water bath they did not notice any visible surface cracks. However, specimens cured under 50% relative humidity conditions had lots of cracks within one day. The average crack width is three times greater than for OPC concrete [19]. One possible way to reduce shrinkage is via the application of shrinkage reducing admixtures (SRA), which are commonly used for OPC concrete. The effect of SRA on alkali-activated slag was studied by Palacios and Puertas [20]. They observed that polypropyleneglycol-based admixture reduces autogenous shrinkage by 85% and drying shrinkage by 50% in waterglass-activated slag mortars, but the effect strongly depends on curing conditions. However, the SRA retards the alkali activation of slag, with longer delays at higher dosages of admixture.

The main aim of this work is to apply multi-walled carbon nanotubes (MWCNTs) as a shrinkage reducing admixture for AAS-based mortars. Regarding the properties of MWCNTs, they have a great potential to reduce the cracking tendency of silicate-based materials caused by autogenous and drying shrinkage, which is one of the essential problems arising during the practical application of materials in the building industry [21,22].

Carbon nanotubes exhibit extraordinary mechanical properties, with the Young's modulus of an individual nanotube being around 1 TPa and tensile stresses being in the range of 65–93 GPa [23]. MWCNTs are thus the most promising nanomaterials for enhancing the mechanical fracture properties of building materials, and their resistance to crack propagation. Some problems have appeared connected with the aggregation of MWCNTs, which reduces the efficiency of single nanotubes. Nevertheless, effective dispersion can be achieved by applying ultrasonic or high shear rate mechanical dispersion with the use of a surfactant [24].

Since microcracks have a strong negative effect on mechanical performance, the efficiency of MWCNTs as a potential nanoscale reinforcement and shrinkage reducing agent can be monitored by the fracture behaviour of the composite material and by acoustic emission methods. In this study, fracture testing and acoustic

methods were applied to determine the performance of MWCNTs in AAS mortars.

## 2. Experimental methods

### 2.1. Materials

The alkali-activated slag mortars used in the tests were composed of granulated blast furnace slag and water glass. Slag supplied by Kotouč, s.r.o. (CZ) was ground to a fineness of about 380 m<sup>2</sup> kg<sup>-1</sup> (Blaine). The average grain size of the slag obtained by laser granulometry was  $d_{50} = 15.5 \mu\text{m}$  and  $d_{90} = 38.3 \mu\text{m}$ , indicating that 50% or 90%, respectively, of all grains is smaller than a given value. The slag was neutral with a basicity coefficient  $M_b = (\text{CaO} + \text{MgO})/(\text{SiO}_2 + \text{Al}_2\text{O}_3)$  equal to 1.08, and its chemical composition was (wt%): SiO<sub>2</sub> (39.66), Al<sub>2</sub>O<sub>3</sub> (6.45), Fe<sub>2</sub>O<sub>3</sub> (0.47), CaO (40.12), MgO (9.50), Na<sub>2</sub>O (0.33), K<sub>2</sub>O (0.55), MnO (0.65), SO<sub>3</sub> (0.72). A commercial sodium silicate solution (Vodní sklo, CZ) with SiO<sub>2</sub>/Na<sub>2</sub>O = 1.6 and 43 wt% of dry mass was used as an activator. Quartz sand with a maximum grain size of 2.5 mm was used as aggregate. Multi-walled carbon nanotubes (Arkema, France) were used as received. Since MWCNTs are commonly not water-soluble, the received MWCNTs already contained 55% of carboxymethyl cellulose as a dispersing agent. Carbon nanotubes were used in the form of 1 and 5% dispersions. In order to prepare the aqueous dispersions, the procedure prescribed by the producer was followed. MWCNT pellets were dissolved in hot water and dispersed bundles of MWCNTs were further disintegrated by mechanical homogenizer (3 h at 14,000 rpm).

### 2.2. Sample preparation

Seven different mixtures of alkali-activated slag mortars were prepared (see Table 1). The MWCNT content was 0.05, 0.10, 0.15, 0.20, 0.50 and 1.0% of the weight of the slag, and the results of the tests were compared with a reference mixture, which was prepared without MWCNTs but following the same procedure. The mixtures were cast into 40 × 40 × 160 mm prismatic moulds and left to set. The hardened specimens were immersed in water for 27 days, then pulled out of the water and allowed to dry spontaneously under ambient conditions for 24 h prior to fracture testing.

### 2.3. Testing procedure

#### 2.3.1. Fracture tests

Experiments were carried out on a Heckert FPZ 10/1 mechanical testing machine with the measuring range 0–2000 N. During the experiment, the three-point bending test was performed on specimens with a central edge notch cut to about 1/3 of specimen depth. The load span was 120 mm. A load–deflection ( $F$ – $d$ ) diagram was recorded and used for the calculation of elasticity modulus from the first (almost linear) part of the  $F$ – $d$  diagram, and for the calculation of effective fracture toughness and specific fracture energy. The  $F$ – $d$  diagrams for selected specimens (one for each type of material) are shown in Fig. 1.

The modulus elasticity value was determined according [25] using following formula:

$$E_c = \frac{P_i}{4B\delta_i} \left( \frac{S}{W} \right)^3 \left[ 1 + \frac{5qS}{8P_i} + \left( \frac{W}{S} \right)^2 \left\{ 2.70 + 1.35 \frac{qS}{P_i} \right\} - 0.84 \left( \frac{W}{S} \right)^3 \right] + \frac{9}{2} \frac{P_i}{B\delta_i} \left( 1 + \frac{qS}{2P_i} \right) \left( \frac{S}{W} \right)^2 F_1(\alpha_0),$$

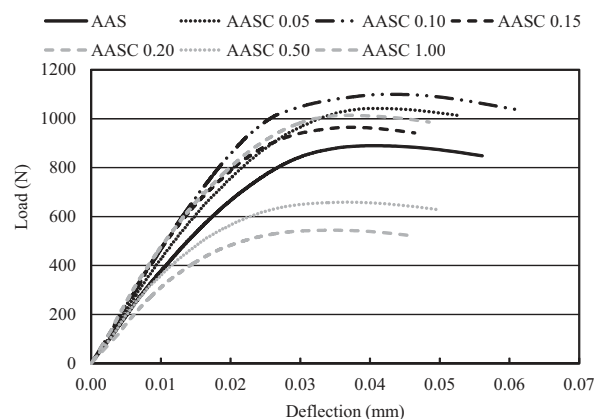


Fig. 1. Load vs. deflection diagrams for selected three-point bended notched specimens.

Table 1  
Mixture compositions.

Component	Slag (g)	Water glass (g)	MWCNTs (g)	Aggregate (g)	Water (ml)
AAS	450	180	0	1350	95
AAS 0.05	450	180	22.5 <sup>a</sup>	1350	72.5
AAS 0.10	450	180	45 <sup>a</sup>	1350	50
AAS 0.15	450	180	67.5 <sup>a</sup>	1350	27.5
AAS 0.20	450	180	90 <sup>a</sup>	1350	5
AAS 0.50	450	180	45 <sup>b</sup>	1350	62
AAS 1.00	450	180	90 <sup>b</sup>	1350	32

<sup>a</sup> 1% dispersion of MWCNTs.

<sup>b</sup> 5% dispersion of MWCNTs.

where  $P_i$  is the load in the initial linear elastic range;  $\delta_i$  is the midspan deflection corresponding to load level  $P_i$ ;  $B$  is the width of the specimen;  $W$  is the depth of the specimen;  $S$  is the span length;  $q$  is the self-weight of the specimen per unit length and  $F_1(\alpha_0) = \int_0^{\alpha_0} xY^2(x)dx$ , with  $\alpha_0 = a_0/W$ , and  $Y(x)$  is function of geometry for three-point bend beam ( $a_0$  – initial notch depth) [25].

The effective fracture toughness value was determined using the Effective Crack Model [25], which combines the linear elastic fracture mechanics and crack length approaches.

$$K_{Ice} = \frac{3P_{max}S}{2BW^2} Y(\alpha_e) \sqrt{a_e},$$

where  $P_{max}$  is the maximum load;  $a_e$  is the effective crack length and  $Y(\alpha_e)$  is the function of the geometry.

An estimate of specific fracture energy was obtained from the  $F$ - $d$  diagram according to the RILEM method (using the work-of-fracture value) [26]. Specific fracture energy value was determined according formula:

$$G_F = \frac{W_F^*}{B(W - a_0)},$$

where  $W_F^*$  is the area under the load vs. deflection curve.

Informative compressive strength values were also determined for all specimens on the fragments remaining after the fracture experiments had been performed.

Micrographs of the AAS samples after fracture testing were taken directly from the fracture cross-section in SE mode on a Tescan MIRA3 XMU scanning electron microscope. The micrographs were taken from dry samples that were sputtered with gold.

### 2.3.2. Acoustic emission

The initiation of cracks during the fracture tests was also monitored via the acoustic emission (AE) method. AE is the term for the noise emitted by materials and structures when they are subjected to stress. Stresses can be mechanical, thermal or chemical in nature. The noise emission is caused by the rapid release of energy within a material due to events such as crack formation that occur under applied stress, generating transient elastic waves which can be detected by piezoelectric sensors. In this case the AE method detects and characterizes the development of the fracture cracking process and only evaluates the damaging activity while it is occurring [27]. A guard sensor eliminated mechanical and electrical noise. Four acoustic emission sensors were attached to the surface of the specimen with beeswax (Fig. 2). Acoustic emission signals were recorded by DAKEL XEDO measuring equipment with four IDK-09 acoustic emission sensors with a 35 dB preamplifier.

When monitoring the cracking tendency of AAS mortar during hardening, fresh slurry was placed into a cylindrical mould. A steel waveguide was then inserted into the slurry and the AE sensor was attached to its free end with beeswax (Fig. 2). The intensity threshold of the signals that were detected was set to 0.8 V with 30 dB gain. This allowed us to eliminate background noise and record only the emissions produced due to the cracking of the material.

The specimens used for monitoring the hardening process were then subjected to impact-echo testing. For the impact-echo method a short-duration mechanical impulse (a hammer blow) was applied to the surface of the specimen during the test and the response was detected by means of a piezoelectric sensor. The impulse is reflected from the surface but also from microcracks and defects present in the specimen. The emitted resonance frequencies were determined by means of frequency analysis using a Fast Fourier Transform. A MIDI piezoelectric sensor was used to pick up the response and the respective impulses were directed into the input of a TiePie engineering Handyscope HS3 two-channel oscilloscope with 16 bit resolution.

## 3. Results

### 3.1. Mechanical fracture parameters

The mean values (obtained from 3 independent measurements) and standard deviations (presented as error bars) of the compressive strengths of the tested AAS composites are depicted in Fig. 3. The compressive strength value increased with the addition of 0.05, 0.1, 0.15, 0.2, and 0.5% of MWCNTs by 3, 27, 17, 19 and 10%, respectively, whereas for the specimens with 1.0% of MWCNTs the compressive strength decreased by 13% in comparison with the reference mixture.

The mean values and standard deviations of selected mechanical fracture parameters (modulus of elasticity  $E_c$ , effective fracture toughness  $K_{Ice}$  and specific fracture energy  $G_F$ ) obtained from the recorded  $F$ - $d$  diagrams [25,26] using academic *StiCrack* software [28] are summarized in Figs. 4–6. A similar trend as in the case of compressive strength was detected for the modulus of elasticity values: the values increased with the addition of up to 0.5% of MWCNTs: this increase reached 37% in the case of an MWCNT content of 0.15% of the weight of the slag.

The effective fracture toughness value increased with the addition of 0.05, 0.1, 0.15 and 0.2% of MWCNTs by 13, 31, 12 and 12%, respectively. For higher amounts of MWCNTs this parameter decreased. The specific fracture energy value only increased with the addition of MWCNT content of 0.10% of the weight of the slag (by 28%). For other amounts of MWCNTs, the values obtained for this parameter decreased. The greatest decrease (by 35%) was detected in the case of the mixtures with 0.5 and 1.0% of MWCNTs.

### 3.2. Acoustic emission and impact-echo testing

Acoustic emission signals which were received during the three-point bending testing of the specimens before fracture occurred were analysed. The attention was focused on four basic parameters: the number of events, and the amplitude, duration and energy of the AE signals (Table 2). Different types of cracks generate different AE signals, and these differences can be related to the properties of the material [29,30].

Once the AE transducer captures a signal over a certain level, an AE event is recorded. The number of AE events corresponds to the material's ability to resist fracture. The occurrence of a large number of cracks generates a rather large number of events prior to fracture. The highest number of events was shown by the reference sample without MWCNTs. As the amount of MWCNTs increases, the number of AE events becomes slightly smaller. It is assumed that the greater the number of acoustic events detected during crack propagation, the higher the resistance is against complete fracture [31]. This idea presumes that, when a number of small

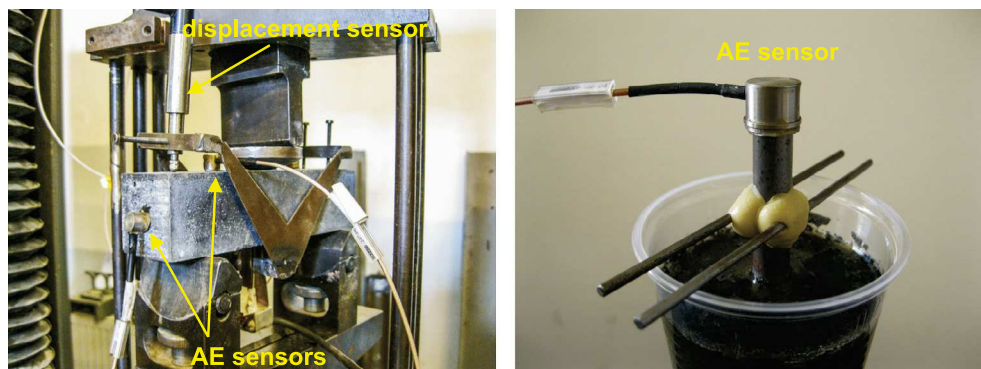


Fig. 2. Fracture test configuration in testing machine (left), measurement of AE activity during hardening of AAS composites.

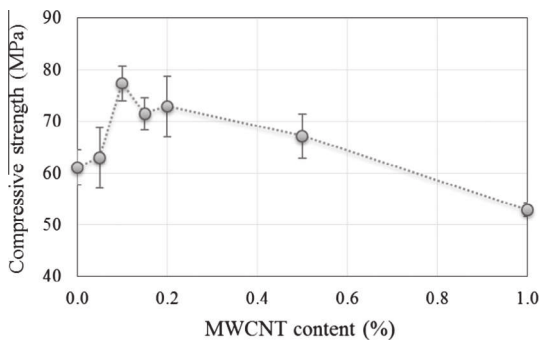


Fig. 3. Compressive strength of AAS composites with various amounts of MWCNTs.

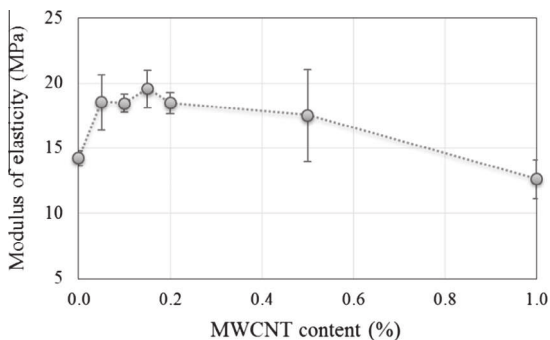


Fig. 4. Modulus of elasticity of AAS composites with various amounts of MWCNTs.

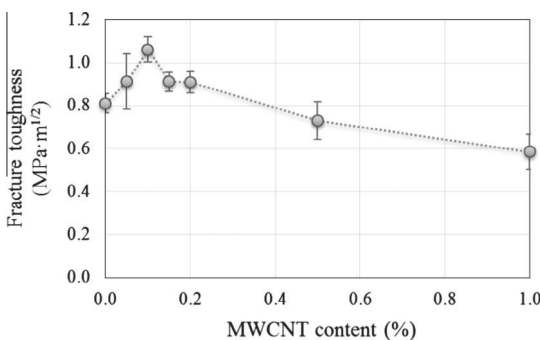


Fig. 5. Fracture toughness of AAS composites with various amounts of MWCNTs.

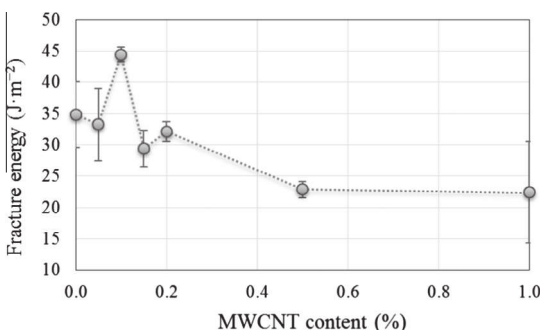


Fig. 6. Fracture energy of AAS composites with various amounts of MWCNTs.

cracks appears, part of the energy accumulated by the stress applied during three-point bending is released and dissipated. Such a material is able to resist the complete rupture, hence, it is tough, whereas in brittle materials the energy is suddenly released after reaching a critical stress. High number of AE events was

Table 2

Mean values of selected parameters obtained from AE measurements (coefficients of variation in %).

	Number of AE events (-)	Amplitude of AE signals (mV)	Duration of AE signals ( $\mu$ s)	Energy of AE signals $10^{-5}$ (V s)
AAS	9 (4.0)	2475 (1.2)	1650 (0.7)	1.24 (3.2)
AASC 0.05	2 (7.6)	2569 (2.8)	1323 (1.6)	0.69 (11.2)
AASC 0.10	7 (4.2)	2780 (0.9)	1289 (0.3)	1.30 (4.1)
AASC 0.15	6 (3.7)	2365 (2.4)	1277 (0.6)	2.68 (9.2)
AASC 0.20	7 (5.6)	2283 (1.3)	1275 (0.7)	2.35 (5.4)
AASC 0.50	3 (6.3)	2217 (1.9)	1183 (0.4)	0.77 (5.2)
AASC 1.00	2 (12.4)	2232 (2.4)	1195 (1.1)	0.33 (10.0)

recorded for composites with 0.1–0.2% of MWCNTs but also for the reference sample, which is in a bit of contradiction with mechanical parameters. However, nanotubes play a role of reinforcement on the nanoscale level and reduce the total number of microcracks, which is then reflected in a decreased number of AE events.

Amplitude is the greatest measured voltage in a waveform. This is an important parameter in AE inspection because it determines the detectability of the signal. Signals with amplitudes below the operator-defined minimum threshold are not recorded. A higher amplitude indicates the formation of a larger and more significant crack [32]. Amplitude values varied between 2217 and 2780 mV. With the addition of MWCNTs the amplitude slightly increased, reaching its maximum with 0.1% of MWCNTs, and then decreased again.

The duration of an AE signal is the time difference between the crossing of the first and last threshold. The duration of AE signals achieved for samples with MWCNTs was 20–28% lower compared to the reference sample. However, the decrease in the duration of AE signals with increasing amounts of MWCNTs was not so significant. This shows that when MWCNTs are present the attenuation of AE signals is more significant even at very low dosages of MWCNTs.

The last monitored parameter was AE energy, which is directly proportional to the area under the AE waveform. The highest AE energy values were obtained for the specimens labelled AASC 0.15 and AASC 0.20. We can see that MWCNT contents of up to 0.2% caused an increase in the energy level of the AE signal, while higher contents had an adverse effect. A small discrepancy concerning this trend was observed for the AASC 0.05 mixture. This might be explained by the unreasonably small number of AE events and high variability of the data achieved for this mixture.

The acoustic emission method was also used to monitor the hardening process of AAS mortars. In order to evaluate the formation of microcracks during hardening, we focused on the most commonly-used AE parameter, which is the number of signals overshooting a preset limit. ‘Number of overshoots’ refers to the number of pulses emitted by the circuitry measuring the signal voltage that exceed the threshold for a given time interval. The number of microcracks in the specimen can be inferred directly from such AE activity. Since the most important processes which are involved in the formation of hard structure occur at an early age, Fig. 7 shows the cumulative number of overshoots over time during the first 10 days after mixing. It is evident that the reference mixture exhibits the highest number of overshoots and that the curve is still increasing at the end of the measuring period. When MWCNTs are added, an increased number of overshoots can be observed within the first 96 h, but then the frequency of received signals drops considerably. A higher amount of MWCNTs in the mixture (AASC 0.50, AASC 1.00) reduced the number of overshoots at the early age of hydration; however, both curves increase almost linearly during the whole period. This means the frequency of AE events is still almost the same.

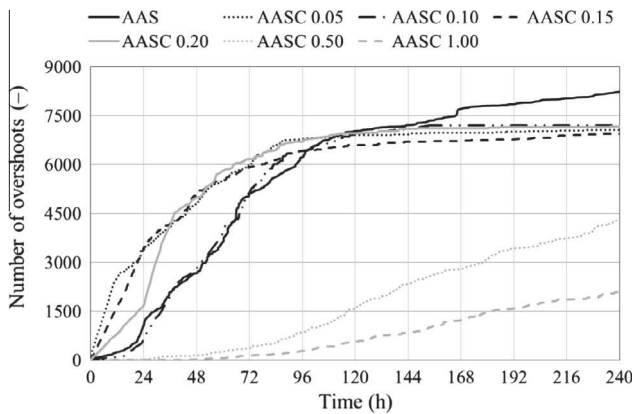


Fig. 7. Cumulative number of AE overshoots recorded during hardening of AAS mortars with MWCNTs.

The impact-echo method was employed to determine structural changes in alkali-activated slag composite with increasing amounts of MWCNTs. Changes in the local density of the material due to the presence of MWCNTs are reflected in a shift in resonance frequencies (Fig. 8). The increase in the dominant frequency is very steep (from 1.9 to 9.3 kHz) when up to 0.2% of MWCNTs are added. However, with further addition of MWCNTs the frequency drops again to 2.4 kHz. It can be assumed that a higher frequency indicates fewer imperfections in the structure such as cracks or areas with different density. From this point of view, the composite with 0.2% of MWCNTs by weight exhibits the most compact structure with probably the lowest number of cracks.

### 3.3. Microstructure

The effect of MWCNTs on the microstructure of AAS composites was investigated by means of scanning electron microscopy. The micrograph in Fig. 9a shows MWCNTs dispersed in the AAS matrix. Some of the nanotubes have been partially pulled out of the matrix during the fracture process, even though they are well bonded to the aluminosilicate structure via hydrogen bonds of carboxymethyl cellulose. In most of the cases the nanotubes failed throughout their whole cross-section; however, some stretched nanotubes with narrowed cross-sections were also observed, still bridging the crack (Fig. 9b). This effect may be explained by the slippage of the inner and outer shells of the MWCNTs, which was observed by Yamamoto et al. [33]. When tensile stress is applied, the AAS matrix cracks. As the crack width increases, some of the nanotubes' outer shells fail, allowing the inner shells to be pulled

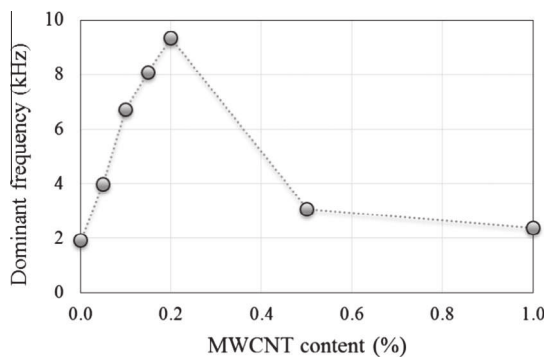


Fig. 8. Dominant frequency of impact-echo signal for AAS composites with various amounts of MWCNTs.

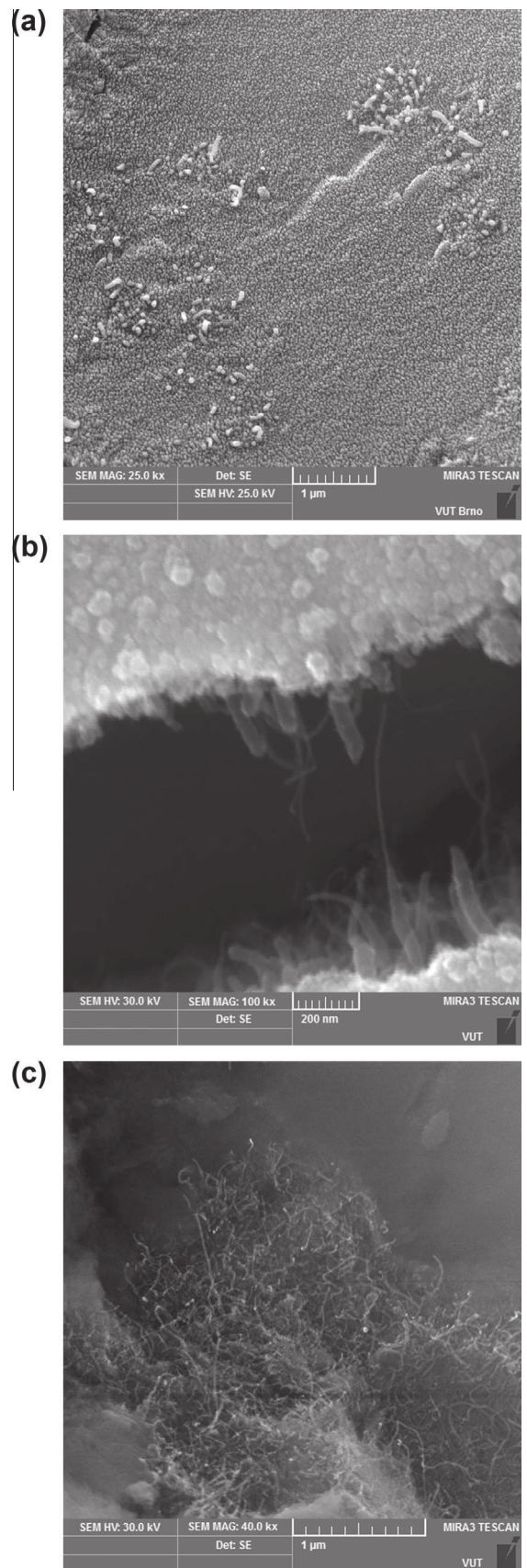


Fig. 9. MWCNTs dispersed in AAS composite (a), MWCNT crack bridging (b), bundles of MWCNT in AASC 1.0 specimen.

away from the wall while fragments of the outer shells remain attached to the matrix.

The micrographs for the mixtures containing 0.5 and 1.0% of MWCNTs revealed that at such high concentrations the nanotubes form large bundles (Fig. 9c). These bundles are usually free of the AAS matrix, so they form voids of some kind in the hard structure of the AAS, which cause its weakening.

#### 4. Discussion

The addition of a small amount of MWCNTs has been proven to have a positive effect on the mechanical properties of cement paste [34]. Kosta-Gdoutos et al. [22] suggested that MWCNTs strongly reinforce the cement paste matrix by increasing the amount of high stiffness C-S-H. In this paper, the same presumption was adopted for the improvement of the mechanical fracture properties of alkali-activated slag. The results of compressive strength and modulus of elasticity measurements show that the addition of up to 0.5% of MWCNTs can improve these parameters, which is in a good agreement with previous findings for cement or geopolymer composites [22,24,35]. Although MWCNTs improve Young's modulus by 30–40% over plain AAS mortar, their amount up to 0.5% have only negligible effect on its variation. This suggests that to achieve higher stiffness of the AAS composite small amount of well dispersed MWCNTs are needed. The highest value of the compressive strength was achieved with 0.1% of MWCNTs, which is in accordance with findings published by Khater et al. [36] for the AAS mortar activated with NaOH. However, these parameters strongly depend on the quality of dispersion of MWCNTs, their character, whether they are functionalized or not, and also on the aspect ratio of a single nanotube [22,37].

The fracture toughness of the specimens reinforced with MWCNTs was significantly improved by just a small addition of MWCNTs (0.05–0.2%) having the maximum value for 0.1%. This enhancement is caused by both reinforcing effect of well dispersed nanotubes and increased compaction and homogeneity of AAS matrix because MWCNTs fill in the space between hydration products, hence reducing the amount of fine pores [24]. The fracture energy considerably increased only for AASC 0.10 mixture. However, with respect to high coefficients of variation of some results, it can be suggested that it follows similar trend as was observed for the fracture toughness. Amounts of MWCNTs higher than 0.2% caused both fracture toughness and fracture energy to deteriorate considerably. Presented results suggest that for the effective improvement of the mechanical fracture properties of AAS mortar an MWCNT content of 0.1% is the most effective in resisting fracture propagation, which is a good agreement with results observed for cement pastes [37,38].

These conclusions are also supported by AE measurements which can provide information about what happens within a material immediately prior to fracture. A small number of AE events indicate that the AAS material is relatively brittle, but the values obtained for the amplitude and energy of AE signals correlate well with fracture parameters. The achievement of high AE energies and amplitudes for composites with 0.15 and 0.20% of MWCNTs implies that carbon nanotubes cause the accumulation of energy on the crack propagation front during mechanical loading. Such behaviour can be explained by the enormous tensile strength of nanotubes and the good bond between nanotubes and matrix, which means that more energy is needed to break the tubes or pull them out of the matrix. The attenuation of AE signal duration with an increasing amount of MWCNTs shows that carbon nanotubes are able to partially absorb acoustic waves and dissipate the energy released by crack formation.

The monitoring of the hardening process via the AE method showed that the addition of MWCNTs decreased the number of

overshoots that were observed within 10 days. Since these hits are proportional to the number of microcracks caused by autogenous and drying shrinkage it can be concluded that MWCNTs reduce the cracking tendency of AAS matrix; however, this might not necessarily bring an improvement in fracture properties.

The deterioration of almost all parameters observed for specimens containing 0.5 and 1.0% of MWCNTs can be attributed to imperfect nanotube dispersion and homogenization. Since the amount of MWCNTs is very high in this case, it was necessary to prepare a more concentrated solution, in which nanotubes tend to form bundles. These bundles then cause local imperfections in the AAS matrix, acting as stress concentrators, even though the total number of microcracks is reduced.

#### 5. Conclusions

The fracture properties of alkali-activated slag composites with various amounts of MWCNTs as reinforcement have been investigated. It has been shown that the addition of MWCNTs in the range of 0.05–0.2% of the mass of slag improves the mechanical fracture properties of alkali-activated slag. Compressive strength, modulus of elasticity, and effective fracture toughness were improved for all these dosages; however, the results achieved as regards the stated parameters suggest that the optimum concentration lies around 0.1%.

The acoustic emission method appears to be a suitable tool for determining the behaviour of alkali activated slag mortar specimens with added MWCNTs during stable crack propagation from an initial crack/notch. Stable crack propagation is followed by a number of AE signals until fracture takes place. The measured AE signal parameters are in good accordance with the recorded fracture parameters and support the conclusions obtained from fracture tests.

Amounts of MWCNTs higher than 0.2% cause deterioration in the fracture properties of alkali-activated slag. Although a high content of MWCNTs reduces the total number of microcracks, it introduces too many imperfections to the AAS matrix and causes the composite to become more brittle, so that fewer crack propagation events are needed before the complete fracture of the specimen.

#### Acknowledgement

This outcome has been achieved with the financial support of the Czech Science Foundation, project No. 13-09518S (NANO-FRAM), and the Ministry of Education, Youth and Sports of the Czech Republic under the "National Sustainability Programme I", project No. LO1408 (AdMaS UP).

#### References

- [1] Y. Keun-Hyeok, J. Yeon-Back, C. Myung-Sug, T. Sung-Ho, Effect of supplementary cementitious materials on reduction of CO<sub>2</sub> emissions from concrete, *J. Cleaner Prod.* 103 (2015) 774–783.
- [2] M. Weil, K. Dombrowski, A. Buchwald, Life-cycle analysis of geopolymers, in: J. L. Provis, J.S.J. Van Deventer (Eds.), *Geopolymers: Structures, Processing, Properties and Industrial Applications*, Woodhead Publishing Limited, Cambridge, 2009, pp. 194–210.
- [3] B.C. McLellan, R.P. Williams, J. Lay, A. van Riessen, G.D. Corder, Costs and carbon emissions for geopolymer pastes in comparison to ordinary Portland cement, *J. Cleaner Prod.* 19 (10) (2011) 1080–1090.
- [4] Y. Keun-Hyeok, S. Jin-Kyu, S. Keum-II, Assessment of CO<sub>2</sub> reduction of alkali-activated concrete, *J. Cleaner Prod.* 39 (2013) 265–272.
- [5] C. Shi, P.V. Krivenko, D. Roy, *Alkali-Activated Cements and Concretes*, Taylor & Francis, Oxon, 2006.
- [6] P.V. Krivenko, *Alkaline cements*, in: P.V. Krivenko (Ed.), *1st International Conference on Alkaline Cements and Concretes*, 1994, pp. 11–13. Kiev.
- [7] K. Byfors, G. Klingstedt, V. Lehtonen, H. Pyy, L. Romben, Durability of concrete made with alkali activated slag, *ACI SP Proc.* 114 (1989) 1429–1468.

- [8] T. Bakharev, J.G. Sanjayan, Y.B. Cheng, Resistance of alkali-activated slag concrete to acid attack, *Cem. Concr. Res.* 33 (10) (2003) 1607–1611.
- [9] T. Bakharev, J.G. Sanjayan, Y.B. Cheng, Sulfate attack on alkali-activated slag concrete, *Cem. Concr. Res.* 32 (2) (2002) 211–216.
- [10] T. Bakharev, Resistance of geopolymer materials to acid attack, *Cem. Concr. Res.* 35 (4) (2005) 658–670.
- [11] P. Rovnaníková, P. Bayer, Corrosion resistance of alkali activated aluminosilicate materials, in: *Innovations and Developments in Concrete Materials and Construction*, Proceedings of the International Conference, Thomas Telford, London, 2002, pp. 373–381.
- [12] L. Zuda, P. Rovnaník, P. Bayer, R. Černý, Effect of high temperatures on the properties of alkali activated aluminosilicate with electrical porcelain filler, *Int. J. Thermophys.* 29 (2) (2008) 693–705.
- [13] L. Zuda, P. Rovnaník, P. Bayer, R. Černý, Thermal properties of alkali-activated aluminosilicate composite with lightweight aggregates at elevated temperatures, *Fire Mater.* 35 (4) (2011) 231–244.
- [14] P. Rovnaník, P. Bayer, P. Rovnaníková, Characterization of alkali activated slag paste after exposure to high temperatures, *Constr. Build. Mater.* 47 (2013) 1479–1487.
- [15] M. Guerrieri, J. Sanjayan, F. Collins, Residual strength properties of sodium silicate alkali activated slag paste exposed to elevated temperatures, *Mater. Struct.* 43 (6) (2010) 765–773.
- [16] A.M. Rashad, Y. Bai, P.A.M. Basheer, N.C. Collier, N.B. Milestone, Chemical and mechanical stability of sodium sulfate activated slag after exposure to elevated temperature, *Cem. Concr. Res.* 42 (2) (2012) 333–343.
- [17] M.A. Cincotto, A.A. Melo, W.L. Repette, Effect of different activators type and dosages and relation with autogenous shrinkage of activated blast furnace slag cement, in: G. Grieve, G. Owens (Eds.), *Proceedings of the 11th International Congress on the Chemistry of Cement*, 2003, pp. 1878–1888. Durban.
- [18] F.G. Collins, J.G. Sanjayan, Microcracking and strength development of alkali-activated slag concrete, *Cem. Concr. Compos.* 23 (4) (2001) 345–352.
- [19] F.G. Collins, J.G. Sanjayan, Cracking tendency of alkali-activated slag concrete subjected to restrained shrinkage, *Cem. Concr. Res.* 30 (5) (2000) 791–798.
- [20] M. Palacios, F. Puertas, Effect of shrinkage-reducing admixtures on the properties of alkali-activated slag mortars and pastes, *Cem. Concr. Res.* 37 (5) (2007) 691–702.
- [21] F. Sanchez, K. Sobolev, Nanotechnology in concrete – a review, *Constr. Build. Mater.* 24 (11) (2010) 2060–2071.
- [22] M.S. Konsta-Gdoutos, Z.S. Metaxa, S.P. Shah, Highly dispersed carbon nanotube reinforced cement based materials, *Cem. Concr. Res.* 40 (7) (2010) 1052–1059.
- [23] T. Belytschko, S.P. Xiao, G.C. Schatz, R. Ruoff, Atomistic simulations of nanotube fracture, *Phys. Rev. B* 65 (23) (2002) 235430–235437.
- [24] M.S. Konsta-Gdoutos, Z.S. Metaxa, S.P. Shah, Multi-scale mechanical and fracture characteristics and early-age strain capacity of high performance carbon nanotube/cement nanocomposites, *Cem. Concr. Compos.* 32 (2) (2010) 110–115.
- [25] B.L. Karihaloo, *Fracture Mechanics and Structural Concrete*, Longman Scientific & Technical, Harlow, 1995.
- [26] RILEM Committee FMT 50, Determination of the fracture energy of mortar and concrete by means of three-point bend test on notched beams, *Mater. Struct.* 18 (4) (1985) 285–290.
- [27] C.U. Grosse, M. Ohtsu, *Acoustic Emission Testing*, Springer-Verlag, Berlin, 2008.
- [28] M. Stibor, Fracture parameters of quasi-brittle materials and their determination (PhD thesis), Brno University of Technology, 2004 (in Czech).
- [29] M. Iwanami, T. Kamada, S. Nagataki, Application of acoustic emission technique for crack monitoring in RC beams, *JCA Proc. Cem. Concr.* 51 (1997) 192–197.
- [30] Z. Li, Y. Xi, Application of acoustic emission technique to detection of concrete cracking and rebar corrosion, in: *NDT-CE: International Symposium Non-Destructive Testing in Civil Engineering*, 1995, pp. 613–620. Berlin.
- [31] V.M. Malhotra, N.J. Carino, *Handbook on Nondestructive Testing of Concrete*, second ed., CRC Press, 2003.
- [32] M. Iwanami, T. Kamada, S. Nagataki, Application of acoustic emission technique for crack monitoring in RC beams, *JCA Proc. Cem. Concr.* 43 (1997) 192–197.
- [33] G. Yamamoto, S. Liu, N. Hub, T. Hashida, Y. Liu, Cheng Yan, Prediction of pull-out force of multi-walled carbon nanotube (MWCNT) in sword-in-sheath mode, *Comput. Mater. Sci.* 60 (1) (2012) 7–12.
- [34] G.Y. Li, P.M. Wang, X. Zhao, Mechanical behavior and microstructure of cement composites incorporating surface-treated multi-walled carbon nanotubes, *Carbon* 43 (6) (2005) 1239–1245.
- [35] M. Saafi, K. Andrew, P.L. Tang, D. Mc Ghon, S. Taylor, M. Rahman, S. Yang, X. Zhou, Multifunctional properties of carbon nanotube/fly ash geopolymeric nanocomposites, *Constr. Build. Mater.* 49 (2013) 46–55.
- [36] G.M. Khater, H.A. Abd el Gawaad, Characterization of alkali activated geopolymer mortar doped with MWCNT, *Constr. Build. Mater.* 102 (2016) 329–337.
- [37] Y. Hu, D. Luo, P. Li, Q. Li, G. Sun, Fracture toughness enhancement of cement paste with multi-walled carbon nanotubes, *Constr. Build. Mater.* 70 (2014) 332–338.
- [38] B. Wang, Y. Han, S. Liu, Effect of highly dispersed carbon nanotubes on the flexural toughness of cement-based composites, *Constr. Build. Mater.* 46 (2013) 8–12.



## II.3 FRACTURE RESPONSE OF SELECTED CONCRETE SPECIMENS

Concrete belongs to the most common building material used in various civil engineering applications. Fracture mechanics can be a useful and powerful tool for the analysis of the growth of distributed cracking and its localization in concrete. The articles present results of selected topics connected with the fracture behaviour of standard concrete specimens.

### II.3.1

Kucharczyková, B., Šimonová, H., Kocáb, D., Topolář, L. Advanced Evaluation of the Freeze–Thaw Damage of Concrete Based on the Fracture Tests. *Materials*. 2021, Vol. 14, Article No. 6378. doi: <https://doi.org/10.3390/ma14216378> (Q3–Materials science, multidisciplinary; 1 citation without self-citations of all authors according to WoS)

#### II.3.1 *Description*

The article presents the results of an experimental program aimed at the assessment of freeze–thaw (F–T) resistance of concrete based on the evaluation of the fracture tests accompanied by the acoustic emission measurement. The main objective of this article was to bring the specifics, advantages, and disadvantages of the fracture tests performed in context to the F–T damage closer to the professional and general public. A comparison of the results of fracture tests with the commonly used approaches shows that all testing methods lead to the same conclusion. However, the fracture test evaluation provides more detailed information about the internal structure deterioration due to the F–T exposition.

#### II.3.1 *Role of the author – the percentage of contribution: 40 %*

Hana Šimonová is a co-author of this article who took part in the concept, the methodology and the detailed data processing and evaluation of performed fracture experiments of the presented research. Furthermore, she prepared the original draft of the article's parts describing detailed fracture test evaluation.

### II.3.2

Lehký, D., Kucharczyková, B., Šimonová, H., Daněk, P. Comprehensive fracture tests of concrete for the determination of mechanical fracture parameters. *Structural Concrete*. 2022, Vol. 23, Iss. 1, pp. 505–520. <https://doi.org/10.1002/suco.202000496> (Q2–Engineering, civil; 2 citations without self-citations of all authors according to WoS)

#### II.3.2 *Description*

The article describes the process and summarizes the main results and the data trends of the extensive experimental program, which was designed and performed to support the development of a comprehensive multilevel approach for experimental–computational determination of the mechanical fracture parameters of concrete. The aim was to determine parameters independent of the test configuration or the size of the test. The 3PB and WST were performed simultaneously using three different geometrically similar specimen sizes and two well-separated depths of initial notches.

II.3.2 *Role of the author – the percentage of contribution: 25 %*

Hana Šimonová is the co-author of this article responsible for the detailed experimental data processing and evaluation of performed 3PB and WST fracture experiments of the presented research. Furthermore, she prepared the original draft of the article's parts describing detailed fracture test evaluation which was later reviewed in cooperation with other co-authors.

## Article

# Advanced Evaluation of the Freeze–Thaw Damage of Concrete Based on the Fracture Tests

Barbara Kucharczyková \*, Hana Šimonová, Dalibor Kocáb and Libor Topolář

Faculty of Civil engineering, Brno University of Technology, Veveří 331/95, 602 00 Brno, Czech Republic; simonova.h@vutbr.cz (H.Š.); dalibor.kocab@vutbr.cz (D.K.); libor.topolar@vutbr.cz (L.T.)

\* Correspondence: barbara.kucharczykova@vutbr.cz; Tel.: +420-541-147-527

**Abstract:** This paper presents the results of an experimental program aimed at the assessment of the freeze–thaw (F–T) resistance of concrete based on the evaluation of fracture tests accompanied by acoustic emission measurements. Two concretes of similar mechanical characteristics were manufactured for the experiment. The main difference between the C1 and C2 concrete was in the total number of air voids and in the A300 parameter, where both parameters were higher for C1 by about 35% and 52%, respectively. The evaluation of the fracture characteristics was performed on the basis of experimentally recorded load–deflection and load–crack mouth opening displacement diagrams using two different approaches: linear fracture mechanics completed with the effective crack model and the double-K model. The results show that both approaches gave similar results, especially if the nonlinear behavior before the peak load was considered. According to the results, it can be stated that continuous AE measurement is beneficial for the assessment of the extent of concrete deterioration, and it suitably supplements the fracture test evaluation. A comparison of the results of fracture tests with the resonance method and splitting tensile strength test shows that all testing methods led to the same conclusion, i.e., the C1 concrete was more F–T-resistant than C2. However, the fracture test evaluation provided more detailed information about the internal structure deterioration due to the F–T exposure.

**Keywords:** freeze–thaw; fracture; toughness; energy; double-K; crack extension; crack opening; acoustic emission; RMS

**Citation:** Kucharczyková, B.; Šimonová, H.; Kocáb, D.; Topolář, L. Advanced Evaluation of the Freeze–Thaw Damage of Concrete Based on the Fracture Tests. *Materials* **2021**, *14*, 6378. <https://doi.org/10.3390/ma14216378>

Academic Editor: Grzegorz Ludwik Golewski

Received: 27 September 2021

Accepted: 22 October 2021

Published: 25 October 2021

**Publisher's Note:** MDPI stays neutral with regard to jurisdictional claims in published maps and institutional affiliations.



**Copyright:** © 2021 by the authors. Licensee MDPI, Basel, Switzerland. This article is an open access article distributed under the terms and conditions of the Creative Commons Attribution (CC BY) license (<http://creativecommons.org/licenses/by/4.0/>).

## 1. Introduction

Concrete belongs to the most common building materials used in various civil engineering applications. The world produces about 4.4 billion tons of concrete annually, of which a substantial portion is consumed for the construction of transportation networks with strict requirements for their durability. This means that, in addition to basic strength and deformation parameters, the characteristics related to water, air permeability, and cracking tendency are strictly monitored under different weather conditions.

The alternation of positive and negative temperatures (freeze–thaw cycles) is considered one of the most destructive processes that substantially influence the durability of concrete structures [1]. It can be stated that the freeze–thaw (F–T) resistance of concrete expresses the resistance of the concrete to the interaction of all physical, mechanical, and fracture processes that act together at one moment. The rate of the deterioration of the concrete structure depends on the number of F–T cycles, as well as on the absolute values of alternating temperatures.

There are various testing approaches and procedures (direct and indirect) for the assessment of the F–T resistance under laboratory conditions, which are adjusted to the actual weather conditions of a particular world region or country, and they mainly differ in

the length of the F–T cycle, temperature range, monitoring intervals, monitored characteristics, and the limit number of F–T cycles or the limit value prescribed for a decrease in the monitored characteristic [2]. The relative changes in compressive and tensile strength or dynamic modulus of elasticity, monitored as a function of changes in mass and length, are the most common parameters used for examination of the macroscopic performance of concrete materials exposed to F–T cycles [1]. Although researchers have indicated that the fracture behavior is more sensitive to F–T damage, the fracture tests are performed rather rarely and the fracture behavior is, in this case, still frequently neglected [3].

There are reasonable arguments for why the fracture characteristics should be suitable for the assessment of the rate of F–T deterioration. They arise from the essence of the fracture theory which deals with the resistance of the material to crack initiation and propagation [4]. Fracture toughness and fracture energy are basic and the most commonly used parameters to express the fracture behavior of the materials. The F–T resistance is mostly examined through the variations in the value of fracture energy or fracture toughness [5–7].

The F–T resistance of concrete depends on the quality of components and the overall composition of the fresh concrete, as well as on the quality of compaction and curing after its placing. In the hardened state, the F–T resistance depends on the quality of the cement matrix, aggregate, and interfacial transition zone (ITZ) between the aggregate and cement matrix. The air-entraining admixture is commonly used for enhancing the F–T resistance of concrete [8]. In this case, the air voids are intentionally spread in fresh concrete to obtain a uniform air-void system, containing a predefined minimum of voids smaller than 300 microns in the hardened concrete. It was observed that the presence of closed air voids influences the evolution of the fracture damage, which differs compared to ordinary non-air-entrained concrete, especially in the coalescence of voids and cracks [8,9].

The main objective of this paper was to present the specifics, advantages, and disadvantages of the fracture tests performed in the context of F–T damage to the professional and general public. A wide range of fracture parameters were evaluated in the paper to discuss the sensitivity of a particular parameter to the extent of concrete deterioration due to F–T cycling. In addition, the results of acoustic emission (AE) measurements during the fracture tests, which is a tool for nondestructive monitoring of active changes in progress during the loading of concrete specimens, are presented. These results were compared with the results of the commonly used testing approaches, i.e., changes in fundamental resonant frequency, mass, compressive strength, and tensile strength.

## 2. Materials and Methods

Two types of ordinary concrete, C1 and C2, with natural aggregate were designed for the experiment. The composition of both concretes per 1 m<sup>3</sup> is given in Table 1.

**Table 1.** Composition of C1 and C2 concrete in kg per 1 m<sup>3</sup> of fresh concrete and basic characteristics of fresh concretes.

Components/Characteristics	C1	C2
Cement CEM I 42.5 R	390	390
Sand 0–4 mm (Tovačov, CZ)	810	810
Gravel 4–8 mm (Luleč, CZ)	160	160
Gravel 8–16 mm (Olbramovice, CZ)	760	760
Admixture Sika ViscoCrete-4035	1.00	0.40
Air-entraining admixture LPS A 94	0.55	0.20
Admixture Sika ViscoFlow-25	1.60	0.64
Water	178	198
w/c	0.46 (0.43 *)	0.51 (0.47 *)
Density of fresh concrete (kg/m <sup>3</sup> )	2290	2340
Air content (%)	4.3–5.0	2.1–2.5
Workability (flow-table test) (mm)	420/430	410/420

\* Value after subtraction of the admixtures and aggregate absorption.

The ready-mix concretes were prepared in a concrete plant and supplied to the laboratory for molding the test specimens. A combination of two plasticizing admixtures Sika ViscoCrete-4035 (superplasticizer with a fast effect) and Sika ViscoFlow-25 (plasticizer with delayed effect and stabilizing character) [10] was used to retain the workability and stability of ready-mix concrete for a longer time, as needed for the transportation and molding of quite a large number of the test specimens. Prismatic specimens with nominal dimensions of 100 mm × 100 mm × 400 mm were prepared and, after demolding, were cured in the water bath until the time of testing. In both cases, the age of the test specimens at the start of the F–T tests was at least 90 days when the strength characteristics were already stabilized. In total, 12 test specimens were prepared from each concrete for the fracture tests. In both cases, three test specimens served as reference (non-frost-attacked) specimens, while the remaining specimens were subjected to the F–T cycles.

### 2.1. Freeze–Thaw Test

The F–T tests were performed according to the standard ČSN 73 1322 [11] valid for the testing of the F–T resistance of concrete in the Czech Republic. This procedure specifies the F–T cycles within the temperature range from  $-18\text{ }^{\circ}\text{C}$  to  $+20\text{ }^{\circ}\text{C}$ . Each F–T cycle consists of 4 h of air-freezing and 2 h of thawing in the water bath, see Figure 1(c).

An automatic freeze–thaw cabinet KD 20 (manufactured by EKOFROST s.r.o., Olomouc, Czech Republic) was used for the experiment, see Figure 1. In this particular case, the interval for nondestructive monitoring and for the measurement of dimensions and mass of the test specimens was set to 25 F–T cycles. The fracture tests were performed after 0 (non-frost attacked), 50, 100, and 200 cycles. Each test set contained three test specimens. The total duration of the 200 cycles was 56 days. The reference non-frost-attacked specimens of both C1 and C2 concretes were stored in the water bath until the 50 F–T cycles were finished on the other set of specimens. Then, the reference non-frost-attacked specimens were tested at the same time as the set of specimens subjected to 50 F–T cycles.

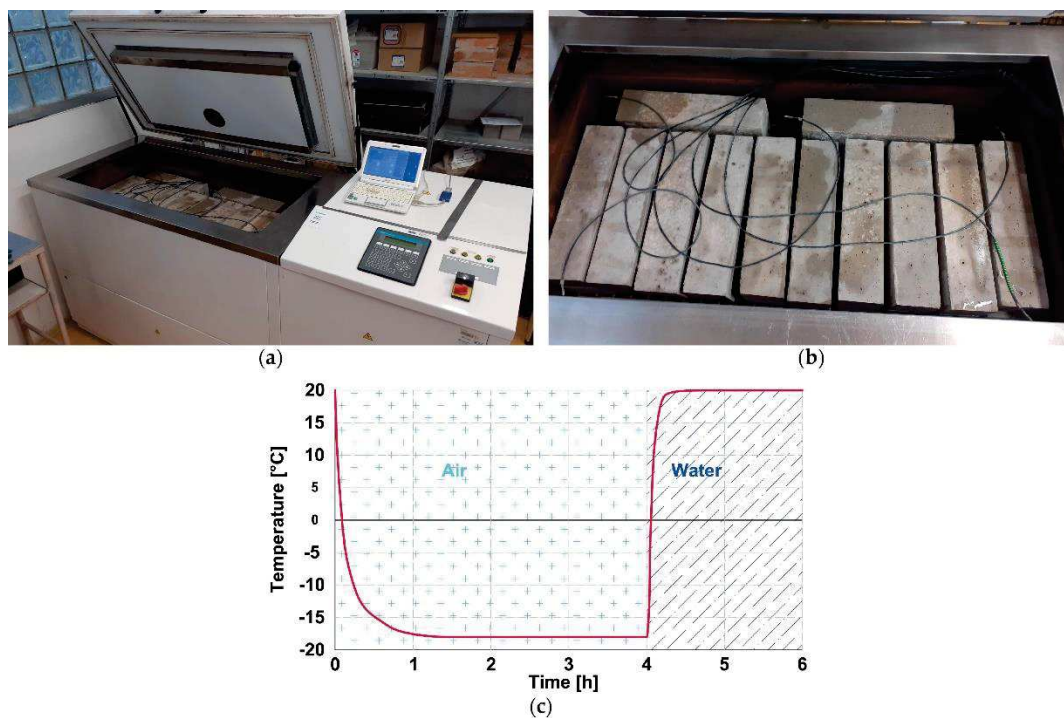


**Figure 1.** Arrangement of freeze–thaw test: (a) automatic freeze–thaw cabinet KD 20; (b) detail of specimens arrangement during F–T test; (c) one F–T cycle.

### 2.2. Test Method for Fundamental Longitudinal Frequency

A nondestructive test based on the resonance method (see Figure 2) was employed to monitor the development of the dynamic modulus of elasticity  $E_{rL}$  and dynamic Poisson's ratio  $\mu_r$  of concretes during the F–T test. All specimens were measured before the start of the F–T test. The specimens subjected to the F–T action were measured at regular intervals (after each 25 F–T cycles) throughout the F–T test. The natural frequency of longitudinal and torsional vibrations was measured using a Handyscope HS4 oscilloscope equipped with an acoustic sensor. The readers are referred to [12] for more details about the principle of measurement. The absolute values of  $E_{rL}$  and  $\mu_r$  were calculated in compliance with ASTM C215-19 [13] as follows:

$$E_{rL} = 4 \frac{L}{WB} m f_L^2,$$

where  $E_{rL}$  is the dynamic modulus of elasticity,  $L$  is the length of specimens,  $W$  and  $B$  are cross-section dimensions,  $m$  is the mass of specimens, and  $f_L$  is the fundamental longitudinal frequency.

$$\mu_r = \frac{E_{rL}}{2 \cdot G_r} - 1,$$

where  $\mu_r$  is the dimensionless dynamic Poisson's ratio, and  $G_r$  is the dynamic modulus of rigidity, calculated as

$$G_r = 4 \frac{LR}{WB} m f_t^2,$$

where  $R$  is the shape factor (1.183 for a square cross-section prism), and  $f_t$  is the fundamental torsional frequency.

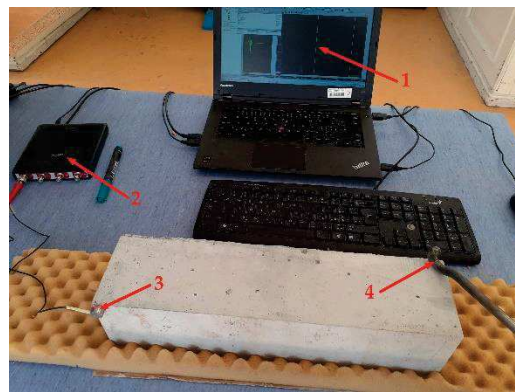


**Figure 2.** Measurement of resonant frequencies (1—computer equipped with software for determination of resonant frequencies; 2—Handyscope HS4 oscilloscope; 3—acoustic sensor; 4—impact hammer).

### 2.3. Acoustic Emission Method

The AE method is a tool for the nondestructive monitoring of active changes in a material produced during the loading of concrete specimens. The principle of the method consists of the continuous monitoring of the acoustic response caused by crack initiation and propagation during the loading of the specimen. To analyze the extent and progress of the specimen deterioration, it is very important to define an appropriate method for AE signal identification even before the start of the measurement. The most widely used approach is based on the setup of a signal threshold to distinguish failure. This specific approach presumes that each signal exceeding this threshold indicates a certain type of material disruption. The extent of material deterioration can be determined as a function of the number of AE events (counts) or the time of signal duration [14]. However, in case individual AE signals occur successively very close to each other, their separation can be

problematic, which leads to errors in their evaluation (e.g. false counts) as reported in [15]. It was proven that, in such cases, the root-mean-square (RMS) value of the AE signal envelope is more effective for evaluation [15]. The RMS is an AE parameter that is proportional to the square root of the quantum of energy transmitted by the AE wave. The RMS value increases with the increasing deterioration of the material during loading [16,17].

In the experiment presented herein, the monitoring of the AE activity was done using a double-channel unit DAKEL ZEDO with the following input parameters: the threshold value for counts was 0.561 mV, the threshold value for individual AE hits was 56  $\mu$ V, the sampling frequency of AE hits was set to 10 MHz, and the cutoff frequency of the low-pass filter was set to 800 kHz. The total gain was 59 dB (pre-amplifier 34 dB and amplifier 25 dB). The AE sensors were attached to the specimens with beeswax in a thin layer. The extent of specimen deterioration was expressed by the cumulative value of RMS calculated for specific load intervals.

#### 2.4. Fracture Test

Before testing, all test specimens were provided with an artificial notch with a depth of approximately one-third of the specimen height using a diamond blade saw. The test specimens were subjected to three-point bending tests (span length was 300 mm) with a constant displacement increment of 0.02 mm/min. This allowed obtaining the whole record of the load–deflection ( $F$ – $d$ ) and load–crack mouth opening displacement ( $F$ – $CMOD$ ) diagrams. In all cases, the test was terminated at a deflection of the specimens of at least 0.6 mm (the value of loading force was already close to zero). The surfaces, especially those near the artificial notch, of all test specimens were inspected using a digital microscope with a magnification of 250 $\times$  to verify the presence of microcracks just before the start of the test.

A multifunctional testing machine LaborTech with a loading range of 250 kN (equipped with an output channel for the loading force), an inductive sensor with a measurement range of 2 mm, a strain gauge, and a Quantum data-taker were used for testing. This apparatus allowed a precise setup of the test and a continual record of all measured quantities. The inductive sensor was used for the measurement of specimen deflection. It was mounted on the front of a special frame bedded on the upper surface of the specimens during the test (see Figure 3). The frame was constructed to measure the deflection of twofold values in the middle of the span length. The strain gauge was used for the measurement of the crack mouth opening displacement (CMOD). It was mounted between two blades glued on the bottom surface of the specimens symmetrically to the artificial notch. The arrangement of the test is shown in Figure 3.

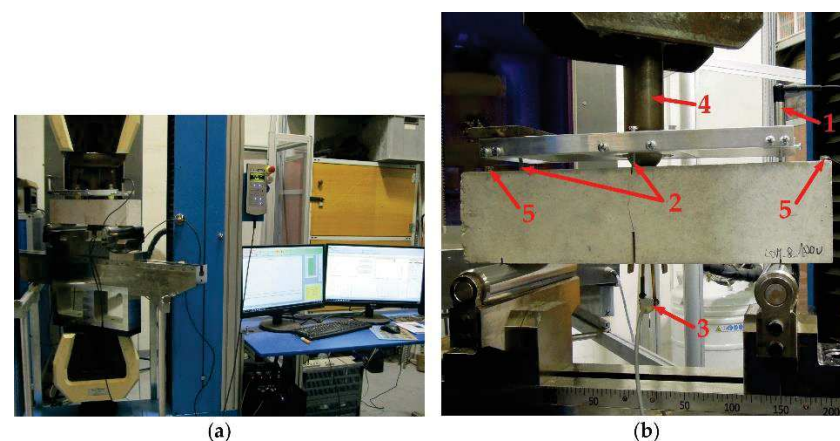


**Figure 3.** (a) Arrangement of fracture tests; (b) details of the test specimens and sensors (1—inductive sensor in a frame; 2—rectifying screws in the middle of the span and above the support; 3—strain gauge between the blades; 4—applied load; 5—acoustic emission sensors).

All fractured specimens were further used for the determination of the compressive and splitting tensile strength on specimen fragments.

### 2.5. Evaluation of the Fracture Tests

All the recorded  $F$ - $d$  and  $F$ - $CMOD$  diagrams were processed using GTDiPS software before their evaluation [18] (refer to [19] for more details).

#### 2.5.1. Fracture Toughness

The fracture toughness value was determined using the linear elastic fracture mechanics approach for brittle fracture. This parameter is related to the stress field near the tip of the crack. The fracture toughness value  $K_{Ic}$  is calculated as follows [4]:

$$K_{Ic} = \frac{6M_{\max}}{BW^2} Y(\alpha) \sqrt{a}, \quad (1)$$

where  $M_{\max}$  is the bending moment due to the maximum load  $F_{\max}$  and self-weight,  $B$  is the specimen width,  $W$  is the specimen depth,  $Y(\alpha)$  is a function of geometry [4], and  $a$  is the initial notch depth.

In this case, a geometry function for three-point bending configuration proposed by Brown and Srawley (1966) was used [4].

$$Y(\alpha) = 1.93 - 3.07\alpha + 14.53\alpha^2 - 25.11\alpha^3 + 25.80\alpha^4, \quad (2)$$

where  $\alpha = a/W$  is the relative notch depth.

#### 2.5.2. Effective Fracture Toughness

Several adaptations of linear elastic fracture mechanics have been proposed to cover the nonlinear behavior of a material. One of them is the effective crack model (ECM) [4], which includes the effect of the pre-peak nonlinear behavior of a real concrete structure containing the initial notch through an equivalent elastic structure containing a notch of effective length  $a_e > a$ . The effective crack length  $a_e$  is calculated from the secant stiffness of the concrete specimen corresponding to the maximum load  $F_{\max}$  and matching midspan deflection  $d_{F_{\max}}$ . The value of  $a_e$  for the prismatic specimen with a central edge notch tested in the three-point bending configuration was determined according to [4] from the following relationship:

$$d_{F_{\max}} = \frac{F_{\max}}{4BE} \left(\frac{S}{W}\right)^3 \left[ 1 + \frac{5qS}{8F_{\max}} + \left(\frac{W}{S}\right)^2 \left\{ 2.70 + 1.35 \frac{qS}{F_{\max}} \right\} - 0.84 \left(\frac{W}{S}\right)^3 \right] + \frac{9F_{\max}}{2BE_c} \left(1 + \frac{qS}{2F_{\max}}\right) \left(\frac{S}{W}\right)^2 F_1(\alpha_e), \quad (3)$$

where  $E$  is the static modulus of elasticity calculated from the initial part of the recorded  $F$ - $d$  diagrams according to Stibor [20],  $q$  is the self-weight of the specimens per unit length,  $S$  is span length, and

$$F_1(\alpha_e) = \int_0^{\alpha_e} xY^2(x)dx, \quad (4)$$

where  $\alpha_e = a_e/W$  is relative notch depth, and  $Y(x)$  is the function of geometry shown in Equation (2), where  $\alpha$  is replaced by  $\alpha_e$ . Since the effective crack length  $a_e$  is expressed in Equation (4) as the argument of integral, the problem is solved using an iterative method.

Subsequently, the effective fracture toughness  $K_{Ice}$  value was calculated using a linear elastic fracture mechanics formula (Equation (1)), where  $\alpha$  was replaced with  $\alpha_e$  in compliance with [4].

#### 2.5.3. Specific Fracture Energy

The complete  $F$ - $d$  diagrams, including their post-peak parts, were employed to determine the work of fracture  $W_F$  value, which was given by the area under the diagram. In this case,  $W_F$  was calculated according to Stibor [20], where the area under the measured

diagrams, the effect of the unmeasured part, and the self-weight of the specimen were considered. After that, the specific fracture energy  $G_F$  value was determined according to the RILEM method [21].

$$G_F = \frac{W_F}{(W - a)B}. \quad (5)$$

The value of fracture energy was also investigated when the area under the curve was divided into two parts (see Figure 4). The first part  $G_{F,1}$  considers the area under the  $F-d$  diagram up to the maximum load  $F_{max}$ , and the second part  $G_{F,2}$  considers the remaining area under the  $F-d$  diagram.

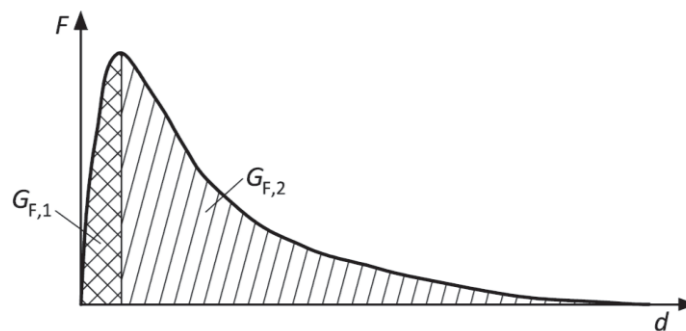


**Figure 4.** The considered parts of fracture energy.

#### 2.5.4. The Double-K Fracture Model Parameters

The double-K fracture (2K) model [22] was used for the evaluation of the  $F-CMOD$  diagrams to determine selected fracture parameters. This model allowed the calculation of the parameters describing different phases of the fracture process. The unstable fracture toughness  $K_{Ic}^{un}$  is defined as the critical stress intensity factor corresponding to the maximum load  $F_{max}$ , and it represents the phase of unstable crack propagation. This parameter is of similar meaning to the effective fracture toughness used in the ECM by Karihaloo [4]. The equivalent elastic crack length  $a_c$  was determined from the following equation [22]:

$$CMOD_{F_{max}} = \frac{6F_{max}Sa_c}{BW^2E}V(\alpha_c), \quad (6)$$

where  $CMOD_{F_{max}}$  is the  $CMOD$  corresponding to maximum load  $F_{max}$ , and

$$V(\alpha_c) = 0.76 - 2.28\alpha_c + 3.87\alpha_c^2 - 2.04\alpha_c^3 \frac{0.66}{(1 - \alpha_c)^2}, \quad (7)$$

where  $\alpha_c = (a_c + H_0)/(W + H_0)$ ;  $H_0$  is the thickness of blades fixed on the bottom surface of the specimens between which the strain gauge was placed.

When the equivalent elastic crack length  $a_c$  is known,  $K_{Ic}^{un}$  was determined according to Equation (1), where  $a_c$  was substituted by  $a$ , and the geometry function in this case was expressed as follows [4]:

$$Y\left(\frac{a_c}{W}\right) = \frac{1.99 - \frac{a_c}{W}\left(1 - \frac{a_c}{W}\right)\left(2.15 - 3.93\frac{a_c}{W} + 2.70\left(\frac{a_c}{W}\right)^2\right)}{\left(1 + 2\frac{a_c}{W}\right)\left(1 - \frac{a_c}{W}\right)^{3/2}}. \quad (8)$$

The important parameter for nonlinear fracture mechanics calculation is the relationship between the stress and crack opening displacement (see Figure 5).

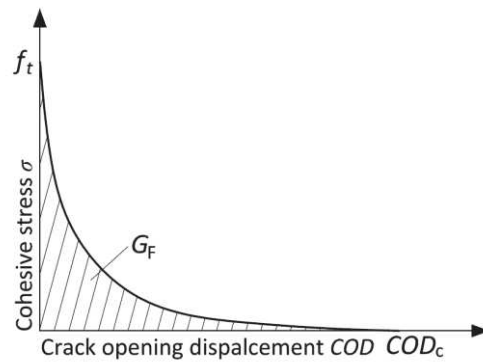


**Figure 5.** The parameters of softening function.

The fracture energy  $G_F$  is a derivative parameter of this relationship, which represents the area under this curve (softening function). There are two methods to obtain the parameters of the softening function. The first is based on the experimental determination of  $G_F$  from the uniaxial tensile strength test with deformation-controlled loading. The  $G_F$  is then calculated as the area under the  $\sigma$ – $COD$  diagram. However, it is quite hard to perform such a test in a stable way for concrete specimens, i.e., to also record the post-peak branch of the diagram. The other method consists of an indirect method of determination of  $COD_c$ . In this case,  $G_F$  and  $f_t$ , determined experimentally from the 3PBT and uniaxial tensile test, respectively, and a suitable shape of the softening function are the input parameters [23]. In the 2K model, the softening function has to be known to calculate the cohesive toughness at critical condition  $K_{Ic}^c$ , which can be interpreted as an increase in the resistance to crack propagation caused by the bridging of aggregate grains and other toughening mechanisms in the fracture process zone (FPZ) [22].

In this paper, the nonlinear softening function according to Hordijk [23], and  $G_F$  and  $f_t$  obtained by inverse analysis [24] were used for the calculation of related fracture parameters. The cohesive stress  $\sigma(CTOD_c)$  at the tip of an initial notch at the critical state could be then obtained from this softening function.

$$\sigma(CTOD_c) = f_t \left\{ \left[ 1 + \left( c_1 \frac{CTOD_c}{COD_c} \right)^3 \right] \exp \left( -c_2 \frac{CTOD_c}{COD_c} \right) - \frac{CTOD_c}{COD_c} (1 + c_1^3) \exp(-c_2) \right\}, \quad (9)$$

where  $f_t$  is the tensile strength,  $c_1 = 3$  and  $c_2 = 6.93$  and are the material constants, which were taken from [23], and  $CTOD_c$  is the critical crack-tip opening displacement according to Jenq and Shah [25][Jeng 1985].

$$CTOD_c = CMOD_{F_{\max}} \left( \left( 1 - \frac{a}{a_c} \right)^2 + \left( 1.081 - 1.149 \frac{a}{W} \right) \left( \frac{a}{a_c} - \left( \frac{a}{a_c} \right)^2 \right) \right)^{\frac{1}{2}}. \quad (10)$$

$COD_c$  is the critical crack opening displacement calculated according to

$$COD_c = \frac{5.136 G_F}{f_t}. \quad (11)$$

The values of fracture energy  $G_F$  and tensile strength  $f_t$  were obtained by an inverse analysis based on an artificial neural network using the FraMePID-3PB Software [24]. The principle consists of the identification of the material parameters, which gives identical  $F$ – $d$  diagram responses to those obtained during real-time specimen loading. It is presumed that such strength is very close to the uniaxial tensile strength.

Subsequently, the linear function for the calculation of cohesive stress  $\sigma(x)$  along the length of the equivalent elastic crack can be formulated as follows:

$$\sigma(x) = \sigma(CTOD_c) + \frac{x-a}{a_c-a} (f_t - \sigma(CTOD_c)). \quad (12)$$

When this relation is known, the cohesive toughness  $K_{Ic}^c$  is determined as follows:

$$K_{Ic}^c = \int_{a/a_c}^1 2 \sqrt{\frac{a_c}{\pi}} \sigma(U) F\left(U, \frac{a_c}{W}\right) dU, \quad (13)$$

where the substitution  $U = x/a_c$  is used, and  $F(U, a_c/W)$  is determined according to [26] [Xu 1999].

$$F\left(U, \frac{a_c}{W}\right) = \frac{3.52(1-U)}{\left(1-\frac{a_c}{W}\right)^{3/2}} - \frac{4.35-5.28U}{\left(1-\frac{a_c}{W}\right)^{1/2}} + \left(\frac{1.30-0.30U^2}{(1-U^2)^{1/2}} + 0.83-1.76U\right) \left[1 - (1-U)\frac{a_c}{W}\right]. \quad (14)$$

The following formula based on the formerly obtained parameters was used to calculate the initial cracking toughness  $K_{Ic}^{ini}$ :

$$K_{Ic}^{ini} = K_{Ic}^{un} - K_{Ic}^c, \quad (15)$$

where  $K_{Ic}^{ini}$  represents the phase of stable crack propagation.

Lastly, the load level  $F_{ini}$ , which expresses the load at the outset of stable crack propagation from the initial notch, was determined according to

$$F_{ini} = \frac{4 \cdot S_M \cdot K_{Ic}^{ini}}{S \cdot Y(\alpha) \cdot \sqrt{a}}, \quad (16)$$

where  $S_M$  is the section modulus (calculated as  $S_M = 1/6 \cdot B \cdot W^2$ ),  $S$  is the span length, and  $Y(\alpha)$  is the geometry function (Equation (8)), where  $\alpha = a/W$  is used instead of  $a_c/W$ .

### 3. Results and Discussion

In this section, the results of the performed experiments are presented in tables and figures. Table 2 summarizes the characteristics of the air-void (A-V) system in the hardened non-frost-attacked concretes. These parameters merely serve as informative for this paper as the support for the interpretation of the related results. The results listed in Table 2 show basic and one of the most important differences between investigated concretes, namely, the total A-V content and the number of voids smaller than 300 microns were about 35% and 52% higher for concrete C1 compared to C2. This implies that concrete C1 should be more resistant to F-T than concrete C2. On the other hand, according to the paste-air ratio, the cement paste in concrete C2 should be denser and less permeable for the water medium.

**Table 2.** Air-void system of hardened concretes: average value (standard deviation).

Parameter	C1	C2
Total air-void content (%)	4.26 (0.372)	2.77 (0.127)
Specific surface (mm <sup>-1</sup> )	24.4 (2.74)	23.0 (1.56)
Paste-air ratio	7.22 (0.64)	11.75 (0.54)
Spacing factor (mm)	0.23 (0.019)	0.30 (0.026)
A <sub>300</sub> (%)	1.31 (0.048)	0.63 (0.014)

Table 3 summarizes the mechanical and fracture characteristics of non-frost-attacked concretes. All characteristics were determined at the same time when the set exposed to 50 F-T cycles was tested. Comparing the results, including their variability, it can be stated

that the basic mechanical characteristics such as dynamic modulus of elasticity and compressive strength were similar for both concretes. Moreover, the critical force for the start of unstable crack propagation ( $F_{max}$ ) was also very similar. Similar results could also be observed in the values of selected fracture characteristics, such as crack strength, fracture toughness, unstable fracture toughness, and effective crack extension. The difference between these parameters for C1 and C2 was up to 5%. The highest difference is recorded in the value of fracture energy ( $G_F$ ), which was about 14% higher for concrete C2. The values of  $G_{F,1}$  and  $G_{F,2}$  suggest that this difference was especially caused by the different post-peak behavior of investigated concretes;  $G_{F,2}$  was about 16% higher for C2, whereas  $G_{F,1}$  was almost the same for both concretes. A similar difference was recorded in the values of splitting tensile strength, which was about 15% lower for C2 compared to C1, but the variability for C2 was more than twofold higher. Similarly, the values of  $F_{ini}$  (critical force for the start of stable crack propagation), initial fracture toughness, and critical crack opening displacement ( $COD_c$ ) could not be simply compared because of the high differences in variability recorded for each concrete, which was about twofold higher (more than threefold for  $COD_c$ ) for C1 compared to C2.

**Table 3.** Mechanical, fracture, and AE characteristics of non-frost attacked concretes C1 and C2: average value (standard deviation).

Parameter	C1	C2
Dynamic modulus of elasticity (GPa)	43.330 (0.976)	42.980 (0.727)
Compressive strength * (MPa)	60.0 (0.1)	57.0 (2.6)
Splitting tensile strength * (MPa)	5.41 (0.4)	4.61 (0.85)
Crack strength (MPa)	5.02 (0.16)	5.35 (0.40)
Tensile strength, identification (MPa)	3.20 (0.37)	2.99 (0.21)
Load level $F_{ini}$ (kN)	3.41 (0.59)	3.95 (0.36)
Maximum load $F_{max}$ (kN)	5.13 (0.13)	5.31 (0.40)
Effective fracture toughness (MPa.m <sup>1/2</sup> )	1.249 (0.105)	1.371 (0.093)
Fracture toughness (MPa.m <sup>1/2</sup> )	0.773 (0.022)	0.823 (0.062)
Fracture energy $G_F$ (J/m <sup>2</sup> )	127.7 (12.33)	146.0 (15.5)
Fracture energy $G_{F,1}$ (J/m <sup>2</sup> )	22.2 (3.00)	23.4 (1.88)
Fracture energy $G_{F,2}$ (J/m <sup>2</sup> )	105.5 (9.71)	122.7 (14.89)
Initial fracture toughness (MPa.m <sup>1/2</sup> )	0.520 (0.09)	0.619 (0.056)
Unstable fracture toughness (MPa.m <sup>1/2</sup> )	1.225 (0.145)	1.205 (0.128)
Effective crack extension (mm)	16.91 (2.6)	17.83 (1.4)
Equivalent crack extension (mm)	15.56 (3.5)	13.00 (3.9)
Critical crack tip opening displacement (mm)	0.0244 (0.003)	0.0243 (0.007)
RMS <sub>cumu</sub> _F <sub>max</sub> (mV)	0.1663 (0.0405)	0.124 (0.0182)

\* Determined on the fragments of fractured specimens.

The results of the F–T tests are presented in figures below. All parameters (except the changes in mass and dynamic Poisson's ratio) are displayed as the relative values of the results obtained for frost and non-frost-attacked specimens of particular concrete as follows:

$$RV_n = \frac{P_n}{P_0}, \quad (17)$$

where  $RV_n$  is a relative value of a particular material characteristic determined for  $n$  F–T cycles ( $n = 0, 50, 100, \text{ and } 200$ ),  $P_n$  is an average value of the set of specimens determined for a particular material characteristic after  $n$  F–T cycles,  $P_0$  is an average value of the set of non-frost-attacked specimens determined for the particular material characteristic (for  $n = 0$ ;  $RV_n = 1$ ).

The error bars represent the relative standard deviation of the results for a particular set of specimens.

$$RSD_n = RV_n \cdot CoV_n, \quad (18)$$

where  $RSD_n$  is a relative value of the standard deviation of a particular material characteristic determined for  $n$  F–T cycles ( $n = 0, 50, 100,$  and  $200$ ),  $SSD_n$  is a sample standard deviation of the set of specimens determined for a particular material characteristic after  $n$  F–T cycles, and  $CoV_n$  is a coefficient of variation of the set specimens determined after  $n$  F–T cycles.

The decrease in mass and almost constant value of dynamic Poisson's ratio (see Figure 6) implies that the specimens are not significantly disturbed by macrocracks throughout the F–T test duration. As already indicated by other authors [27–31], the presence of significant cracks causes an increase in mass and changes in the values of Poisson's ratio. It can be presumed that a small decrease in mass indicates desiccation of saturated test specimens during the freezing phase. A slow increase in mass recorded after 125 and 175 F–T cycles for C1 and C2, respectively, may indicate slow water uptake of the test specimens due to the existence of microcracks, which were also observed on the surface of the test specimens using a digital microscope (see Figures 7 and 8). The water uptake led partially to the healing of existed or newly formed cracks. This behavior was observed for both concretes. In the case of C2, the width of observed surface cracks was higher than for C1, which implies that the existed cracks were not fully healed for C2 (see Figure 8), as observed for C1.

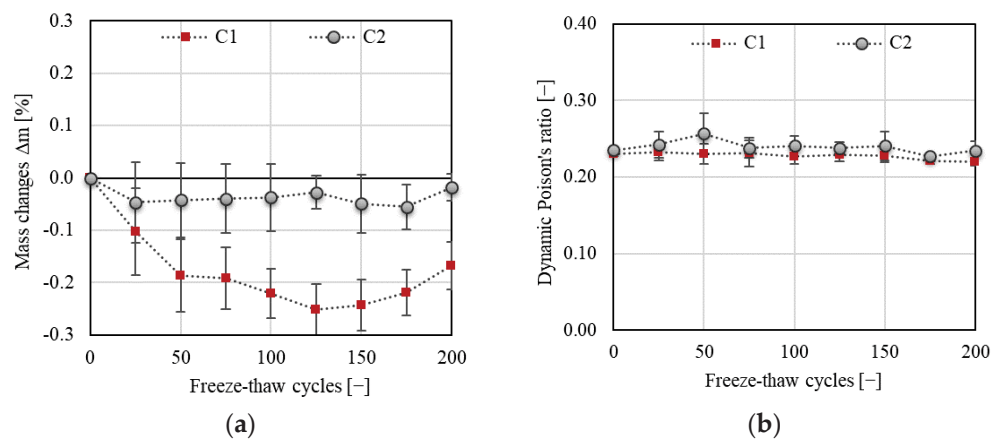
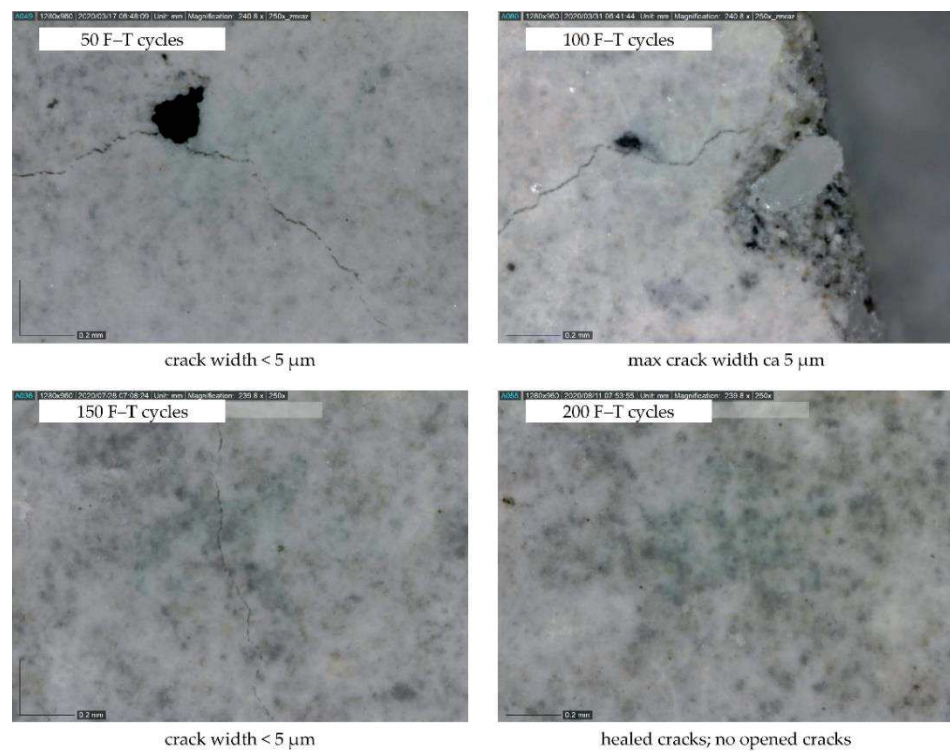
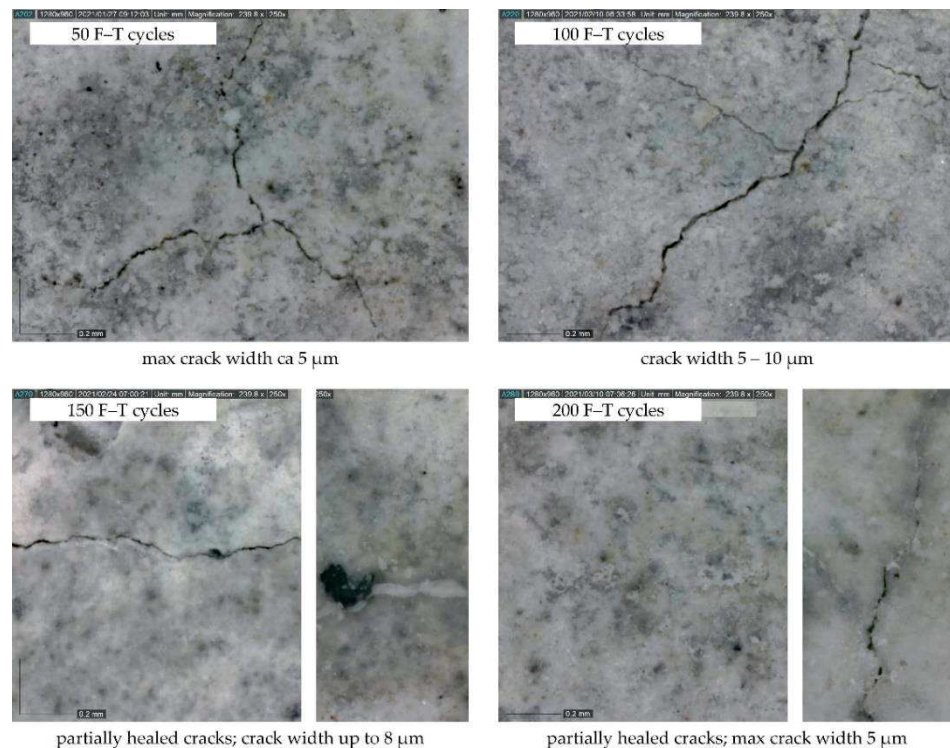


Figure 6. (a) Changes in mass; (b) Poisson's ratio.



**Figure 7.** Microcracks on the specimen surface (C1; magnification 250 $\times$ ).



**Figure 8.** Microcracks on the specimen surface (C2; magnification 250 $\times$ ).

Although none of the concretes showed visible disruption, there were differences in the development of the dynamic modulus of elasticity and compressive strength (see Figure 9) for C1 and C2. It can be observed that concrete C1 exhibited better F-T resistance than concrete C2. The decrease in  $E_{FL}$  was about 5% and was quite stabilized after reaching 25 F-T cycles for C1. No decrease in the compressive strength was observed for C1. In both cases, the results exhibited low variability. The situation differed for concrete C2;

a gradual decrease in  $E_{rL}$  and compressive strength up to about 20% was observed upon reaching 100 F–T cycles, after which the values of both parameters started to grow. The final decrease was about 15% and 4% for  $E_{rL}$  and compressive strength, respectively. The long-term experience of the authors with the utilization of the resonance method as a non-destructive technique for monitoring of the F–T damage in concrete suggests that a decrease in  $E_{rL}$  of about 15% indicates a decrease in the flexural or splitting tensile strength of at least about 25% [32,33]. This presumption is confirmed by the results presented in Figure 10a; the decrease in splitting tensile strength was about 40% for C2.

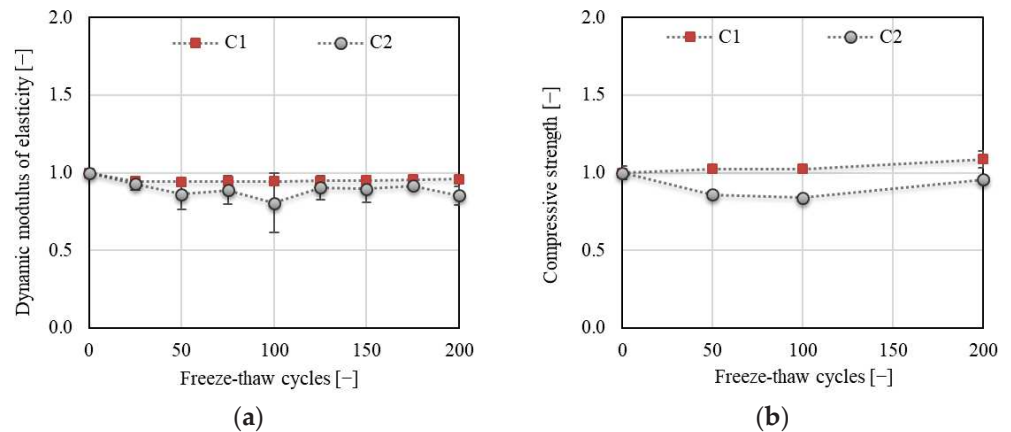


Figure 9. (a) Dynamic modulus of elasticity ( $E_{rL}$ ); (b) compressive strength.

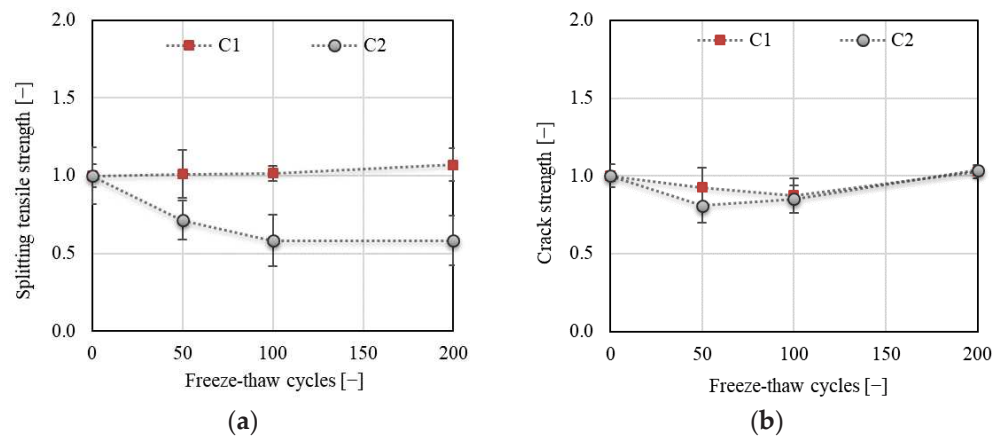


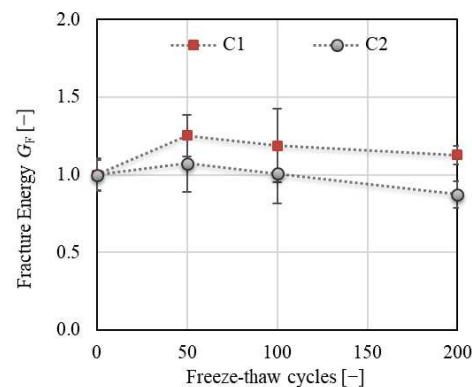
Figure 10. (a) Splitting tensile strength; (b) crack strength.

Figure 10 displays the changes in tensile characteristics of the investigated concretes during the F–T test. Two types of strength were determined: splitting tensile (in compliance with ČSN EN 12390-6 [34] on the fragments of specimens) and flexural strength determined on the notched specimens during fracture test (crack strength according to the terminology in the branch of fracture mechanics [35]). It can be stated that the results are rather contradictory. In the case of splitting tensile strength, a slight increase was observed for C1, while a gradual decrease of about 40% was recorded for C2 after 200 F–T cycles (see Figure 10a). This indicates that concrete C2 is not F–T-resistant according to the Czech standard [11]. On the other hand, a gradual decrease of about 16% after 100 F–T cycles for C1 and about 20% after 50 F–T cycles for C2 followed by an increase was observed for the crack strength. The crack strength was of the same value after 200 F–T cycles as before the start of freezing (see Figure 10b). It can be supposed that the differences in the development of tensile strengths originated in the loading regime, especially since the loading rate was extremely different. In the case of splitting tensile strength, the specimens are loaded

by load increment at a rate of 0.05 MPa/s, whereas, during the fracture test, the specimens were loaded with a displacement increment at the rate of 0.02 mm/min.

The figures below display an advanced evaluation of the F–T damage based on the fracture mechanics of quasi-brittle materials. Note that the results of fracture tests are often accompanied by a high variability, which may in some cases reach more than 20%. The reason for this variability can be found in the test method itself. The method is based on the very slow loading of specimens; therefore, all microdefects are reflected in the resulting parameters. Another reason results from evaluation approaches, especially when the evaluation of the results is to a large extent based on the theoretical hypotheses, as is, e.g., the case in the double- $K$  model. The assessment of fracture tests herein was based on an evaluation of  $F$ – $d$  and also  $F$ – $CMOD$  diagrams. The results based on the evaluation of  $F$ – $d$  diagrams are presented first.

Specific fracture energy  $G_F$  (see Figure 11) is one of the most commonly used parameters for the assessment of the degree of F–T deterioration. The total fracture energy was calculated herein based on the  $F$ – $d$  diagrams (see Section 2.5.3, Equation (5)). The results showed an increase in  $G_F$  of about 25% for C1 followed by a slight decrease after 50 F–T cycles. Nevertheless, the final value was about 12% higher than the value before the start of freezing. Similar findings were reported by Wardeh [36], who attributed this phenomenon to the presence of a microcrack network, which needs higher energy dissipation to complete fracture of the concrete. A slight increase of about 7% followed by a decrease with a final value of about 13% after 200 F–T cycles was observed for C2, which indicates an increase in brittleness with an increasing number of F–T cycles. Note that the value of  $G_F$  is strongly influenced by the area of the fracture surface. Commonly, a projection of the fractured ligament area is used for calculation, which can substantially influence the absolute value of  $G_F$ . The actual fractured area can be more precisely specified by scanning the relief of the fracture surface using laser scanning techniques, which is labor- and time-consuming [37,38].



**Figure 11.** Specific fracture energy  $G_F$ .

Figure 12 displays the total fracture energy divided into two parts (see Section 2.5.3, Figure 4);  $G_{F,1}$  represents the initial part of the energy consumed from the start of the fracture test up to the peak load, whereas  $G_{F,2}$  represents the post-peak part of the fracture energy. The results show a substantial increase (of about 60%) in the value of  $G_{F,1}$  for C1 after 50 F–T cycles, while almost the same value was recorded for C2 throughout the F–T test. According to the tensile behavior of concrete, as reported by Wardeh [36], the presence of a higher number of microcracks in C1 developed during the initial phase of loading could be confirmed, as also reflected in the post-peak behavior. However, the variability of the results was much higher for C1 than for C2 (see Figure 12a).

The energy  $G_{F,2}$  exhibited almost the same trend for both concretes with a different value of decrease at the end of the F–T test. The value of  $G_{F,2}$  increased by about 20% and 10% for C1 and C2, respectively, after 50 F–T cycles and was almost the same as before the

start of freezing for C1, while a decrease of about 14% was observed for C2 after 200 F–T cycles.

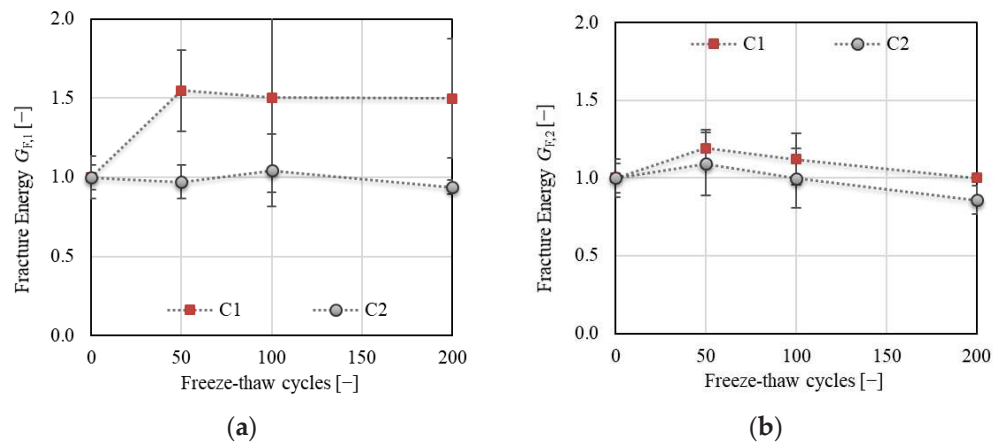


**Figure 12.** (a) Fracture energy  $G_{F,1}$  (up to the peak load); (b) fracture energy  $G_{F,2}$  (post-peak part).

Figure 13 displays the development of fracture toughness  $K_{Ic}$ , determined according to the linear elastic fracture mechanics approach (Figure 13a) and effective fracture toughness  $K_{Ic,ce}$ , which includes the nonlinear behavior of concrete before reaching the peak load (Figure 13b). The trend of  $K_{Ic}$  development was the same as observed for the crack strength throughout the F–T test (see Figure 10b). This complies with the linear fracture mechanics approach [4]. A different trend was observed for  $K_{Ic,ce}$  (see Figure 13b). The increase in this value was about 16% and even 25% after 50 and 200 F–T cycles, respectively, for concrete C1. On the other hand, a decrease of about 24% followed by a slow increase for concrete C2 was recorded after 50 F–T cycles. The final decrease in the value of  $K_{Ic,ce}$  was about 8% for C2. Moreover, the effective crack extension increased for C1 (of about 40%) and decreased for C2 (of about 20%) throughout the F–T test (see Figure 14a). This indicates increasing nonlinearity caused by a higher number of microcracks along the FPZ before failure in C1 due to the F–T exposure. According to the results, it can be stated that concrete C2 became more brittle due to exposure to F–T cycles compared to concrete C1.

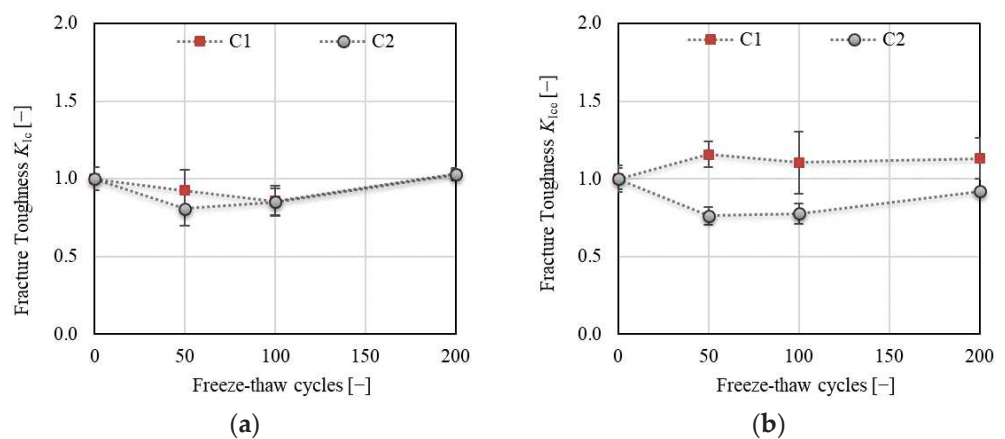


**Figure 13.** (a) Fracture toughness  $K_{Ic}$ ; (b) effective fracture toughness  $K_{Ic,ce}$ .

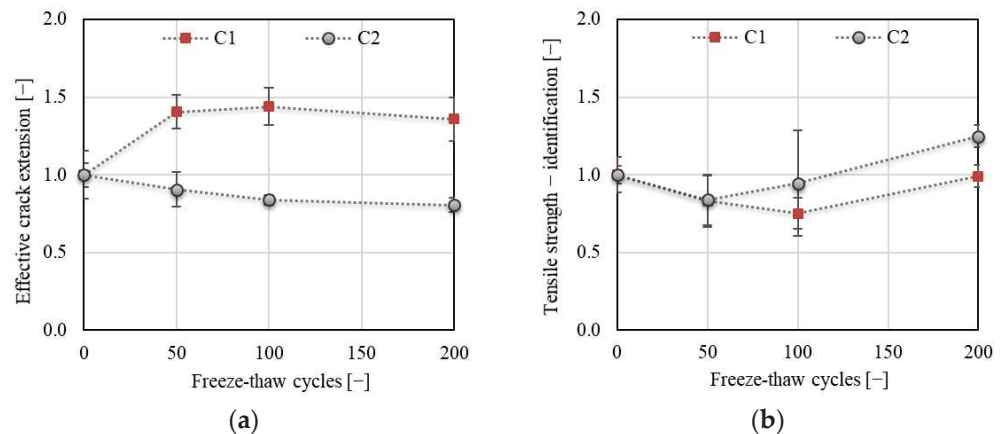
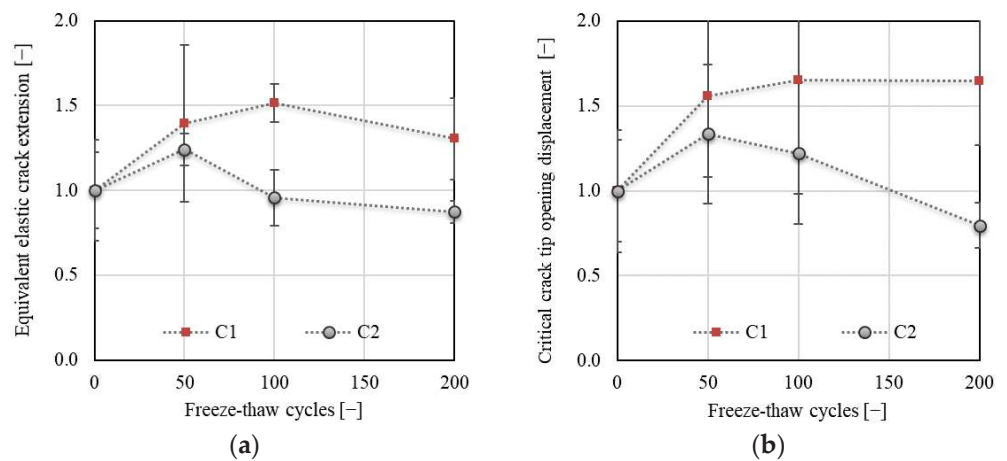


**Figure 14.** (a) Effective crack extension; (b) tensile strength from identification.

Other fracture parameters were obtained from the  $F$ - $CMOD$  diagrams evaluated using the double- $K$  fracture model, which allowed an analysis of different phases of the fracture process. Note that the tensile strength needed for the estimation of the softening function was in this case obtained via an indirect method (see Section 2.5.4). The development of the tensile strength identified according to [24] for a particular test set and concrete is displayed in Figure 14b. The results obtained based on the identification presumed a decrease in the value of tensile strength by about 20% for the specimens subjected to 50 F-T cycles for both concretes. A re-increase in tensile strength was expected after 100 and after 50 F-T cycles for C1 and C2, respectively. In the case of C2, it was expected that the tensile strength would be about 20% higher after 200 F-T cycles than that estimated for the specimens before the start of freezing. The increasing trend of development identified for specimens subjected to 100 and 200 F-T cycles did not correspond to the trend of crack strength development obtained from fracture tests for C2 concrete (see Figure 10b). The trend of tensile strength development identified for C1 was in good agreement with the trend of crack strength development (see Figure 10b).

Unstable fracture toughness  $K_{Ic}^{un}$  and cohesive fracture toughness  $K_{Ic}^c$  are two basic fracture parameters determined using the  $F$ - $CMOD$  diagrams. The cohesive fracture toughness  $K_{Ic}^c$ , as a component of unstable fracture toughness  $K_{Ic}^{un}$ , reflects the cohesive mechanisms in the FPZ. Many micro-failure mechanisms such as matrix microcracking, debonding of the cement-matrix interface, crack deflection, grain bridging, and crack branching, which consume energy during the crack propagation, are responsible for the stress transfer [22]. If the component of cohesive fracture toughness  $K_{Ic}^c$  is subtracted from the unstable fracture toughness, the value of initiation fracture toughness  $K_{Ic}^{ini}$  is obtained. The critical values of the fracture toughness are obtained at the load level  $F_{max}$ , upon reaching the equivalent elastic crack extension and critical crack-tip opening displacement ( $CTOD_c$ ).

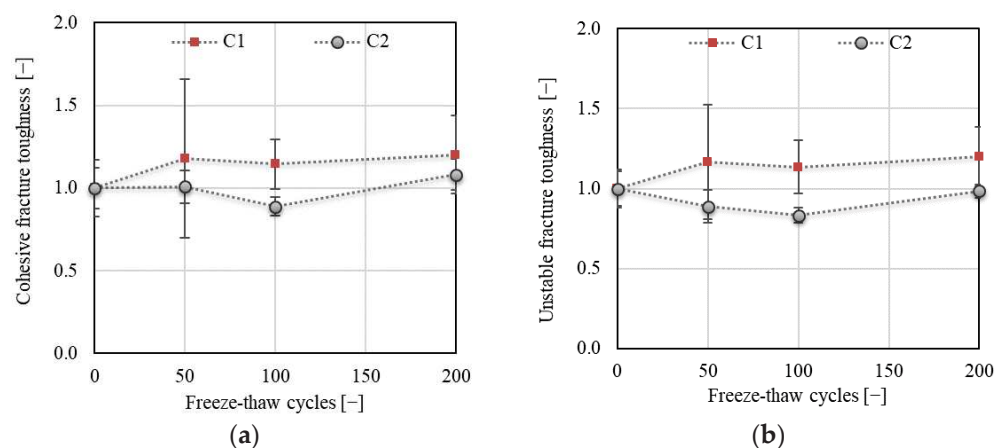
Figure 15a shows an increase in value of equivalent elastic crack extension (calculated using Equation (6)) of about 50% followed by a drop after 100 F-T cycles for C1. Concerning the C2 concrete, an increase of about 24% was followed by a steep drop observed after 50 F-T cycles. The final values recorded after 200 F-T cycles were about 30% higher and 12% lower for C1 and C2, respectively, when compared to the values before the start of freezing. The increase in equivalent elastic crack extension indicates an increasing nonlinear behavior before the failure caused by an increasing number of microcracks in the material due to the F-T action [34]. Simultaneously, more energy was consumed to completely break the material (see Figure 11 or Figure 12); thus, it behaved more ductile.



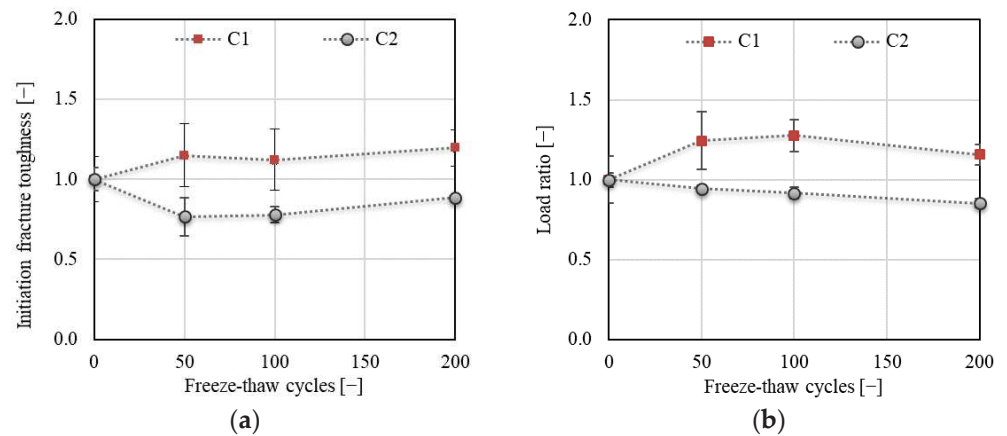
**Figure 15.** (a) Equivalent elastic crack extension; (b) critical crack-tip opening displacement (CTOD).

Figure 15b shows an increase in the value of  $CTOD_c$  of more than 60% for C1 after 200 F–T cycles. This indicates an increase in the fictitious crack width before the failure due to F–T exposure. An increase of about 34% followed by a steep decrease of about 50% was recorded for C2 after 50 F–T cycles. This indicates a gradual increase in brittleness of C2 with an increasing number of F–T cycles.

The above results correspond to the results of fracture toughness obtained using the 2K model. As shown in Figure 16 or Figure 17a, an increase of about 20% was recorded for C1 concrete for cohesive ( $K_{Ic}^c$ ), unstable ( $K_{Ic}^{un}$ ), and initial fracture ( $K_{Ic}^{ini}$ ) toughness after 50 F–T cycles, after which all toughness components were already stabilized during the remainder of the F–T test. In the case of concrete C2, the trend of development slightly differed for the three toughness components. No decrease in  $K_{Ic}^c$  was recorded after 50 F–T cycles, while a gradual and steep decrease was recorded for  $K_{Ic}^{un}$  and  $K_{Ic}^{ini}$ , respectively. A maximum decrease of about 11% and 17% followed by an increase in the value of cohesive and unstable fracture toughness, respectively, was observed after 100 F–T cycles. The final value of cohesive fracture toughness was about 8% higher compared to the value before the start of freezing.



**Figure 16.** (a) Cohesive fracture toughness  $K_{Ic}^c$ ; (b) unstable fracture toughness  $K_{Ic}^{un}$ .



**Figure 17.** (a) Initiation fracture toughness  $K_{Icini}$ ; (b) load  $F_{ini}/F_{max}$  ratio.

The increase in cohesive fracture toughness recorded for C1 reflects the action of the cohesive forces in the FPZ, which led to softening of the material [36], and it indicates the energy absorbed by the cohesive stresses acting on the fictitious crack during the stable crack propagation [39].

The descending trend of  $K_{Ic}^{un}$ ,  $K_{Ic}^{ini}$ , and  $K_{Ic}^c$  indicates higher deterioration of C2 accompanied by more brittle failure due to the F–T action compared to C1 concrete.

Figure 17b shows the development of the  $F_{ini}/F_{max}$  ratio for both concretes during the F–T test. The results show a gradual increase of up to 27% for C1 after 100 F–T cycles. The final value after 200 F–T cycles was about 16% higher than before the start of freezing. A gradual decrease of up to 15% was recorded for C2 after 200 F–T cycles. The increasing load ratio indicates an extension of the linear part of the diagram, which expresses the later onset of the stable crack propagation, i.e., the resistance to the crack onset increased during the F–T exposure for C1 concrete until reaching 100 F–T cycles.

All these parameters together indicate an enhanced resistance of C1 concrete to brittle fracture.

AE signals were continuously recorded throughout the fracture tests to evaluate the extent of the deterioration of the concrete specimens due to exposure to F–T cycles. The changes in the RMS value were evaluated for selected load levels  $F_{ini}$  and  $F_{max}$ . The changes in loading force at the selected load levels are displayed separately in Figure 18. The main changes in the values of  $F_{ini}$  were recorded for both concretes after 50 F–T cycles. After that, the value of  $F_{ini}$  was almost stabilized for both concretes. Concerning  $F_{max}$ , a gradual decrease was observed for both concretes up to 100 F–T cycles, after which the value of  $F_{max}$  increased for C1 and C2. The variability in the loading forces was reflected in the evaluation of the RMS values, which was determined for the region of the average value of  $F_{ini} \pm$  standard deviation. The same procedure was applied for the load level  $F_{max}$  and region  $0$ – $F_{max}$ .

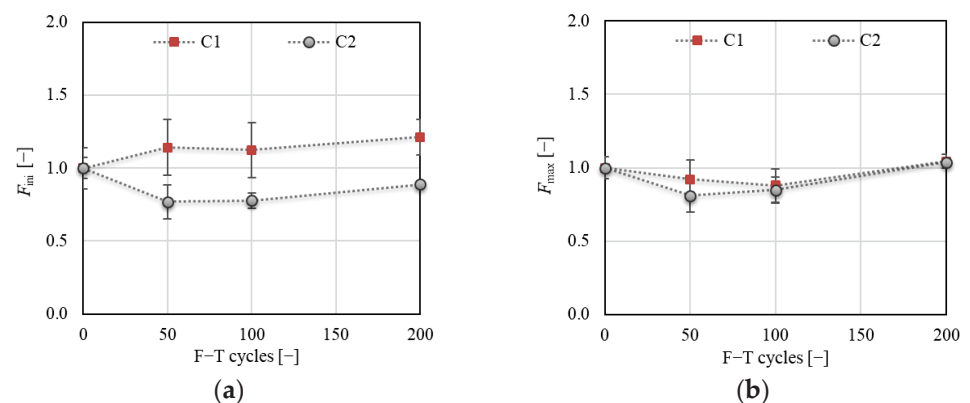


**Figure 18.** (a) Load level  $F_{ini}$ ; (b) load level  $F_{max}$ .

It is important to emphasize that AE results are influenced by two different loading processes which are concurrently in progress. The first is the F–T action, which proceeds continuously, and the second one is the fracture test performed after a selected number of F–T cycles. Considering that the F–T cycles act as a continuous loading and unloading process, failure occurs due to the progressive damage of the internal structure of concrete, which is reflected in a decrease in the acoustic signal amplitude or a shifting of the dominant frequency, as reported in [40]. This irreversible damage is then reflected in the AE parameters recorded during the fracture tests. It is supposed that a decrease in the strength of the AE signal is lower for specimens with a higher degree of internal disruptions.

The results of AE show a gradual decrease in RMS values for both concretes at all investigated load levels (see Figure 19). However, a higher decrease was in all cases recorded for C2 concrete. This indicates that the internal structure of C2 concrete was strongly disturbed with an increasing number of F–T cycles, during which the growth and coalescence of existing microcracks and the formation of new microcracks occurred. A lower acoustic response is recorded for disturbed structural bonds compared to those that are non-disturbed. A gradual decrease in RMS of about 40% and 70% for C1 and C2, respectively, was recorded at the load level  $F_{ini}$  (expected crack initiation) after 200 F–T cycles. Almost the same descending trend of RMS for C1 was recorded when evaluated for the load range of 0 up to the  $F_{max}$ . The increasing deterioration of C2 was reflected in a steep decrease in RMS, the value of which was negligible compared to the non-frost-attacked specimens after 200 F–T cycles. Although the resonance test showed a resistance of C1 concrete to the F–T action, the AE measurement revealed a gradual degradation of internal structure, as reflected in a decrease in RMS value of about 40% after 200 F–T cycles. This proved the evolution of the microcrack network during the pre-peak loading phase, which was reflected in the increase of the fracture toughness, crack extension, and fracture energy.

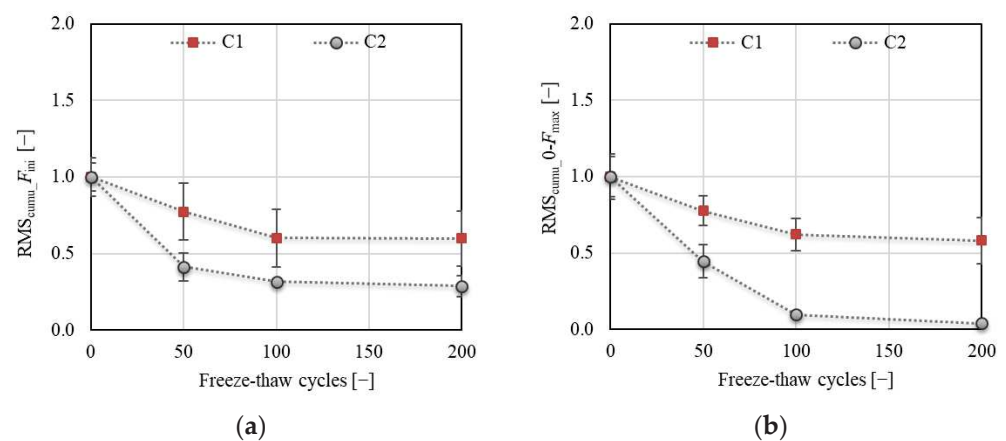


**Figure 19.** Acoustic emission: (a) RMS<sub>cumu</sub> for  $F_{ini}$ ; (b) RMS<sub>cumu</sub> for interval 0– $F_{max}$ .

The presented results are only a small part of an extensive experimental investigation focused on the F–T damage of concrete tested in the laboratory and on-site. The results of the performed experimental–numerical analysis indicate the high potential of employing fracture mechanics as a tool for the assessment of F–T damage, especially if the double-K model is also employed. The performed investigation also investigates the issue of methods for inverse analysis which might be adjusted to the pre-cracked material (due to the F–T action) submitted to the fracture tests. This novel approach provides a wider range of evaluated fracture parameters than usually presented in this context; thus, it is not possible to fully support the discussion with the literature. However, we believe that it could build a base for further investigation and a comparison of results with other research groups.

#### 4. Conclusions

This paper presented the results of an experimental program aimed at the assessment of F–T resistance of concrete based on fracture test evaluation, accompanied by acoustic emission measurement. Two concretes of similar mechanical characteristics were manufactured for the experiment. The main differences between the C1 and C2 concrete were in the total number of air voids and in the parameter  $A_{300}$ , which were both higher for C1. It is important to emphasize that both concretes did not exhibit macro-defects throughout the F–T test duration, i.e., no surface scaling or macrocracks were observed.

The evaluation of the fracture characteristics was performed on the basis of experimentally recorded  $F-d$  and  $F-CMOD$  diagrams using two different approaches: linear fracture mechanics completed with the effective crack model and double-K model. It was observed that both approaches gave similar results, especially if the nonlinear behavior before the peak load was considered.

The changes in the root-mean-square (RMS) of the acoustic emission signal were evaluated from the continuous AE measurement.

According to the results, the following conclusions can be drawn:

- It can be supposed that C1 concrete exhibited better resistance to the F–T action compared to C2. All fracture parameters together indicated an enhancing resistance of C1 concrete to brittle fracture during the F–T test.
- It can be stated that the continuous AE measurement is beneficial for the assessment of the extent of concrete deterioration and suitably supplements the fracture test evaluation.
- The results showed that the F–T damage was more reflected in the fracture toughness parameters than in the fracture energy.
- The F–T damage of the investigated concretes was reflected in the value of fracture energy, which increased with an increase in the microcrack network and decreased for concrete with a more seriously damaged structure. To confirm the presence of microcracks, it seems to be beneficial to calculate the fracture energy  $G_{F,1}$  and  $G_{F,2}$  separately for pre- and post-peak load phases. The presence of microcracks led to an increase in the pre-peak fracture energy  $G_{F,1}$  (see Figure 12a). It can be stated that an increase in  $G_{F,1}$  for concrete C1 was caused especially by softening in the FPZ, as reflected by the increase in the value of effective and unstable fracture toughness (see Figure 13b or Figure 16b) and in the post-peak behavior.
- It can be stated that the F–T damage was notably reflected in the characteristics of the fictitious crack represented herein by the effective crack extension and critical crack-tip opening displacement. Both parameters indicate the ductility/brittleness of the material. According to the results, it can be supposed that an increase in crack extension and opening indicates increasing nonlinear behavior before failure, implying an increase in ductility of C1 during F–T exposure. On the other hand, the C2 became more brittle with an increasing number of F–T cycles (see Figure 14a or Figure 15).
- The double-K model seems to be beneficial for the evaluation of F–T damage because it enables distinguishing the different phases of crack propagation. Additionally, it provides the possibility to calculate the cohesive component of the fracture toughness, which represents the action of cohesive forces along the fictitious crack and indicates the risk of brittle fracture.
- Comparing the results of fracture tests with the resonance method and splitting tensile strength test, it can be stated that all testing methods gave the same conclusion, i.e., C1 concrete is more F–T-resistant than C2. However, the fracture test evaluation provided more detailed information about the internal structure deterioration due to F–T exposure.
- The decrease in fracture parameters of C2 concrete corresponded well to the decrease in dynamic modulus of elasticity (see Figure 9a) recorded during the F–T test. Unfortunately, there are no criteria for related damage factors determined by the Czech

standard. It can be supposed that the microcracks indicated by the fracture parameters for C1 were reflected by a slight decrease in its dynamic modulus (about 5%) determined by the resonance method. However, it is not possible to assess the ductility or brittleness using the resonance method.

- The main disadvantages of the fracture test performed in the context of F–T resistance are the time consumption (one test lasts at least 40 min), labor intensiveness, and the process of evaluation, which limit its wider utilization in standard practice.

**Author Contributions:** Conceptualization, B.K., H.Š., and D.K.; methodology, B.K., H.Š., and D.K.; validation, B.K., H.Š., and D.K.; formal analysis, H.Š. and D.K.; investigation, B.K., H.Š., D.K., and L.T.; data curation, B.K., H.Š., D.K., and L.T.; writing—original draft preparation, B.K. and H.Š.; writing—review and editing, H.Š. and D.K.; visualization, B.K., H.Š., and D.K.; supervision, B.K. All authors have read and agreed to the published version of the manuscript.

**Funding:** This research was funded by the Czech Science Foundation, grant number 19-22708S.

**Institutional Review Board Statement:** Not applicable.

**Informed Consent Statement:** Not applicable.

**Data Availability Statement:** The data presented in this study are available on request from the corresponding author.

**Conflicts of Interest:** The authors declare no conflicts of interest. The funders had no role in the design of the study; in the collection, analyses, or interpretation of data; in the writing of the manuscript, or in the decision to publish the results.

## References

1. Qin, X.-C.; Meng, S.-P.; Cao, D.-F.; Tu, Y.-M.; Sabourova, N.; Grip, N.; Ohlsson, U.; Blanksvärd, T.; Sas, G.; Elfgrén, L. Evaluation of freeze-thaw damage on concrete material and prestressed concrete specimens. *Constr. Build. Mater.* **2016**, *125*, 892–904. <https://doi.org/10.1016/j.conbuildmat.2016.08.098>.
2. Kuosa, H.; Ferreira, M.; Leivo, M. *Freeze-Thaw Testing CSLA Projekt—Task 1: Literature Review* Research Report VTT-R-07364-12; VTT technical Research Centre of Finland: Espoo, Finland, 2013. <https://doi.org/10.13140/2.1.3736.8000>.
3. Ma, Z.; Zhao, T.; Yang, J. Fracture Behavior of Concrete Exposed to the Freeze-Thaw Environment. *J. Mater. Civ. Eng.* **2017**, *29*, 04017071. [https://doi.org/10.1061/\(Asce\)Mt.1943-5533.0001901](https://doi.org/10.1061/(Asce)Mt.1943-5533.0001901).
4. Karihaloo, B.L. *Fracture Mechanics and Structural Concrete*, 1st ed.; Longman Scientific & Technical: Harlow, Essex, UK, 1995; p. 330.
5. Dong, Y.; Su, C.; Qiao, P.; Sun, L. Microstructural damage evolution and its effect on fracture behavior of concrete subjected to freeze-thaw cycles. *Int. J. Damage Mech.* **2018**, *27*, 1272–1288. <https://doi.org/10.1177/1056789518787025>.
6. Huang, M.; Duan, J.; Wang, J. Research on Basic Mechanical Properties and Fracture Damage of Coal Gangue Concrete Subjected to Freeze-Thaw Cycles. *Adv. Mater. Sci. Eng.* **2021**, *2021*, 6701628. <https://doi.org/10.1155/2021/6701628>.
7. Wardah, G.; Ghorbel, E. Freezing-Thawing Cycles Effect on the Fracture Properties of Flowable Concrete. In Proceedings of the 8th International Conference on Fracture Mechanics of Concrete and Concrete Structures, FraMCoS-8, Toledo, Spain, 10–14 March 2013; International Center for Numerical Methods in Engineering (CIMNE): Barcelona, Spain, 2013; pp. 1818–1827.
8. Zhang, Z.; Ansari, F. Fracture mechanics of air-entrained concrete subjected to compression. *Eng. Fract. Mech.* **2006**, *73*, 1913–1924. <https://doi.org/10.1016/j.engfracmech.2006.01.039>.
9. Jin, S.; Zhang, J.; Huang, B. Fractal analysis of effect of air void on freeze–thaw resistance of concrete. *Constr. Build. Mater.* **2013**, *47*, 126–130. <https://doi.org/10.1016/j.conbuildmat.2013.04.040>.
10. Sika CZ: <https://cze.sika.com/> (accessed on 19 October 2021).
11. ČSN 73 1322 *Determination of Frost Resistance of Concrete (in Czech)*; ÚNMZ: Prague, Czech Republic, 1968.
12. Kocáb, D.; Halamová, R.; Bílek, V. Ratio between dynamic Young’s moduli of cementitious materials determined through different methods. In Proceedings of the SPECIAL CONCRETE AND COMPOSITES 2020: 17th International Conference, Bystřice nad Pernštejnem, Czech Republic, 14–15 October 2020; AIP Publishing: Melville, NY, USA, 2021; Volume 2322, p. 020011.
13. *ASTM C215-19: Standard Test Method for Fundamental Transverse, Longitudinal, and Torsional Resonant Frequencies of Concrete Specimens*; ASTM International: West Conshohocken, PA, USA, 2019.
14. Barsoum, F.F.; Suleman, J.; Korcak, A.; Hill, E.V.K. Acoustic Emission Monitoring and Fatigue Life Prediction in Axially Loaded Notched Steel Specimens. *J. Acoust. Emiss.* **2009**, *27*, 40–63.
15. Shateri, M.; Ghaib, M.; Svecova, D.; Thomson, D. On acoustic emission for damage detection and failure prediction in fiber reinforced polymer rods using pattern recognition analysis. *Smart Mater. Struct.* **2017**, *26*, 065023. <https://doi.org/10.1088/1361-665x/aa6e43>.

16. Panasiuk, K.; Kyzioł, L.; Dudzik, K.; Hajdukiewicz, G. Application of the Acoustic Emission Method and Kolmogorov-Sinai Metric Entropy in Determining the Yield Point in Aluminium Alloy. *Materials* **2020**, *13*, 1386. <https://doi.org/10.3390/ma13061386>.
17. Niewiadomski, P.; Hoła, J. Failure process of compressed self-compacting concrete modified with nanoparticles assessed by acoustic emission method. *Autom. Constr.* **2020**, *112*, 103111. <https://doi.org/10.1016/j.autcon.2020.103111>.
18. Frantík, P.; Mašek, J. GTDiPS Software, 2015. Available online: <http://gtdips.kitnarf.cz/> (accessed on 1 October 2020).
19. Šimonová, H.; Kucharčzyková, B.; Bílek, V.; Malíková, L.; Miarka, P.; Lipowczan, M. Mechanical Fracture and Fatigue Characteristics of Fine-Grained Composite Based on Sodium Hydroxide-Activated Slag Cured under High Relative Humidity. *Appl. Sci.* **2020**, *11*, 259. <https://doi.org/10.3390/app11010259>.
20. Stibor, M. Fracture Parameters of Quasi-Brittle Materials and Their Determination (in Czech). Ph.D. Thesis, Brno University of Technology, Brno, Czech Republic, 2004.
21. RILEM TC – 50 FMC (Recommendation). Determination of the fracture energy of mortar and concrete by means of three-point bend tests on notched beams. *Mater. Struct.* **1985**, *18*, 287–290. <https://doi.org/10.1007/bf02472918>.
22. Kumar, S.; Barai, S.V. *Concrete Fracture Models and Applications*; Springer LLC: Berlin, Germany, 2011; p. 262.
23. Hordijk, D.A. Local Approach to Fatigue of Concrete. Ph.D. Thesis, Technische Universiteit Delft, Delft, The Netherlands, 1991.
24. Lehký, D.; Keršner, Z.; Novák, D. FraMePID-3PB software for material parameter identification using fracture tests and inverse analysis. *Adv. Eng. Softw.* **2014**, *72*, 147–154. <https://doi.org/10.1016/j.advengsoft.2013.10.001>.
25. Jenq, Y.S.; Shah, S.P. Two parameter fracture model for concrete. *J Eng Mech* **1985**, Vol. 111(10), pp. 1227–1241. [https://doi.org/10.1061/\(ASCE\)0733-9399\(1985\)111:10\(1227\)](https://doi.org/10.1061/(ASCE)0733-9399(1985)111:10(1227))
26. Xu, S.; Reinhardt, H.W. Determination of double-K criterion for crack propagation in quasibrittle fracture, Part II: Analytical evaluating and practical measuring methods for three-point bending notched beams. *Int J Fract* **1999**, Vol. 98(2), pp. 151–177.
27. Wawrzeniuk, J.; Molendowska, A. Evaluation of Concrete Resistance to Freeze-thaw Based on Probabilistic Analysis of Damage. *Procedia Eng.* **2017**, *193*, 35–41. <https://doi.org/10.1016/j.proeng.2017.06.183>.
28. Kee, S.-H.; Kang, J.W.; Choi, B.-J.; Kwon, J.; Candelaria, M.D. Evaluation of Static and Dynamic Residual Mechanical Properties of Heat-Damaged Concrete for Nuclear Reactor Auxiliary Buildings in Korea Using Elastic Wave Velocity Measurements. *Materials*. **2019**, *12*, 2695. <https://doi.org/10.3390/ma12172695>.
29. Stein, T.; Gafoor, A.; Dinkler, D. Modeling inelastic-anisotropic damage behavior of concrete considering lateral deformation. *PAMM* **2021**, *20*, e202000225. <https://doi.org/10.1002/pamm.202000225>.
30. Poinard, C.; Malecot, Y.; Daudeville, L. Damage of concrete in a very high stress state: Experimental investigation. *Mater. Struct.* **2010**, *43*, 15–29. <https://doi.org/10.1617/s11527-008-9467-6>.
31. Prasad, M.; Xiaobing, S. Post-cracking Poisson Ratio of Concrete in Steel-Concrete-Steel Panels Subjected to Biaxial Tension Compression. *IOP Conf. Ser. Mater. Sci. Eng.* **2020**, *758*, 012081. <https://doi.org/10.1088/1757-899x/758/1/012081>.
32. Kocáb, D.; Kucharčzyková, B.; Daněk, P.; Vymazal, T.; Hanuš, P.; Halamová, R. Destructive and non-destructive assessment of the frost resistance of concrete with different aggregate. *IOP Conf. Ser. Mater. Sci. Eng.* **2018**, *379*, 012022.
33. Kocáb, D.; Lišovský, M.; Žitt, P. Experimental determination of freeze-thaw resistance in self-compacting concretes. *IOP Conf. Ser. Mater. Sci. Eng.* **2019**, *549*, 012019. <https://doi.org/10.1088/1757-899x/549/1/012019>.
34. ČSN EN 12390-6: *Testing Hardened Concrete—Part 6: Tensile Splitting Strength of Test Specimens*; ÚNMZ: Prague, Czech Republic, 2010.
35. *ASTM E1823-20b: Standard Terminology Relating to Fatigue and Fracture Testing*; ASTM International: West Conshohocken, PA, USA, 2020.
36. Wardeh, G.; Ghorbel, E. Prediction of fracture parameters and strain-softening behavior of concrete: Effect of frost action. *Mater. Struct.* **2013**, *48*, 123–138. <https://doi.org/10.1617/s11527-013-0172-8>.
37. Sobek, J.; Frantík, P.; Trčka, T.; Lehký, D. Fractal Dimension Analysis of Three-Point Bending Concrete Test Specimens. *MATEC Web Conf.* **2020**, *323*, 01011. <https://doi.org/10.1051/mateconf/202032301011>.
38. Rhee, I.; Lee, J.S.; Roh, Y.-S. Fracture Parameters of Cement Mortar with Different Structural Dimensions Under the Direct Tension Test. *Materials* **2019**, *12*, 1850. <https://doi.org/10.3390/ma12111850>.
39. Ding, Y.; Bai, Y.-L.; Dai, J.-G.; Shi, C.-J. An Investigation of Softening Laws and Fracture Toughness of Slag-Based Geopolymer Concrete and Mortar. *Materials* **2020**, *13*, 5200. <https://doi.org/10.3390/ma13225200>.
40. Topolář, L.; Kocáb, D.; Pazdera, L.; Vymazal, T. Analysis of Acoustic Emission Signals Recorded during Freeze-Thaw Cycling of Concrete. *Materials* **2021**, *14*, 1230. <https://doi.org/10.3390/ma14051230>.

# Comprehensive fracture tests of concrete for the determination of mechanical fracture parameters

David Lehký  | Barbara Kucharczyková | Hana Šimonová | Petr Daněk

Faculty of Civil Engineering, Brno  
University of Technology, Brno, Czech  
Republic

## Correspondence

David Lehký, Brno University of  
Technology, Faculty of Civil Engineering,  
Brno, Czech Republic.  
Email: lehky.d@fce.vutbr.cz

## Funding information

Grantová Agentura České Republiky,  
Grant/Award Number: 19-09491S

## Abstract

Advanced experimental evaluation of the mechanical fracture properties of quasi-brittle materials is an important part of the design, assessment, and computational modeling of structures made of these materials. The aim is to determine parameters independent of the test configuration or the size of the test specimens. This paper presents the results of an extensive experimental program which is part of the development of a comprehensive multilevel approach for experimental–computational determination of the mechanical fracture parameters of concrete. Three-point bending and wedge-splitting tests were performed simultaneously using three different geometrically similar specimen sizes and two well-separated depths of initial notches. Before the start of the main testing program, the pilot tests that were performed were aimed at the design of the most appropriate concrete mixture. Special attention was paid to the selection of a maximum aggregate grain size. In order to study the process of concrete aging and the development of its mechanical properties, the accompanying destructive and non-destructive tests were carried out at different ages of hardening. Fracture parameters were evaluated using the effective crack-length formulation and work-of-fracture method. Finally, the size-independent specific fracture energy was back-calculated from the measured specific fracture energy.

## KEYWORDS

inverse analysis, mechanical fracture parameters, size-effect test, three-point bending test, true fracture energy, wedge-splitting test

## 1 | INTRODUCTION

The quasi-brittle fracture of cement-based materials, such as concrete, is a wide field of research, in which different aspects of the mechanics and physics of fracture are investigated. The theory of concrete fracture, despite all the

efforts of numerous researchers, still does not provide a clear answer to the problem of the fracture processes in concrete. Fracture mechanics can be a useful and powerful tool for the analysis of the growth of distributed cracking and its localization in concrete. The understanding of the phenomena tied to the dissipation of energy in its various forms and the identification of microscopic properties and their interactions with macroscopic variables are the topics found to be most challenging. The science of fracture mechanics emphasizes material characterization techniques and a translation of specimen data to design.

Discussion on this paper must be submitted within two months of the print publication. The discussion will then be published in print, along with the authors' closure, if any, approximately nine months after the print publication.

A fundamental fracture parameter is fracture energy, which represents cracking resistance and ductility of concrete, and is generally considered as a material property. The most commonly used method for measuring fracture energy is via the work-of-fracture method recommended by RILEM.<sup>1</sup> The original intention of the RILEM definition of fracture energy was that the material constant determined by the tensile softening curve, as stated by the fictitious crack model, could also be measured from the load versus load-point displacement curve. However, the values determined by this method are dependent on the size and shape of the test specimen, as demonstrated and analyzed by several authors in the last decades.<sup>2–8</sup>

Several researchers have analyzed this size effect on fracture energy measurements according to the RILEM procedure, and they have proposed modifications to obtain the size-independent specific fracture energy of concrete. The two most popular methods for measuring the size-independent (or true) fracture energy of concrete are based on the local fracture energy model of Hu and Wittman<sup>9</sup> and the proposal of Elices, Guinea and Planas<sup>10–12</sup> that provides experimental corrections to avoid energy dissipations. Karihaloo, Abdalla, and Imjai<sup>2,13</sup> showed that the size-independent specific fracture energy can be obtained by testing only two specimens of the same size but with notches that are well-separated. Both approaches are interrelated as they apply some corrections to the final part of the force versus displacement diagram in the work-of-fracture test. The local fracture energy model considers the effect of the crack when it approaches the back-face free boundary surface of the specimen toward the end of the test. On the other hand, the method developed by Elices, Guinea and Planas consists in determining the non-measured work-of-fracture by adjusting the tail of the measured diagram that also corresponds to the final part of the test. Based on an experimental comparative analysis of both approaches, Cifuentes et al.<sup>14</sup> concluded that either method can be used to obtain a unique value for the size-independent fracture energy of concrete.

A constant value of fracture energy is required also when simulating the tensile cracking of concrete via a finite element analysis. Here both the crack band model<sup>15</sup> and the cohesive crack model<sup>16</sup> are representative approaches in practical analyses. Both of them treat the tensile softening relationship together with fracture energy as a fundamental material property. It was shown that parameters of softening models cannot be unambiguously identified neither from the standard size effect tests nor from the tests of the complete load versus load-point displacement curve of specimens of one size. A combination of both types of tests is required.<sup>17</sup>

Current research aims to develop a complex multi-level approach for the experimental–computational determination of mechanical fracture parameters of concrete as a typical quasi-brittle material which are independent of the test configuration or the size of the test specimens. This includes testing, advanced evaluation, and soft computing-based identification of specimens of multiple sizes and test configurations, while also analyzing fracture processes using multiscale modeling approaches. This paper summarizes the main results and the data trends of the experimental part of the whole procedure.

When designing this experimental program, we paid special attention to the creation of a consistent set of experimental data. Three-point bending and wedge-splitting tests were performed simultaneously using three different geometrically similar specimen sizes and two well-separated depths of initial notches. All the specimens were made from the same batch of concrete, were of the same age, all went through the same curing regime, and the same laboratory conditions during the test. They were tested in the same manner with a stable mode of control using the same testing machines. Further companion specimens were cast simultaneously from the same batch to determine the basic characteristics of the concrete used, and to study the process of aging and the development of its mechanical properties. The obtained experimental data will serve as a cornerstone for the development and calibration of size-independent numerical models at the macro- and meso-level, and also for the identification of material parameters using inverse analysis.

## 2 | FRACTURE TEST PROGRAM

### 2.1 | Test specimens

The proposed experimental program consisted of simultaneously performed three-point bending tests (3PBT) and wedge-splitting tests (WST) using three different specimen sizes in the ratio 1:3, see Figure 1. In order to follow the procedure of Abdalla and Karihaloo,<sup>2</sup> specimens with two well-separated depths of notches were tested for each size and test configuration. The shallow initial notches have a relative notch depth of  $a_0/D = 0.2$ , where  $a_0$  is the notch depth and  $D$  is the overall depth of the specimen. The value for the deep notches was 0.5. Note that in the case of the smallest WST specimens, the shallow notches were omitted due to the required cut-out size for seating the jigs and wedge. Three specimens were tested for each testing case with the exception of the smallest WST specimens with the deep notches, in this instance six specimens were tested.

Nominal depths  $D$  of prismatic specimens tested in 3PBT configuration were 100, 200, and 300 mm. Lengths of specimens were  $4D$ , loading spans were  $3D$ , see Figure 1 top. Specimens for WST had the same nominal length and depth  $D$  equal to 100, 200, and 300 mm, see Figure 1 bottom. All specimens for both 3PBT and WST, respectively, had the same width of 100 mm, that is, specimen sizes differed only in two dimensions. In total, 42 specimens were tested during the main testing campaign. A comparison of specimen sizes tested in both test configurations is shown in Figure 2. A schematic view of both test configurations is depicted in Figure 3.

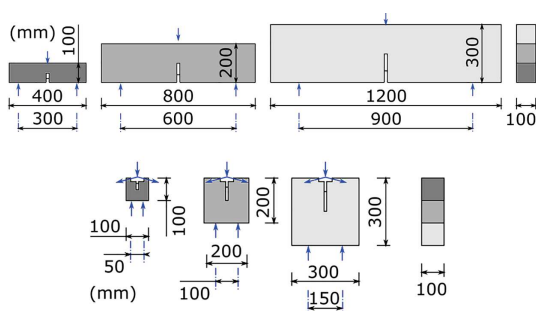


**FIGURE 1** Schematic view of a specimen with three different sizes and each with shallow and deep notches tested in three-point bending (top) and wedge-splitting (bottom) configurations

In this paper, the individual specimens are labeled with respect to the above-mentioned attributes as follows. The first letter indicates the test configuration and can be either “B” for 3PBT or “W” for WST. The number in the second position indicates the nominal depth  $D$  of the specimen, which is either 100, 200, or 300. The letter in the third position indicates the depth of the initial notch and can be either “S” as a shallow or “L” for a deep (large) notch. The final number stands for the serial number of the specimen.

## 2.2 | Mixture design and pilot tests

Before the start of the main testing program, the pilot tests that were performed aimed at the design of the most appropriate concrete mixture. Since the aim of the test campaign was to study fracture properties, the mixture design was driven by the need for obtaining the stable records of the whole load versus displacement diagrams, including their descending parts, after reaching the maximum load-bearing capacities of the tested specimens. Special attention was paid to the selection of a maximum aggregate grain size. There was an intention to use a concrete mixture widely used in the field of engineering, but also taking into account the above-mentioned response stability and the limitation given by the ratio of fracture

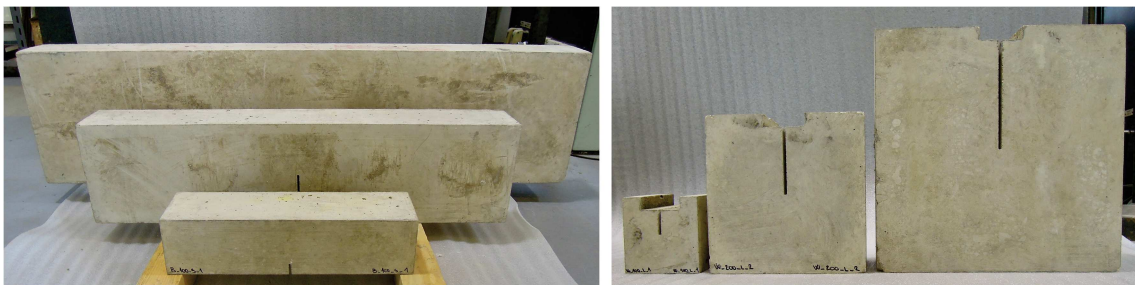


**FIGURE 2** Specimens of three different sizes tested in three-point bending (left) and wedge-splitting (right) configurations

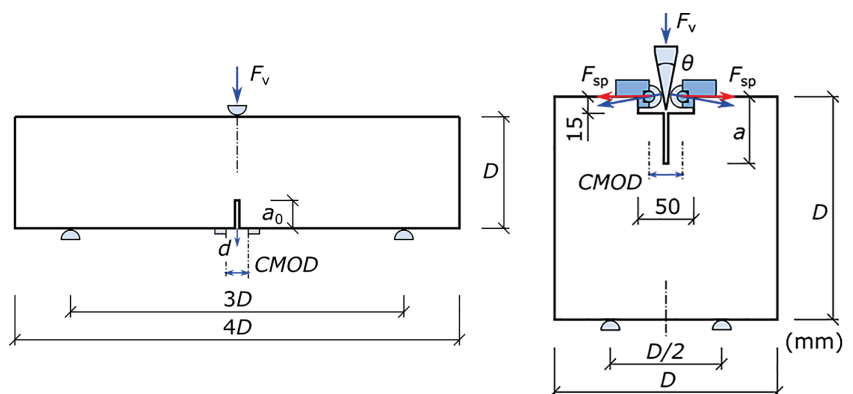


**FIGURE 3** Schematic view of the three-point bending (left) and wedge-splitting (right) test configurations

surface size to the maximum aggregate size, such as in the case of the smallest specimens with the deepest notches. Therefore, two concrete mixtures were designed to be of C30/37 strength class and differing in the maximum aggregate grain size, which was 8 and 16 mm. The aggregate to cement weight ratios ( $a/c$ ) were 4.79 and 5.44, the binder to aggregate weight ratios ( $b/a$ ) were 0.51 and 0.46, and the water to cement ratio ( $w/c$ ) were 0.61 and 0.62 for the mixtures with 8 and 16 mm grain size, respectively. The cement matrix was manufactured using CEM 42.5 R Portland cement. The plasticizer SikaPlast-501 W was used in the amount of 1% of cement weight to maintain the workability of the fresh concrete.

Both 3PBT and WST specimens were tested during the pilot tests to compare the results for both testing configurations. In the case of 3PBT, the smallest specimens with nominal depths  $D = 100$  mm were tested. In the case of WST, the middle-size specimens with nominal depths  $D = 200$  mm were used to also check the stability of the loading process for the specimens expecting more brittle damage. With respect to the planned main tests, two sets of specimens with different depths of the initial notches, shallow (S) and deep (L), were manufactured from each of the two concrete mixtures. Note that the names of pilot test specimens are in agreement with the naming introduced in the previous section, but an additional number, which can be either “8” or “16”, has been added as a name prefix to indicate the maximum aggregate grain size utilized in the concrete mixture.

The pilot test results confirmed a good initial mixture design. Figure 4 shows a comparison of force versus displacement (midspan deflection) and force versus crack mouth opening displacement (CMOD) diagrams. All the tested pilot specimens showed stable responses during the entirety of the loading process. Pre-peak and post-peak behaviors are quite similar for both mixture types. For deep notch cases (L), a slightly slowed softening can be observed just after reaching the top of the diagram for concrete with 16 mm maximum grains compared to one with 8 mm maximum grains. This property can probably

be attributed to the larger aggregate grains that are located in the fracture process zone during the development of cracks. A smaller crack-resistant area means greater sensitivity to the presence of larger aggregates.

The mixture with the maximum aggregate grain size of 16 mm was selected for the production of specimens for the main testing campaign based on the pilot test results. All mixture components were in agreement with the pilot tests. Specimens were stored in wet conditions with a relative humidity greater than 90% for the whole period of hardening. An average bulk density of hardened concrete at 97 days was  $2,320 \text{ kg/m}^3$ . All tests and results described in the following sections are related to the main testing campaign.

### 2.3 | Testing of mechanical parameters

The process of concrete aging and development of its mechanical properties was analyzed by performing compression tests, splitting tensile tests, and non-destructive tests based on the resonance method for the determination of dynamic modulus of elasticity, see Figure 5. The accompanying tests were carried out at different ages of hardening, see Section 4.1. The ages of the specimens in the main tests were from 101 to 104 days. Three to six test specimens were used for the determination of the particular mechanical parameters of accompanying tests.

Compressive and tensile splitting strength tests were performed using cubic test specimens with nominal dimensions of 150 mm in compliance with European standards EN 12390 part 3<sup>18</sup> and 6.<sup>19</sup> A non-destructive test based on the resonance method was used for the determination of the dynamic modulus of elasticity  $E_{\text{DYN}}$ . The natural frequency of longitudinal vibrations was measured on the specimens with nominal dimensions of  $100 \times 100 \times 400$  mm using a Handyscope HS4 oscilloscope equipped with an acoustic emission sensor, see Figure 5 left. For more details about the principle of measurement refer to Kocáb et al.<sup>20</sup> The absolute value of

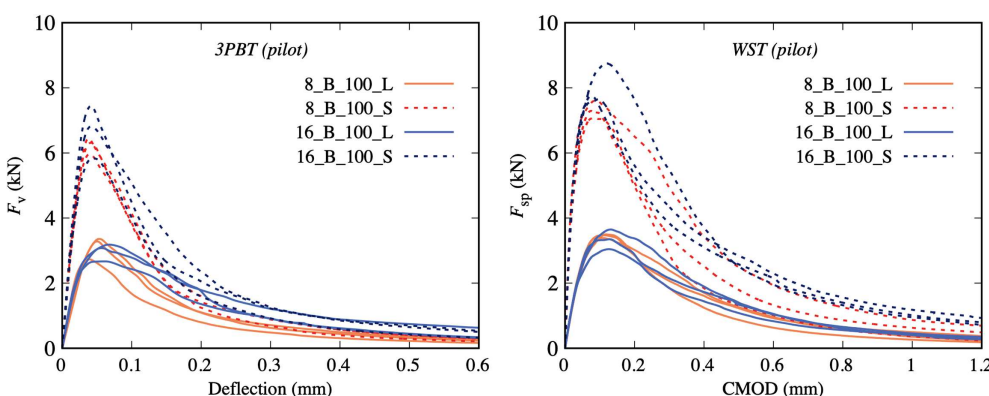


**FIGURE 4** Pilot test results—force versus displacement diagrams from three-point bending tests (left) and force versus crack mouth opening displacement diagrams from wedge-splitting tests (right) for two different concrete mixtures and two depth of initial notches



**FIGURE 5** Measurement of the natural frequency of longitudinal vibrations (left), splitting tensile test (middle), and static modulus of elasticity test (right)

$E_{\text{DYN}}$  was calculated in compliance with the ČSN 731372<sup>21</sup> as:

$$E_{\text{DYN}} = 4 \cdot L^2 \cdot f_L^2 \cdot \rho. \quad (1)$$

where  $L$  is the length of the specimen,  $f_L$  is the natural frequency of longitudinal vibrations,  $\rho$  is the bulk density of the tested material.

Static modulus of elasticity ( $E_{\text{C,S}}$ ) was determined using the prismatic test specimens with nominal dimensions of  $100 \times 100 \times 400$  mm according to the European standard EN 12390 part 13,<sup>22</sup> method B. Strain was calculated from the length changes measured using two strain gauges placed symmetrically to the central axis of the test specimens (see Figure 5 right). The initial gauge length was 200 mm. The compressive strength test was performed on the accompanying set of specimens of the same dimensions to determine the stress levels of the loading cycles.

Static modulus of elasticity was also calculated from the initial part of the recorded force versus displacement diagrams described in the following section for 3PBT specimens according to Stibor<sup>23</sup>:

$$E_{\text{B}} = \frac{F_{\text{v},i}}{4Bd_i} \left( \frac{S}{D} \right)^3 \left[ 1 - 0.387 \frac{D}{S} + 12.13 \left( \frac{D}{S} \right)^{2.5} \right] + \frac{9F_{\text{v},i}}{2Bd_i} \left( \frac{S}{D} \right)^2 F_1(\alpha_0) \quad (2)$$

where  $F_{\text{v},i}$  is the vertical force in the ascending linear part of the diagram;  $d_i$  is deflection at midspan corresponding with load  $F_{\text{v},i}$ ,  $B$  is specimen width,  $S$  is span length (see Figure 2), and  $F_1(\alpha_0) = \int_0^{\alpha_0} xY^2(x)dx$

with  $\alpha_0 = a_0/D$  ( $a_0$  is the depth of the initial notch), and  $Y(x)$  is the geometry function for the three-point bending configuration proposed by Brown and Strawley, see Karihallo<sup>24</sup>:

$$Y(\alpha) = A_0 + A_1\alpha + A_2\alpha^2 + A_3\alpha^3 + A_4\alpha^4 \quad (3)$$

coefficients  $A_0$  to  $A_4$  for the 3PBT specimen were taken according to Karihallo<sup>24</sup> and  $\alpha$  is relative notch depth (here  $\alpha = \alpha_0$ ).

For WST specimens the following equation according to Kumar and Barrai<sup>25</sup> was used:

$$E_{\text{W}} = \frac{F_{\text{sp},i}}{\text{BCMOD}_i} V_1(\alpha_0) \quad (4)$$

where  $F_{\text{sp},i}$  is splitting force in the ascending linear part of the diagram;  $\text{CMOD}_i$  is the crack mouth opening displacement corresponding with load  $F_{\text{sp},i}$ , and  $V_1(\alpha_0)$  is the compliance function for the used test configuration—generally an  $M$  degree polynomial function:

$$V_1(\alpha_0) = \sum_{m=0}^M c_m \alpha_0^m \quad (5)$$

In this case, the sixth-degree polynomial was used, and its dimensionless constants  $c_m$  were obtained according to the procedure described in Veselý et al.<sup>26</sup> In ANSYS FEM software, numerical simulations of the performed WST were conducted in the framework of the linear elastic fracture mechanics theory. The compliance function  $V_1(\alpha_0)$  is constructed from three overlapping sections to obtain higher accuracy.

## 2.4 | Testing of fracture parameters

As mentioned above, both three-point bending and wedge-splitting tests, respectively, were carried out to determine the selected concrete fracture properties. All specimens were tested within 1 week at approximately 100 days of hardening. Both tests were conducted using the stiff multi-purpose mechanical testing machine LabTest 6.250 with the load range of 0–250 kN. The loading process was governed by a constant increment of displacement of 0.02 mm/min during the entirety of testing. Examples of both test configurations are depicted in Figure 6. WST setup was according to Tschegg.<sup>27</sup> In the case of 3PBT, the vertical displacement was measured using the inductive sensor mounted in a special measurement frame placed on a top surface of the specimens (see Figure 6 left). Crack mouth opening displacement was measured using a displacement transducer mounted between blades fixed on the bottom surface of the test specimens, close to the initial notch. In the case of WST, the CMOD was measured in the horizontal axis of the bearings using the inductive sensors mounted

symmetrically to the central axis of the test specimens. The sensors were fixed in a special measuring frame placed on a top surface of the specimens (see Figure 6 right).

The outcome of each test is a vertical force versus midspan deflection diagram (in the case of 3PBT) and vertical force versus crack mouth opening displacement (CMOD, in the case of WST), see Figure 7. In the case of WST, it is necessary for the further determination of mechanical fracture parameters to recalculate the vertical force  $F_v$  to horizontal splitting force  $F_{sp}$  according to:

$$F_{sp} = \frac{F_v}{2\text{tg}\theta} \quad (6)$$

where  $\theta$  is the half-angle of the splitting wedge; in this case,  $\theta = 30^\circ/2 = 15^\circ$ .

The diagrams recorded during the tests were subsequently processed to obtain the appropriate input values for subsequent diagram evaluations using the selected fracture model. The processing of diagrams, in this case, incorporated the erasing of duplicate points, the moving



**FIGURE 6** Test configurations of a three-point bending test (left) and wedge-splitting test (right)

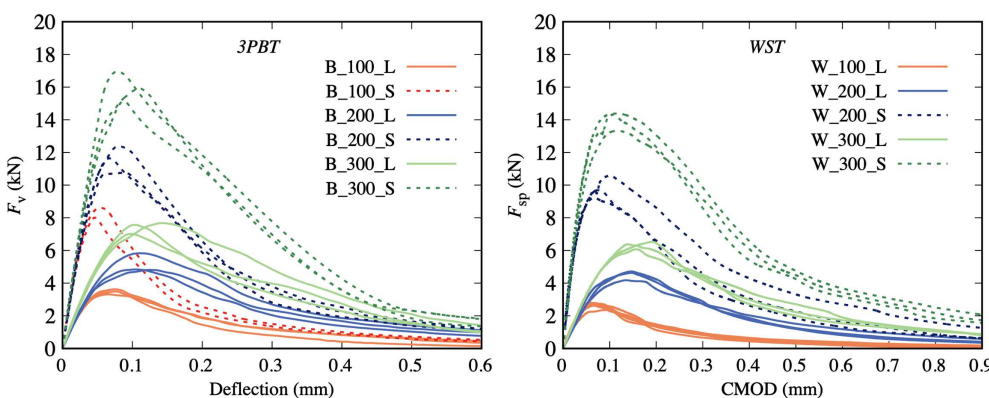


**FIGURE 7** Force versus displacement diagrams from three-point bending tests (left) and force versus crack mouth opening displacement diagrams from wedge-splitting tests (right) for all tested sizes and depth of initial notches

of the origin of the coordinate system, the smoothing of the diagram, and the reduction of the number of points. The attention was also focused on the stability loss which can occur due to the deficient stiffness of the test equipment compared to the specimen stiffness. This stability loss appears as an interruption in the recorded values of monitored parameters. The work of fracture and fracture energy values determined from measured diagrams without this correction could be overestimated. In this case, the stability loss occurred during the loading of some specimens with a higher depth (3PBT – 200 and 300 mm, WST – 300 mm) and a shallow initial notch. The processing of recorded diagrams was performed in GTDiPS software,<sup>28</sup> which is based on advanced transformation methods used for the processing of extensive point sequences.

During the loading process, the strains on the surfaces of the tested specimens were digitally measured using a system with two high-frequency cameras, see examples in Figure 8. Obtained data will be later used for the analysis of the initiation and development of the fracture process zone and its correlation with the fractal properties of the cracked surface obtained with the help of optical profilometry.

### 3 | DETERMINATION OF FRACTURE PARAMETERS

The specific fracture energy  $G_f$  according to the RILEM recommendation (1985)<sup>1</sup> is the average energy given by dividing the total work of fracture by the projected

fracture area (i.e., the area of the initially uncracked ligament). Therefore, for a 3PBT specimen of depth  $D$  and initial notch length  $a_0$ , the fracture energy is given by:

$$G_f = \frac{1}{(D-a_0)B} \left( \int F_v dd + m_g d_{\max} \right). \quad (7)$$

where  $B$  is the specimen width,  $F_v$  is the measured vertical force,  $m_g$  is the specimen weight,  $d$  is the midspan deflection, and  $d_{\max}$  is the maximum vertical deflection at failure. For the WST specimen, the fracture energy is given by:

$$G_f = \frac{1}{(D-a_0)B} \int F_{sp} d\text{CMOD}. \quad (8)$$

where  $F_{sp}$  is the horizontal splitting force calculated according to Equation 6, and CMOD is a crack mouth opening displacement measured in the horizontal axis of the bearings.

In the case of 3PBT, the effective fracture toughness  $K_{Ice}$  was determined based on the  $F_v-d$  diagrams using the effective crack model.<sup>24</sup> First, the effective crack length  $a_e$  corresponding with the maximum load  $F_{v,\max}$ , and matching deflection at midspan  $d_{Fv,\max}$  was calculated according to Karihaloo.<sup>24</sup> Subsequently, the effective fracture toughness values were calculated using a linear elastic fracture mechanics formula according to Karihaloo<sup>24</sup>:

$$K_{Ice} = \frac{6M_{\max}S}{BD^2} Y(\alpha_e) \sqrt{a_e} \quad (9)$$

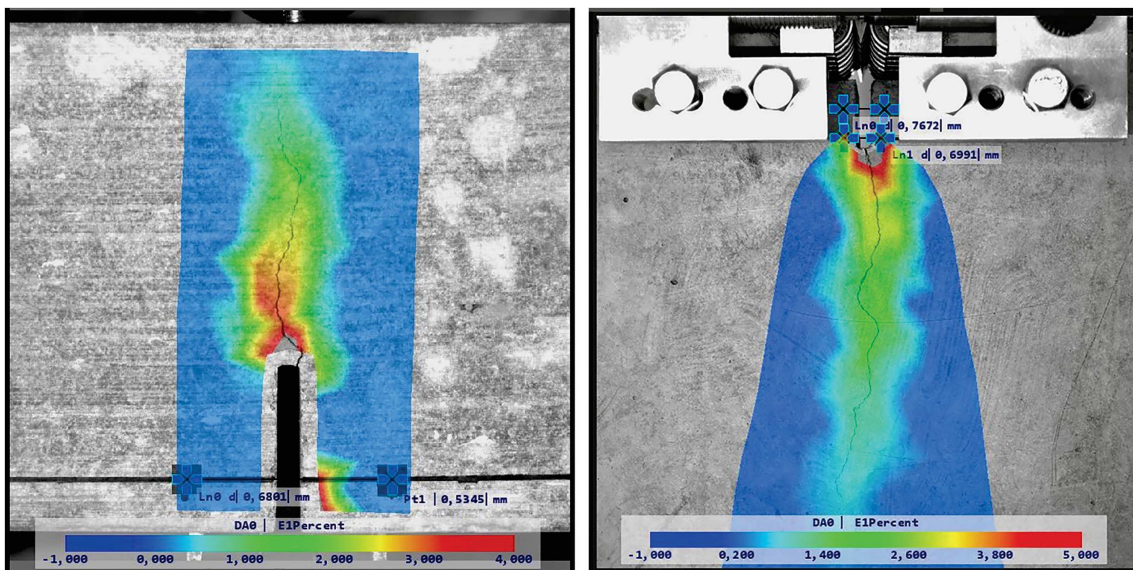


**FIGURE 8** Examples of crack propagation and measured surface strains on selected three-point bending tests (left) and wedge-splitting tests (right) specimens

where  $Y(\alpha_e)$  is the geometry function (3) with  $\alpha_e = a_e/D^{24}$  and  $M_{\max}$  is the bending moment due to the maximum applied vertical force  $F_{v,\max}$  and self-weight of the beam.

In the case of WST, the fracture toughness was determined based on the  $F_{sp}$ - $CMOD$  diagrams using the double- $K$  fracture model<sup>25,29</sup>:

$$K_{Ic}^{un} = \sqrt{2\pi} \frac{F_{sp,\max}}{B\sqrt{D}} g_1(\alpha) \quad (10)$$

where  $F_{sp,\max}$  is maximum splitting force,  $\alpha = a_c/D$ ,  $a_c$  is the critical effective crack length,  $g_1(\alpha)$  is geometry function for the used test configuration – generally an  $M$  degree polynomial function:

$$g_1(\alpha) = \sum_{m=0}^M c_m \alpha^m \quad (11)$$

In this case, the sixth-degree polynomial was used, and its dimensionless constants  $c_m$  were obtained according to the procedure described in Reference 26. In ANSYS FEM software, numerical simulations of the performed WST were conducted in the framework of the linear elastic fracture mechanics theory. The geometry function  $g_1(\alpha)$  is constructed from three overlapping sections to obtain higher accuracy.

## 4 | RESULTS

### 4.1 | Mechanical parameters

The mean values and coefficients of variation (CoV) of compressive strength, splitting tensile strength, dynamic modulus of elasticity, and static modulus of elasticity obtained at different ages of hardening are summarized in Table 1. From the time development of the properties, especially the dynamic modulus of elasticity, it can be

stated that at the time of the main tests the concrete was already sufficiently matured, and its properties were stabilized. The values of static modulus of elasticity obtained from the fracture tests for all the tested specimens are summarized in Table 2 together with the mean value and CoV for each set. Note that these values correspond to about 100 days of concrete hardening when the main testing was carried out.

The mean value of the compressive strength of concrete at 24 days of hardening was 43.8 MPa, see Table 1. This value is in a good agreement with EN 1990-1-1 recommendations, where the mean value of the compressive strength at 28 days is estimated from the characteristic value according to simplified formula and for the C30/37 strength class it is 38 MPa. Compressive strength further increased by 10 MPa during an additional two and half months of curing, see Table 1. Splitting tensile strength obtained at 24 days of hardening was 3.04 MPa. This is partially comparable with the mean value of the tensile strength of 2.9 MPa recommended in EN 1992-1-1.<sup>30</sup> During further hardening, the value increased by an additional 0.2 MPa until the main tests were performed.

The value of static modulus of elasticity 30.6 GPa obtained according to standard recommendations (see the last row of Table 1) is in a good agreement with the values obtained from fracture tests in both configurations (see Table 2 and Figure 9). The mean values (CoV) of modulus of elasticity calculated from all fracture test specimens with different sizes but the same testing configuration are 30.5 GPa (11.9%) for 3PBT and 29.2 GPa (10.3%) for WST. Also note that according to EN 1992-1-1<sup>30</sup> the mean value of modulus of elasticity is about 33 GPa for C30/37 strength class; its coefficient of variation should be considered as 15% according to JCSS Probabilistic Model Code.<sup>31</sup> The obtained results are in good agreement with both standards. As expected, the dynamic modulus of elasticity reaches a slightly higher value at 94 days of hardening compared to the static modulus.

**TABLE 1** Mean values (CoV in %) of selected mechanical properties of tested concrete at different ages of hardening

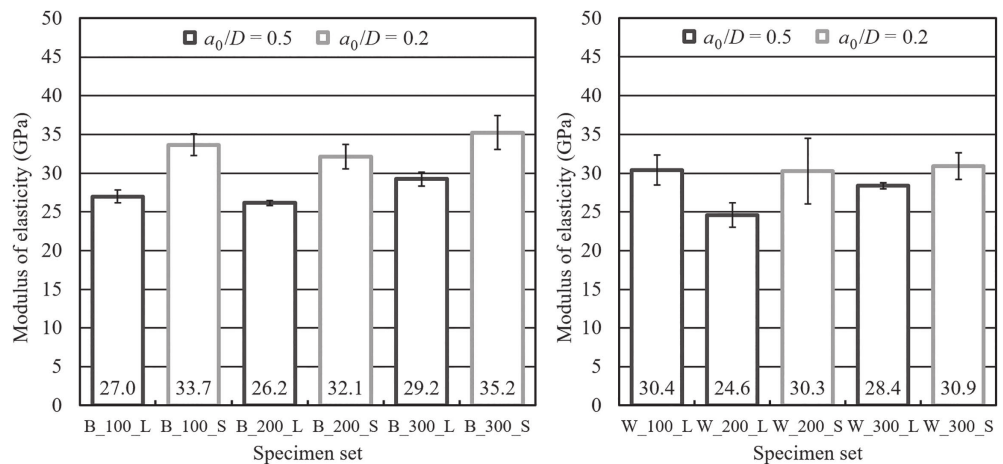
Property	Concrete age (days)			
	4	24	42	97
Compressive strength $f_c$ (MPa)	—	43.8 (3.7)	—	53.8 (1.3)
Splitting tensile strength $f_{st}$ (MPa)	—	3.04 (0.6)	—	3.24 (19.1)
Dynamic modulus of elasticity $E_{DYN}$ (GPa)	31.8 (1.1)	36.9 (1.1)	37.8 (1.2)	37.8 (1.3)
Static modulus of elasticity $E_{C,S}$ (GPa)	—	—	—	30.6 (1.2)

Abbreviation: CoV, coefficients of variation.

**TABLE 2** Values of static modulus of elasticity for specimens tested in three-point bending (left) and wedge splitting (right) configurations

Specimen	Static modulus of elasticity $E_B$		Specimen	Static modulus of elasticity $E_W$	
	Values (GPa)	Mean (CoV in %)		Values (GPa)	Mean (CoV in %)
B_100_L	26.6	27.0 (3.0)	W_100_L	28.9	30.4 (6.3)
	27.9			28.4	
	26.5			32.9	
B_100_S	32.9	33.7 (4.2)	W_200_L	29.2	24.6 (6.4)
	35.3			26.3	
	32.8			23.2	
B_200_L	25.8	26.2 (1.2)	W_200_S	26.4	30.3 (14.0)
	26.5			34.8	
	26.2			29.7	
B_200_S	31.4	32.1 (4.8)	W_300_L	28.0	28.4 (1.4)
	33.9			28.8	
	31.1			28.3	
B_300_L	28.2	29.2 (3.1)	W_300_S	32.9	30.9 (5.6)
	29.9			29.7	
	29.6			30.2	
B_300_S	37.6	35.2 (6.2)			
	33.4				
	34.7				

Abbreviation: CoV, coefficients of variation.

**FIGURE 9** Modulus of elasticity for specimens tested in three-point bending (left) and wedge-splitting (right) configurations calculated from the recorded force versus displacement diagrams

The highest variabilities of experimentally determined mechanical parameters were 19.1% for splitting tensile strength obtained at 94 days and 14.0% in the case of modulus of elasticity obtained from W\_200\_S specimens. These values are below the values commonly recommended for reliability calculations, see for example, JCSS Probabilistic Model Code<sup>31</sup> where recommended CoV for tensile strength is up to 30% and for modulus of elasticity up to 15%.

## 4.2 | Fracture parameters

Values of work of fracture  $W_f$ , specific fracture energy  $G_f$ , and fracture toughness calculated for 3PBT specimens are summarized in Table 3 together with the mean value and CoV for each set. Values for the same parameters calculated for specimens subjected to WST are summarized in Table 4. Mean values and standard deviations are also depicted in Figure 10. Note that a number in specimen

**TABLE 3** Values of work of fracture, specific fracture energy, and fracture toughness for specimens tested in the three-point bending configuration

Specimen	Work of fracture $W_f$		Fracture energy $G_f$		Fracture toughness $K_{Ice}$	
	Values (Nm)	Mean (CoV in %)	Values (J/m <sup>2</sup> )	Mean (CoV in %)	Values (MPa·m <sup>1/2</sup> )	Mean (CoV in %)
B_100_L	1.05	0.99 (13.4)	208.6	195.6 (12.3)	1.408	1.354 (7.0)
	0.84		167.9		1.409	
	1.08		210.3		1.245	
B_100_S	1.53	1.58 (9.3)	189.1	197.2 (9.2)	1.326	1.338 (22.2)
	1.75		218.0		1.642	
	1.47		184.5		1.047	
B_200_L	1.81	2.05 (12.8)	182.0	204.5 (12.1)	1.351	1.496 (9.0)
	2.01		200.6		1.618	
	2.33		231.0		1.519	
B_200_S	3.53	3.36 (6.6)	219.5	207.8 (6.8)	1.555	1.456 (6.3)
	3.44		211.8		1.373	
	3.11		192.2		1.439	
B_300_L	3.58	3.11 (13.6)	232.1	201.9 (13.6)	1.701	1.635 (15.4)
	2.76		178.4		1.370	
	2.99		195.3		1.276	
B_300_S	5.95	5.56 (6.2)	244.7	227.9 (6.4)	1.527	1.354 (13.8)
	5.40		221.0		1.483	
	5.32		217.9		1.894	

Abbreviation: CoV, coefficients of variation.

name indicates its nominal depth while “L” and “S” stand for the deep, and shallow notch.

A quick look at the results listed in Tables 3 and 4, and Figures 10 and 11 show that the values of the fracture parameters are typically dependent on the size of the tested specimens and the initial uncracked ligament. Details will be discussed in the next section. When comparing the results of both test configurations (3PBT vs. WST) for individual specimen sizes and taking into account greater variability, positive correlations can be found, especially in the case of fracture toughness, see the last columns of Tables 3 and 4 and Figure 11. A slightly better agreement was obtained for specimens with uncracked ligaments with a depth of 100 to 160 mm (B\_200\_L, B\_200\_S, and B\_300\_L specimens). In the case of the smallest and largest specimens, the deviations are slightly larger. A similar trend can be observed for the values of work of fracture and fracture energy, but here the differences are significantly larger for outer sizes, see the left and middle columns of Tables 3 and 4 and Figure 10. The results of 3PBT are once again in a good agreement with those obtained by WST when analyzing the mean values calculated from all fracture test specimens with different sizes but the same testing

configuration. The mean fracture energy is 205.8 J/m<sup>2</sup> for 3PBT and 215.3 J/m<sup>2</sup> for WST, the mean effective fracture toughness is 1.455 MPa/m<sup>1/2</sup> for 3PBT and 1.460 MPa/m<sup>1/2</sup> for WST.

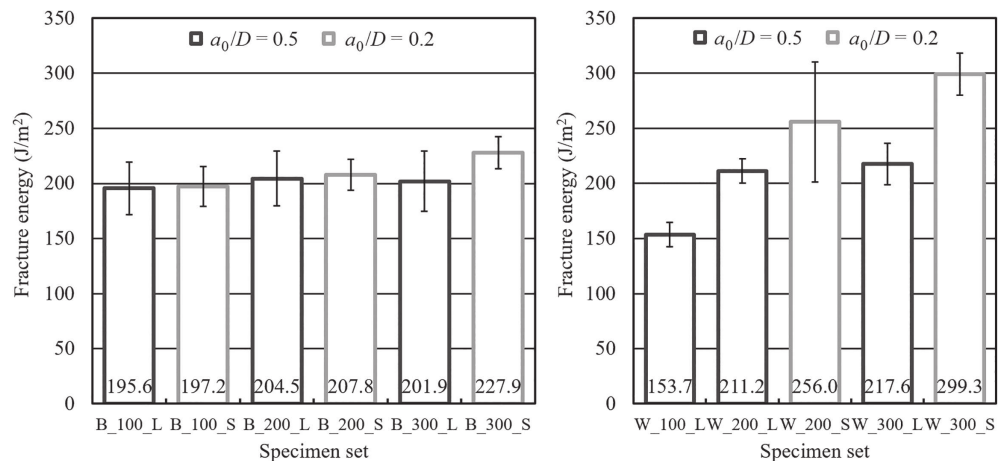
When comparing the results, it is necessary to take into account the greater variability of the obtained fracture parameters. In Figures 10 and 11, error bars are drawn for each test case corresponding to the magnitude of the *SD*. Note that for an approximately normal data set, the values within these boundaries account for about 68% of the set. The greater variability of fracture parameters compared to mechanical parameters fully corresponds to the failure mechanism in both fracture tests. In contrast to, for example, the compression test, the failure zone is localized in a narrow strip above the crack mouth (fracture process zone). The failure is then more sensitive to local weaknesses in the microstructure of the material as seen from the crack path in Figure 8. This point will also emerge in connection with higher variations in tensile strength, see the CoV of the tensile splitting strength. Our previous tests also confirmed the variability of the fracture energy in the range of 15 to 25% depending on the tested material composition.

**TABLE 4** Values of work of fracture, specific fracture energy, and unstable fracture toughness for specimens subjected to the wedge-splitting test

Specimen	Work of fracture $W_f$		Fracture energy $G_f$		Fracture toughness $K_{Ic}^{un}$	
	Values (Nm)	Mean (CoV in %)	Values ( $J/m^2$ )	Mean (CoV in %)	Values ( $MPa \cdot m^{1/2}$ )	Mean (CoV in %)
W_100_L	0.81	0.77 (6.8)	161.7	153.7 (7.2)	1.354	1.224 (7.6)
	0.80		161.0		1.260	
	0.77		154.0		1.289	
	0.80		159.7		1.128	
	0.67		132.2		1.123	
	0.77		153.8		1.188	
W_200_L	2.24	2.12 (5.0)	222.4	211.2 (5.2)	1.358	1.454 (7.0)
	2.03		200.4		1.560	
	2.10		210.7		1.443	
W_200_S	5.10	4.14 (20.7)	317.5	256.0 (21.3)	1.695	1.547 (8.3)
	3.84		236.9		1.473	
	3.47		213.7		1.472	
W_300_L	3.07	3.31 (7.6)	199.1	217.6 (8.6)	1.467	1.536 (12.1)
	3.57		236.6		1.394	
	3.30		217.0		1.747	
W_300_S	7.78	7.25 (6.5)	319.3	299.3 (6.3)	1.883	1.778 (5.1)
	7.12		296.8		1.727	
	6.86		281.7		1.725	

Abbreviation: CoV, coefficients of variation.

**FIGURE 10** Specific fracture energy for specimens tested in three-point bending (left) and wedge-splitting (right) configurations



### 4.3 | Size-dependency of parameters

In this section, a dependence of studied mechanical fracture parameters on the specimen size and the depth of the initial uncracked ligament is analyzed. Figure 12 depicts obtained values of modulus of elasticity (top left), fracture energy (top right), and fracture toughness (bottom), all plotted against the depth of the initial

uncracked ligament. Note that the B\_300\_L specimens have slightly smaller ligament depth (150 mm) than the B\_200\_S specimens (160 mm), even if the specimen itself is bigger. Figure 12 left confirms the size-independency of the modulus of elasticity (see also the linear regression for both test configurations). There is some natural variation in the values but, in general, any testing case can be used to test the modulus of elasticity. This statement can

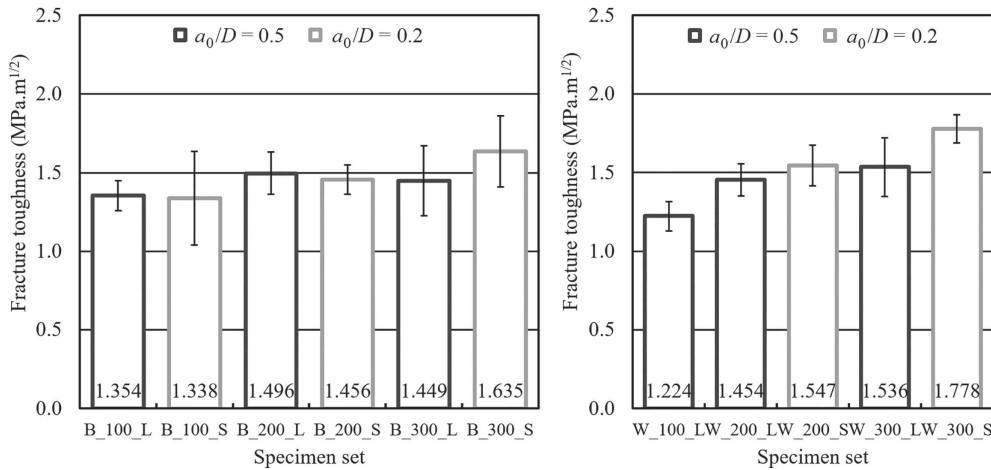


**FIGURE 11** Fracture toughness for specimens tested in three-point bending (left) and wedge-splitting (right) configurations

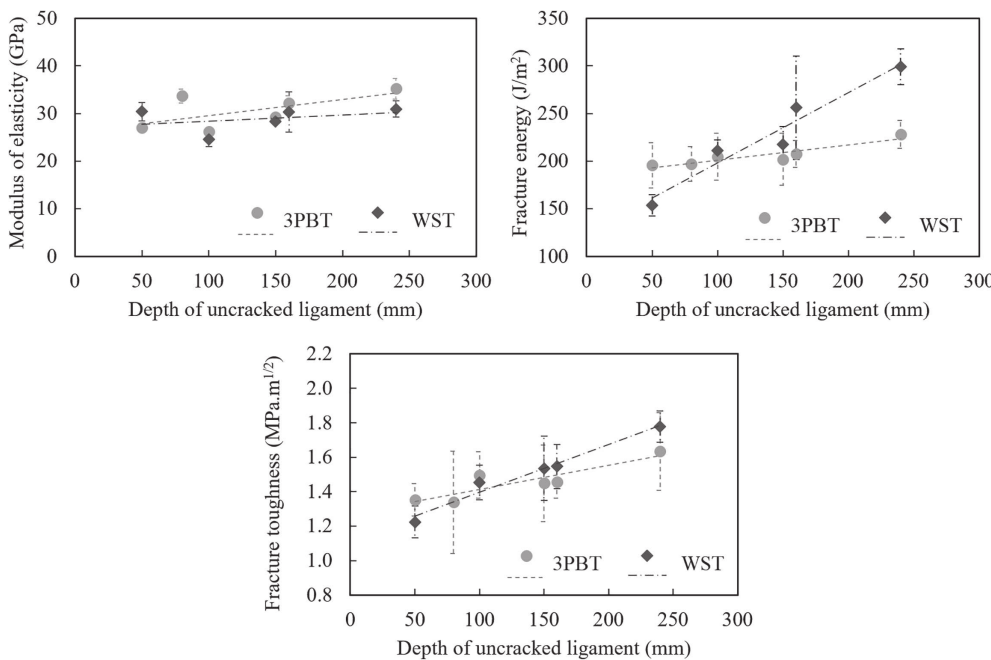


**FIGURE 12** Values of mechanical fracture parameters depending on the depth of the initial uncracked ligament

also be supported by the comparison of statistics determined for all specimens from the given test configuration, as mentioned in Section 4.1.

Results presented in Tables 3 and 4 and Figures 10 and 11 confirm the dependence of fracture parameters on the specimen size, more specifically on the area of the initial uncracked ligament. Although we take into account the relatively large variability of fracture parameters, such a trend is clearly visible in the top right corner and the bottom of Figure 12 where fracture energy and effective fracture toughness are plotted against the depth of the initial uncracked ligament. Note that the specimens B\_200\_S and B\_300\_L are different in size but due to different depths of notches have a similar depth of uncracked ligament – 160 mm for B\_200\_S and 150 mm for B\_300\_L, respectively. The size dependence is more pronounced in WST than in 3PBT. This may be due to

some testing aspects related to 3PBT described by Elices, Guinea, and Planas<sup>10–12</sup> which include various sources of energy dissipation apart from the fracture crack itself. Nevertheless, from a computational mechanics point of view, the true fracture energy, which is one of the crucial material parameters, needs to be determined from fracture tests.

An explanation why fracture energy, which is normalized by uncracked ligament size, is not a constant value lies in the fact that the energy required to create a crack along the crack path is influenced by the size of the fracture process zone (FPZ) which in turn is influenced by the free boundary of the test specimen. To consider the boundary effect on the propagation of FPZ, Hu and Wittman<sup>9</sup> assumed a bilinear fracture energy distribution to explain the ligament effect on the fracture energy of concrete, see the blue line in Figure 13. This bilinear

function consists of a horizontal line with the value of the size-independent fracture energy and a descending branch that reduces to zero at the back surface of the specimen. The transition from  $G_F$  to the rapid decrease occurs at the transition ligament length  $a_l$ , which is given by the intersection of these two lines and it depends on the material properties and specimen size and shape.<sup>32</sup> The measured RILEM fracture energy,  $G_f$ , represents the average of the local fracture energy function over the ligament area (red line in Figure 13).

Based on the bilinear approximation, the size-independent specific fracture energy  $G_F$  can be back-calculated from the measured specific fracture energy  $G_f$  from<sup>33</sup>:

$$G_f\left(\frac{a_0}{D}\right) = \begin{cases} G_F \left(1 - \frac{1}{2} \frac{\frac{a_l}{D}}{1 - \frac{a_0}{D}}\right) & 1 - \frac{a_0}{D} > \frac{a_l}{D} \\ G_F \frac{1}{2} \frac{\left(1 - \frac{a_0}{D}\right)}{\frac{a_l}{D}} & 1 - \frac{a_0}{D} \leq \frac{a_l}{D} \end{cases} \quad (12)$$

The assessment of true fracture energy was performed individually for all specimen sizes where two different depths of notches were available, that is, for all test configurations except WST specimens with a depth of 100 mm. Since two well-separated notches were cut into specimens of each size and test configuration, a well-defined system of Equations (12) has been obtained and solved. Resulting values of true fracture energy  $G_F$  are summarized in Table 5 and Figure 14 for all tested cases. Note that with respect to variability (see error bars in Figure 14 which are of a magnitude of the average standard deviation) the results are quite comparable between various specimen sizes. This is with the exception of the largest WST specimen (the last value in Table 5). Analysis of the test records for the largest WST specimens with shallow notches showed some level of instability in the softening branch of the loading diagram. Although the problematic part of the record has been removed and the missing part of the

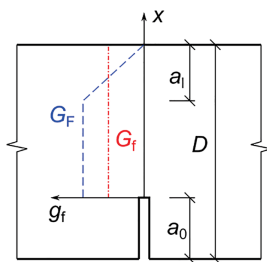


**FIGURE 13** The local fracture energy model of Hu and Wittmann

diagram has been approximated by a polynomial of the third degree, the resulting values of fracture energies may be overestimated. Therefore, the value of size-independent fracture energy calculated from the largest WST specimens was omitted when calculating the average from individual sizes. This average value is 222 J/m<sup>2</sup> and can be considered as the representative size-independent fracture energy of the tested concrete, see the dashed line in Figure 14.

The size-independent asymptotic fracture toughness  $K_{IC}$  and tensile strength  $f_t$  can be determined with the help of the linear boundary effect model (BEM). The effects of the average aggregate size  $G$  (considered here as  $G = G_{\max}/1.5$ , where  $G_{\max}$  is the maximum aggregate size) and the fracture statistics according to Chen et al.<sup>34</sup> and Han et al.<sup>35</sup> were considered. The tensile strength was calculated in relation to the maximum measured force  $F_{\max}$  as:

$$f_t = \frac{F_{\max}}{A_e} = F_{\max} \frac{1.5 \left(\frac{S}{B}\right) \sqrt{1 + \frac{a_e}{3G}}}{D^2 (1 - \alpha) \left(1 - \alpha + \frac{3G}{D}\right)}, \quad (13)$$

where  $A_e$  can be considered the effective area and  $a_e$  is the equivalent crack.

$$a_e = a_0 \left[ \frac{(1 - \alpha)^2 Y(\alpha)}{1.12} \right]^2. \quad (14)$$

**TABLE 5** Values of size-independent fracture energy obtained from both types of tests

Specimen depth (mm)	Fracture energy (J/m <sup>2</sup> )	
	3PBT	WST
100	204	—
200	214	239
300	229	393

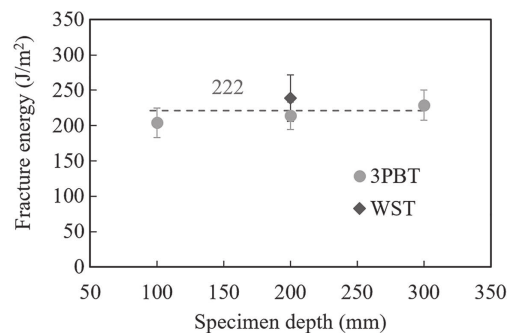


**FIGURE 14** The size-independent fracture energy as a function of specimen depth

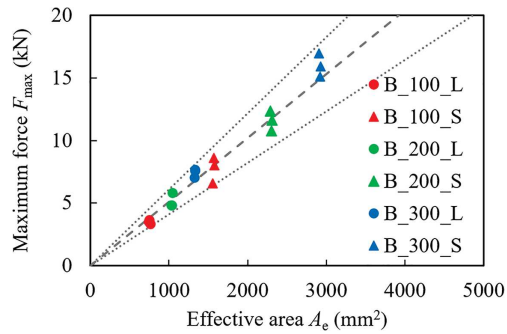


**FIGURE 15** Prediction of fracture load using linear boundary effect model (BEM) and normal distribution analysis

The asymptotic fracture toughness  $K_{Ic}$  was then determined as:

$$K_{Ic} = 2f_t \sqrt{3G}. \quad (15)$$

Reflecting the fact that scatters are inherent properties of heterogeneous materials, it was assumed that the fracture loads  $F_{max}$  and the tensile strength  $f_t$  determined from  $F_{max}$  follow the normal distribution. First, all 3PBT specimens were grouped together and the mean  $\mu$  and standard deviation  $\sigma$  of  $F_{max}$  were evaluated. BEM in conjunction with normal distribution analysis yields the following statistics for the abovementioned parameters:

- the tensile strength  $f_t$ :  $\mu = 5.1$  MPa and  $\sigma = 0.5$  MPa;
- the fracture toughness  $K_{Ic}$ :  $\mu = 1.827$  MPa  $\cdot$  m<sup>1/2</sup> and  $\sigma = 0.177$  MPa  $\cdot$  m<sup>1/2</sup>.

Using these values, inverted Equation (13) predicted the three linear relations for  $F_{max}$ , i.e., the mean, upper and lower bounds with 95% reliability; see the dashed and dotted lines in Figure 15. Note that the slope of the mean curve is the tensile strength. Figure 15 also depicts experimental data from the individual sets of specimens differing in initial notch size and depth.

## 5 | CONCLUSIONS

The paper describes the process and summarizes the main results and the data trends of the extensive experimental program, which was designed and performed to support the development of a comprehensive multilevel approach for the experimental–computational determination of the mechanical fracture parameters of concrete. The setup of the experimental program includes the following aspects:

- Three-point bending and wedge-splitting tests performed simultaneously using three different geometrically similar specimen sizes and two well-separated depths of initial notches.
- Comparable loading rates for all fracture tests in both test configurations.
- Low scatter experiments using specimens that were cast from the same batch of one concrete, with identical curing, virtually the same age of all specimens at the time of main tests, and all fracture tests performed using the same testing machine.
- Complete characterization of the concrete used, in terms of mixture composition and mechanical parameters obtained from compressive strength tests, tensile splitting strength tests, static modulus of elasticity tests, and dynamic modulus of elasticity tests.
- Virtually complete post-peak softening diagrams, with strength reduction by at least 98% of its peak.
- Supporting data from a 2D laser profilometer and two high-frequency cameras for the analyses of the cracked surfaces and development of the fracture process zones.

The obtained results confirmed the good design of the concrete mixture. Both the mean values and variabilities of mechanical fracture parameters are in good agreement with the code recommendations. Obtained variabilities are supposed to be mostly related to natural material uncertainties, and less to the scatter of the testing process. The results of the fracture tests confirmed the dependence of measured fracture energy on the specimen size since its value is influenced by the size of the fracture process zone, which in turn is influenced by the free boundary of the test specimen. That is why specimens of multiple sizes with two well-separated depth of notches were tested and size-independent fracture energy was back-calculated from the measured average energy.

The obtained experimental data will serve as a cornerstone for the development and calibration of size-independent numerical models at the macro- and meso-level and identification of material parameters including the tensile softening model using soft computing-based inverse analysis. The size-effects and dependencies on the tensile softening model will be studied. Since the observed size effect of the fracture energy seems to be attributed to the different shape of FPZ according to the specimen size and geometry, further study is needed to identify the mechanism of the process zone. For this purpose, the 3D topography of cracked surfaces obtained by scanning with a 2D laser profilometer will be studied and the correlation with the strain fields obtained in the fracture test using high-frequency cameras will be analyzed.

## ACKNOWLEDGMENT

This work has been supported by projects MUFRA S No. 19-09491S awarded by the Czech Science Foundation (GACR). We also address special thanks to M. Friedl, Z. Keršner, M. Lipowczan, P. Miarka, D. Novák, L. Novák, J. Sobek, and M. Vyhliđal from the Brno University of Technology for their support in preparing and conducting the experiments.

## DATA AVAILABILITY STATEMENT

Data available on request from the authors.

## ORCID

David Lehký  <https://orcid.org/0000-0001-8176-4114>

## REFERENCES

- RILEM TC – 50 FMC (Recommendation). Determination of the fracture energy of mortar and concrete by means of three-point bend tests on notched beams. *Mater Struct.* 1985;18(4): 287–290.
- Abdalla HM, Karihaloo BL. Determination of size-independent specific fracture energy of concrete from three-point bend and wedge splitting tests. *Mag Concr Res.* 2003;55:133–141.
- Bažant ZP. Analysis of work-of-fracture method for measuring fracture energy of concrete. *J Mater Civ Eng.* 1996;122:138–144.
- Bažant ZP, Kazemi MT. Size dependence of concrete fracture energy determined by RILEM work-of- fracture method. *Int J Fract.* 1991;51:121–138.
- Carpinteri A, Chiaia B. Size effects on concrete fracture energy: Dimensional transition from order to disorder. *Mater Struct.* 1996;29:259–266.
- Hu XZ, Wittmann FH. Fracture energy and fracture process zone. *Mater Struct.* 1992;25:319–326.
- Hu X, Duan K. Mechanism behind the size effect phenomenon. *J Eng Mech.* 2010;136(1):60–68.
- Nallathambi P, Karihaloo BL, Heaton BS. Various size effect in fracture of concrete. *Cem Concr Compos.* 1985;15:117–126.
- Hu X, Wittmann FH. Size effect on toughness induced by crack close to free surface. *Eng Fract Mech.* 2000;65:209–221.
- Elices M, Guinea GV, Planas J. Measurement of the fracture energy using three-point bend tests: Part 3—Influence of cutting the P-d tail. *Mater Struct.* 1992;25:137–163.
- Guinea GV, Planas J, Elices M. Measurement of the fracture energy using three-point bend tests: Part 1—Influence of experimental procedures. *Mater Struct.* 1992;25:212–218.
- Planas J, Elices M, Guinea GV. Measurement of the fracture energy using three-point bend tests: Part 2—Influence of bulk energy dissipation. *Mater Struct.* 1992;25:305–312.
- Karihaloo BL, Abdalla HM, Imjai T. A simple method for determining the true specific fracture energy of concrete. *Mag Concr Res.* 2003;55(5):471–481.
- Cifuentes H, Alcalde M, Medina F. Measuring the size-independent fracture energy of concrete. *Strain.* 2013;49:54–59.
- Bažant ZP, Oh BH. Crack band theory for fracture of concrete. *Mater Struct.* 1983;16:155–177.
- Hillerborg A, Modéer M, Petersson PE. Analysis of crack formation and crack growth in concrete by means of fracture mechanics and finite elements. *Cem Concr Res.* 1976;6:773–782.
- Hoover CG, Bažant ZP, Vorel J, Wendner R, Hubler MH. Comprehensive concrete fracture tests: Description and results. *Eng Fract Mech.* 2013;114:92–103.
- ČSN EN 12390–3 (2009). Testing hardened concrete – Part 3: Compressive strength of test specimens. Prague: ÚNMZ.
- ČSN EN 12390–6 (2010). Testing hardened concrete – Part 6: Tensile splitting strength of test specimens. Prague: ÚNMZ.
- Kocáb, D., Žitt, P., Daněk, P., Čaněk, M., Alexa, M., Hanuš, P. (2019). The influence of specimen size on the dynamic properties of lightweight concrete determined by the resonance method. *IOP Conf Ser: Mater Sci Eng* 583 (1), art. no. 012028.
- ČSN 73 1372 (2012). Non-destructive testing of concrete – Testing of concrete by resonance method. Prague: ÚNMZ.
- ČSN EN 12390–13 (2013). Testing hardened concrete – Part 13: Determination of secant modulus of elasticity in compression. Prague: ÚNMZ.
- Stibor, M. (2004). *Fracture Parameters of Quasi-Brittle Materials and Their Determination*, dissertation thesis. Brno University of Technology, Brno, in Czech.
- Karihaloo BL. *Fracture Mechanics and Structural Concrete*. Harlow, Essex, England: Longman Scientific & Technical, 1995.
- Kumar S, Barrai SV. *Concrete fracture models and applications*. Berlin: Springer, 2011.
- Vesely V, Frantik P, Sobek J, Malikova L, Seitl S. Multi-parameter crack tip stress state description for evaluation of nonlinear zone width in silicate composite specimens in component splitting/bending test geometry. *Fatigue Fract Eng Mater Struct.* 2014;38:1–15. <https://doi.org/10.1111/ffe.12170>.
- Tschegg EK. New equipment for fracture tests on concrete. *Materialprüfung/Mater Test.* 1991;33:338–343.
- Frantik, P., Mašek, J. (2015). GTDiPS software. <http://gtdips.kitnarf.cz/>
- Xu S, Reinhardt HW. Determination of double-K criterion for crack propagation in quasibrittle fracture, part III: Compact tension specimens and wedge splitting specimens. *Int J Fract.* 1999;98(2):179–193.
- EN 1992-1-1 (2004). Eurocode 2: Design of concrete structures - Part 1–1: General rules and rules for buildings. Brussels: CEN.
- JCSS (2002). Joint Committee on Structural Safety – Probabilistic Model Code. <https://www.jcss-lc.org/jcss-probabilistic-model-code/>.
- Hu XZ. Influence of fracture process zone height on fracture energy of concrete. *Cem Concr Res.* 2004;34:1321–1330.
- Duan K, Hu X, Wittman FH. Boundary effect on concrete fracture and non-constant fracture energy distribution. *Eng Fract Mech.* 2003;70:2257–2268.
- Chen Y, Han XG, Hu XZ, Zhu W. Statistics-assisted fracture modelling of small un-notched and large notched sandstone specimens with specimen-size/grain-size ratio from 30 to 900. *Eng Fract Mech.* 2020;235:107134.

35. Han XG, Chen Y, Hu XZ, Liu W, Li QB, Chen SG. Granite strength and toughness from small notched three-point- bend specimens of geometry dissimilarity. *Eng Fract Mech.* 2019; 216:106482.

## AUTHOR BIOGRAPHIES



**David Lehký**, Brno University of Technology, Faculty of Civil Engineering, Brno, Czech Republic. Email: lehky.d@fce.vutbr.cz



**Barbara Kucharczyková**, Brno University of Technology, Faculty of Civil Engineering, Brno, Czech Republic. Email: barbara.kucharczykova@vutbr.cz



**Hana Šimonová**, Brno University of Technology, Faculty of Civil Engineering, Brno, Czech Republic. Email: simonova.h@vutbr.cz



**Petr Daněk**, Brno University of Technology, Faculty of Civil Engineering, Brno, Czech Republic. Email: petr.danek@vutbr.cz

**How to cite this article:** Lehký D, Kucharczyková B, Šimonová H, Daněk P. Comprehensive fracture tests of concrete for the determination of mechanical fracture parameters. *Structural Concrete.* 2022;23:505–520. <https://doi.org/10.1002/suco.202000496>

## **II.4 MECHANICAL FRACTURE PARAMETERS AS INPUTS OF MATERIALS MODELS FOR NUMERICAL MODELLING OF FRACTURE RESPONSE**

For the effective and correct use of a numerical (material) model, it is necessary to tune its parameters using data obtained from experimental measurements. The correct evaluation of such data is becoming a prerequisite for the correct use of numerical models in practice.

Mechanical fracture parameters can be primarily obtained through the direct evaluation of mechanical and fracture tests. The second option is to obtain mechanical fracture parameters indirectly – based on a combination of fracture testing and inverse analysis.

The articles listed below present the example of using experimentally obtained data as input values for verification of numerical simulations of fracture response of selected fine-grained composites.

### **II.4.1**

Lehký, D., Lipowczan, M., Šimonová, H., Keršner, Z. 2021. A hybrid artificial neural network-based identification system for fine-grained composites. *Computers and Concrete*. 2021, Vol. 28, Iss. 4, pp. 369–378, doi: <https://doi.org/10.12989/cac.2021.28.4.369> (Q2–Engineering, civil; 1 citation without self-citations of all authors according to WoS)

#### *II.4.1 Description*

The paper describes a method for the identification of selected parameters of mortars and other fine-grained brittle matrix composites using a hybrid artificial neural network-based identification system. The cornerstone of the method is the use of an artificial neural network, which is utilized as a surrogate model of the inverse link between the measured specimen response parameters and the sought material parameters. The ability of the proposed system to identify mechanical fracture parameters of fine-grained brittle matrix composites with variable response while maintaining sufficient accuracy has been confirmed. The resulting numerical obtained  $F-d$  diagrams by FEM analysis with material inputs based on identified parameters were compared with diagrams acquired from experiments. Good agreement was achieved between the numerically and experimentally obtained  $F-d$  diagrams.

#### *II.4.1 Role of the author – the percentage of contribution: 25 %*

Hana Šimonová is the co-author of this article responsible for the detailed experimental data processing and evaluation of performed 3PB fracture experiments which were used as inputs for verification of the proposed method. Furthermore, she prepared the original draft of the article's parts describing the experimental part which was later reviewed in cooperation with other co-authors.

## II.4.2

Malíková, L., Šimonová, H., Kucharczyková, B. Crack deflection under mixed-mode conditions in the fine-grained composites based on water glass-activated slag. *Journal of multiscale modelling*. 2022, Vol. 13, Iss. 1, Article No. 2144004. doi: 10.1142/S1756973721440042 (WoS: 000729587700001; Q3–Mathematics, Interdisciplinary applications-ESCI (2021))

### II.4.2 *Description*

In this paper, the crack propagation under mixed-mode (I + II) conditions in a semi-circular disc under the 3PB test configuration is observed experimentally. Furthermore, FEM numerical simulations were performed to obtain the theoretical value of the initial kink angle of crack propagation via multi-parameter fracture criteria. The mutual comparison of the values of the crack deflection angles obtained numerically and experimentally was presented. The results obtained prove that utilization of the multi-parameter fracture criteria can bring more accurate results.

### II.4.2 *Role of the author – the percentage of contribution: 33 %*

Hana Šimonová is a co-author of this paper responsible for the preparation and evaluation of fracture tests of prismatic and semi-circular disc specimens made of an alkali-activated fine-grained composite. Furthermore, she prepared the original draft of the article's parts describing the material and fracture tests.

# A hybrid artificial neural network-based identification system for fine-grained composites

David Lehký\*, Martin Lipowczan<sup>a</sup>, Hana Šimonová<sup>b</sup> and Zbyněk Keršner<sup>c</sup>

Faculty of Civil Engineering, Brno University of Technology, Veveří 331/95, 602 00 Brno, Czech Republic

(Received October 1, 2020, Revised October 22, 2021, Accepted October 23, 2021)

**Abstract.** Recent interest in the development of innovative building materials has brought about the need for a detailed assessment of their mechanical fracture properties. The parameters for these need to be acquired, and one of the possible ways of doing so is to obtain them indirectly - based on a combination of fracture testing and inverse analysis. The paper describes a method for the identification of selected parameters of mortars and other fine-grained brittle matrix composites. The cornerstone of the method is the use of an artificial neural network, which is utilized as a surrogate model of the inverse relation between the measured specimen response parameters and the sought material parameters. Due to the potentially wide range of composite mixtures and hence the wide range of experimental responses likely to be gained from individual specimens, an ensemble of artificial neural networks was created. It allows the entire range of variants to be covered and provides resulting parameter values with sufficient precision. Such a system is also easy to expand if a composite with properties outside the current range is tested. The capabilities of the proposed identification system are demonstrated on two selected types of fine-grained composites with different specimen responses. The first group of specimens was made of composite based on alkali-activated slag with standardized and natural sand investigated within the time interval of 3 to 330 days of aging. The second tested composite contained alkali-activated fly ash matrix, and the effect of the addition of natural fibers on fracture response was investigated.

**Keywords:** artificial neural network; ensemble; fine-grained composites; mechanical fracture parameters; network inverse analysis; neural

## 1. Introduction

Due to the increasing worldwide emphasis on the environmental and economic sustainability of material production, much current research is focused on the development of innovative building materials. In the category of cement-based composites, attention is being given to materials with various types of added inclusions (fibers, angular glass, etc., see e.g., Stebbings *et al.* 2002, Daskiran *et al.* 2016) or materials where the standard Portland cement matrix is modified by selected additives such as polymers, redispersible powders or existing waste materials. In recent years, attention has also been given to the development of various non-traditional binders as modern alternatives to Portland cement. One wide group of these binders is that of alkali-activated materials (Provis and van Deventer 2014). In all cases, the matrix is a decisive element that determines the properties of the final composite. When studying matrix behavior, its mechanical fracture properties are determined by conducting laboratory fracture tests on small-size specimens. In many cases, attention is focused on analyzing the properties associated

with resistance to crack formation and propagation, rather than on the maximum strength of the material. Mechanical fracture parameters help us to understand the relation between the macroscopic response of the specimen and its microstructural evolution during cracking. This is crucial in the design and modeling of newly developed composites.

Mechanical fracture parameters can be primarily obtained through the direct evaluation of fracture test data via the effective crack model (Karihaloo 1995) and the work-of-fracture method recommended by RILEM (1985). The second option is to obtain mechanical fracture parameters indirectly-based on a combination of fracture testing and inverse analysis. The inverse approach has several advantages, such as its ability to identify parameters which have no physical meaning (i.e., the parameters of some material models) or parameters whose direct testing and evaluation is difficult or impossible. In this paper, the tensile strength of the composite is such a parameter. Over the last few decades, a great deal of attention has been devoted to the development of inverse methods for the determination of the parameters driving the quasi-brittle fracture behavior of coarse-grained concrete (Bui 1994, Stavroulakis 2001, Maier *et al.* 2006, Zimmermann *et al.* 2014, Zimmermann and Lehký 2015). The methods used to acquire the mechanical fracture parameters of coarse-grained concrete using experimental data from fracture tests and the artificial neural network-based (ANN) inverse analysis method was introduced in Novák and Lehký (2006). The parameters of coarse-grained composites are typically evaluated from the

\*Corresponding author, Associate Professor  
E-mail: lehky.d@fce.vutbr.cz

<sup>a</sup>Ph.D. student

<sup>b</sup>Ph.D.

<sup>c</sup>Professor

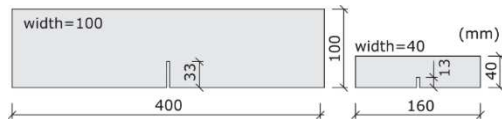


Fig. 1 Typical specimen size for coarse-grained composites (left) and fine-grained composites (right) used in a three-point bending fracture test

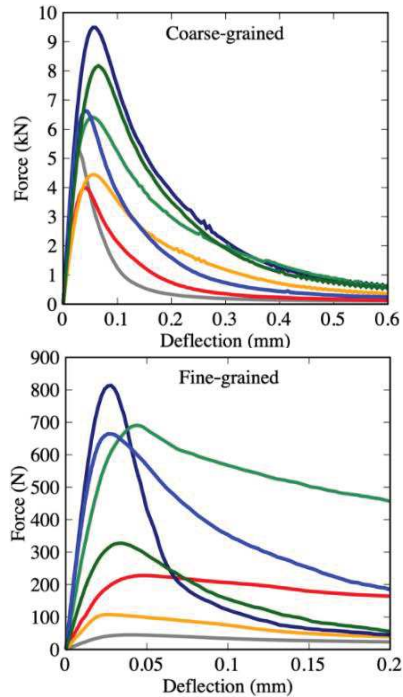


Fig. 2 A comparison of typical responses in the form of force vs. deflection diagrams for coarse-grained concretes (top) and fine-grained composites (bottom) tested via a three-point bending fracture test

response of a notched prismatic specimen with the nominal dimensions  $100 \times 100 \times 400$  mm (Fig. 1 left) tested in the three-point bending configuration. In this paper, the inverse method is utilized and extended to identifying the parameters of fine-grained brittle matrix composites. Their properties are typically determined from smaller test specimens with the nominal dimensions  $40 \times 40 \times 160$  mm (Fig. 1 right).

As mentioned above, fine-grained materials may have various compositions and contain different inclusions, which result in very diverse responses during fracture tests. Fig. 2 depicts selected responses in the form of force vs. midspan deflection diagrams which were obtained in our laboratories when testing coarse-grained concretes (Fig. 2 top) and fine-grained brittle-matrix composites (Fig. 2 bottom). Such findings led us to the decision to create a robust and extensible hybrid identification system that is applicable to a wide range of materials. This needs to deal with diversity prompted the implementation of an ensemble of neural networks within the system. The activation of a particular ANN is controlled by the response of the studied material.

The method employed for parameter identification, which combines nonlinear simulations with the stratified

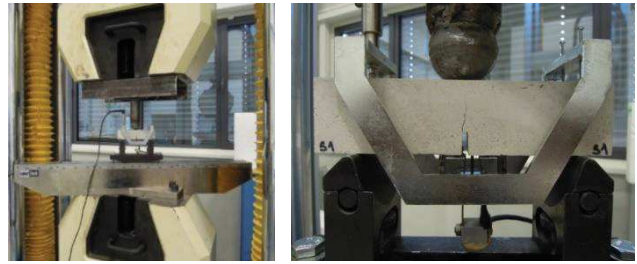


Fig. 3 Fracture test configuration, including the auxiliary frame and the sensors for measuring the midspan deflection and the crack mouth opening displacement (left), an example of crack propagation during the test (right)

sampling training of an artificial neural network, is relatively time-consuming, of high complexity, and requires some knowledge of soft computing methods (Novák and Lehký 2006). Therefore, the whole procedure has been implemented in the FraMePID-3PB software tool (Lehký *et al.* 2014) for standard coarse-grained concrete. The existing identification system has now been expanded to allow the identification of parameters for mortars and other fine-grained brittle matrix composites.

## 2. Identification of mechanical fracture parameters

### 2.1 Laboratory experiments

Mechanical fracture parameters are usually determined based on the direct evaluation of fracture test records in suitable configurations (three-point bending, wedge splitting, etc.). In this case, based on the long-term experience of the authors as well as the relative simplicity and availability of the testing equipment, three-point bending (3PB) tests were conducted on standard prismatic specimens with a central edge notch. The standard specimens used to determine the material characteristics of mortars and fine-grained composites are typically of the above-mentioned nominal size of  $40 \times 40 \times 160$  mm. The specimens intended for fracture tests were provided with an initial stress concentrator. In the center of the prism a notch was cut to a depth of about  $1/3$  of the specimen depth using a diamond blade saw. The load span was set to 120 mm.

In order to perform a stable fracture test and also to record the post-peak behavior during the test, the testing machine is required to be stiff enough compared to the stiffness of the tested specimen. Loading during the fracture test is performed at an approximately constant controlled displacement rate, which is chosen so that the maximum force is reached within a few minutes after the start of the test, and which is slow enough to record the post-peak behavior. In the case of the fracture test for fine-grained composites described in the applications section (Section 3) of this paper, the constant increment of displacement was set to  $0.02$  mm/min. The fracture tests were conducted using a Lab Test 6.250 stiff multi-purpose mechanical testing machine with a load range of  $0$ - $250$  kN. The deflection of the center of the prism and the corresponding force was recorded until the prism was completely

separated into two halves. The deflection was measured using an inductive sensor mounted in a special measurement frame placed on the specimen (see Fig. 3).

The outcome of each test is a force-deflection diagram ( $F-d$  diagram), which is subsequently used for mechanical fracture parameter determination. An example of a 3PB fracture test configuration is shown in Fig. 3.

## 2.2 Artificial neural network-based inverse analysis

The concept of inverse analysis is based on the transition from the measured response to the sought parameters. In this method, the test is simulated via Finite Element Modeling (FEM), and the results of the simulation are compared to those measured during the experiment using an error function. This function quantifies the difference between the computed and measured data; in a subsequent phase it is minimized with respect to the sought parameters via a suitable optimization technique. Novák and Lehký (2006) proposed an ANN-based inverse method in which fracture test response data are directly transformed into the desired mechanical fracture parameters:  $\mathbf{R} \rightarrow \mathbf{P}$ . The ANN is used here as a surrogate model of an unknown inverse function between the input mechanical fracture parameters and the corresponding response parameters

$$\mathbf{P} = f^{-1}(\mathbf{R}) = f_{\text{ANN}}(\mathbf{R}) \quad (1)$$

ANNs are mathematical models inspired by biological neuron systems (see e.g., Cichocki and Unbehauen 1993). An ANN is a signal processing system composed of a large number of simple processing elements, called artificial neurons. These are interconnected by direct links and cooperate to perform parallel distributed processing in order to solve a desired computational task. One of the attractive features of ANNs is their ability to adapt themselves to special conditions by changing their connection strengths or structure. In our case a feed-forward multi-layer network type was used. In this type of network, artificial neurons are organized into different layers and the information only moves in the forward direction: data leaves the input nodes and passes through hidden nodes (if any) to the output nodes. If the output of the whole ANN is required, the outputs of all previous layers must be calculated layer by layer starting from the input layer. The output of the  $k$ th neuron in the  $u$ th layer of the network is

$$y_k^u = f^u \left( \sum_{j=1}^J (w_{kj}^u y_j^{u-1}) + b_k^u \right) = f^u \sum_{j=1}^J x_j^u \quad (2)$$

where  $w_{kj}^u$  is the synaptic weight of the connection between the  $k$ th neuron in the  $u$ th layer (current) and the  $j$ th neuron in the  $(u-1)$ th layer (previous),  $y_j^{u-1}$  is the output of the  $j$ th neuron in the previous layer,  $b_k^u$  is the bias of the  $k$ th neuron in the current layer, and  $f^u$  is the transfer function of the current layer. If the current layer  $u$  is the last one, then the vector  $y^u$  is the output vector  $\mathbf{P}$  of the ANN which contains the set of sought material parameters.

Outside its structure and the types of utilized transfer functions, the behavior of an ANN is determined by the values of synaptic weights and biases. These parameters are

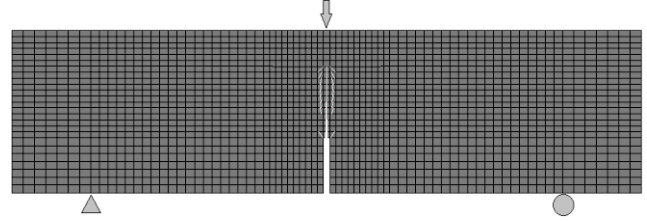


Fig. 4 FEM model of the three-point bending test adapted for numerical simulations, including damage distribution at peak force

adjusted during the training process, where a set of example pairs of inputs and corresponding outputs  $(r, p), r \in \mathbf{R}, p \in \mathbf{P}$  is introduced to the network. The aim of the subsequent optimization procedure is to find a neural network function  $f_{\text{ANN}}: \mathbf{R} \rightarrow \mathbf{P}$  in the allowed class of functions that matches the examples. This is performed by minimizing the following error function

$$E_r = \frac{1}{2} \sum_{i=1}^N \sum_{k=1}^K (p_{ik}^o - p_{ik}^t)^2, \quad (3)$$

where  $N$  defines the size of the training set,  $K$  defines the number of output neurons,  $p_{ik}^t$  is the desired (target) output of the  $k$ th output neuron for the  $i$ th input signal and  $p_{ik}^o$  is the real output of the same neuron for the same input signal, which depends on the current network parameters. ANN training is an optimization task which can be solved via an appropriate minimization method. Genetic algorithms were combined with gradient descent methods for the purpose of training all the ANNs mentioned later in this paper.

At the end of the identification process, the trained ANN is used to transfer the input data—a measured response in the form of an  $F-d$  diagram obtained from the fracture test - to the desired material parameters. The following three fundamental parameters of fine-grained brittle matrix composites are subject to identification: modulus of elasticity  $E$ , tensile strength  $f_t$ , and specific fracture energy  $G_F$ . At the same time, the intrinsic brittleness called characteristic length  $l_{ch}$  can immediately be determined using the identified parameters as  $l_{ch} = E \cdot G_F / f_t^2$ . This parameter can be used to estimate the size of the fracture process zone (Karihaloo 1995). Other parameters, e.g., compressive strength, were omitted from identification based on sensitivity analysis.

The set for training the ANN was prepared numerically using an FEM model (Fig. 4), which simulated a three-point bending test with random realizations of material parameters. Note that the searched material parameters were considered as statistically independent when creating the training set in order to achieve the best coverage of the design space and to make the ANN surrogate model as general as possible. Conveniently, it was possible to employ the ATENA FEM program (Červenka *et al.* 2016) for the numerical simulation of the fracture test. The 3D Nonlinear Cementitious 2 material model was selected to govern the gradual evolution of localized damage. The tensile behavior was governed by the Rankine-type criterion with exponential softening as described by Hordijk (1991), while

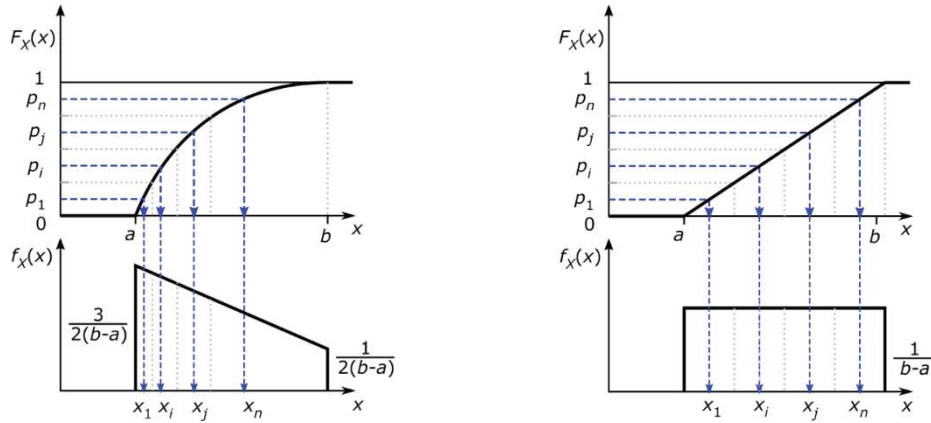


Fig. 5 Generating random samples from the descending trapezoidal probability distribution (left), and the rectangular distribution (right)

the Menétrey-Willam (1995) yield surface with hardening and softening phases was used for the behavior in compression. The fracture model employs the orthotropic smeared crack formulation and the rotational crack model with the mesh-adjusted softening modulus both in tension and compression. This model is defined on the basis of characteristic element dimensions in tension and compression to ensure objectivity in the strain-softening regime. Further details are available in (Červenka *et al.* 2016). The analysis is performed under plane stress conditions. Four-node iso-parametric quadrilateral elements were used for finite element discretization. Fig. 4 shows the finite element mesh adopted in this analysis. Nonlinear solution was performed using the Newton-Raphson iterative method.

Random realizations of material parameters  $\mathbf{P}$  are generated with the help of the stratified Latin hypercube sampling simulation method (McKay *et al.* 1979, Novák *et al.* 2014) and by performing the inverse transformation of the distribution function in order to reflect the probability distribution of the parameter. As shown by Lehký and Šomodíková (2017), the use of an ANN as a surrogate model can be very computationally efficient, especially in combination with the stratified sampling method. Uniform distribution was used for the modulus of elasticity and tensile strength, while a descending trapezoidal distribution was selected for the specific fracture energy in order to generate more samples with lower values (Fig. 5). This improves the accuracy of inverse analysis for composite mixtures with lower fracture energy values. The probability density and cumulative distribution functions of the descending trapezoidal distribution are

$$f_X(x) = \frac{3b - a - 2x}{2(b - a)^2}, \quad (4)$$

$$F_X(x) = \frac{(3b - a)(x - a) - x^2 + a^2}{2(b - a)^2}, \quad (5)$$

while the probability density and cumulative distribution functions of the rectangular distribution are

$$f_X(x) = \frac{1}{b - a} \quad (6)$$

$$F_X(x) = \frac{x - a}{b - a}. \quad (7)$$

All four functions are valid for  $a \leq x \leq b$ , where  $a$  and  $b$  are the lower and upper limits of the fracture energy, respectively, see Fig. 5.

The random responses from the computational model  $\mathbf{R}$  and the corresponding random realizations of parameters  $\mathbf{P}$  serve as input-output elements for the ANN training set. After training, the ANN is ready to solve the main task, which is to provide the best material parameters in order for the numerical simulation to achieve the best agreement with the experiment. This is performed by simulating a network using the measured responses as an input. This results in a set of identified material parameters. As is clear from the procedure, optimization is not performed on the searched parameters, but the ANN parameters are optimized during the training process. The trained ANN is then used in a closed form without any need for further optimization. This is particularly useful for the software implementation of the method, as it can be used as a black box without any necessary knowledge of soft computing and optimization methods.

### 2.3 A hybrid artificial neural network system

Due to the potentially wide range of fine-grained brittle matrix composite mixtures and hence the wide range of experimental responses that may be obtained from individual specimens, the decision was made to create a set of artificial neural networks that would cover the entire range of variants and provide resulting parameter values with sufficient precision. Such a construct, which is made up of many neural networks that are jointly used to solve a particular task, is called a neural network ensemble (NNE, Zhou *et al.* 2002). The fundamental mathematical idea of an NNE rationally originates from the weak law of large numbers in probability (Durrett 2010). According to the law, the average of the results obtained from a large number of trials should be close to the expected value and will tend to become closer as more trials are performed. From the practical point of view and with a view to minimizing computational effort, this theory is combined with the

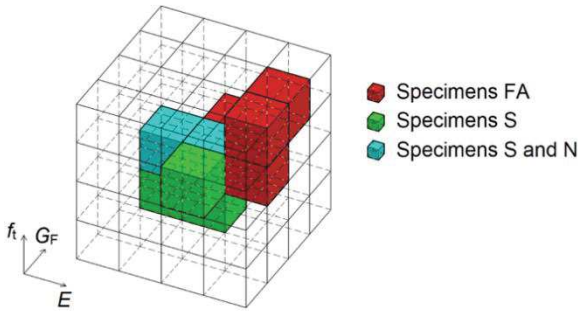


Fig. 6 Neural network ensemble-based identification system with examples of active subspaces

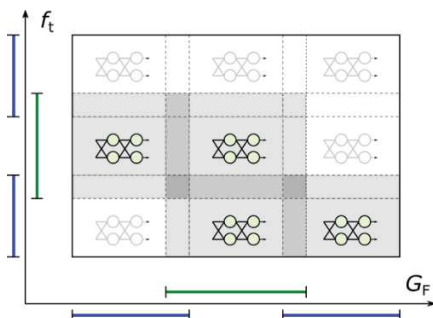


Fig. 7 Neural network ensemble-based identification system with examples of activated ANNs displayed in a two-dimensional view

mathematical optimization concept that many can be better than all (Zhou *et al.* 2002). We propose a hybrid identification system in which the robust ANNs are used both individually and as an NNE depending on the test response of the analysed specimen. Such a system automatically selects the best strategy in order to provide the most accurate results for a wide range of specimen responses while maintaining reasonable computational demands.

A three-dimensional space defined by three mechanical fracture parameters-modulus of elasticity  $E$ , tensile strength  $f_t$ , and specific fracture energy  $G_F$ -is divided into several subspaces, see Fig. 6. Every subspace contains a single robust ANN trained for a limited range of parameters. The current version of NNE can identify fine-grained composites whose parameter values fall approximately in the following ranges: the modulus of elasticity is from 0.3 to 65 GPa, tensile strength is from 0.1 to 7 MPa, and fracture energy is from 3 to 660 J/m<sup>2</sup>. However, due to its modularity, the system can be easily expanded if a composite with properties outside the current range is tested. Fig. 7 depicts an example of an identification system with activated ANNs, shown here in a two-dimensional view for clarity.

The ANNs in the individual subspaces are of the feed-forward multi-layered type and have the following structure: 3 inputs, 1 hidden layer containing 6 neurons with a nonlinear transfer function (hyperbolic tangent), and 1 output layer containing 3 neurons with a linear transfer function, see Fig. 8. Each of the output neurons correspond to one of the identified material parameters, and each of the inputs corresponds to one parameter extracted from an  $F$ - $d$

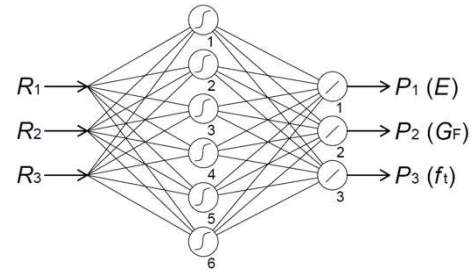


Fig. 8 Diagram of the utilized feed-forward multi-layer network

diagram. The first response parameter is the force at 0.006 mm of deflection, the second is the peak force and the third is the fracture work computed by numerical integration using the trapezoidal rule.

All subspaces use the same ANN structure as mentioned above. Different ANN structures were tested varying in the number of layers and neurons for different composites in order to maximize accuracy while reducing model complexity and thus the tendency to overfit. The selected structure represented the optimal solution for all tested composites. The reason can be found in the predetermined failure mode of the specimen given by the used three-point bending test of the beam with a central edge notch, where the crack initiates from the top of the notch and propagates towards the point where the load is applied. The change in the shape of the nonlinear response of the test specimen made of quasi-brittle material is then fully controlled by the current parameter values while maintaining the same ANN surrogate model.

To avoid network overfitting, a relatively large and diverse data set was used, in which random samples were generated using stratified sampling as described in Section 2.2. The training set samples were generated using 50 to 100 simulations. The test set was chosen as 4% of the training set based on the authors' experience. Due to the relatively narrow range of each network and the smoothness of the search space, the convergence in network training was very fast and the obtained results were stable for different randomly generated initial network parameters.

A suitable subspace for the analyzed specimen is automatically selected and the corresponding ANN is activated based on an initial analysis of the experimental response data. The set of mechanical fracture parameters is calculated by simulating the ANN with the obtained response parameters. As shown in Fig. 7, the adjacent subspaces partially overlap (the parameter value overlap is approximately 10%). Therefore, some specimens may have material parameters which are situated close to the boundaries of a subspace and thus may belong to several overlapping subspaces. In this case, the respective activated ANNs are ensembled and participate in identification together. The final set of parameters is obtained via the suitable combination of the results obtained from all the activated ANNs. It can be calculated as a simple or weighted average. The second method takes into account the fact that the accuracy of an ANN decreases with the distance from the center of its subspace. Fig. 9 depicts an example involving two overlapping subspaces: on this

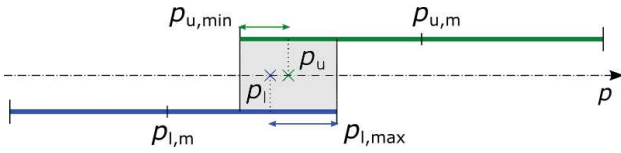


Fig. 9 The calculation of weight factors for specimens in the overlapping area of two subspaces

occasion it is for a simplified case with a single parameter  $p$ .

The final weighted value of parameter  $p$  is then calculated as

$$p = w_i p_i \quad (8)$$

with  $n=2^k$  overlapping subspaces for  $k$  parameters;  $p_i$  is the value of the parameter obtained from an ANN for the  $i$ th subspace (see  $p_l$  and  $p_u$  in Fig. 9). The weighting coefficient  $w_i$  of the  $i$ th subspace is dependent on the relative distance  $\lambda_i$  of parameter  $p_i$  from its mean point. For the lower subspace  $l$  (see Fig. 9)

$$\lambda_i = \frac{p_{l,max} - p_i}{p_{l,max} - p_{l,m}} \quad (9)$$

For the upper subspace  $u$

$$\lambda_i = \frac{p_i - p_{u,min}}{p_{u,m} - p_{u,min}} \quad (10)$$

where  $p_{u,min}$  is the minimum border of the upper subspace,  $p_{l,max}$  is the maximum border of the lower subspace, and  $p_{u,m}$  and  $p_{l,m}$  are the means of the upper and lower subspace, respectively. The weighting coefficient is then calculated as

$$w_i = \frac{\lambda_i}{\sum_{i=1}^n \lambda_i} \quad (11)$$

### 3. Testing and applications

The proposed hybrid ANN-based identification system has been tested and utilized for the inverse determination of the mechanical fracture parameters of various brittle matrix composite mixtures. Two selected applications are presented in this section.

#### 3.1 Fine-grained composites with alkali-activated slag-based matrix investigated during specimen aging

During recent decades, research into the use of various non-traditional binders as modern alternatives to Portland cement has attracted a great deal of scientific attention. As was mentioned above, one wide group of these binders is that of alkali-activated matrix-based materials (AAMs). AAMs are formed via the dissolution of a suitable aluminosilicate precursor in the presence of an alkaline activator, typically sodium hydroxide or sodium water glass. The composition and properties of the final composite strongly depend on the chemistry of both the precursor and the alkaline activator, as well as on curing

Table 1 Mean values (CoV in %) for selected mechanical fracture parameters of composite specimens in mortar sets S and N at four investigated specimen ages

Parameter	S (3 d)	S (28 d)	S (107 d)	S (330 d)
$E$ (GPa)	7.1 (3.5)	8.9 (21.0)	10.4 (4.1)	10.3 (5.7)
$G_F$ (J/m <sup>2</sup> )	46.6 (21.7)	34.0 (14.1)	51.9 (9.7)	63.8 (4.1)
$f_t$ (MPa)	1.34 (16.3)	1.48 (7.5)	1.67 (5.6)	2.04 (3.4)
$l_{ch}$ (mm)	205 (56.9)	139 (29.5)	195 (17.9)	159 (6.3)
	N (3 d)	N (28 d)	N (107 d)	N (330 d)
$E$ (GPa)	5.3 (4.6)	8.3 (5.5)	8.8 (8.0)	10.3 (3.2)
$G_F$ (J/m <sup>2</sup> )	40.7 (9.9)	47.7 (23.1)	49.6 (8.0)	65.8 (6.6)
$f_t$ (MPa)	1.71 (13.5)	1.64 (14.5)	1.69 (19.9)	2.59 (11.5)
$l_{ch}$ (mm)	76 (23.4)	163 (57.8)	165 (37.8)	104 (21.4)

conditions (Provis and van Deventer 2014).

A fine-grained composite with an alkali-activated slag (AAS) based matrix and an alternative activator was selected as a first example of application. Two sets of AAS mortars with a sand-to-binder ratio of 3:1 were selected for the purposes of the experiment. The difference between them lay in the type of sand used; the first mortar was made using standardized CEN siliceous sand and the second mortar using natural sand. The type of sand was used to distinguish between the two mortar sets: S (standard) and N (natural). Details about the individual mortar compositions, the production of specimens and curing conditions can be found in Šimonová *et al.* (2020). The fracture tests were performed at the age of 3, 28, 107 and 330 days of hardening. Three independent measurements were carried out for each composite mixture and investigated specimen age.

Table 1 summarizes the mean values (obtained from 3 independent measurements) and coefficients of variation (CoV) of selected mechanical fracture parameters of the S and N specimen sets obtained from the  $F-d$  diagrams, i.e., the statistics for the modulus of elasticity  $E$ , fracture energy  $G_F$  and tensile strength  $f_t$  obtained from identification using a neural network ensemble, as well as the characteristic length  $l_{ch}$ .

The set of activated ANNs is depicted in Fig. 6. A total of five ANNs were activated in order to identify the mechanical fracture parameters of twelve specimens from set S: see the green and green-blue subspaces in Fig. 6. Two ANNs were activated for twelve specimens from set N: see the green-blue subspaces in Fig. 6. Note that the green-blue subspaces were shared by both sets.

The modulus of elasticity values gradually increased with specimen age for both mortar sets. The fracture energy value gradually increased with specimen age for mortar set N. In the case of mortar set S, the fracture energy value decreased between the age of 3 and 28 days. After that, a gradual increase with specimen age was also monitored. In the case of mortar set S, the tensile strength value gradually increased with specimen age. The tensile strength is the same between the age of 3 and 107 days when the CoV is taken into account for mortar set N. Despite the different development of the monitored mechanical fracture parameters during hardening, the values were similar at the

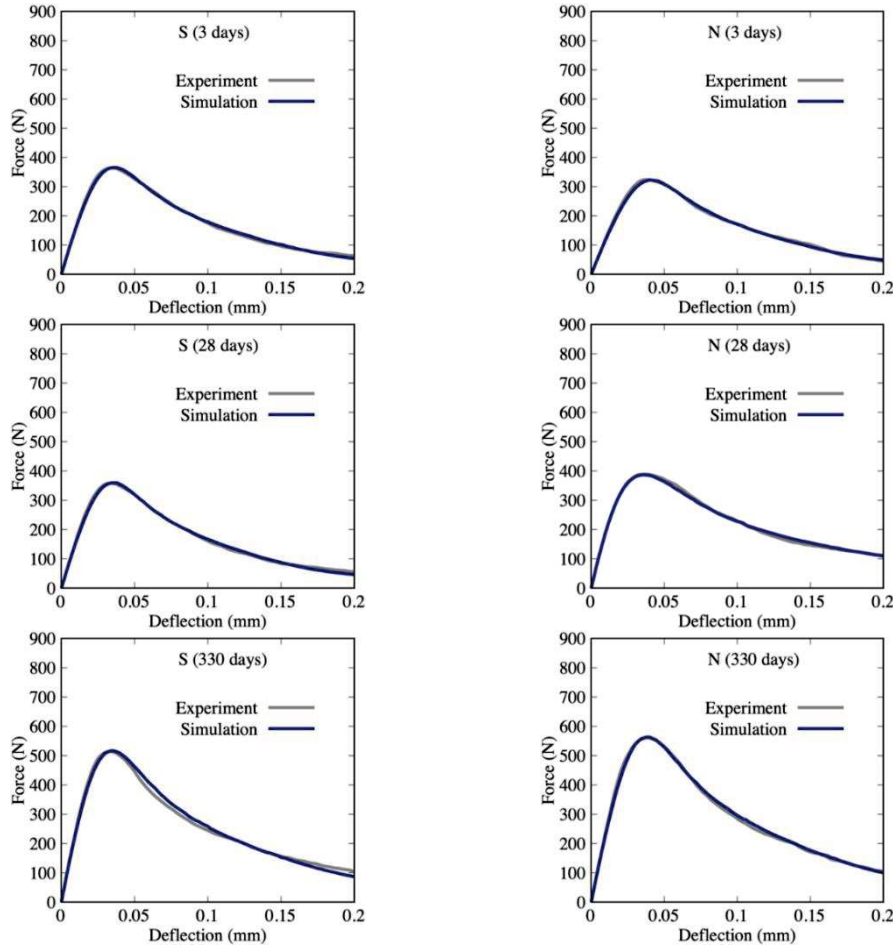


Fig. 10 Selected  $F-d$  diagrams of S (left) and N (right) composites tested at 3 (top) 28 (middle) and 330 (bottom) days of hardening: experiment vs. numerical simulation

age of 330 days for both composites. The characteristic length (intrinsic brittleness) slightly fluctuated with the age of both composites, though composite S appears to be slightly more ductile than N.

The identified parameters were verified. The obtained material parameters were used in the computational model and numerical FEM analysis was carried out. The resulting numerical  $F-d$  diagrams are compared in Fig. 10 with the experimental diagrams for selected specimens from both sets tested at various days of hardening. The numerical comparison of the agreement of the diagrams is given in Table 2 with help of the mean absolute percentage error (MAPE). It was calculated:

1. For the whole  $F-d$  diagram as

$$MAPE_{F-d} = \frac{100}{n} \sum_{i=1}^n \frac{|F_{e,i} - F_{s,i}|}{F_{e,i}}, \quad (12)$$

where  $F_{e,i}$  is the experimental response (force),  $F_{s,i}$  is the simulated response, and  $n$  is the discretization rate, here  $n = 100$  in all cases.

2. For the maximum load-bearing capacity  $F_{max}$  (the peak of the  $F-d$  diagram) as

$$MAPE_{max} = 100 \frac{|F_{e,max} - F_{s,max}|}{F_{e,max}}. \quad (13)$$

Table 2 Numerical comparison of the  $F-d$  diagrams of composites S and N

Criterion	S (3 d)	S (28 d)	S (107 d)	S (330 d)
$MAPE_{F-d}$ (%)	3.80	5.78	4.64	3.79
$MAPE_{max}$ (%)	0.68	0.39	0.46	0.29
$MAPE_W$ (%)	0.70	0.98	0.13	0.63
	N (3 d)	N (28 d)	N (107 d)	N (330 d)
$MAPE_{F-d}$ (%)	5.78	4.47	7.67	5.82
$MAPE_{max}$ (%)	0.64	0.32	0.38	0.85
$MAPE_W$ (%)	1.17	0.19	0.47	1.06

3. For the fracture work  $W$ , which is an important indicator when analyzing material fracture. It is related to the area under the  $F-d$  diagram and was calculated using the trapezoidal rule.

$$MAPE_W = 100 \frac{|W_e - W_s|}{W_e}, \quad (14)$$

$$W = \int_0^{d_n} F dd \approx \frac{d_n}{2n} \sum_{i=1}^n (F_{i-1} + F_i), \quad (15)$$

where maximum deflection  $d_n = 0.2$  mm, i.e., the length of each equidistant sub-interval, is 0.002 mm. The values

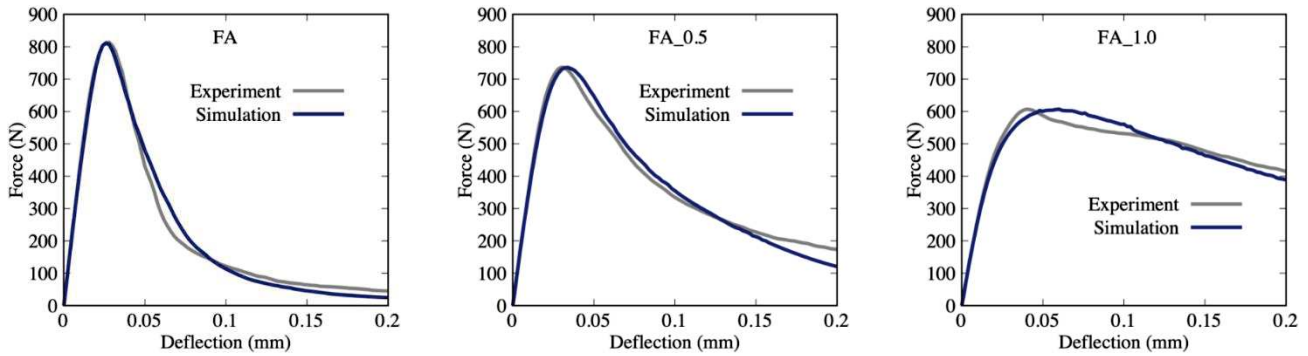


Fig. 11 Selected  $F$ - $d$  diagrams of FA composite: experiment vs. numerical simulation

given in Table 2 were calculated as the average of three measurements.

Along with parameter identification using the ANN-based inverse method, it is also convenient to perform the direct evaluation of mechanical fracture parameters from test responses using, e.g., the effective crack length method (Karihaloo 1995) and the work-of-fracture method (RILEM 1985). These provide more complex information regarding the fracture behavior of newly developed composites. The results obtained for both groups of specimens with these methods can be found in Šimonová *et al.* (2020). The trend of the change in the modulus of elasticity and specific fracture energy during the aging of the specimens is in good agreement with the values obtained via the identification method presented in this paper.

### 3.2 Fine-grained composites with alkali-activated fly-ash matrix with natural fibers

The mechanical properties and application possibilities of AAMs are very similar to those of materials based on ordinary Portland cement. Their major disadvantage is their increased shrinkage during the hardening period, which eventually results in volume contraction, microcracking and the deterioration of tensile and bending properties (Cincotto *et al.* 2003, Ye *et al.* 2017). The addition of different types of fiber to alkali-activated matrix might lead to a reduced cracking tendency and improved tensile properties for these materials (Li *et al.* 2004, Ravikumar *et al.* 2015, Nedeljkovic *et al.* 2018).

The fine-grained composite with alkali-activated fly ash-based matrix with a different amount of natural fibers was selected as a second application. The experimental program was designed to investigate the influence of different volume percentages of hemp fibers (vol%=0.5 and 1.0) on the mechanical parameters and mechanical fracture behavior of composite. The hemp fibers were used as a sustainable alternative to the steel and synthetic fibers which are employed to reduce the cracking tendency in alkali-activated fine-grained composites. The first set of specimens was a reference set and was designated as FA. The remaining two sets contained different volume percentages of hemp fibers (0.5 and 1.0%) and were designated as FA\_0.5 and FA\_1.0. Details about individual mortar compositions, the production of specimens and curing conditions can be found in Šimonová *et al.* (2019).

Table 3 Mean values (CoV in %) for selected mechanical fracture parameters of FA composite

Parameter	FA	FA_0.5	FA_1.0
$E$ (GPa)	17.6 (5.9)	16.6 (5.4)	12.6 (7.6)
$G_F$ (J/m <sup>2</sup> )	53.5 (22.1)	86.3 (19.9)	229.5 (9.9)
$f_t$ (MPa)	4.34 (5.3)	3.41 (13.6)	1.88 (11.2)
$l_{ch}$ (mm)	51 (32.9)	129 (34.6)	838 (24.5)

Table 4 Numerical comparison of the  $F$ - $d$  diagrams of FA composite

Criterion	FA	FA_0.5	FA_1.0
MAPE $_{F-d}$ (%)	18.75	12.44	4.40
MAPE $_{max}$ (%)	0.24	0.25	0.19
MAPE $_W$ (%)	0.61	0.09	0.32

Three independent measurements were carried out for each composite mixture.

The presence of hemp fibers led to a relatively wide range of responses from the tested specimens, as was confirmed by the recorded  $F$ - $d$  diagrams. A total of four ANNs were activated in order to identify the mechanical fracture parameters of nine specimens. The set of activated ANNs is depicted in Fig. 6, see the red subspaces. Table 3 summarizes the mean values (obtained from 3 independent measurements) and coefficients of variation (CoV) of selected mechanical fracture parameters of the FA specimen sets obtained from the  $F$ - $d$  diagrams, i.e., statistics for the modulus of elasticity  $E$ , fracture energy  $G_F$  and tensile strength  $f_t$  obtained from identification using a neural network ensemble, and the characteristic length  $l_{ch}$ .

The identified parameters were verified. The obtained material parameters were used in the computational model and numerical FEM analysis was carried out. The resulting numerical  $F$ - $d$  diagrams are compared with the experimental diagrams for selected specimens from all three sets in Fig. 11. The numerical comparison is given in Table 4 via the MAPE criteria, see Eqs. (12)-(15).

The addition of hemp fibers to alkali-activated matrix should lead to a reduction in the cracking tendency of these materials and improve their tensile properties. The addition of hemp fibers caused a decrease in modulus of elasticity, especially in the case of a higher dosage of fibers. A significant gradual decrease in tensile strength was observed with the addition of fibers. In contrast, the

addition of hemp fibers had a positive effect on the post-peak behavior of composite. The fracture energy increased by more than four times with the addition of 1.0 vol% of hemp fibers to the alkali-activated matrix. The characteristic length increased with the fiber content very substantially. Due to the presence of the fibers, the intrinsic ductility of the composite became very high.

The results of the direct evaluation of mechanical fracture parameters from test responses using the effective crack length method (Karihaloo 1995) and the work-of-fracture method for the FA specimens can be found in Šimonová *et al.* (2019). The trend of the change in the modulus of elasticity and specific fracture energy with the addition of hemp fibers is in good agreement with the values obtained via the identification method presented in this paper.

#### 4. Conclusions

The paper describes a hybrid artificial neural network-based identification system for fine-grained brittle matrix composites. It is made up of an expandable set of neural networks which are independently or jointly used to solve a particular task. The collaboration of multiple neural networks for a specimen which occupies a remote region close to the boundaries of multiple subspaces results in more accurate parameters compared to the parameters provided by a single ANN. The ability of the proposed system to identify mechanical fracture parameters of mortars and other fine-grained brittle matrix composites with variable response while maintaining sufficient accuracy has been confirmed.

In the paper, identification for two groups of specimens made from fine-grained alkali-activated composites was carried out. The resulting numerical  $F$ - $d$  diagrams obtained by FEM analysis with material inputs based on identified parameters were compared with diagrams acquired from experiments. Good agreement was achieved between the numerically and experimentally obtained  $F$ - $d$  diagrams. The parameters which can be obtained from inverse analysis are important, as they can be used to quantify structural resistance against crack initiation and propagation, as well as to compare studied or developed composites. They can also be employed for the definition of material models for the deterministic or stochastic simulation of the quasi-brittle/ductile response of composites/members using a stochastic FEM model based on non-linear fracture mechanics principles. Moreover, knowledge of the three identified parameters allows the quantification of the intrinsic brittleness/ductility of the investigated composites without any further demands, and thus enables one to obtain an estimation of the fracture process zone size (length).

Newly produced composites may exhibit significantly different properties from conventional cementitious composites. This often happens in the early age of specimen hardening, which is accompanied by various chemical processes, and when the properties of the composite are not yet fully stabilized. Also, inclusions such as organic fibers significantly affect the resulting behavior of the composite, including its intrinsic brittleness/ductility, as shown in the

second example. Therefore, an important advantage of the proposed system is that it is easy to expand if a composite with properties outside the current range is tested. The system can also be simply expanded to identify specimens with modified dimensions or other notch depths if needed.

As can be seen from the identification procedure and the applications presented, NNE identifies parameters sequentially for one particular specimen at a time, i.e., at a deterministic level. The parameter uncertainties are then quantified using mathematical statistics. However, the system is inherently general and thus extensible in the future to identify material parameters directly as random variables defined by their probability distributions and statistical moments based on the random response of fracture tests. This approach would be particularly suitable when testing large sets of specimens (ten or more specimens).

#### Acknowledgments

The authors would like to express their thanks for the support provided from the Czech Science Foundation project MUFRA No. 19-09491S and the specific university research project No. FAST-J-20-6413 granted by Brno University of Technology. We also address special thanks to Barbara Kucharčzyková from Brno University of Technology for conducting the fracture tests whose results were used in the applications section of this paper.

#### References

- Bui, H.D. (1997), "Inverse problems in the mechanics of materials", Editions of the University of Karadanga.
- Červenka, V., Jendele, L. and Červenka, J. (2000), "ATENA Program Documentation-Part 1", Cervenka Consulting sro.
- Cochocki, A. and Unbehauen, R. (1993), *Neural Networks for Optimization and Signal Processing*, John Wiley and Sons, Inc..
- Cincotto, M.A., Melo, A.A. and Repette, W.L. (2003), "Effect of different activators type and dosages and relation with autogenous shrinkage of activated blast furnace slag cement", *Proceedings of 11th International Congress on the Chemistry of Cement*, 1878-1888, Durban, May.
- Daskiran, E.G., Daskiran, M.M. and Gencoglu, M. (2016), "Development of fine grained concretes for textile reinforced cementitious composites", *Comput. Concrete*, **18**(2), 279-295. <https://doi.org/10.12989/cac.2016.18.2.279>.
- Durrett, R. (2010), *Probability: Theory and Examples*, Cambridge University Press, New York.
- Hordijk, D.A. (1991), "Local approach to fatigue of concrete", Ph.D. Dissertation of Philosophy, Delft University of Technology.
- Karihaloo, B.L. (1995), *Fracture Mechanics and Structural Concrete*, Longman Scientific and Technical, New York, USA.
- Lehký, D., Keršner, Z. and Novák, D. (2014), "FraMePID-3PB software for material parameters identification using fracture test and inverse analysis", *Adv. Eng. Softw.*, **72**, 147-154. <https://doi.org/10.1016/j.advengsoft.2013.10.001>.
- Lehký, D. and Šomodíková, M. (2017), "Reliability calculation of time-consuming problems using a small sample artificial neural network-based response surface method", *Neur. Comput. Appl.*,

- 28(6), 1249-1263. <https://doi.org/10.1007/s00521-016-2485-3>.
- Li, B., Chen, M., Cheng, F. and Liu, L. (2004), "The mechanical properties of polypropylene fiber reinforced concrete", *J. Wuhan Univ. Tech. Mater. Sci. Ed.*, **19**(3), 68-71. <https://doi.org/10.1007/BF02835065>.
- Maier, G., Bociarelli, M., Bolzon, G. and Fedele, R. (2006), "Inverse analyses in fracture mechanics", *Int. J. Fract.*, **138**(1), 47-73. <https://doi.org/10.1007/s10704-006-7153-7>.
- McKay, M.D., Beckman, R.J. and Conover, W.J. (2000), "A comparison of three methods for selecting values of input variables in the analysis of output from a computer code", *Technometrics*, **42**(1), 55-61.
- Menétrey, P. and Willam K.J. (1995), "Triaxial failure criterion for concrete and its generalization", *ACI Struct. J.*, **92**(3), 311-318.
- Nedeljkovic, M., Lukovic, M., Van Breguel, K., Hordijk, D. and Ye, G. (2018), "Development and application of an environmentally friendly ductile alkali-activated composite", *J. Clean. Prod.*, **180**, 524-538. <https://doi.org/10.1016/j.jclepro.2018.01.162>.
- Novák, D. and Lehký, D. (2006), "ANN inverse analysis based on stochastic small-sample training set simulation", *Eng. Appl. Artif. Intel.*, **19**(7), 731-740. <https://doi.org/10.1016/j.engappai.2006.05.003>.
- Novák, D., Vořechovský, M. and Teplý, B. (2014), "FReET: Software for the statistical and reliability analysis of engineering problems and FReET-D: Degradation module", *Adv. Eng. Softw.*, **72**, 179-192. <https://doi.org/10.1016/j.advengsoft.2013.06.011>.
- Provis, J.L. and Van Deventer, J.S. (2013), *Alkali Activated Materials: State-of-the-Art Report, RILEM TC 224-AAM*, 13, Springer Science and Business Media.
- Ravikumar, C.S., Ramasamy, V. and Thandava-Moorthy, T.S. (2015), "Effect of fibres in concrete composites", *Int. J. Appl. Eng. Res.*, **10**(1), 419-430.
- Recommendation, R.D. (1985), "Determination of the fracture energy of mortar and concrete by means of three-point bend tests on notched beams", *Mater. Struct.*, **18**(106), 285-290.
- Stavroulakis, G.E. (2001), *Inverse and Crack Identification Problems in Engineering Mechanics*, Springer Science and Business Media.
- Stebbing, T.F., Chandler, H.W., Henderson, R.J. and MacPhee, D.E. (2002), "Enhancing the toughness of high performance cement systems", *Innov. Dev. Concrete Mater. Constr.*, 269-279.
- Simonova, H., Dragaš, J., Kucharczykova, B., Kersner, Z., Ignjatović, I., Komljenović, M. and Nikolić, V. (2018), "Fracture Behaviour of Geopolymer Mortars Reinforced with Hemp Fibres", *fib 2018-Better, Smarter, Stronger*, **13**, 583-578.
- Šimonová, H., Kucharczyková, B., Bílek, V., Jr. and Kocáb, D. (2020), "Mechanical fracture characterization of alkali-activated slag mortars with standardized and natural sand", *MATEC Web of Conferences, SPACE 2019*, **310**, 00021. <https://doi.org/10.1051/mateconf/202031000021>.
- Ye, H., Cartwright, CH., Rajabipour, F. and Radlinska, A. (2017), "Understanding the drying shrinkage performance of alkali-activated slag mortars", *Cement Concrete Compos.*, **76**, 13-24. <https://doi.org/10.1016/j.cemconcomp.2016.11.010>.
- Zhou, Z.H., Wu, J. and Tang, W. (2002), "Ensembling neural networks: many could be better than all", *Artif. Intel.*, **137**(1-2), 239-263. [https://doi.org/10.1016/S0004-3702\(02\)00190-X](https://doi.org/10.1016/S0004-3702(02)00190-X).
- Zimmermann, T., Strauss, A., Lehký, D., Novák, D. and Keršner, Z. (2014), "Stochastic fracture-mechanical characteristics of concrete based on experiments and inverse analysis", *Constr. Build. Mater.*, **73**, 535-543. <https://doi.org/10.1016/j.conbuildmat.2014.09.087>.
- Zimmermann, T. and Lehký, D. (2015), "Fracture parameters of concrete C40/50 and C50/60 determined by experimental testing and numerical simulation via inverse analysis", *Int. J. Fract.*, **192**(2), 179-189. <https://doi.org/10.1007/s10704-015-9998-0>.

CC

## Crack Deflection Under Mixed-Mode Loading Conditions in Fine-Grained Composites Based on Water Glass-Activated Slag

Lucie Malíková<sup>\*,‡,§</sup>, Hana Šimonová<sup>\*,¶</sup> and Barbara Kucharczyková<sup>†,||</sup>

<sup>\*</sup>Brno University of Technology  
Faculty of Civil Engineering  
Institute of Structural Mechanics  
Veveří 331/95, 602 00 Brno, Czech Republic

<sup>†</sup>Brno University of Technology  
Faculty of Civil Engineering  
Institute of Building Testing  
Veveří 331/95, 602 00 Brno, Czech Republic

<sup>‡</sup>Institute of Physics of Materials  
Czech Academy of Sciences, v.v.i.  
Žitkova 22, 616 69 Brno, Czech Republic

<sup>§</sup>malikova.l@fce.vutbr.cz

<sup>¶</sup>simonova.h@vutbr.cz

<sup>||</sup>barbara.kucharczykova@vutbr.cz

Received 27 September 2021

Accepted 22 November 2021

Published 2 March 2022

This paper is devoted to an analysis of the crack deflection angle in a semi-circular disc made of a fine-grained composite based on water glass-activated slag. Three-point bending together with an inclined crack ensures the crack propagation in I + II mixed mode. Generally, concrete material exhibits quasi-brittle fracture behavior, which is difficult to understand. Multi-parameter fracture mechanics (MPFMs) concept shall help us to describe the crack propagation and the influence of choice of a suitable distance for application of generalized fracture criteria is investigated. In this work, the well-known maximum tangential stress (MTS) criterion as well as strain energy density (SED) criterion are applied in their multi-parameter (MP) form to find the initial kink angle. Williams power expansion is used to approximate the crack-tip stress field. Its coefficients need to be calculated numerically via combination of the finite-element (FE) solution and over-deterministic method. Results are discussed and recommendations are stated regarding the critical length parameter as well as the number of the Williams expansion (WE) coefficients.

*Keywords:* Crack deflection; mixed-mode loading; fine-grained composite.

### 1. Introduction and Motivation

Quasi-brittle materials are very extended kind of material. This group includes, for instance, concrete, as the archetypical case, fiber-reinforced concrete, shale and

<sup>‡</sup>Corresponding author.

various rocks, fiber-polymer composites, coarse-grained or toughened ceramics, refractories, bone, cartilage, dentine, dental cements, biological shells, many biomaterials, stiff soils, silt, grouted soils, sea ice, consolidated snow, cold asphalt concrete, coal, various printed materials, rigid foams, wood, paper, carton, etc., all brittle materials on the micrometer scale and much more.<sup>1</sup> Therefore, it is still strongly relevant to investigate its fracture behavior.<sup>2,3</sup>

As mentioned above, fracture response of concrete has typically the quasi-brittle nature. It can be also stated that concrete is the most common construction material,<sup>4</sup> whose properties can be varied by adding different additives. Aggregates like fibers (made of various materials) can improve the fracture resistance of the material by means of enlarging the fracture process zone (FPZ). Nowadays, there is a big effort to suggest an environment-friendly alternative to commonly used steel, glass, synthetic, carbon and/or other fibers.<sup>5,6</sup> Another possibility is the use of geopolymers<sup>7</sup> resulting from alkali reaction, which activates secondary raw or waste products. Several basic properties of alkali-activated composites (AAC) can be found, for instance, in Ref. 8 and/or demonstrations/analyses of their practical application are presented in Ref. 9.

Such a fine-grained composite based on water glass-activated slag is investigated in this paper. The crack propagation under mixed-mode (I + II) conditions in a semi-circular disc under three-point bending (SCB) is observed experimentally. Furthermore, finite-element (FE) numerical simulations were performed to obtain theoretical value of the initial kink angle of crack propagation via multi-parameter (MP) fracture criteria: maximum tangential stress (MTS) criterion and strain energy density (SED) criterion.

## 2. Theory and Methodology

Basic theoretical terms and methodological principles are explained in the following text before the analysis is described.

### 2.1. Near-crack-tip stress and displacement field

The multi-parameter fracture mechanics (MPFMs) concept is applied because it has been shown that it can be helpful when the fracture response of quasi-brittle material is analyzed.<sup>10</sup> The crucial idea of the MPFM is utilization of the Williams expansion (WE) for approximation of the near-crack-tip stress/displacement field,

$$\sigma_{ij} = \sum_{n=1}^{\infty} \frac{n}{2} r^{\frac{n}{2}-1} f_{ij}(n, \theta) A_n + \sum_{m=1}^{\infty} \frac{m}{2} r^{\frac{m}{2}-1} g_{ij}(m, \theta) B_m \quad (1)$$

and

$$u_i = \sum_{n=0}^{\infty} r^{\frac{n}{2}} f_i(n, \theta, E, \nu) A_n + \sum_{m=0}^{\infty} r^{\frac{m}{2}} g_i(m, \theta, E, \nu) B_m. \quad (2)$$

Equation (1) holds for stress tensor and Eq. (2) for displacement vector, and both were derived for a homogeneous elastic isotropic cracked body subjected to an arbitrary remote loading.<sup>11</sup> The symbols are as follows:

- $i, j$  are considered in the Cartesian  $(x, y)$  or polar  $(r, \theta)$  coordinate system placed at the crack tip;
- $f_{ij}, g_{ij}$  represent known functions corresponding to loading mode I, II in the stress tensor series;
- $f_i, g_i$  represent known functions corresponding to loading mode I, II in the displacement vector series;
- $A_n, B_m$  express unknown coefficients of the WE.

The coefficients of the higher-order terms of the WE need to be determined numerically for the cracked configuration under the study. In this work, they were obtained through the over-deterministic method which combines the FE numerical solution with the least squares method for solution of an over-determined system of equations; see the following section.

## 2.2. Over-deterministic method

Over-deterministic method serves for calculation of coefficients of higher-order terms of the WE. Its advantage consists in a simple utilization, when the displacements of a selected set of nodes around the crack tip obtained from a common FE analysis are taken as inputs for Eq. (2). When conditions for an over-determined system of equations are fulfilled, the coefficients of higher-order terms of the WE can be calculated through the least squares regression technique; for more details see, for instance, Ref. 12.

## 2.3. Fracture criteria for estimation of the crack deflection angle

In this paper, the crack deflection angle under I + II mixed-mode loading is investigated for a novel environment-friendly fine-grained composite material. In the following text, the generalized MTS and SED criteria are presented.

### 2.3.1. Generalized MTS criterion

Generally, MTS criterion is based on the idea that a crack will propagate in a direction where the tangential stress tensor component  $\sigma_{\theta\theta}$  reaches its maximum.<sup>13</sup> The condition described above can be mathematically written by means of derivatives and the crack deflection angle  $\gamma = \theta$  when the following relations are fulfilled:

$$\frac{\partial \sigma_{\theta\theta}}{\partial \theta} = 0 \quad \text{and} \quad \frac{\partial^2 \sigma_{\theta\theta}}{\partial \theta^2} < 0. \quad (3)$$

### 2.3.2. Generalized SED criterion

Similarly, the SED criterion is based on the idea that a crack will propagate in a direction where the SED factor  $\Sigma$  reaches its minimum,<sup>14,15</sup>

$$\frac{\partial \Sigma}{\partial \theta} = 0 \quad \text{and} \quad \frac{\partial^2 \Sigma}{\partial \theta^2} > 0, \quad \text{where } \Sigma = \frac{1}{2\mu} \left[ \frac{\kappa + 1}{8} (\sigma_{rr} + \sigma_{\theta\theta})^2 - \sigma_{rr}\sigma_{\theta\theta} + \sigma_{r\theta}^2 \right]. \quad (4)$$

In Eq. (4),  $\sigma_{ii}$  are stress tensor components in the polar coordinate system, symbol  $\mu$  represents the shear elastic modulus and symbol  $\kappa$  stands for Kolosov's constant.

## 3. Parameters of the Experimental/Numerical Study

Now, the parameters of the material, experimental setup and numerical models are presented.

### 3.1. Fine-grained composite material properties

Alkali-activated blast furnace slag-based fine-grained composite with slag to sand ratio 1:3 (by weight) was prepared. Slag was activated with water glass of silicate modulus ( $\text{SiO}_2$  to  $\text{Na}_2\text{O}$  molar ratio) equal to 2.34; the water glass dose was adjusted to 6%  $\text{Na}_2\text{O}$  with respect to the slag weight. The water to slag ratio was adjusted to 0.45 including both water present in water glass and extra added water before mixing. Lignosulfonate-based plasticizer was added in an amount corresponding to 1% of the slag weight.

The basic mechanical fracture properties of the AAC (necessary for definition of the corresponding material model in ANSYS FE software) were determined experimentally on prisms with standardized dimensions  $40 \times 40 \times 160 \text{ mm}^3$ :

- static modulus of elasticity of 32 GPa, see Ref. 16;
- dynamic Poisson's ratio of 0.21, see Ref. 17.

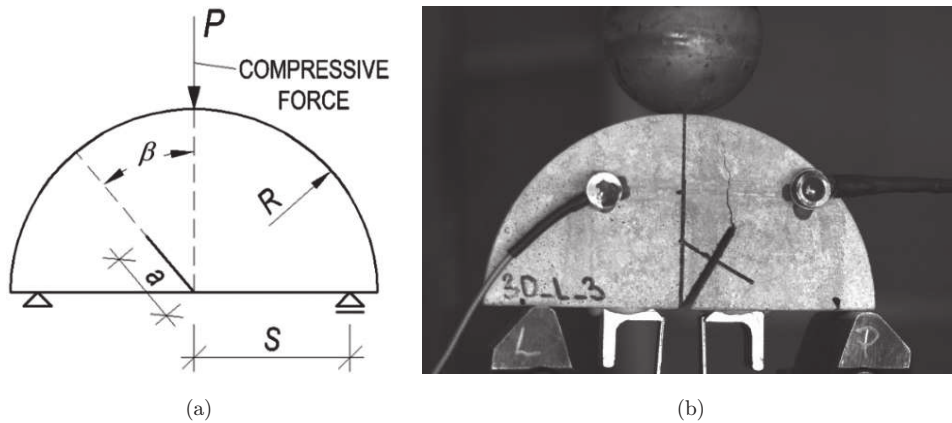


Fig. 1. Experimental setup of the SCB specimen: (a) schema; (b) laboratory measurement.

Table 1. Dimensions of the SCB specimen; see Fig. 1(a).

Dimension	$R$ [mm]	$S$ [mm]	$a$ [mm]	$\beta$ [°]
Value	50	40	25	30, 40 and 50

### 3.2. Experimental setup

The crack deflection under I + II mixed-mode loading was studied on semi-circular discs with an inclined crack loaded under three-point bending; see Fig. 1.

The dimensions of the SCB specimens according to Fig. 1(a) can be found in Table 1, where the values of the SCB radius, half-span between the supports, crack length and crack inclination angle are presented.

## 4. FE Numerical Model

As it has been described above, the knowledge of the WE higher-order terms' coefficients requires a common FE solution of the fracture mechanics problem. The SCB specimen with an inclined crack was therefore modeled in the ANSYS commercial software by means of quadrilateral 8-node PLANE183 elements. For definition of the linear elastic material model, the properties presented in Table 1 were applied. The square-root crack tip singularity was modeled through shifted mid-side nodes in the first row of triangular elements around the crack tip (implemented command KSCON in the FE code). Displacements of the nodes at the distance of 4 mm from the crack tip were used for application of the ODM; more details on the efficiency and accuracy of the method are published, for instance, in Ref. 18.

## 5. Results and Discussion

In this section, the mutual comparison of the values of the crack deflection angles obtained numerically and experimentally is presented. Experimental results, plotted in Fig. 2, are product of three individual measurements. The numerical study involves change of several parameters, such as the number of the initial WE terms considered during fracture criteria application ( $N$ ,  $M = 1, 2, \dots, 10$ ) and/or the value of the critical distance where the criteria are applied ( $r_c = 0.1, 0.5, 1.0$  and  $1.5$  mm). In Fig. 2, the values of the crack deflection angle  $\gamma$  for the SCB specimen with an inclined crack can be seen ( $\beta = 30^\circ$  for (a) and (b),  $\beta = 40^\circ$  for (c) and (d) and  $\beta = 50^\circ$  for (e) and (f)). The plots on the left side of Fig. 2 are obtained via the MP MTS criterion, whereas the plots on the right side of Fig. 2 are obtained via the MP SED criterion.

Based on the dependences presented in Fig. 2, the following conclusions can be stated:

- The crack deflection angle increases for SCB specimens with a crack with a larger angle of inclination (according to experimental as well as numerical results).

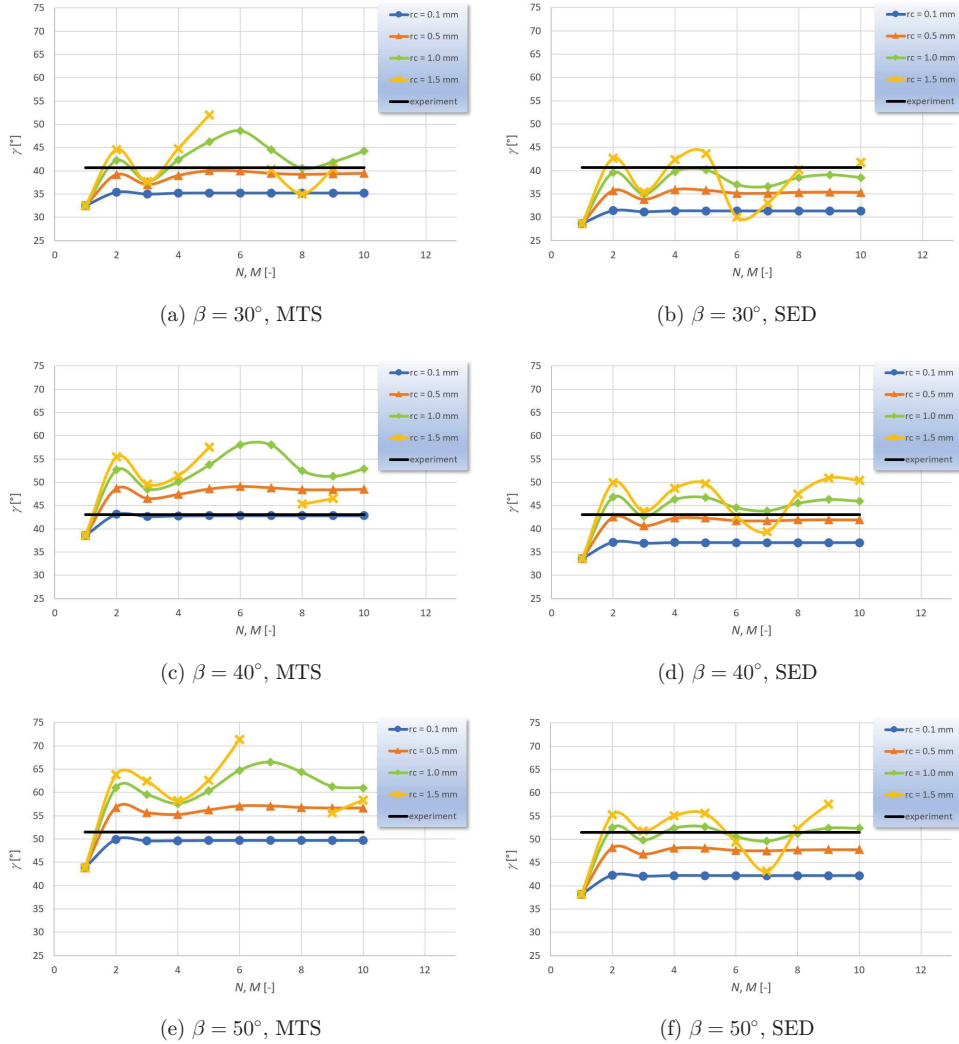


Fig. 2. Dependence of the crack deflection angle on the number of the initial WE terms considered in MP MTS ((a), (c), (e)) and SED criterion ((b), (d), (f)) for various critical distances  $r_c$ .

- The crack deflection angle calculated via the classical (one-parameter) form of the fracture criteria (both MTS and SED) is rather far away from the experimentally obtained values.
- A proper choice of the critical distance for application of the MP fracture criteria depends on the one hand on the type of the criterion and on the other hand on the level of I + II mixed mode conditions (i.e., on the initial crack inclination angle in the SCB specimen):
  - Generally, the values of the crack deflection angle calculated via the MP SED criterion are slightly lower than the values determined via the MP MTS criterion.

- The data show that when the MP MTS criterion shall be applied, rather lower critical distance  $r_c$  is to be chosen (0.1 mm or 0.5 mm) when the crack deflection angle needs to be estimated.
- The MP SED criterion seems to give the more accurate results when applied at the distance of 1.0 mm or 0.5 mm depending on the mixed-mode level.
- Whereas the crack deflection angle values converge with the increasing number of the initial terms of the WE considered in the fracture criteria when applied at smaller critical distances from the crack tip, their values rather oscillate when larger critical distances are utilized.

## 6. Conclusions

Crack deflection angles under I + II mixed-mode conditions in an SCB specimen have been investigated both experimentally and numerically by means of MP fracture criteria. The results obtained prove that utilization of the MP fracture criteria can bring more accurate results. Influence of the proper choice of the critical distance where the fracture criteria are applied is also investigated. The results presented show that the value of  $r_c$  strongly influences the crack deflection angle estimated via MP MTS and SED criteria. Whereas the MP SED criterion gives better results at distances about 1.0 or 0.5 mm from the crack tip, MP MTS criterion works well at even smaller distances (up to 0.5 mm). It has been shown that the appropriate critical distance corresponds also to the mixed-mode level (i.e., to the value of the crack inclination angle). These observations can help for more precise assessment of the fracture behavior of fine-grained composites based on water glass-activated slag and similar ones.

## Acknowledgments

Financial support from the Czech Science Foundation (Project No. 21-08772S) and from the Faculty of Civil Engineering, Brno University of Technology (Project No. FAST-S-21-7338) is gratefully acknowledged.

## References

1. H. T. Nguyen, M. Pathirage, G. Cusatis and Z. P. Bažant, Gap test of crack-parallel stress effect on quasibrittle fracture and its consequences, *ASME J. Appl. Mech.* **87**(7) (2020) 071012.
2. H. T. Nguyen, M. Pathirage, M. Rezaei, M. Issa, G. Cusatis and Z. P. Bažant, New perspective of fracture mechanics inspired by gap test with crack-parallel compression, *Proc. Natl. Acad. Sci. USA* **117**(25) (2020) 14015.
3. K. Kirane and Z. P. Bažant, *Fracture and Fatigue: Part A — Concrete and Composites — Structural Engineering Handbook*, eds. M. Mahamid, E. H. Gaylord and C. N. Gaylord (McGraw Hill, New York, 2020), p. 165.
4. P.-C. Aitcin, *High Performance Concrete* (E. & F. N. Spon, London, 1998).

5. E. A. Awwad, B. Hamad, M. Mabsout and H. Khatib, Sustainable concrete using hemp fibers, *Constr. Mater.* **166**(1) (2012) 45.
6. I. Merta and E. K. Tschegg, *Constr. Build. Mater.* **40** (2013) 991.
7. V. Nikolic, M. Komljenovic, N. Junuzovic and T. Ivanovic, The influence of mechanical activation of fly ash on the toxic metals immobilization by fly ash-based geopolymers, *Key Eng. Mater.* **76** (2018) 3.
8. V. Bilek, J. Hurta, P. Done and L. Zidek, Development of alkali-activated concrete for structures - Mechanical properties and durability, *Perspect. Sci.* **7** (2016) 190.
9. V. Bilek, J. Hurta, P. Done, L. Zidek and T. Zajdlik, Hybrid alkali activated concretes - conception and development for practical application, *Solid State Phenom.* **249** (2016) 3.
10. L. Malíková, Multi-parameter fracture criteria for the estimation of crack propagation direction applied to a mixed-mode geometry, *Eng. Fract. Mech.* **143** (2015) 32.
11. M. L. Williams, On the stress distribution at the base of a stationary crack, *J. Appl. Mech.* **24** (1957) 109.
12. M. Ayatollahi and M. Nejati, An over-deterministic method for calculation of coefficients of crack tip asymptotic field from finite element analysis, *Fatigue Fract. Eng. Mater. Struct.* **34**(3) (2011) 159.
13. F. Erdogan and G. C. Sih, On the crack extension in plates under plane loading and transverse shear, *J. Basic Eng.* **55**(6) (1963) 519.
14. G. C. Sih, Some basic problems in fracture mechanics and new concepts, *Eng. Fract. Mech.* **5** (1973) 365.
15. G. C. Sih, Strain energy density factor applied to mixed mode crack problems, *Int. J. Fract. Mech.* **10** (1974) 305.
16. B. L. Karihaloo and P. Nallathambi, *Cem. Concr. Res.* **19** (1989) 603.
17. ASTM C215-19: Standard Test Method for Fundamental Transverse, Longitudinal, and Torsional Resonant Frequencies of Concrete Specimens, ASTM International (2019).
18. L. Šestáková, How to enhance efficiency and accuracy of the over-deterministic method used for determination of the coefficients of the higher-order terms in williams expansion, *Appl. Mech. Mater.* **245** (2013) 120.

## II.5 FRACTURE BEHAVIOUR OF SELECTED QUASI-BRITTLE COMPOSITES CONTAINING DIFFERENT KINDS OF WASTE MATERIALS

The building industry consumes a huge amount of raw materials for the production of building materials. Cement-based composites are the most commonly applied quasi-brittle structural materials in the world and the environmental aspects related to the production and use of cement and concrete have got a growing importance. The manufacturing process of cement significantly contributes to the global emissions of CO<sub>2</sub>. There are two possible ways of reducing the negative impact of the building industry. One way is to utilize secondary raw materials as supplementary cementitious materials. The other way is to use some alternative binders instead of ordinary Portland cement. The alkali-activated aluminosilicate materials are one representative of such types of binders. Also, the aggregate is an important component of any cement-base composite and covers from 60 % to 80 % of its volume. Partial replacement of aggregate by waste material (secondary raw material) leads to savings of energy and natural sources. The environmentally guided trend of research leads also to the use of a sustainable alternative to steel and synthetic materials, which are used as dispersed reinforcement in quasi-brittle materials. Naturally available fibres produced from different types of plants (e.g. hemp, flax) grown locally make a renewable, biodegradable and relatively cheap alternative.

The articles listed below present results of selected types of quasi-brittle composites made using different types of waste materials.

### II.5.1

Simonova, H., Kucharczykova, B., Topolar, L., Kersner, Z., Merta, I., Dragas, J., Ignjatovic, I., Komljenovic, M., Nikolic, V. Crack initiation of selected geopolymers mortar with hemp fibres. *Procedia Structural Integrity: ECF22 – Loading and Environmental effects on Structural Integrity*. 2018, Vol. 13, pp. 578–583. <https://doi.org/10.1016/j.prostr.2018.12.095> (5 citations without self-citations of all authors according to WoS)

#### II.5.1 Description

This paper aimed to quantify particularly fracture properties of selected types of mortars prepared with AAB and hemp fibres. Especially, attention was paid to the quantification of two different levels of crack propagation using the 2K fracture model. The initiation of cracks during the fracture tests was also monitored by the acoustic emission method.

#### II.5.1 Role of the author – the percentage of contribution: 20 %

Hana Šimonová is the main author of this article who took part in the concept, the methodology and the detailed data processing and evaluation of performed fracture experiments of the presented research. Furthermore, she prepared the original draft of the article which was later reviewed in cooperation with other co-authors.

### II.5.2

Šimonová, H., Zahálková, J., Rovnaníková, P., Bayer, P., Keršner, Z., Schmid, P. Mechanical Fracture Parameters of Cement Based Mortars with Waste Glass Powder. *Procedia Engineering: Structural and Physical Aspects of Construction Engineering*. Elsevier, 2017, Vol. 109, pp. 86–91. doi: 10.1016/j.proeng.2017.05.311 (6 citations without self-citations of all authors according to WoS)

#### II.5.2 Description

The topic of this study was the utilization of ground glass as a partial replacement of cement in mortars. The waste glass came from broken equipment and glassware from chemical laboratories. The mechanical properties were investigated during the composite's ageing. The standard tests were complemented by fracture tests at the age of 28 days.

#### II.5.2 Role of the author – the percentage of contribution: 30 %

Hana Šimonová is the main author of this article who took part in the concept of the article and the detailed data processing and evaluation of performed fracture experiments of the presented research. Furthermore, she prepared the original draft of the article which was later reviewed in cooperation with other co-authors.

### II.5.3

Seitl, S., Miarka, P., Šimonová, H., Frantík, P., Keršner, Z., Domski, J., Katzer, J. Change of Fatigue and Mechanical Fracture Properties of a Cement Composite due to Partial Replacement of Aggregate by Red Ceramic Waste. *Periodica Polytechnica Civil Engineering*. 2019, Vol. 63, No. 1, pp. 152–159. <https://doi.org/10.3311/PPci.12450> (Q4–Engineering, civil; 5 citations according WoS)

#### II.5.3 Description

This research programme aimed to contribute to the complex analysis of the effect of red ceramic waste aggregate on fatigue and mechanical fracture properties of fine-grained cement-based composites. The effect of the possible replacement of natural aggregate by recycled one on fatigue and mechanical fracture properties and environmental impact were discussed.

#### II.5.3 Role of the author – the percentage of contribution: 14 %

Hana Šimonová is a co-author of this article responsible for the detailed experimental data processing and performing the corrections of data to obtain the more accurate values of the fatigue parameters corresponding to the age of the specimen when the cyclic test is performed.



Available online at [www.sciencedirect.com](http://www.sciencedirect.com)

ScienceDirect

Procedia Structural Integrity 13 (2018) 578–583

Structural Integrity

Procedia

[www.elsevier.com/locate/procedia](http://www.elsevier.com/locate/procedia)

ECF22 – Loading and Environmental effects on Structural Integrity

## Crack initiation of selected geopolymer mortars with hemp fibers

Hana Simonova<sup>a,\*</sup>, Barbara Kucharczykova<sup>a</sup>, Libor Topolar<sup>a</sup>, Zbynek Kersner<sup>a</sup>,  
Ildiko Merta<sup>b</sup>, Jelena Dragas<sup>c</sup>, Ivan Ignjatovic<sup>c</sup>, Miroslav Komljenovic<sup>d</sup>, Violeta Nikolic<sup>d</sup>

<sup>a</sup>Brno University of Technology, Faculty of Civil Engineering, Veveří 331/95, 602 00 Brno, Czech Republic

<sup>b</sup>Technische Universität Wien, Faculty of Civil Engineering, Adolf-Blamauer-Gasse 1-3, 1030 Vienna, Austria

<sup>c</sup>University of Belgrade, Faculty of Civil Engineering, Bulevar kralja Aleksandra 73, 11000 Belgrade, Serbia

<sup>d</sup>University of Belgrade, Institute for Multidisciplinary Research, Kneza Višeslava 1, 11030 Belgrade, Serbia

---

### Abstract

The aim of this paper is to quantify particularly fracture properties of selected types of mortars prepared with an alkali activated binder and hemp fibers. The main attention is focused on evaluation of three-point bending fracture tests of prismatic specimens with an initial central edge notch made of alkali activated fly ash mortars. The load versus crack mouth opening displacement ( $F$ - $CMOD$ ) diagrams were recorded during the fracture tests and subsequently evaluated using the Double- $K$  fracture model. This model allows the quantification of two different levels of crack propagation: initiation, which corresponds to the beginning of stable crack growth, and the level of unstable crack propagation. The course of fracture tests was also monitored by acoustic emission method.

© 2018 The Authors. Published by Elsevier B.V.

Peer-review under responsibility of the ECF22 organizers.

*Keywords:* Geopolymer, hemp fibre, fracture test, acoustic emission, crack initiation, Double- $K$  model.

---

### 1. Introduction

The manufacturing of cement is highly energy intensive because of the extreme heat required to produce it, resulting in high pollution, carbon dioxide ( $CO_2$ ) emissions and consequently in global warming and climate change. Producing a ton of cement generates nearly a ton of  $CO_2$  and alarmingly the cement industry alone emits around 7–10% of the total  $CO_2$  on Earth (Aïtcin and Mindess (2011), Scrivener et al. (2016)). Since the cement production is permanently growing by 2.5% annually, these numbers will become even worse. For that reason, there is the increased effort to

---

\* Corresponding author. Tel.: +420 541 147 381.

E-mail address: [simonova.h@vutbr.cz](mailto:simonova.h@vutbr.cz)

developed innovative environmental friendly building materials as an alternative to ordinary Portland cement-based concrete. The alkali activated materials (AAMs) belongs to a promising alternative to traditional cement (Provis and van Deventer (2014), Shi et al. (2006)). AAMs are solid calcium silicate or aluminosilicate materials (so-called geopolymers) formed by alkali activation of solid prime materials (metallurgical slags, coal combustion-based fly ashes, ground granulated blast furnace slag, etc.). The manufacture of AAMs emits up to 80% less CO<sub>2</sub> than that of the ordinary cement.

The same like cement concrete, AAMs also belongs to quasi-brittle materials with low energy absorption capacity under tensile load. To overcome this problem different types of steel or synthetic fibers are used in concrete. Environmentally guided trend of research leads the use of sustainable alternative to steel and synthetic materials. Naturally available fibers produced from different types of plants (e.g. hemp, flax) grown locally make a renewable, biodegradable and relatively cheap alternatives (Zhou and Kastiukas (2017)).

The works published in technical and research papers are currently focused on of AAMs but unfortunately limited information on the fracture properties of these composites is available in the literature (Sarker et al. (2013)). Therefore, the main attention of this paper is focused on the evaluation of three-point bending fracture tests of prismatic specimens with an initial central edge notch made of selected fly ash based geopolymer mortars reinforced with hemp fibers. Especially, the attention is paid to the quantification of two different levels of crack propagation using the Double-*K* fracture model (Reindhardt and Xu (1999), Kumar and Barrai (2011)). The initiation of cracks during the fracture tests was also monitored by the acoustic emission method, e.g. Grosee and Ohtsu (2008).

## 2. Experimental part

### 2.1. Material and specimens

The prism specimens with nominal dimensions 40 × 40 × 160 mm made of geopolymer mortars were studied. In total three set of specimens were tested. The first one was reference, designated as AAFAM, another two sets contained different volume percentage of hemp fibers (0.5 and 1.0 %), designated as AAFAM\_0.5 and AAFAM\_1.0, respectively. The power plant fly ash, sodium silicate solution as alkali activator, river sand with maximum grain size 8 mm, water and hemp fibers with length of 10 mm were used to produce the sets of specimens. All geopolymer mortar specimens were prepared according to the previously optimized procedure by Komljenovic et al. (2010). More details about mortars mix design, specimens' production and curing conditions can be found in Simonova et al. (2018).

### 2.2. Fracture tests

Based on the test requirements, the test specimens were before testing provided with an initial central edge notch and subsequently subjected to the fracture tests in the three-point bending configuration. The nominal depth of notch was about 1/3 of the specimen height and span length was set to 120 mm. The fracture tests were performed in very stiff multi-purpose mechanical testing machine LabTest 6-1000.1.10. The load range of testing machine is 0 to 1000 kN. The loading procedure was performed with the requirement of a constant increment of displacement which was set to 0.02 mm/min. In this way, the diagram of loading force *F* in relation to the crack mouth opening displacement *CMOD* during the fracture test was recorded. The *CMOD* value was measured using the extensometer (crack opening displacement transducer), placed between blades fixed close to the notch, connected to the HBM Quantum X data logger during the loading test. All measured parameters (time, loading force and crack mouth opening) were continuously recorded into the data logger with a frequency of 5 Hz.

All performed fracture tests were accompanied by the measurements using the acoustic emission (AE) technique. During the fracture tests, the AE signals were detected using four magnetic sensors (MDK-13) which were placed for all specimens at the same positions (two sensors on the upper surface, two sensors in the longitudinal axis of the specimen placed on its ends). The AE sensors were attached by magnets to the pre-prepared metal strips fixed by beeswax onto the surface of the individual specimens. Measured AE signals were amplified by a 35 dB amplifier and transmitted to the universal measuring and diagnostic system DAKEL-XEDO which was developed by the diagnostics department of Czech company DAKEL-ZD Rpety. This equipment allows recording and digital processing of AE signals. The overall fracture test configuration and positions of AE sensors can be seen in Fig. 1.

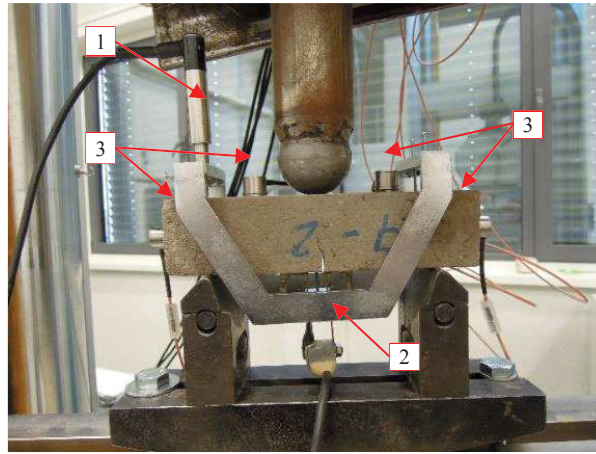


Fig. 1. Fracture test configuration: detail of the specimen with position of sensors (1 – deflection sensor fixed in the measurement frame, 2 – extensometer, 3 – AE sensors).

### 3. Double- $K$ fracture model

The Double- $K$  fracture model was utilized to evaluate mechanical fracture parameters from  $F$ – $CMOD$  diagrams. In principle, this model combines the concept of cohesive forces acting on the faces of the fictitious (effective) crack increment with a criterion based on the stress intensity factor (details can be found in numerous publications – e.g. in Kumar and Barrai (2011)). The advantage of this model is that it describes different levels of crack propagation: an initiation part which corresponds to the beginning of stable crack growth (at the level where the stress intensity factor,  $K_{Ic}^{ini}$ , is reached), and a part featuring unstable crack propagation (after the unstable fracture toughness,  $K_{Ic}^{un}$ , has been reached).

In this case, the unstable fracture toughness  $K_{Ic}^{un}$  was numerically determined first, followed by the cohesive fracture toughness  $K_{Ic}^c$ . When both of these values were known, the following formula was used to calculate the initiation fracture toughness  $K_{Ic}^{ini}$ :

$$K_{Ic}^{ini} = K_{Ic}^{un} - K_{Ic}^c. \quad (1)$$

Details regarding the calculation of both unstable and cohesive fracture toughness can be found e.g. in Kumar and Barrai (2011) or Zhang and Xu (2011). Calculation of parameter  $K_{Ic}^{un}$  is dependent on geometry function  $F_1(\alpha)$  which is defined for the case of three-point bending configuration as:

$$F_1(\alpha) = \frac{1.99 - \alpha(1-\alpha)(2.15 - 3.93\alpha + 2.7\alpha^2)}{(1+2\alpha)(1-\alpha)^{3/2}}, \text{ and } \alpha = \frac{a_c}{D}, \quad (2)$$

where  $a_c$  is the critical effective crack length and  $D$  is the specimen depth.

Generally, in the cohesive crack model, the relation between the cohesive stress  $\sigma$  and the effective crack opening displacement  $COD$  is referred to as the cohesive stress function  $\sigma(COD)$ . The cohesive stress  $\sigma(CTOD_c)$  at the tip of the initial notch of length  $a_0$  at the critical state can be obtained from the softening curve. In this paper, bilinear softening curve was used. When using the bilinear softening curve, two cases may occur. In case I ( $CTOD_c \leq COD_s$ ),  $\sigma(CTOD_c)$  value can be determined according to the formula:

$$\sigma(CTOD_c) = f_t - (f_t - \sigma_s) \frac{CTOD_c}{COD_s}, \quad (3)$$

where  $f_t$  is the tensile strength, in this case determined by identification, see details in Šimonová et al. (2018),  $CTOD_c$  is critical crack tip opening displacement, see e.g. Kumar and Barai (2011),  $\sigma_s$  and  $COD_s$  are the ordinate and abscissa

at the point of slope change of the bilinear softening curve, respectively. According to Petersson (1981), the  $\sigma_s$  and  $COD_s$  values can be considered using the following equations:

$$\sigma_s = \frac{1}{3}f_t, \text{ and } COD_s = \frac{2}{9}COD_c, \quad (4)$$

where  $COD_c$  is the critical crack opening displacement. In this paper,  $COD_c$  is calculated using value of fracture energy  $G_F$  determined via work-of-fracture method, see details in Simonova et al. (2018), according to this formula:

$$COD_c = \frac{3.6G_F}{f_t}. \quad (5)$$

In case II ( $COD_s \leq CTOD_c \leq COD_c$ ),  $\sigma(CTOD_c)$  value can be determined according to the formula:

$$\sigma(CTOD_c) = \frac{\sigma_s}{COD_c - COD_s} (COD_c - CTOD_c). \quad (6)$$

Finally, the value of the load  $F_{ini}$  was determined according to equation (7). This value can be defined as the load level at the beginning of stable crack propagation from the initial crack/notch:

$$F_{ini} = \frac{4 \cdot W \cdot K_{Ic}^{ini}}{S \cdot F_1(\alpha_0) \cdot \sqrt{a_0}}, \quad (7)$$

where  $W$  is section modulus (determined as  $W = 1/6 \cdot B \cdot D^2$ ),  $S$  is span length, and  $F_1(\alpha_0)$  is geometry function according to equation (2), where  $\alpha_0$  (the  $a_0/D$  ratio) is used instead of  $\alpha$ .

#### 4. Results

The mean values (and coefficients of variation) of the selected parameters obtained using Double- $K$  fracture model are summarized in Table 1: unstable fracture toughness  $K_{Ic}^{un}$ , the  $K_{Ic}^{ini} / K_{Ic}^{un}$  ratio, i.e. the ratio expressing the resistance to stable crack propagation, the critical crack opening displacement  $COD_c$ , load level at the beginning of stable crack propagation from the initial notch  $F_{ini}$  and the  $F_{ini} / F_{max}$  ratio, i.e. the ratio between the load level at the beginning of stable crack propagation and maximum load obtained during the test.

As can be seen from Table 1, the value of unstable fracture toughness is not significantly influenced by addition of hemp fibers into the geopolymer matrix. On the contrary, the resistance to stable crack propagation, in this case expressed by  $K_{Ic}^{ini} / K_{Ic}^{un}$  ratio, was increased up to 40% in the case of specimens with the hemp fibers in amount of 1%. The similar trend was observed in the case of load ratio, where the addition of hemp fibers in amount of 1% led to increase of the load ratio about 55%.

Table 1. Mean values of selected parameters (coefficients of variation in %).

Parameter	Unit	AAFAM	AAFAM_0.5	AAFAM_1.0
Fracture toughness $K_{Ic}^{un}$	MPa·m <sup>1/2</sup>	0.493 (5.4)	0.503 (3.9)	0.504 (20.8)
$K_{Ic}^{ini} / K_{Ic}^{un}$ ratio	–	0.415 (19.8)	0.510 (5.5)	0.588 (16.9)
Critical crack opening displacement $COD_c$	mm	0.033 (25.2)	0.056 (26.3)	0.249 (27.2)
Load level $F_{ini}$	N	389.8 (23.3)	482.2 (9.6)	470.7 (1.7)
$F_{ini} / F_{max}$ ratio	–	0.477 (17.2)	0.599 (4.1)	0.740 (5.8)

For selected specimen from each set, the records of three-point bending test in form of  $F$ – $CMOD$  diagrams coupled with acoustic emission results (AE counts) and outputs of Double- $K$  fracture model (load level  $F_{ini}$ ) are shown in the Figs. 2 to 4. The capability to observe the damage propagation in real time during the specimens loading is one of the AE measurement benefit (Ohtsu (2015)). Therefore, first occurrence of higher number of AE counts should correspond to the beginning of stable crack propagation from the initial crack/notch, which is in this case also represented by the load level  $F_{ini}$  estimated by Double- $K$  model.

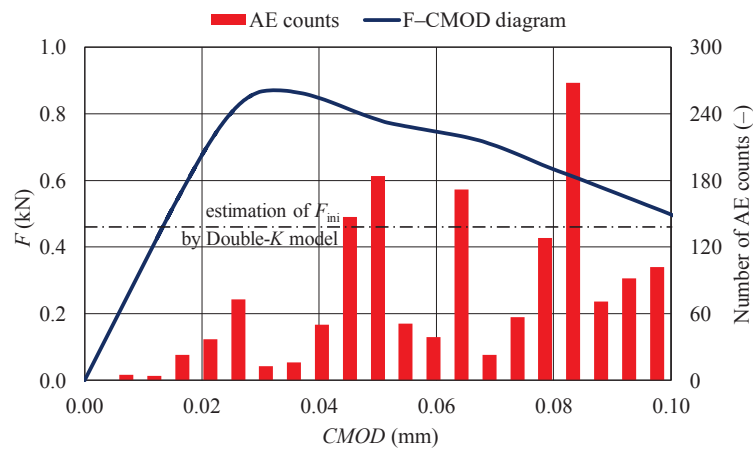


Fig. 2.  $F$ - $CMOD$  diagram with AE counts for specimen AAFAM\_2.

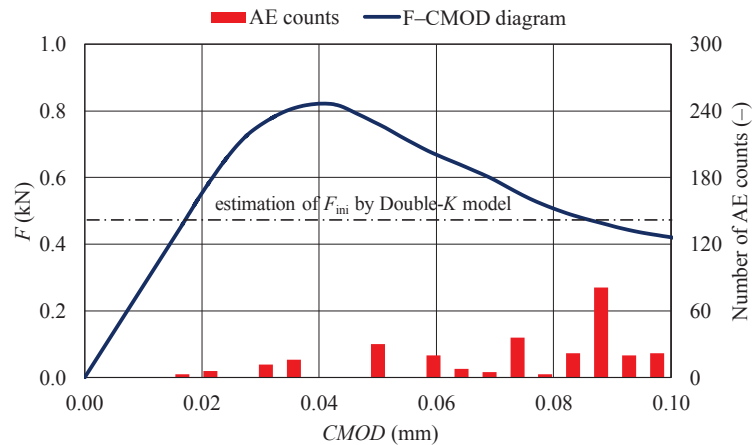


Fig. 3.  $F$ - $CMOD$  diagram with AE counts for specimen AAFAM\_0.5\_1.

## Conclusions

The aim of this study was to quantify the effect of hemp fibers on crack propagation in geopolymer mortars. From the presented experimental research results the following conclusions can be drawn:

- the resistance to stable crack propagation increased up to 40% in the case of specimens with the hemp fibers in amount of 1 %;
- the unstable crack propagation is not significantly influenced by addition of hemp fibers into the geopolymer matrix;
- the estimation of beginning of stable crack growth from initial notch by acoustic emission method is in good agreement with estimation based on Double- $K$  fracture model.

The addition of fibers into alkali activated matrix should lead to reduction in the cracking tendency and improvement in tensile properties of these materials. It seems that the obtained results comply with these assumptions, but it is necessary to perform more tests to confirm these pilot results. One of the issue has to be solved is also the degradation of natural fibers in alkaline environment, therefore it is important to monitored fracture behavior during the material ageing.

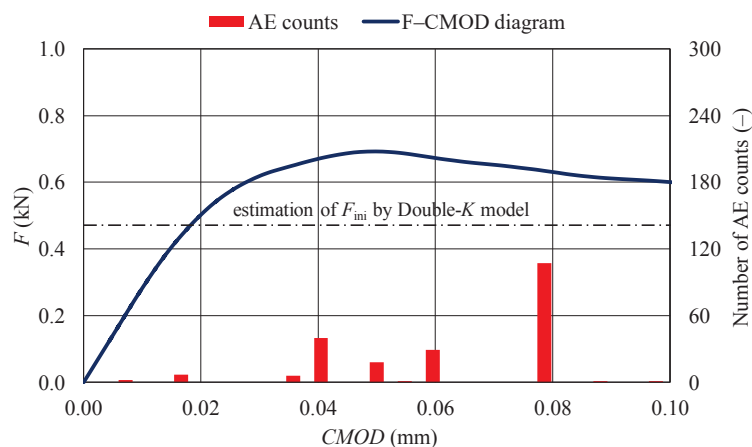


Fig. 4.  $F$ - $CMOD$  diagram with AE counts for specimen AAFAM\_1.0\_2.

## Acknowledgements

The financial support of the Czech Science Foundation, project No. 18-12289Y, is gratefully acknowledged. This outcome has been achieved with the support of projects Nos. 8J18AT009 and ID DS-2016-0060 (CZ ID 8X17060).

## References

- Aitcin P. C., Mindess S., 2011. Sustainability of concrete. CRC Press, London, pp. 328.
- Grosse, Ch. U., Ohtsu, M., 2008. Acoustic Emission Testing. Springer-Verlag, Berlin, pp. 416.
- Komljenović, M., Bašćarević, Z., Bradić, V., 2010. Mechanical and microstructural properties of alkali-activated fly ash geopolymers. Journal of Hazardous Materials 181, No. 1–3, 35–42.
- Kumar, S., Barai, S. V., 2011. Concrete Fracture Models and Applications. Springer, Berlin, pp. 406.
- Ohtsu, M. (Ed.) 2015. Acoustic emission and related non-destructive evaluation techniques in the fracture mechanics of concrete: fundamentals and applications. Woodhead Publishing, pp. 318.
- Petersson, P. E., 1981. Crack growth and development of fracture zone in plain concrete and similar materials, Report No. TVBM-1006, Lund Institute of Technology.
- Provis, J. L., van Deventer, J. S. (eds), 2014. Alkali activated materials: state-of-the-art report, RILEM TC 224-AAM. Springer, Dordrecht, pp. 388.
- Reinhardt, H. W., Xu, S., 1999. Crack extension resistance based on the cohesive force in concrete. Eng. Fracture Mechanics 64, 563–587.
- Sarker, P. K., Haque, R., Ramgolam, K. V., 2013. Fracture behaviour of heat cured fly ash based geopolymer concrete. Materials and Design 44 580–586.
- Scrivener, K. L., John, V. M. C., Gartner, E. M., 2016. Eco-efficient cements: Potential, economically viable solutions for a low- $CO_2$  cement-based materials industry. United Nations Environment Programme, Paris.
- Shi, C., Krivenko, P., Roy, D., 2006. Alkali-Activated Cements and Concretes. CRC Press, Taylor & Francis group, Oxon, pp. 392.
- Simonova, H., Dragas, J., Kucharczykova, B., Kersner, Z., Ignjatovic, I., Komljenovic, M., Nikolic, V., 2018. Fracture Behaviour of Geopolymer Mortars Reinforced with Hemp Fibres, fib 2018 Congress, Melbourne, Australia, in print.
- Šimonová, H., Lipowczan, M., Lehký, D., Kucharczyková, B., Keršner, Z., 2018. Identification of mechanical fracture parameters for estimation of statistical properties of geopolymer mortars. Beton- und Stahlbetonbau International Probabilistic Workshop 2018, in print.
- Zhang, X., Xu, S., 2011. A comparative study on five approaches to evaluate double-K fracture toughness parameters of concrete and size effect analysis. Engineering Fracture Mechanics 78, 2115–2138.
- Zhou, X., Kastiukas, G., 2017. Engineering Properties of Treated Natural Hemp Fiber-Reinforced Concrete. Frontiers in Building Environment 3, Article 33, 1–9.



Structural and Physical Aspects of Construction Engineering

Mechanical Fracture Parameters of Cement Based Mortars  
with Waste Glass Powder

Hana Šimonová<sup>a,\*</sup>, Jana Zahálková<sup>a</sup>, Pavla Rovnaníková<sup>a</sup>, Patrik Bayer<sup>a</sup>,  
Zbyněk Keršner<sup>a</sup>, Pavel Schmid<sup>a</sup>

<sup>a</sup>Brno University of Technology, Faculty of Civil Engineering, Veveří 331/95, 602 00 Brno, Czech Republic

---

**Abstract**

Glass is an amorphous solid substance with pozzolanic properties that can be used as a partial substitute for ordinary Portland cement (OPC) in cement based composites. In the research conducted for this paper, the PC was partially replaced by fine-ground waste laboratory borosilicate glass (in mixtures where 5, 10, 15 and 20 % by mass was substituted). Beam specimens with the dimensions 40 × 40 × 160 mm were prepared from each mixture. After demoulding, the specimens were kept under standard laboratory conditions. Basic tests were conducted at the age of 7, 28, 56, and 90 days: the compressive ( $f_c$ ) and flexural ( $f_t$ ) strengths were determined according to the ČSN EN 1015-11 standard. Specimens were also subjected to fracture testing at the age of 28 days. The beam specimens with an initial central edge notch were tested in three-point bending. Load vs. displacement diagrams were recorded and modulus of elasticity ( $E$ ), fracture toughness ( $K_{Ic}^c$ ) and fracture energy ( $G_F^*$ ) were determined. It was found, that strength increased with specimen age: at the age 28 days this increase was 12–33 % in case of  $f_c$ , and 6–15 % as regards  $f_t$ . The values obtained for almost all the parameters decreased with the increasing dosage of glass as a replacement for cement: compared to a reference composite this decrease was 22–40 % in the case of  $f_c$ , 24–28 % for  $f_t$ , 3–5 % for  $E$ , 9–29 % for  $K_{Ic}^c$ , and 30–50 % for  $G_F^*$ ; exceptions were recorded for glass replacement doses of 5 and 10 %, where increases of 2–6 % for  $f_c$  and 8–10 % for  $E$  were obtained.

© 2017 The Authors. Published by Elsevier Ltd. This is an open access article under the CC BY-NC-ND license (<http://creativecommons.org/licenses/by-nc-nd/4.0/>).

Peer-review under responsibility of the organizing committee of SPACE 2016

*Keywords:* Mortar; cement; glass powder; fracture test.

---

---

\* Corresponding author. Tel.: +420 541 147 381.  
E-mail address: [simonova.h@fce.vutbr.cz](mailto:simonova.h@fce.vutbr.cz)

## 1. Introduction

Presently, great emphasis is being placed on protecting the environment through reductions in carbon dioxide emissions. Carbon dioxide is produced during combustion processes, as well as due to other activities. Large quantities of CO<sub>2</sub> are also produced by the lime and cement industries, which both manufacture the energy intensive products (lime and cement production is carried out at temperatures above 1000°C). The effort to reduce CO<sub>2</sub> emissions is leading to the use of supplementary cementitious materials (SCMs) as partial substitutes for Portland cement. SCMs are natural or technogenic materials of a pozzolanic character, such as fly ash, burnt clays, zeolites, diatomite, etc. Pozzolanic activity requires the presence of amorphous SiO<sub>2</sub>. Glass is an amorphous material with SiO<sub>2</sub> content; it reacts with calcium hydroxide formed through cement hydration. Calcium silicate hydrate products are formed during a pozzolanic reaction [1–4]. The topic of this study was the verification of options of ground glass as a partial replacement for cement in pastes; the waste glass came from broken equipment and glassware from chemical laboratories.

## 2. Materials and methods

Portland cement CEM I 42.5 R (Českomoravský cement, a. s., Radotín Cement Works), fine-ground waste laboratory borosilicate glass (see Tab. 1 for chemical composition and Fig. 1 for micrographs), standard sand with a grain size within the range of 0–2.5 mm, and mixing water were used to produce test specimens with nominal dimensions of 40 × 40 × 160 mm. The glass grains have an irregular shape with size between 1 to 10 μm. After demoulding, the specimens were immersed in water bath at a temperature of 21 ± 1°C. The pozzolanic activity of 719 mg Ca(OH)<sub>2</sub> / 1 g of used glass was measured by the modified Chapelle test. The grain size of the glass ranged from 0.1 to 700 μm ( $d_{10} = 7.44 \mu\text{m}$ ,  $d_{50} = 63.71 \mu\text{m}$ ,  $d_{90} = 333.50 \mu\text{m}$ ). A water/binder ratio was chosen that achieved a fresh cement mortar consistency of 160 ± 5 mm when tested on a shaking table in accordance with Czech standard ČSN EN 1015-3 [5].

Mechanical tests were conducted when the specimens reached the age of 7, 28, 56 and 90 days. Basic mechanical properties were tested according to ČSN EN 1015-11 [6]: bulk density, compressive strength ( $f_c$ ), and flexural strength ( $f_t$ ). Mixtures/mortars in which the cement was replaced by 5 to 20 % of waste chemical glass by cement weight are marked DSM. The results are compared below with those gained for a reference composite, which is designated REF. The proportional compositions of all mixtures are shown in Tab. 2.

Table 1. Chemical composition of fine-ground waste laboratory borosilicate glass.

	B <sub>2</sub> O <sub>3</sub>	SiO <sub>2</sub>	Al <sub>2</sub> O <sub>3</sub>	Fe <sub>2</sub> O <sub>3</sub>	K <sub>2</sub> O	Na <sub>2</sub> O
Content [%]	10.5	78.5	2.94	0.186	1.09	4.55

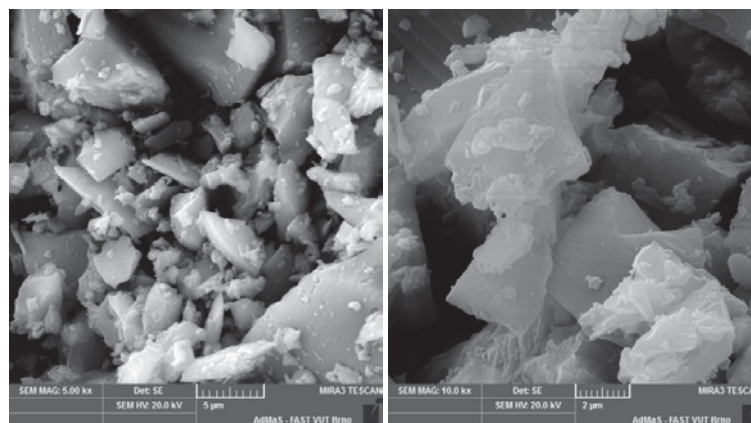


Fig. 1. Micrographs of waste chemical glass.

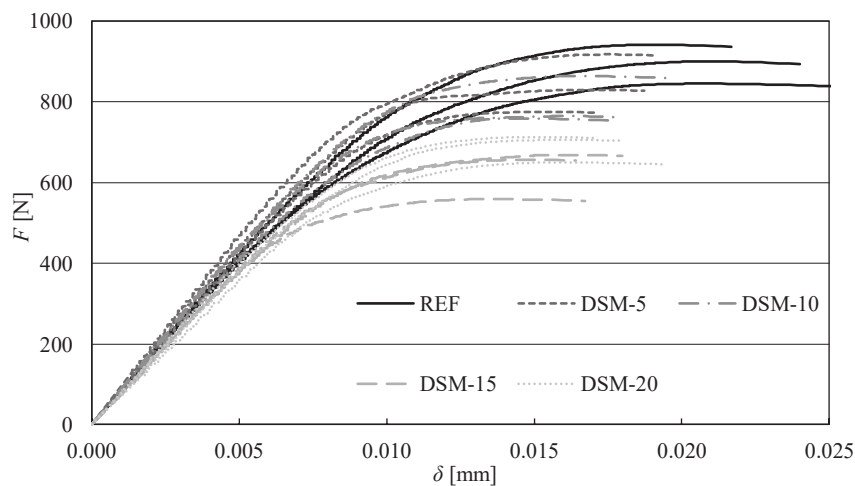
Table 2. Mix proportions and designations.

	Cement	Waste glass powder	Sand	Water	Spreading [mm]	Water to binder ratio
REF	1.00	0.00	3	0.560	158 × 162	0.560
DSM-5	0.95	0.05	3	0.571	159 × 163	0.571
DSM-10	0.90	0.10	3	0.580	165 × 166	0.580
DSM-15	0.85	0.15	3	0.586	165 × 164	0.586
DSM-20	0.80	0.20	3	0.591	157 × 160	0.591

### 3. Fracture tests

The mechanical fracture parameters of hardened mortars are typically determined from experiments conducted on specimens in standard test configurations. If displacement increment loading is performed, it is possible to record load versus displacement diagrams ( $F$ - $\delta$  diagrams) during the course of the tests. The first, almost linear part of these diagrams is used to estimate the modulus of elasticity ( $E$ ). Afterwards – using equivalent elastic crack models, for example – the required set of parameters is determined: critical effective crack length, effective fracture toughness ( $K_{Ic}^e$ ), and (using the determined modulus of elasticity) effective toughness [7]. The work of fracture (or rather the specific fracture energy) is calculated from complete  $F$ - $\delta$  diagrams after appropriate corrections have been made taking into consideration potential stability loss during loading [8–11]. In this case, it wasn't possible to reconstruct the descending part of the  $F$ - $\delta$  diagrams, and therefore the work of fracture  $W^*$  is determined as the area under the  $F$ - $\delta$  diagrams before stability loss occurs during loading, and then the fracture energy is calculated as  $G_F^* = W^*/A_{lig}$ , where  $A_{lig}$  is the cross-section of a bended specimen reduced in depth by a notch.

Beam specimens with nominal dimensions of  $40 \times 40 \times 160$  mm fabricated for the determination of the above-mentioned mechanical fracture parameters of the studied mortars were subjected to fracture tests using the three-point bending test configuration at the age of 28 days. The load span was 120 mm. The initial notch was made before testing with a diamond blade saw. The depth of the notch was approximately 33 % of the depth of each specimen. The fracture tests were carried out using a Heckert FP 10/1 testing machine with a measuring range of 0–2000 N. The loading of the specimens was continuous and required constant midspan displacement increments. The  $F$ - $\delta$  diagrams for the studied mortars are shown in Fig. 2.

Fig. 2. Load  $F$  versus displacement  $\delta$  diagrams for the studied mortars.

#### 4. Results

The mechanical properties of the specimens in relation to their age are summarized in Tables 3–5 via mean values. The bulk density values do not change considerably with specimen age in the case of any of the studied mortars. The mortars in which the cement was replaced by waste chemical glass show decreases in bulk density up to 3 % with increasing of replacement level of cement for all investigated specimen ages.

The  $f_c$  value at the age of 7 days reached 90 % of the value obtained at the age of 28 days for the REF mortar; in the case of mortars with waste chemical glass, 71–77 % of the REF mortar's  $f_c$  was attained. The  $f_c$  at the age of 90 days is about 20 % higher in comparison with that at 28 days for the REF mortar, while in the case of mortars with waste chemical glass it is about 15 % higher, with the exception of mortar DSM-20, for which it is more than 30 % higher.

The  $f_t$  value at the age of 7 days reached about 80 % of the value attained at the age of 28 days by the REF mortar; in the case of mortars with waste chemical glass it is 73–83 % of the REF value. The  $f_t$  at 90 days is about 10 % higher in comparison with the REF mortar at 28 days, and in the case of mortars with waste chemical glass a similar trend was observed.

The  $f_c$  and  $f_t$  values were gradually decreased for all investigated specimen ages in the case of mortars in which the cement was replaced by waste chemical glass. The only exception is the DSM-5 mortar, where a slight increase in  $f_c$  of up to 5 % was observed in specimens at the age of 28 and 56 days. At the age of 28 days, a decrease in  $f_c$  and  $f_t$  of about 30 % was observed in the case when 20% of the cement was replaced by waste chemical glass.

Table 3. Bulk density of mortars.

	Bulk density [kg/m <sup>3</sup> ]			
	7 days	28 days	56 days	90 days
REF	2240	2240	2250	2240
DSM-5	2200	2220	2230	2230
DSM-10	2200	2200	2230	2200
DSM-15	2190	2200	2200	2170
DSM-20	2170	2170	2190	2180

Table 4. Compressive strength of mortars.

	Compressive strength [MPa]			
	7 days	28 days	56 days	90 days
REF	39.0	43.0	45.5	52.0
DSM-5	33.5	45.5	46.5	51.0
DSM-10	30.0	42.0	43.5	49.0
DSM-15	26.0	34.5	38.5	40.0
DSM-20	23.5	30.5	34.5	40.5

Table 5. Flexural strength of mortars.

	Flexural strength [MPa]			
	7 days	28 days	56 days	90 days
REF	9.7	12.0	12.4	13.1
DSM-5	7.9	10.8	10.9	11.4
DSM-10	7.8	9.8	10.1	10.8
DSM-15	7.8	9.3	9.9	10.2
DSM-20	7.2	8.6	9.1	9.9

The mean values and standard deviations of selected mechanical fracture parameters at the age of 28 days obtained from recorded  $F-\delta$  diagrams [6, 7] (i.e.  $E$ ,  $K_{Ic}^e$  and  $G_F^*$ ) are summarized in Figures 3–5. When 5 or 10% of the cement is replaced by waste glass powder, the  $E$  value increases by 8 or 10 %, respectively, in comparison with the reference mortar. In the case of higher cement replacement, the  $E$  value decreases by up to 5 % in comparison with the reference mortar.

The  $K_{Ic}^e$  value gradually decreases as cement is replaced by waste chemical glass. A similar trend was observed as in the case of  $f_c$  and  $f_t$ , with the highest decrease of about 30 % being recorded in the case when 20% of the cement was replaced by waste chemical glass.

The  $G_F^*$  value also decreases as cement is replaced by waste chemical glass. In this case, the effect of cement replacement by waste chemical glass is highest, with a decrease in the range of 30–50 % being observed.

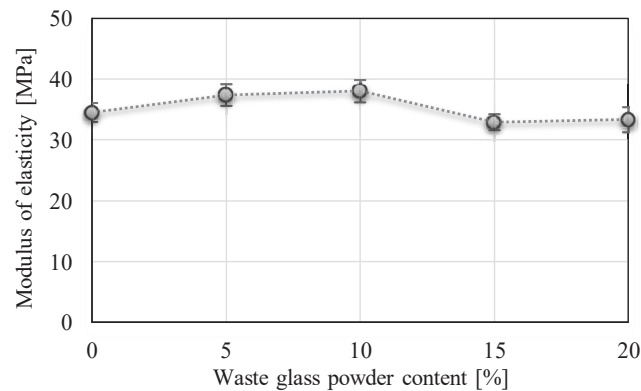


Fig. 3. Modulus of elasticity  $E$  of the studied mortars: mean values and standard deviations.

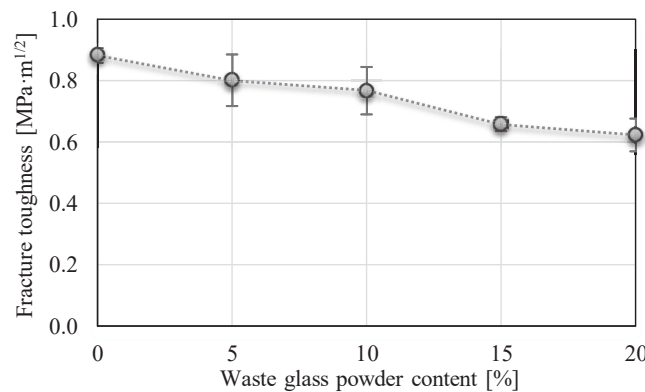


Fig. 4. Effective fracture toughness  $K_{Ic}^e$  of the studied mortars: mean values and standard deviations.

## 5. Conclusions

The replacement of cement by waste glass powder while maintaining a constant fresh mixture consistency causes a decrease in the values of all the monitored parameters of hardened mortars. Compared with the reference cement mortar, the compressive and flexural strength and effective fracture toughness of the studied mortars decreases somewhat gradually by up to 30 % for the highest dose of waste glass powder, while the fracture energy falls by up to 50 %. In case of modulus of elasticity, a slight increase was observed for lower amounts of waste glass powder.

From the above-mentioned results it can be concluded that waste glass is a suitable pozzolanic material for the replacement of Portland cement up to 10%. From the point of view of mechanical properties after 90 days, the results are close to the reference cement paste; at doses above 10% they are significantly worse than the mechanical properties of reference cement paste. The strength's values are decreasing because of a very slow pozzolanic reaction of glass, but their increase is expected in time.

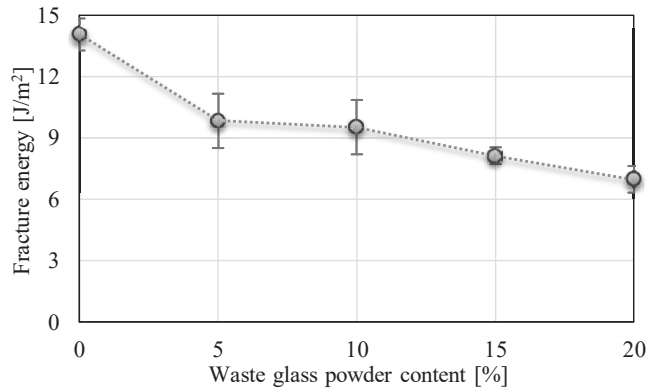


Fig. 5. Specific fracture energy  $G_f^*$  of the studied mortars: mean values and standard deviations.

### Acknowledgements

This outcome has been achieved with the financial support of the Czech Science Foundation under project No 14-04522S “Investigation of processes at the formation of solid structure in the silicon oxide-Portland cement system in relation to the properties of binder”.

### References

- [1] V. Vaitkevičius, E. Šerelis, H. Hilbig, The effect of glass powder on the microstructure of ultra high performance concrete. *Construction and Building Materials*. 68 (2014) 102–109.
- [2] M. Kamli, A. Ghahremaninezhad. Effect of glass powder on the mechanical and durability properties of cementitious materials. *Construction and Building Materials*. 98 (2015) 407–416.
- [3] K. L. Scrivener, A. Nonat, Hydration of cementitious materials, present and future, *Cement and Concrete Research*. 41 (2011) 651–665.
- [4] A. Khmiri, M. Chaabouni, B. Samet, Chemical behaviour of ground waste glass when used as partial cement replacement in mortars, *Constr. Build. Mater.* 44 (2013) 74–80.
- [5] ČSN EN 1015-3, European standard: Methods of test for mortar for masonry - Part 3: Determination of consistence of fresh mortar (by flow table), Czech Standards Institute, 1999.
- [6] ČSN EN 1015-11, European standard: Methods of test for mortar for masonry - Part 11: Determination of flexural and compressive strength of hardened mortar, Czech Standards Institute, 1999.
- [7] B. L. Karihaloo. *Fracture Mechanics and Structural Concrete*, Longman Scientific & Technical, New York, 1995.
- [8] RILEM TC-50 FMC Recommendation. Determination of the fracture energy of mortar and concrete by means of three-point bend test on notched beams, *Materials & Structures*. 18 (1985) 285–290.
- [9] V. Veselý, P. Frantík, An application for the fracture characterization of quasi-brittle materials taking into account fracture process zone influence, *Advances in Engineering Software*. 72 (2014) 66–76.
- [10] J. Němeček, Z. Keršner, P. Schmid, I. Havlíková, H. Šimonová, L. Topolář, V. Veselý, P. Rovnaník, Fracture Process in a Fine-Grained Cement-Based Composite Monitored with Nanoindentation and Acoustic Emission, *Key Engineering Materials*. 662 (2015) 47–50.
- [11] P. Frantík, J. Mašek. GTDiPS software, <http://gtdips.kitnarf.cz/>, 2015.

# Change of Fatigue and Mechanical Fracture Properties of a Cement Composite due to Partial Replacement of Aggregate by Red Ceramic Waste

Stanislav Seitl<sup>1,2</sup>, Petr Miarka<sup>2</sup>, Hana Šimonová<sup>2</sup>, Petr Frantík<sup>2</sup>, Zbyněk Keršner<sup>2</sup>, Jacek Domski<sup>3</sup>, Jacek Katzer<sup>3\*</sup>

<sup>1</sup> Institute of Physics of Materials,  
Academy of Science of the Czech Republic  
602 00 Brno, Žižkova 22, Czech Republic

<sup>2</sup> Faculty of Civil Engineering, ,  
Brno University of Technology,  
602 00 Brno, Veveří 331/95, Czech Republic

<sup>3</sup> Faculty of Civil Engineering,  
Environmental and Geodetic Sciences,  
Koszalin University of Technology,  
75-453 Koszalin, ul. Śniadeckich 2, Poland

\* Corresponding author, e-mail: [jacek.katzer@tu.koszalin.pl](mailto:jacek.katzer@tu.koszalin.pl)

Received: 23 April 2018, Accepted: 05 December 2018, Published online: 08 January 2019

## Abstract

Fine-grained cement-based composites used in civil engineering and construction industry are usually made of cement-based matrix and natural aggregate (such as sand, gravel, crushed stone, etc.). Red ceramic waste aggregate is considered as a perspective replacement of a part of natural aggregate in modern environmentally oriented building materials. Fine-grained cement composite with natural aggregate partially replaced by ceramic waste aggregate usually show different mechanical fracture characteristics from ordinary fine-grained concrete. The specimens were tested at six different ages. This was the reason for conducting the research programme. Altogether, 6 fine-grained cement mixtures with various proportions of natural and red ceramic waste aggregate were prepared. The aim of this paper is to present and compare mechanical fracture properties obtained from static and fatigue tests. Bulk density, flexural and compressive cube strength, fracture toughness and fatigue properties (S–N – Wöhler curve) were of special interest. All of these tests are important for a practical application of concrete with ceramic aggregate for structures. All the results were statistically analysed and they showed that the fatigue and mechanical fracture properties were improved or at least kept up with the increasing levels of red ceramic waste aggregate. Environmental impact of application in construction industry of composites in question is discussed.

## Keywords

ceramic waste, aggregate, strength characteristics, fatigue properties, S–N curve

## 1 Introduction

Concrete is considered the second (after water) most utilized material in the world. It was estimated that the world uses twenty-five billion tonnes of concrete every year [1, 2]. Concrete is the mixture of cement, aggregate and water in which the aggregate constitutes 65–80 % of total volume. The increase in industrialization and urbanization rates due to economic and population growth has turned construction industry into one that consumes the most of natural resources and generates solid waste that negatively

impacts the environment [3]. It is justified to affirm that the use of recycled aggregate is a way to reduce the impact concrete production may cause to the environment [4, 5]. Incorporating the maximum possible amount of recycled material in concrete would contribute to the reduction of greenhouse gases emission as well as to minimize the amount of energy spent in concrete production. Kumar Sharma et al. [6] mentioned that for the concrete containing polished granite waste, concrete with up to 20 % of

natural coarse aggregate substituted by granite waste could be recommended for all applications, while concrete with 20 % to 40 % of natural coarse aggregate substituted by granite waste could be recommended for non-structural applications, pavements etc.

Ceramic is one of the oldest and most commonly harnessed material in the history of mankind. It has been used for multiple and varied applications such as pottery, chinaware and sanitary ware [7, 8]. Ceramic is also harnessed in construction industry as building material (e.g. for ceramic floor and wall tiles, for various building bricks and hollow blocks). The global volume of construction and demolition waste is dominated by red ceramic waste [9, 10, 11]. It was proven that the most promising recycling process of red ceramic waste is utilizing it for concrete production as coarse aggregate [12]. Worldwide, there is a significant and growing research effort to efficiently use ceramic waste in construction industry [13]. Replacing natural coarse aggregate by waste ceramic aggregate is one of a rapidly developing recycling technology. Waste ceramic aggregate significantly influences the homogeneity of mechanical characteristics of cast concrete. Populations of test results (of any tested property) of any concrete based on waste ceramic are characterized by significantly higher standard deviation [9, 14]. This phenomenon significantly limits possible applications of waste ceramic aggregate concrete. Currently, waste ceramic aggregate concretes are only used for construction elements characterized by less demanding mechanical characteristics. In this context, this research programme aims to contribute to the complex analysis of the effect of red ceramic waste aggregate (RCWA) on fatigue and mechanical fracture properties of fine-grained cement composite. Such properties as: bulk density, flexural strength, compressive strength, fracture toughness and Wöhler curve properties were tested during the research programme. The specimens were tested at six different ages (3, 7, 14, 28, 90, and 780). The impact of partial and full replacement of natural aggregate by RCWA on fatigue characteristics, mechanical fracture properties and environmental is discussed.

## 2 Materials and specimen preparation

Assessment of mechanical characteristics of fine-grained cement composites with RCWA was conducted utilizing mortar test specimens made in standard steel moulds (40 mm × 40 mm × 160 mm). CEM I 42.5 R was used as a binder. A reference composite was prepared using mix proportions of a standardized mortar for cement tests ( $w/c = 0.5$ ). The volume composition of the mortar is presented in Fig. 1.

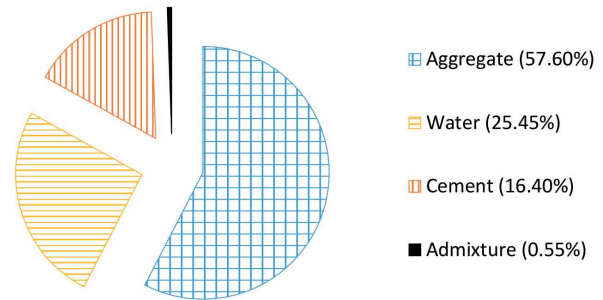


Fig. 1 Volume composition of the cement mortar

Both used aggregates ( $d \leq 2$  mm): natural sand and RWCA were mirroring grading characteristics of the standardized sand according to EN 191-1 [15]. The natural sand was replaced by volume due to lower bulk density of RWCA. The created mixtures are marked from 1 to 6, where mixture 1 contains only natural aggregate and mixtures from 2 to 6 contain increasing volumes of RCWA (6.35 %, 12.70 %, 19.05 %, 25.40 %, 31.75 % respectively). All studied mixtures were prepared using a small laboratory mixer for mortars. The amount of cement, water and admixture was equal to 450 g, 225 g and 5 g respectively for one batch (allowing casting of three specimens). These amounts were constant for all cast composites. No adjustment of fresh batches on the level of uniform value of plasticity or workability was carried out. Due to the fact that porous and dry red ceramic sucks the water whenever possible, it is impossible to assess the real composition of the mix and subsequently the value of  $w/c$  ratio. During the current research programme admixture was used to maintain the similar workability of all the mixes but the amount of water absorbed by the RCWA is unknown. One may argue that the fresh mortars had to have different  $w/c$  influencing the strength values of individual batches. In authors opinion it is a combined effect of a difference in value of  $w/c$  and internal curing which is happening afterwards. Basically, the more water is sucked by RCWA the lower value of  $w/c$ , hence the larger strength of hardened composite, and larger scale of internal curing also influencing strength characteristics. The initial amount of natural sand was equal to 1350 g. The procedure for mixture preparation and compaction of a standardized cement mortar was used for preparation of all mixes. The volume of each mixture was equal to 30 dm<sup>3</sup>. Immediately after mixing, fresh mixture was poured into steel moulds. The prism specimens with nominal dimensions of 40 mm × 40 mm × 160 mm were prepared for testing. The specimens were demoulded at the age of 24 hours and placed in a water tank with constant water temperature of  $20 \pm 1^\circ\text{C}$ .

**Table 1** Composition of studied mixtures

Com- posite	Cement	Water	Sand	RWCA	Super- plasticizer	Bulk density
	(g)	(g)	(g)	(g)	(g)	(kg/m <sup>3</sup> )
1	450	225	1350	0	5	2270
2	450	225	1215	101	5	2235
3	450	225	1080	202	5	2185
4	450	225	945	304	5	2135
5	450	225	788	394	5	2125
6	450	225	657	493	5	2110

They were cured in these conditions until the tests were performed. The specimens were firstly used for the flexural test. The remaining halves of the specimens after flexural strength tests were subsequently used for compressive strength tests. Easy compaction of fresh mixture is an important property enabling achieving the maximum possible strength of any cement composite. It was observed that in case of mixtures with RCWA, workability is deteriorating with the increasing amount of added RCWA. This phenomenon was described by Rashid et al. [16] The decrease in workability is partially caused by RCWA being capable of absorbing significant amount of water [8, 17] due to porosity. Other reason for the reduction of the workability is shape of the RCWA [17]. The amount of water required for maintaining the fluidity of fine-grained cement composite only with RCWA is very high. Therefore, the maximum volume of natural aggregate replacement by RCWA was limited to 493 g/1350 g (see Table 1). To ensure desired workability, all mixtures were modified by the addition of a commercially available superplasticizer based on polymers and characterized by density of 1.07 kg/dm<sup>3</sup> and pH equal to 4.4 ± 1.0.

Designers of civil engineering structures use or refer to the composite 1 design curve as the lower bound for their analyses. It is well known [18] that cement industry produces a significant amount of CO<sub>2</sub>. Ultimately, the produced CO<sub>2</sub> affects the environment. Therefore, environmental impact of fine-grained cement composite is evaluated using the volume of raw materials: cement, sand and RCWA aggregate etc. In studied mixtures of fine-grained cement composites with RCWA, volume of raw materials is calculated by using data from Table 1 and normalized with the control specimen.

The volume of raw material is reduced almost linearly with the increase in RCWA. About 20 and 25 % reduction is observed with 30 and 36% replacement of natural aggregate by RCWA, respectively (see Fig. 2).

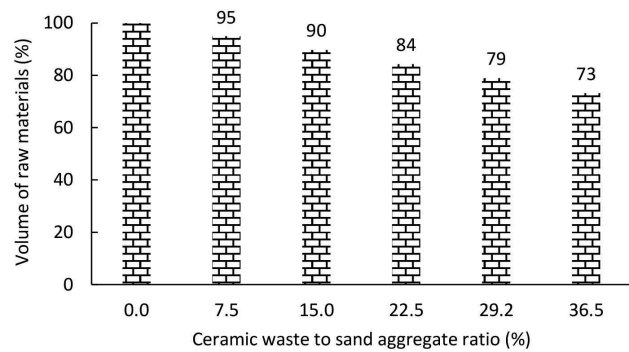


**Fig. 2** Environmental impact assessment for all tested fine-grained composites with RCWA

### 3 Methods of testing

The flexural and compressive strength tests were conducted in compliance with EN 196-1. The flexural strength tests were conducted using a three point bending test (3PBT) on prismatic specimens (40 mm × 40 mm × 160 mm). The compressive strength test was conducted on halves of prismatic specimens remaining after performing flexural strength tests. For calculation of fracture toughness values, the data from 3PBT was evaluated. The 3PBT was successfully used for such evaluations by numerous researchers [19, 20 21]. Notched (by a diamond blade saw) prism specimens with nominal dimensions 40 mm × 40 mm × 160 mm are prepared for the test. The notch must keep a crack – length relation equal to 0.1. The span length for this test is equal to 120 mm. During the test, the maximum values of force were recorded. Then linear elastic fracture mechanics (LEFM) equation was used [22]:

$$K = \sigma \sqrt{\pi a} f(a/W), \tag{1}$$

where:  $a$  – crack length,  $W$  – width of a specimen,  $f$  – dimensionless functions for ratio span/width = 3 is Eq.(2),  $K$  – stress intensity factor,  $\sigma$  – corresponding load Eq.(3)

$$f(a/W) = 0.9926 + 0.4862(a/W) - 12.479(a/W)^2 + 73.153(a/W)^3 - 124.29(a/W)^4, \tag{2}$$

used by Wu [23], Karihaloo [19], Tada [22], etc.

$$\sigma = 3SP / (2BW^2), \tag{3}$$

where:  $S$  – span,  $P$  – force,  $B$  – thickness,  $W$  – width of a specimen.

When the force reaches maximum value  $P_{max}$  the value of the stress intensity factor  $K_I$  is called fracture toughness  $K_{IC}$ . Fatigue properties were also gained from 3PBT. The depth of the notches was 4 mm for fatigue tests. The fatigue tests were carried out at the Laboratory of

High-cycle Fatigue Group at the Institute of Physics of Materials at Brno University of Technology. The controlled values for temperature and relative humidity were equal to  $22 \pm 2^\circ\text{C}$  and  $50\% \pm 2\%$  respectively. The fatigue experiments were carried out using a computer-controlled servo-hydraulic testing machine under load control. The stress ratio  $R$  (defined as quotient of minimum  $P_{\min}$  and maximum  $P_{\max}$  load of a sinusoidal wave in each cycle) was equal to 0.1. The load frequency used for all tests was equal to 10 Hz. Fatigue endurance limit was determined on the basis of an  $S-N$  curve. The limit of  $2 \times 10^6$  cycles to fracture was used to consider the applied stress amplitude as safe for loading during the whole component lifetime. The testing procedure based on applying cyclic loading with defined stress amplitude to determine the number of cycles to the fracture was described by multiple researchers [24, 25, 26].

#### 4 Results and discussion

The bulk density of all hardened composites after 28 days of curing is presented in Fig. 3 [27, 28]. One of the advantage of using the RWCA is that the value of bulk density slightly decreases with an increased amount of RWCA used as a replacement of natural aggregate.

Mixtures with natural aggregate are characterized by higher bulk density due to weight of aggregate in comparison with RWCA. Bulk density of reference mixture is equal to  $2270 \text{ kg/m}^3$ . The bulk density of the composite with the maximum amount of RWCA is reduced by 7% in comparison to a composite with no RWCA. Similar trends have been described by Medina et al. [17]. The obtained results from the flexural test and adequate coefficient of variation (CoV) are presented in Table 2.

The mean values and coefficients of variation are introduced for specimens at the age of 3, 7, 14, 28, 90, and 180 days. It is observed that flexural strength increase with age. For specimens of age from 3 to 28 days, there is observed expected increase of about 10–15% in the flexural strength (for mixture 6 it is only 6%). From 28 to 180 days of specimens' age, increase in the flexural strength of 24–30% was observed for all mixtures. Mixtures with RCWA yielded higher flexural strength in comparison with the control fine-grained cement composite (mixture 1) for the same specimens' ages. It is worth noticing that with the increasing substitution rate of natural aggregate with RWCA the flexural and compressive strength increase with increasing age of the specimens. The obtained results from the compressive strength test are mentioned in Table 3.

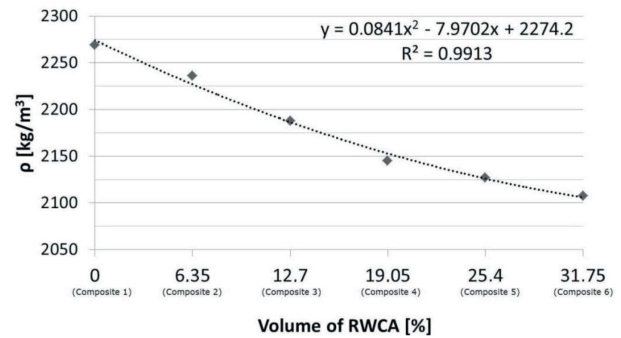


Fig. 3 Influence of RWCA addition on bulk density of hardened composite

Table 2 Mean values of flexural strength in MPa (CoV in %)

Com- posite	Age of specimens					
	3 days	7 days	14 days	28 days	90 days	180 days
1	4.9 (6.2)	5.5 (3.4)	6.1 (1.5)	5.7 (2.8)	7.3 (3.4)	7.5 (2.4)
2	5.7 (2.9)	6.1 (5.4)	6.3 (1.7)	6.3 (5.9)	7.7 (6.2)	8.5 (5.6)
3	6.0 (2.5)	6.6 (6.1)	6.7 (4.2)	6.9 (4.6)	8.4 (3.2)	9.2 (2.3)
4	6.0 (4.2)	6.8 (1.4)	7.4 (2.6)	7.6 (13.8)	7.9 (1.4)	10.3 (3.9)
5	6.6 (4.0)	7.8 (1.5)	8.1 (2.8)	7.3 (6.8)	8.1 (8.3)	10.3 (4.9)
6	7.3 (2.8)	7.8 (3.8)	8.7 (3.7)	7.8 (0.7)	8.2 (11.5)	10.8 (7.0)

Table 3 Mean values of the compressive strength in MPa (CoV in %)

Com- posite	Age of specimens					
	3 days	7 days	14 days	28 days	90 days	180 days
1	32.0 (1.3)	34.2 (1.9)	39.6 (5.3)	46.1 (1.9)	61.4 (1.9)	62.0 (3.1)
2	34.8 (0.9)	39.3 (0.7)	44.2 (1.7)	51.1 (2.2)	66.9 (2.5)	61.5 (4.2)
3	37.2 (1.5)	43.4 (0.4)	47.1 (1.7)	58.4 (1.2)	77.0 (1.8)	71.3 (2.7)
4	39.3 (1.9)	45.4 (2.3)	51.9 (2.2)	57.2 (9.0)	75.0 (2.6)	80.6 (0.6)
5	42.9 (0.8)	50.6 (2.3)	53.1 (6.2)	61.9 (3.2)	80.4 (2.5)	78.9 (4.6)
6	45.3 (2.4)	50.3 (1.8)	57.7 (2.2)	63.6 (4.1)	80.5 (6.2)	80.1 (5.3)

The mean values and coefficients of variation are introduced for specimens at the age of 3, 7, 14, 28, 90, 180, and 780 days. It is observed that the compressive strength increases with the increasing specimens' age. For specimens

3 to 28 days, about 28–37 % increase in the compressive strength is observed for all mixtures, similar to the results described by Rashid et al. [16]. For specimens 28 to 780 days of age, increase in the compressive strength is between 17–27 %, but major increase was happening at the age of around 90 days. At all testing periods, RCWA mixtures are yielded higher compressive strength than the control fine-grained cement composite mixture 1.

The improvement in mechanical properties (flexural and compressive strength) with addition of RWCA is achieved due to the rough shape of ceramic waste aggregate and hence providing more surface area [29]. The obtained results of fracture toughness for fine-grained cement composite with RCWA at the age of 28 days according to equation 1 are presented in Table 4. The increase in fracture toughness is 25 % (for mixture 6). It is worth noticing that fracture toughness for mixture 2 and 6 is characterized by the highest value of the CoV (around 10 %).

The fatigue experiments usually last for a long time, which is problematic from the point of view of the ageing of the specimen material. Because of this, the data obtained from the fatigue tests were standardized to a specimens' age of 28 days. Selected approximation curves (Table 5) obtained from compressive strength values over time were used for this purpose. The used procedure was described in details by Šimonová et al. [26]. The measured values of compressive strength were divided with mean value at the age of 28 days (see respective column in Table 3) and this way the relative values for all investigated ages of specimens were obtained. These values were then approximated by the selected function:

$$y = a \left( 1 - \frac{1}{b^{(c+dx)}} \right), \quad (4)$$

where:  $x$  – time in days;  $y$  – the dimensionless relative value of the compressive strength;  $a$  – coefficient representing an asymptote to the approximation curve expressed as the ratio between the theoretical value of the compressive strength at the age  $t = \infty$  and the determined mean value of compressive strength at the age of 28 days;  $b, c, d$  – coefficients expressing the extent of the time-dependent change of compressive strength in the interval  $t = (0, \infty)$ , which is generally dependent on the parameters of the used mixture and also on the conditions of the environment in which the specimens are stored.

Approximation was performed with nonlinear least-square method provided by genetic algorithms implemented in the open source Java GA package as proposed by Frantik [30].

**Table 4** Fracture toughness, K<sub>IC</sub>

Composite	Mean values $K_{IC}$ (MPa·m <sup>1/2</sup> )	CoV (%)
1	0.543	2.51
2	0.539	9.04
3	0.580	4.63
4	0.649	2.83
5	0.666	2.99
6	0.676	10.70

**Table 5** Coefficients of analytical expressions for approximation curves for compressive strength

Com- posite	Advance approximation curve			
	a	b	c	d
1	1.3637	0.3881	-0.6441	-0.0287
2	1.2559	1.4191	1.9086	0.1049
3	1.2532	0.0973	-0.2537	-0.0161
4	1.3717	0.1292	-0.3168	-0.0131
5	1.2962	0.1264	-0.3383	-0.0148
6	1.2635	0.7766	-2.9255	-0.1331

The coefficients of approximation curves of individual series are presented in Table 5. The formula for fitting the experimentally obtained data from fatigue test used in this paper is based on empirically derived  $S-N$  diagrams known as Wöhler curves:

$$S = a \times N^b \quad (5)$$

where:  $a, b$  – the material constants characterising the  $S-N$  curve.

In an ideal, theoretical case, all specimens at a certain stress level would fail after the same number of cycles. However, the fatigue behaviour of heterogeneous material like fine-grained cement composite is far from being ideal, so the results are usually highly scattered. Accordingly, it is necessary to determine not only the analytical expression of the relevant  $S-N$  curve but also a measure of the scatter, such as the coefficient of determination  $R^2$ . According to the equation (5), the power functions and the coefficient of determination for individual series are introduced in following figures (Fig. 4–9). The crosses represent measured data and diamonds represent data standardized at the age of 28 days.

To have a clear view how replacement of natural aggregate by RCWA influences fatigue life, the endurance of all specimens standardized at the age of 28 days are presented in Fig. 10. It can be seen that the fatigue endurance for fine-grained composites with RCWA are consistently higher than reference composite 1 notably in the long life

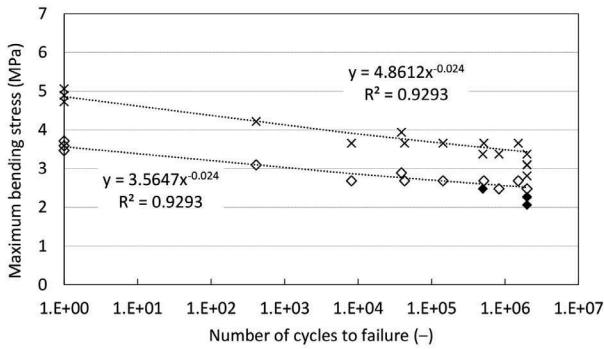


Fig. 4 Fatigue behaviour – mixture 1 (measured and corrected to 28 days age data)

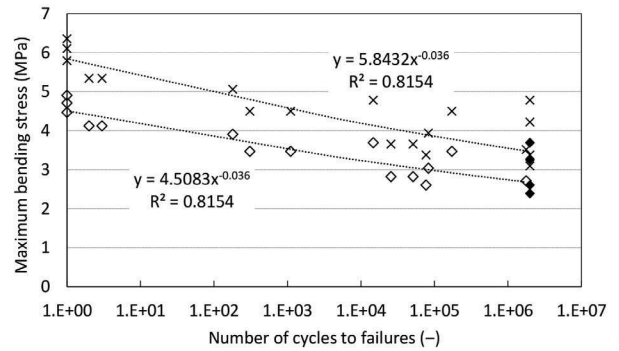


Fig. 8 Fatigue behaviour – mixture 5 (measured and corrected to 28 days age data)

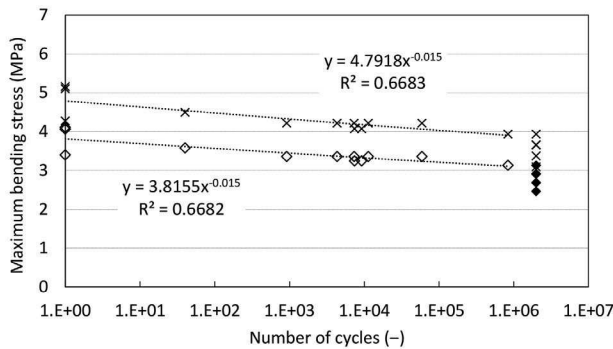


Fig. 5 Fatigue behaviour – mixture 2 (measured and corrected to 28 days age data)

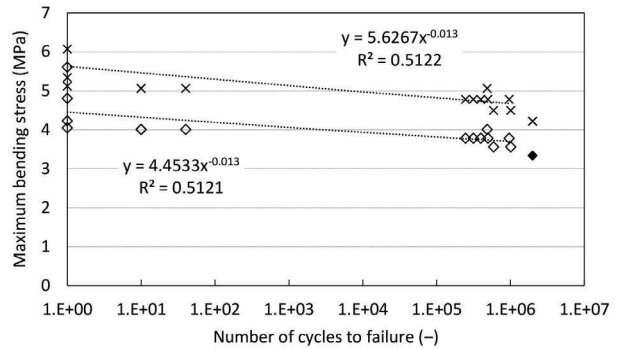


Fig. 9 Fatigue behaviour – mixture 6 (measured and corrected to 28 days age data)

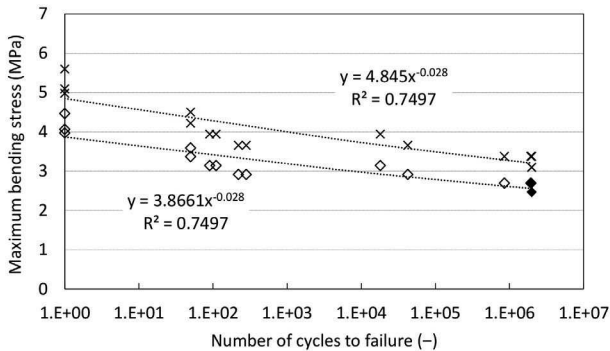


Fig. 6 Fatigue behaviour – mixture 3 (measured and corrected to 28 days age data)

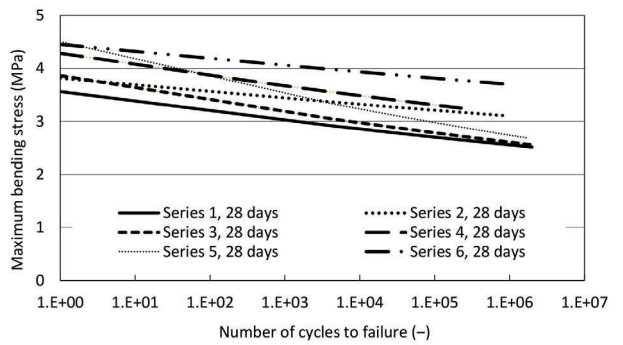


Fig. 10 Mean values of the fatigue performance standardized at the specimens' age of 28 days

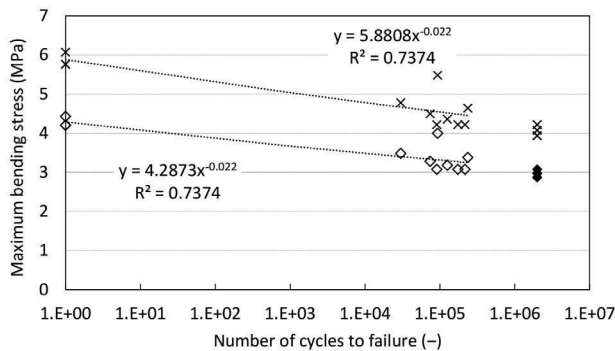


Fig. 7 Fatigue behaviour – mixture 4 (measured and corrected to 28 days age data)

regime ( $2 \times 10^6$  cycles). Basically, with increasing amount of RCWA substitution of natural aggregate the fatigue endurance increases. This trend is as expected from the mechanical analysis because fine-grained composites with RCWA show higher flexural strength.

### 5 Conclusions

The results of this study indicate that the use of RCWA as a replacement for natural aggregate in fine-grained cement composite is certainly feasible and the following conclusions can be drawn from the research programme described in the paper:

1. Mixtures with RCWA allow to achieve the flexural strength, compressive strength and fracture toughness of a cement composite higher than in case of ordinary natural aggregate.
2. With increasing substitution rate of natural aggregate with RCWA the composites bulk density decrease, however, its workability reduces as well.
3. With 36 % replacement of natural sand with RCWA (composite 6) the best fatigue and mechanical fracture properties were achieved.
4. A further study of the influence of the RCWA should be done in order to reveal toughening mechanisms of quasi-brittle materials of this kind.

### Acknowledgement

Financial support from the Czech Science Foundation, project 16-18702S (AMIRI), is gratefully acknowledged. This paper has been worked out under the "National Sustainability Programme I" project "AdMaS UP – Advanced Materials, Structures and Technologies" (No. LO1408) supported by the Ministry of Education, Youth and Sports of the Czech Republic and Brno University of Technology. Results presented in this paper are direct outcome of the specific collaboration agreement between the Koszalin University of Technology, Department of Civil and Environmental Engineering, and the Brno University of Technology, Faculty of Civil Engineering.

### References

- [1] Task Group 3.1 "Environmental Issues in Prefabrication", International Federation for Structural Concrete (fib), Lausanne, Switzerland, Rep. 21, 2003.
- [2] Task Group 3.4 "Environmental Effects of Concrete", International Federation for Structural Concrete (fib), Lausanne, Switzerland, Rep. 23, 2003.
- [3] Behera, M., Bhattacharyya, S. K., Minocha, A. K., Deoliya, R., Maiti, S. "Recycled aggregate from C&D waste & its use in concrete – a breakthrough towards sustainability in construction sector: a review", *Construction and Building Materials*, 68, pp. 501–516, 2014.  
<https://doi.org/10.1016/j.conbuildmat.2014.07.003>
- [4] Limbachiya, M., Meddah, M. S., Ouchagour, Y. "Use of recycled concrete aggregate in fly-ash concrete", *Construction and Building Materials*, 27(1), pp. 439–449, 2012.  
<https://doi.org/10.1016/j.conbuildmat.2011.07.023>
- [5] Arel, H. S. "Recyclability of waste marble in concrete production", *Journal of Cleaner Production*, 131, pp. 179–188, 2016.  
<https://doi.org/10.1016/j.jclepro.2016.05.052>
- [6] Sharma, N. K., Kumar, P., Kumar, S., Thomas, B. S., Gupta, R. C. "Properties of concrete containing polished granite waste as partial substitution of coarse aggregate", *Construction and Building Materials*, 151, pp. 158–163, 2017.  
<https://doi.org/10.1016/j.conbuildmat.2017.06.081>
- [7] Anderson, D. J., Smith, S. T., Au, F. T. K. "Mechanical properties of concrete utilizing waste ceramic as coarse aggregate", *Construction and Building Materials*, 117, pp. 20–28, 2016.  
<https://doi.org/10.1016/j.conbuildmat.2016.04.153>
- [8] de Brito, J., Pereira, A. S., Correia, J. R. "Mechanical behavior of non-structural concrete made with recycled ceramic aggregates", *Cement and Concrete Composites*, 27(4), pp. 429–433, 2005.  
<https://doi.org/10.1016/j.cemconcomp.2004.07.005>
- [9] Cichocki, K., Domski, J., Katzer, J., Ruchwa, M. "Impact resistant concrete elements with nonconventional reinforcement", *Rocznik Ochrona Srodowiska*, 16(2), pp. 1–92, 2014. Available at [http://www.ros.edu.pl/images/roczniki/2014/pp\\_2014\\_02\\_01.pdf](http://www.ros.edu.pl/images/roczniki/2014/pp_2014_02_01.pdf) [Accessed: 05.12.2018]
- [10] Correia, J. R., de Brito, J., Pereira, A. S. "Effects on concrete durability of using recycled ceramic aggregates", *Materials and Structures*, 39(2), pp. 169–177, 2006.  
<https://doi.org/10.1617/s11527-005-9014-7>
- [11] Lapko, A., Grygo, R. "Effectiveness of the use of recycling aggregate concrete for sustainable building structure", *Rocznik Ochrona Srodowiska*, 16(1), pp. 627–638, 2014. Available at [http://www.ros.edu.pl/images/roczniki/2014/pp\\_2014\\_01\\_39.pdf](http://www.ros.edu.pl/images/roczniki/2014/pp_2014_01_39.pdf) [Accessed: 05.12.2018]
- [12] Andreola, F., Barbieri, L., Lancellotti, I., Leonelli, C., Manfredini, T. "Recycling of industrial waste in ceramic manufacturing: State of art and glass case studies", *Ceramics International*, 42(12), pp. 13333–13338, 2016.  
<https://doi.org/10.1016/j.ceramint.2016.05.205>
- [13] Hendriks, Ch. F., Janssen, G. M. T. "Use of recycled materials in construction", *Materials and Structures*, 36(9), pp. 604–608, 2003.  
<https://doi.org/10.1007/BF02483280>
- [14] Senthamarai, R. M., Manoharan, P. D. "Concrete with ceramic waste aggregate", *Cement and Concrete Composites*, 27(9–10), pp. 910–913, 2005.  
<https://doi.org/10.1016/j.cemconcomp.2005.04.003>
- [15] European Standards "Methods of testing cement. Determination of strength, BS EN 196-1", BSI Standards, London, United Kingdom, 2005.
- [16] Rashid, K., Razzaq, A., Ahmad, M., Rashid, T., Tariq, S. "Experimental and analytical selection of sustainable recycled concrete with ceramic waste aggregate", *Construction and Building Materials*, 154, pp. 829–840, 2017.  
<https://doi.org/10.1016/j.conbuildmat.2017.07.219>
- [17] Medina, C., Frías, M., de Rojas, M. I. S. "Microstructure and properties of recycled concretes using ceramic sanitary ware industry waste as coarse aggregate", *Construction and Building Materials*, 31, pp. 112–118, 2012.  
<https://doi.org/10.1016/j.conbuildmat.2011.12.075>
- [18] Matar, W., Elshurafa, A. M. "Striking a balance between profit and carbon dioxide emissions in the Saudi cement industry", *International Journal of Greenhouse Gas Control*, 61, pp. 111–123, 2017.  
<https://doi.org/10.1016/j.ijggc.2017.03.031>

- [19] Karihaloo, B. L. "Fracture Mechanics and Structural Concrete", 1st ed., Longman Scientific & Technical, Harlow, U.K., 1995.
- [20] Pazdera, L., Topolář, L., Šimonová, H., Fojtu, P., Smutný, J., Havlíková, I., Keršner, Z., Rodriguezová, V. "Determine parameters for double-K model at three-point bending by application of acoustic emission method", Applied Mechanics and Materials, 486, pp. 151–156, 2014.  
<https://doi.org/10.4028/www.scientific.net/amm.486.151>
- [21] Veselý, V., Konečný, P., Lehner, P. "Influence of crack propagation on electrical resistivity and ultrasonic characteristics of normal concrete assessed by sequential TPB fracture test", Theoretical and Applied Fracture Mechanics, 80(A), pp. 2–13, 2015.  
<https://doi.org/10.1016/j.tafmec.2015.09.005>
- [22] Tada, H., Paris, P. C., Irwin, G. R. "The Stress Analysis of Cracks Handbook", 3rd ed., The American Society of Mechanical Engineers, New York, U.S.A., 2000.  
<https://doi.org/10.1115/1.801535>
- [23] Wu, S.-X. "Crack length calculation formula for three point bend specimens", International Journal of Fracture, 24(1), pp. R33–R38, 1984.  
<https://doi.org/10.1007/bf00020275>
- [24] Lee, M. K., Barr, B. I. G. "An overview of the fatigue behavior of plain and fibre reinforced concrete", Cement and Concrete Composites, 26(4), pp. 299–305, 2004.  
[https://doi.org/10.1016/s0958-9465\(02\)00139-7](https://doi.org/10.1016/s0958-9465(02)00139-7)
- [25] Seitl, S., Šimonová, H., Keršner, Z., Canteli, A. F. "Evaluation of concrete fatigue measurement using standard and non-linear regression model", Applied Mechanics and Materials, 121–126, pp. 2726–2729, 2012.  
<https://doi.org/10.4028/www.scientific.net/AMM.121-126.2726>
- [26] Šimonová, H., Kucharczyková, B., Havlíková, I., Seitl, S., Keršner, Z. "Complex Evaluation of Fatigue Tests Results of Plain C30/37 and C45/55 Class Concrete Specimen", Key Engineering Materials, 592–593, pp. 801–804, 2014.  
<https://doi.org/10.4028/www.scientific.net/kem.592-593.801>
- [27] Seitl, S., Miarka, P., Klusák, J., Domski, J., Katzer, J., Šimonová, H., Keršner, Z. "Change of a Crack Propagation Rate in Fine-grained Cement-based Composites due to Partial Replacement of Aggregate by Ceramic Waste", Key Engineering Materials, 761, pp. 111–115, 2018.  
<https://doi.org/10.4028/www.scientific.net/KEM.761.111>
- [28] Seitl, S., Vizslay, V., Domski, J., Katzer, J. "Fracture Mechanical Properties of Cement Based Composites with Various Amount of Waste Aggregates", Procedia Engineering, 190, pp. 345–351, 2017.  
<https://doi.org/10.1016/j.proeng.2017.05.347>
- [29] Mehta, P. K., Monteiro, P. J. M. "Concrete: Microstructure, Properties, and Materials", 3rd ed., McGraw-Hill Education, New York City, New York, United States, 2006.
- [30] Frantik, P., Java GA package, GNU GPL licence, 2018. Available at <http://www.kitnarf.cz/java> [Accessed: 05.12.2018]

## CONCLUDING REMARKS

The habilitation thesis summarizes the results and knowledge obtained by solving many partial tasks within the framework of research projects solved at the FCE, BUT in which the author has been involved since 2010. The main emphasis is put on the experimental determination of mechanical fracture and fatigue characteristics of various types of commonly used but also newly developed building composites with the brittle matrix.

The effective solution of comprehensive research tasks requires the cooperation of experts from various scientific fields. Therefore, the author of this thesis has had the opportunity to cooperate with experts from different institutes of the FCE, BUT and also colleagues from foreign universities since the beginning of her research career. This led to the author's engagement in the characterization of fracture behaviour of a whole range of different types of quasi-brittle materials: from mortars/fine-grained composites (lime with different admixtures such as brick powder, metakaolin, bentonite, metaclay [64]; cement with the admixture of slag, fly ash, metakaolin, brick powder, glass powder, zeolite [65–69]; alkali activated slag with different admixtures [70, 71]; alkali activated brick powder [72]; geopolymers with the admixture of nanotubes, different types of fibres [73–75]) to plenty of types of concrete such as plain concrete of different composition (water/cement ratio, with/without superplasticizer [76–78]); concrete with fibres (different types/length/volume of fibres [79, 80]); and composites based on AABs [81, 82]. Also, the fatigue parameters of different types of quasi-brittle materials were investigated [62, 82–84].

Mechanical fracture parameters are primarily obtained through the direct evaluation of fracture test data via the EFM [4] and  $2K$  model [47] and the work-of-fracture method recommended by RILEM [6]. In addition, selected experimental data are used to determination of mechanical fracture parameters indirectly – based on a combination of fracture testing and inverse analysis. The fracture response recorded from the 3PB test of specimens made of selected fine-grained composites is used for verification of the proposed hybrid artificial neural network-based identification system [50, 85]. The parameters which can be obtained from the inverse analysis are important, as they can be used to quantify structural resistance against crack initiation and propagation, as well as to compare studied or developed composites. They can also be employed for the definition of material models for the deterministic or stochastic simulation of the quasi-brittle/ductile response of composites/members using a stochastic finite element method (FEM) model based on non-linear fracture mechanics principles.

The mechanical fracture parameters help us to understand the relation between the macroscopic response of the specimen and its microstructural evolution during cracking of course considering size-effect [3]. This is crucial in the design and modelling of newly developing composites, as well as in the comparison of properties of commonly used and newly develop quasi-brittle composites. These parameters can be beneficial also in the assessment of internal damage of quasi-brittle materials caused by temperature changes. The alternate of the positive and negative temperatures (freeze–thaw cycles) is considered one of the most destructive processes which influence the durability of the structures substantially. As well high

temperatures acting on quasi-brittle materials cause a wide range of physical and chemical processes, which result in changes in the structure of composites and thus affect the mechanical properties. The mechanical fracture parameters bring more complex information about material damage caused by low [86, 87] and high temperatures [88, 89] than standardized methods. Nevertheless, in many cases, the attention is still focused on the maximum strength of the material rather than analyzing the properties associated with resistance to crack formation and propagation.

## REFERENCES

1. Červenka, V., Jendele, L., Červenka, J. *ATENA Program documentation – Part 1: theory*. Červenka Consulting: Prague, 2016.
2. Frantík, P. *FyDiK application*, 2015. <http://fydik.kitnarf.cz/>
3. Bažant, Z.P., Planas, J. *Fracture and Size Effect in Concrete and other Quasibrittle Materials*. CRC Press: Boca Raton, 1998, 640 p.
4. Karihaloo, B.L. *Fracture mechanics and structural concrete*. Longman Scientific & Technical: Harlow, Essex, England, 1995, 330 p.
5. Shah, S.P., Swartz, S.E., Ouyang, Ch. *Fracture mechanics of structural concrete: applications of fracture mechanics to concrete, rock, and other quasi-brittle materials*, 1<sup>st</sup> ed.; John Wiley & Sons, Inc.: New York, 1995, 592 p.
6. RILEM TC – 50 FMC (Recommendation). Determination of the fracture energy of mortar and concrete by means of three-point bend tests on notched beams. *Materials & Structures*. 1985, Vol. 18(4), pp. 287–290. <https://doi.org/10.1007/BF02472918>
7. RILEM TC– 89 FMT (Recommendation). Size-effect method for determining fracture energy and process zone size of concrete. *Materials & Structures*. 1990, Vol. 23, pp. 461–465.
8. Frantík, P. *CheCyId application*, 2017. <http://checyid.kitnarf.cz>
9. Novák, D., Lehký, D. ANN inverse analysis based on stochastic small-sample training set simulation. *Engineering Applications of Artificial Intelligence*. 2006, Vol. 19(7), pp. 731–740. <https://doi.org/10.1016/j.engappai.2006.05.003>
10. Lehký, D., Novák, D., Keršner, Z. FraMePID-3PB software for material parameter identification using fracture tests and inverse analysis. *Advances in Engineering Software*. 2014, Vol. 72, pp. 147–154. <https://doi.org/10.1016/j.advengsoft.2013.10.001>
11. Brühwiler, E., Wittmann, F.H. The wedge splitting test, a new method of performing stable fracture mechanics tests. *Engineering Fracture Mechanics*. 1990, Vol. 35(1–3), pp. 117–125. [https://doi.org/10.1016/0013-7944\(90\)90189-N](https://doi.org/10.1016/0013-7944(90)90189-N)
12. Tschegg, E.K. New equipments for fracture tests on concrete. *Materials Testing*. 1991, Vol. 33, pp. 338–342.
13. Lee, M.K., Barr, B.I.G. An overview of the fatigue behavior of plain and fibre reinforced concrete. *Cement and Concrete Composites*. 2004, Vol. 26 (4), pp. 299–305. [https://doi.org/10.1016/S0958-9465\(02\)00139-7](https://doi.org/10.1016/S0958-9465(02)00139-7)
14. Pryl, D., Červenka, J., Pukl, R. Material model for finite element modelling of fatigue crack growth in concrete. *Procedia Engineering*. 2010, Vol. 2 (1), pp. 203–212. <https://doi.org/10.1016/j.proeng.2010.03.022>
15. Toumi, A., Bascoul, A., Turatsinze, A. Modeling of fatigue crack growth in concrete subjected to mode I crack opening. In *Proc. of the 4<sup>th</sup> Int. Conf. on Fracture Mechanics of Concrete Structures*, de Borst, R. et al, eds. CRC Press: United Kingdom, 2001, pp. 637–640
16. Darweesh, H.H.M. Mortar Composites Based on Industrial Wastes. *International Journal of Materials Lifetime*. 2017, Vol. 3, No. 1, pp. 1–8. doi: 10.12691/ijml-3-1-1
17. Keun-Hyeok, Y., Yeon-Back, J., Myung-Sug, C., Sung-Ho, T. Effect of supplementary cementitious materials on reduction of CO<sub>2</sub> emissions from concrete. *Journal of Cleaner Production*. 2015, Vol. 103, pp. 774–783. <https://doi.org/10.1016/j.jclepro.2014.03.018>
18. Keun-Hyeok, Y., Jin-Kyu, S., Keum-Il, S. Assessment of CO<sub>2</sub> reduction of alkali-activated concrete. *Journal of Cleaner Production*. 2013, Vol. 39, pp. 265–272. <https://doi.org/10.1016/j.jclepro.2012.08.001>

19. McLellan, B.C., Williams, R.P., Lay, J., van Riessen, A., Corder, G.D. Costs and carbon emissions for geopolymers in comparison to ordinary Portland cement. *Journal of Cleaner Production*. 2011, Vol. 19(10), pp. 1080–1090. <https://doi.org/10.1016/j.jclepro.2011.02.010>
20. Chen, W., Jin, R., Xu, Y., Wanatowski, D., Li, B., Yan, L., Pan, Z., Yang, Y. Adopting recycled aggregates as sustainable construction materials: A review of the scientific literature. *Construction and Building Materials*. 2019, Vol. 218, pp. 483–496. <https://doi.org/10.1016/j.conbuildmat.2019.05.130>.
21. Rodrigues, F., Carvalho, M.T., Evangelista, L., de Brito, J. Physical–chemical and mineralogical characterization of fine aggregates from construction and demolition waste recycling plants. *Journal of Cleaner Production*. 2013, Vol. 52, pp. 438–445. <https://doi.org/10.1016/j.jclepro.2013.02.023>.
22. Tošić, N. Marinković, S. Dašić, T. Stanić, M. Multicriteria optimization of natural and recycled aggregate concrete for structural use, *Journal of Cleaner Production*. 2015, Vol. 87, pp. 766–776. <https://doi.org/10.1016/j.jclepro.2014.10.070>.
23. Sharma, N.K., Kumar, P., Kumar, S., Thomas, B.S., Gupta, R.C. Properties of concrete containing polished granite waste as partial substitution of coarse aggregate. *Construction and Building Materials*. 2017, Vol. 151, pp. 158–163. <https://doi.org/10.1016/j.conbuildmat.2017.06.081>
24. Anderson, D.J., Smith, S.T., Au, F.T.K. Mechanical properties of concrete utilizing waste ceramic as coarse aggregate. *Construction and Building Materials*. 2016, Vol. 117, pp. 20–28. <https://doi.org/10.1016/j.conbuildmat.2016.04.153>
25. Johnston, C.D. *Fiber-reinforced Cements and Concretes*. Taylor & Francis Group: London, 2010, 261p.
26. Smarzewski, P. Influence of basalt-polypropylene fibres on fracture properties of high performance concrete. *Composite Structures*. 2019, Vol. 209, pp. 23–33. <https://doi.org/10.1016/j.compstruct.2018.10.070>
27. Kizilkanat, A.B., Kabay, N., Akyüncü, V., Chowdhury, S., Akça, A.H. Mechanical properties and fracture behavior of basalt and glass fiber reinforced concrete: An experimental study. *Construction and Building Materials*. 2015, Vol. 100, pp. 218–224. <https://doi.org/10.1016/j.conbuildmat.2015.10.006>
28. Zhou, X., SAINi, H., Kastiukas, G. Engineering Properties of Treated Natural Hemp Fiber-Reinforced Concrete. *Frontiers in Building Environment*. 2017, Vol. 3, Article 33. <https://doi.org/10.3389/fbuil.2017.00033>
29. Zanichelli, A., Carpinteri, A., Fortese, G., Ronchei, C., Scorza, D., Vantadori, S. Contribution of date-palm fibres reinforcement to mortar fracture toughness. *Procedia Structural Integrity*. 2018, Vol. 13, pp. 542–547. <https://doi.org/10.1016/j.prostr.2018.12.089>
30. Tattersall, H.G., Tappin, G. The work of fracture and its measurement in metals, ceramics and other materials. *Journal of Materials Science*. 1966, Vol. 1, pp. 296–301. doi: 10.1007/BF00550177
31. Ouchterlony, F. Suggested methods for determining the fracture toughness of rocks. *International Journal of Rock Mechanics and Mining Sciences*. 1988, Vol. 25, Iss. 2, pp. 71–96.
32. Šimonová, H., Daněk, P., Frantík, P., Keršner, Z., Veselý, V. Tentative characterization of old structural concrete through mechanical fracture parameters. *Procedia Engineering: Structural and Physical Aspects of Construction Engineering*. 2017, Vol. 109, pp. 414–418. doi: 10.1016/j.proeng.2017.05.357
33. Kucharczyková, B., Šimonová, H., Kocáb, D., Topolář, L. Advanced Evaluation of the Freeze–Thaw Damage of Concrete Based on the Fracture Tests. *Materials*. 2021, Vol. 14, Article No. 6378. doi: <https://doi.org/10.3390/ma14216378>

34. Merta, I., Tschegg, E.K. Fracture energy of natural fibre reinforced concrete. *Construction and Building Materials*. 2013, Vol. 40, pp. 991–997. <https://doi.org/10.1016/j.conbuildmat.2012.11.060>
35. Lehký, D., Kucharczyková, B., Šimonová, H., Daněk, P. Comprehensive fracture tests of concrete for the determination of mechanical fracture parameters. *Structural Concrete*. 2022, Vol. 23, Iss. 1, pp. 505–520. ISSN 1464-4177. <https://doi.org/10.1002/suco.202000496>
36. Irwin, G.R. Analysis of Stress and Strains Near the End of a Crack Traversing the Plate. *Journal of Applied Mechanics*. 1957, Vol. 24, pp. 361–364.
37. Kuruppu, M.D., Chong, K.P. Fracture toughness testing of brittle materials using semi-circular bend (SCB) specimen. *Engineering Fracture Mechanics*. 2012, Vol. 91, pp. 133–150. <https://doi.org/10.1016/j.engfracmech.2012.01.013>
38. Razmi, A., Mirsayar, M.M. On the mixed mode I/II fracture properties of jute fiber-reinforced concrete. *Construction and Building Materials*. 2017, Vol. 148, pp. 512–520. <https://doi.org/10.1016/j.conbuildmat.2017.05.034>
39. Erarslan, N. Analysing mixed mode (I–II) fracturing of concrete discs including chevron and straight-through notch cracks. *International Journal of Solids and Structures*. 2019, Vol. 167, pp. 79–92. <https://doi.org/10.1016/j.ijsolstr.2019.03.005>
40. Xing, Y., Huang, B., Ning, E., Zhao, L., Jin, F. Quasi-Static Loading Rate Effects on Fracture Process Zone Development of Mixed-Mode (I-II) Fractures in Rock-Like Materials. *Engineering Fracture Mechanics*. 2020, Vol. 240, Article No. 107365. <https://doi.org/10.1016/j.engfracmech.2020.107365>
41. Alanazi, N., Susmel, L. Estimating static/dynamic strength of notched unreinforced concrete under mixed mode I/II loading. *Engineering Fracture Mechanics*. 2020, Vol. 240, Article No. 107329. <https://doi.org/10.1016/j.engfracmech.2020.107329>
42. Ruiz, G., de la Rosa, A., Almeida, L.C., Poveda, E., Zhang, X.X., Tarifa, M., Wu, Z.M., Yu, R.C. Dynamic mixed-mode fracture in SCC reinforced with steel fibers: an experimental study. *Int J Impact Eng* 2019, Vol. 129, pp. 101–111. <https://doi.org/10.1016/j.ijimpeng.2019.03.003>
43. Aliha, M.R.M., Mousavi, S.S., Ghoreishi, S.M.N. Fracture load prediction under mixed mode I+II using a stress based method for brittle materials tested with the asymmetric four-point bend specimen. *Theoretical and Applied Fracture Mechanics*. 2019, Vol. 103, Article No. 102249. <https://doi.org/10.1016/j.tafmec.2019.102249>
44. Malíková, L., Miarka, P., Kucharczyková, B., Šimonová, H. Williams expansion utilized for assessment of crack behaviour under mixed-mode loading in alkali-activated fine-grained composite. *Fatigue & Fracture of Engineering Materials & Structures*. 2021, Vol. 44, Iss. 5, pp. 1151–1161. <https://doi.org/10.1111/ffe.13418>
45. Frantík, P., Mašek, J. GTDiPS software, 2015. Available online: <http://gtdips.kitnarf.cz/>
46. Stibor, M. *Fracture Parameters of Quasi-Brittle Materials and Their Determination* (in Czech). Dissertation thesis, Brno University of Technology, Brno, 2004.
47. Kumar, S., Barai, S.V. *Concrete Fracture Models and Applications*. Springer: Berlin, 2011, 262 p.
48. Hordijk, D.A. *Local approach to fatigue of concrete*. PhD Thesis, Technische Universiteit Delft, Delft, Netherlands, 1991.
49. Lehký, D., Keršner, Z., Novák, D. FraMePID-3PB software for material parameter identification using fracture tests and inverse analysis. *Advances in Engineering Software*. 2014, Vol. 72, pp. 147–154. <https://doi.org/10.1016/j.advengsoft.2013.10.001>
50. Lehký, D., Lipowczan, M., Šimonová, H., Keršner, Z. 2021. A hybrid artificial neural network-based identification system for fine-grained composites. *Computers and Concrete*. 2021, Vol. 28, Iss. 4, pp. 369–378. doi: <https://doi.org/10.12989/cac.2021.28.4.369>

51. Jenq, Y.S., Shah, S.P. Two parameter fracture model for concrete. *Journal of Engineering Mechanics*. 1985, Vol. 111, Iss. 10, pp. 1227–1241. [https://doi.org/10.1061/\(ASCE\)0733-9399\(1985\)111:10\(1227\)](https://doi.org/10.1061/(ASCE)0733-9399(1985)111:10(1227))
52. Xu, S., Reinhardt, H.W. Determination of double-K criterion for crack propagation in quasibrittle fracture, Part II: Analytical evaluating and practical measuring methods for three-point bending notched beams. *International Journal of Fracture*. 1999, Vol. 98, Iss. 2, pp. 151–177. <https://doi.org/10.1023/a:1018740728458>
53. Miura, T., Sato, K., Nakamura, H. Influence of primary cracks on static and fatigue compressive behavior of concrete under water. *Construction and Building Materials*. 2021, Vol. 305, Article No. 124755. <https://doi.org/10.1016/j.conbuildmat.2021.124755>
54. Zhang J., Stang H., Li V.C. Experimental study on crack bridging in FRC under uniaxial fatigue tension. *Journal of Materials in Civil Engineering*. 2000, Vol. 12, Iss. 1, pp. 66–73. [https://doi.org/10.1061/\(ASCE\)0899-1561\(2000\)12:1\(66\)](https://doi.org/10.1061/(ASCE)0899-1561(2000)12:1(66))
55. Saini, B.S., Singh, S.P. Flexural fatigue life analysis of self compacting concrete containing 100% coarse recycled concrete aggregates. *Construction and Building Materials*. 2020, Vol. 253, Article No. 119176. <https://doi.org/10.1016/j.conbuildmat.2020.119176>
56. Zhang, J., Li, V.C., Stang, H. Size effect on fatigue in bending of concrete. *Journal of Materials in Civil Engineering*. 2001, Vol. 13, Iss. 6, pp. 446–453. [https://doi.org/10.1061/\(ASCE\)0899-1561\(2001\)13:6\(446\)](https://doi.org/10.1061/(ASCE)0899-1561(2001)13:6(446))
57. Kirane, K., Bažant, Z.P. Size effect in Paris law and fatigue lifetimes for quasibrittle materials: Modified theory, experiments and micro-modeling. *International Journal of Fatigue*. 2016, Vol. 83, pp. 209–220. <https://doi.org/10.1016/j.ijfatigue.2015.10.015>
58. Miarka, P., Seitzl, S., Bílek, V., Cifuentes, H. Assessment of fatigue resistance of concrete: *S-N* curves to the Paris' law curves. *Construction and Building Materials*. 2021, Vol. 341, Article No. 127811. <https://doi.org/10.1016/j.conbuildmat.2022.127811>
59. RILEM Committee 36-RD. Long term random dynamic loading of concrete structures, *Materials & Structures*. 1984, Vol. 17, Iss. 97, pp. 1–28.
60. Věchet, S., Král, P. *Únava materiálu: Únava materiálu úvod*. In NoM I – 6, *Únava materiálu*, 2007. p. 1–9.
61. Weibull, W. *Fatigue testing and analysis of results*. Pergamon press: Oxford, 1961.
62. Šimonová, H., Havlíková, I., Keršner, Z., Seitzl, S. Statistical evaluation of fatigue tests of plain C30/37 and C45/55 class concrete specimens. In: *Proc. of 8th Int. Conf. on Fracture Mechanics of Concrete and Concrete Structures, FraMCoS-8*. Barcelona: International Center for Numerical Methods in Engineering (CIMNE), 2013, pp. 862–867.
63. Abdel-Jawad, Y.A. The maturity method: Modifications to improve estimation of concrete strength at later ages. *Construction and Building Materials*. 2006, Vol. 20, pp. 893–900. <https://doi.org/10.1016/j.conbuildmat.2005.06.022>
64. Šimonová, H., Havlíková, I., Navrátilová, E., Schmid, P., Rovnaníková, P., Keršner, Z. Effect of Admixture Dosage and Specimens Age on Mechanical Fracture Parameters of Lime Mortars Enhanced by Burnt Clays. *Advanced Materials Research: Ecology and New Building Materials and Products*. 2014, Vol. 1000, pp. 356–359. [www.scientific.net/AMR.1000.356](http://www.scientific.net/AMR.1000.356)
65. Bílek, V. Jr., Topolář, L., Šimonová, H., Kucharczyková, B., Havlíková, I., Pazdera, L., KERŠNER, Z. Pilot Study of the Effect of Admixtures in Fine-grained Cement-based Composites on Volume Changes and Fracture Parameters. *Advanced Materials Research: Structural and Physical Aspects of Civil Engineering*. 2014, Vol. 969, pp. 294–297.

66. Rovnaníková, P., Šimonová, H., Schmid, P., Zahálková, J., Bayer, P., Havlíková, I., Keršner, Z. Mechanical Fracture properties of Cement Mortars with Diatomite in relation to their Microstructure. *Advanced Materials Research: Ecological and New Building Materials and Products*. 2015, Vol. 1124, pp. 57–62. doi: 10.4028/www.scientific.net/AMR.1124.57
67. Šimonová, H., Zahálková, J., Rovnaníková, P., Bayer, P., Keršner, Z., Schmid, P. Mechanical Fracture Parameters of Cement Based Mortars with Waste Glass Powder. *Procedia Engineering: Structural and Physical Aspects of Construction Engineering*. 2017, Vol. 109, pp. 86–91. ISSN 1877-7058. doi: 10.1016/j.proeng.2017.05.311
68. Šimonová, H., Schmid, P., Keršner, Z., Rovnaníková, P. Mechanical Fracture Parameters of Fine-grain Concretes with Zeolite: Effect of Composition and Origin of Cements. *Advanced Materials Research: Ecology and New Building Materials and Products*. 2014, Vol. 1000, pp. 330–333. www.scientific.net/AMR.1000.330.
69. Havlikova, I., Bilek, V. Jr., Topolar, L., Simonova, H., Schmid, P., Kersner, Z. Modified Cement-based Mortars: Crack Initiation and Volume Changes. *Materiali in technologie/Materials and technology*. 2015, Vol. 49, Issue 4, pp. 557–561
70. Rovnaník, P., Šimonová, H., Topoláč, L., Bayer, P., Schmid, P., Keršner, Z. Carbon nanotube reinforced alkali-activated slag mortars. *Construction and Building Materials*. 2016, Vol. 119, pp. 223–229. <http://dx.doi.org/10.1016/j.conbuildmat.2016.05.051>
71. Šimonová, H., Frantík, P., Keršner, Z., Schmid, P., Rovnaník, P. Components of the fracture response of alkali-activated slag composites with steel microfibers. *Applied Sciences*. 2019, Vol. 9, No. 9, Article No.1754. <https://doi.org/10.3390/app909175>
72. Šimonová, H., Lipowczan, M., Rozsypalová, I., Daněk, P., Lehký, D., Rovnaníková, P., KERŠNER, Z. Fracture parameters of alkali-activated aluminosilicate composites with ceramic precursor: durability aspects. *Procedia Structural Integrity*. 2021, Vol. 33, pp. 207–214. doi: 10.1016/j.prostr.2021.10.025
73. Šimonová, H., Topolář, L., Schmid, P., Keršner, Z., Rovnaník, P. Effect of Carbon Nanotubes in Metakaolin-based Geopolymer Mortars on Fracture Toughness Parameters and Acoustic Emission Signals. *Brittle Matrix Composites 11*. Warsaw: ZTUREK Research-Scientific Institute and Institute of Fundamental Technological Research, 2015, pp. 261–267.
74. Rovnaník, P., Šimonová, H., Topolář, L., Schmid, P., Keršner, Z. Effect of carbon nanotubes on the mechanical fracture properties of fly ash geopolymer. *Procedia Engineering: Ecology and new building materials and products 2016*. Elsevier, 2016, Vol. 151, pp. 321–328. <http://dx.doi.org/10.1016/j.proeng.2016.07.360>
75. Simonova, H., Kucharczykova, B., Topolar, L., Kersner, Z., Merta, I., Dragas, J., Ignjatovic, I., Komljenovic, M., Nikolic, V. Crack initiation of selected geopolymer mortar with hemp fibres. *Procedia Structural Integrity: ECF22 – Loading and Environmental effects on Structural Integrity*. 2018, Vol. 13, pp. 578–583. <https://doi.org/10.1016/j.prostr.2018.12.095>
76. Šimonová, H., Daněk, P., Frantík, P., Keršner, Z., Veselý, V. Tentative characterization of old structural concrete through mechanical fracture parameters. *Procedia Engineering: Structural and Physical Aspects of Construction Engineering*. 2017, Vol. 109, pp. 414–418. doi: 10.1016/j.proeng.2017.05.357
77. Lehký, D., Kucharczyková, B., Šimonová, H., Daněk, P. Comprehensive fracture tests of concrete for the determination of mechanical fracture parameters. *Structural Concrete*. 2022, Vol. 23, Iss. 1, pp. 505–520. <https://doi.org/10.1002/suco.202000496>

78. Šimonová, H., Havlíková, I., Daněk, P., Keršner, Z., Vymazal, T. The Effect of a Superplasticizer Admixture on the Mechanical Fracture Parameters of Concrete. *Materiali in technologie/Materials and technology*. 2015, Vol. 49, Issue 3, pp. 417–421.
79. Havlíková, I., Šimonová, H., Pail, T., Navrátilová, E., Majtánová, R. V., Keršner, Z. Effect of Softening Function Type in the Double-K Fracture Model for the Evaluation of Fracture Tests on Concrete Specimens with and without polypropylene Fibres. *Proc. of Int. Conf. on ENGINEERING MECHANICS 2013*. Praha: Institute of Thermomechanics, Academy of Sciences of the Czech Republic, v. v. i., 2013, pp. 152–159.
80. Lehký, D., Řoutil, L., Keršner, Z., Novák, D., Šimonová, H., Havlíková, I., Schmid, P. Experimental determination of mechanical fracture parameters of steel fiber reinforced concrete for probabilistic life-cycle assessment. *Concrete – Innovation and Design, fib Symposium Proceedings*. Copenhagen, Denmark: Danish Concrete Society, 2015, pp. 1–8.
81. Šimonová, H., Kucharczyková, B., Topolář, L., Bílek, V., Jr., Keršner, Z. Fracture properties of concrete specimens made from alkali activated binders. *IOP Conf. Series: Materials Science and Engineering*. 2017, Vol. 236, 012068. doi:10.1088/1757-899X/236/1/012068
82. Seitzl, S., Bílek, V., Šimonová, H., Keršner, Z. Mechanical and fatigue parameters of two types of alkali-activated concrete. *Key Engineering Materials: Advances in Fracture and Damage Mechanics XIV*. 2016, Vol. 665, pp. 129–132. doi: 10.4028/www.scientific.net/KEM.665.129
83. Seitzl, S., Miarka, P., Šimonová, H., Frantík, P., Keršner, Z., Domski, J., Katzer, J. Change of Fatigue and Mechanical Fracture Properties of a Cement Composite due to Partial Replacement of Aggregate by Red Ceramic Waste. *Periodica Polytechnica Civil Engineering*. 2019, Vol. 63, No. 1, pp. 152–159. <https://doi.org/10.3311/PPci.12450>
84. Šimonová, H., Veselý, V., Keršner, Z., Culík, L., Mosler, T., Bílek, V. Influence of the Age and Level of Concrete fatigue on Prestressed Railway Sleepers Response: Parametric Study and Experiment. *Advanced Materials Research: Structural and Physical Aspects of Civil Engineering*. 2014, Vol. 969, pp. 218–221.
85. Lipowczan, M., Lehký, D., Šimonová, H., Kucharczyková, B., Keršner, Z. Identification of mechanical fracture parameters of fine-grained brittle matrix composites. *Proceedings of the 2021 session of the 13th fib International PhD Symposium in Civil Engineering*. Switzerland: International Federation for Structural Concrete, 2021, pp. 10–17.
86. Kucharczyková, B., Šimonová, H., Kocáb, D., Topolář, L. Advanced Evaluation of the Freeze–Thaw Damage of Concrete Based on the Fracture Tests. *Materials*. 2021, Vol. 14, Article No. 6378. doi: <https://doi.org/10.3390/ma14216378>
87. Kucharczyková, B., Šimonová, H., Kocáb, D., Fernandes, G. Non-traditional Approach to the Evaluation of the Freeze-thaw Resistance of Concrete based on the Fracture Tests. *MATEC Web of Conferences, MATBUD'2020 – Scientific-Technical Conference: E-mobility, Sustainable Materials and Technologies*. 2020, Vol. 322, Article No. 01015. doi: <https://doi.org/10.1051/matecconf/202032201015>
88. Šimonová, H., Rozsypalová, I., Rovnaníková, P., Daněk, P., Keršner, Z. Thermal Analysis of Concrete from Panels Subjected to Fire Experiments. *Solid State Phenomena: 24th Concrete Days 2017*. 2018, Vol. 272, pp. 47–52. doi: 10.4028/www.scientific.net/SPP.272.47
89. Šimonová, H., Trčka, T., Bejček, M., Rozsypalová, I., Daněk, P., Keršner, Z. Detailed Determination of Mechanical Fracture Parameters of Concrete after Fire Experiments. *Solid State Phenomena: 24th Concrete Days 2017*. 2018, Vol. 272, pp. 220–225. doi: 10.4028/www.scientific.net/SPP.272.220

## LIST OF ABBREVIATIONS AND SYMBOLS

### Abbreviations

AAB	alkali-activated binder
AAS	alkali-activated slag
BUT	Brno University of Technology
CAS	Czech Academy of Sciences
<i>CMOD</i>	crack mouth opening displacement
<i>CMOD</i> <sub><i>F</i><sub>max</sub></sub>	crack mouth opening displacement corresponding to maximum load <i>F</i> <sub>max</sub>
<i>COD</i>	crack opening displacement
<i>COD</i> <sub><i>c</i></sub>	critical crack opening displacement
CO <sub>2</sub>	carbon dioxide
<i>CTOD</i> <sub><i>c</i></sub>	critical crack tip opening displacement
DIC	digital image correlation
ECM	effective crack model
FCE	Faculty of Civil Engineering
FEM	finite element method
FPZ	fracture process zone
F–T	freeze–thaw
IPM	Institute of Physics of Materials
LEFM	linear elastic fracture mechanics
WST	wedge-splitting test
2 <i>K</i>	double- <i>K</i> fracture
3PB	three-point bending

### Symbols – Latin alphabet uppercase letters

<i>A</i> <sub>lig</sub>	ligament area
<i>B</i>	specimen's width
<i>D</i>	specimen's diameter
<i>E</i>	static modulus of elasticity
<i>F</i>	vertical force
$\Delta F$	load range
<i>F</i> <sub><i>a</i></sub>	amplitude of load
<i>F</i> <sub><i>i</i></sub>	vertical force in the ascending linear part of the diagram
<i>F</i> <sub>ini</sub>	load level at the outset of stable crack propagation
<i>F</i> <sub><i>F</i><sub>max</sub></sub>	maximum load of a sinusoidal wave in each cycle
<i>F</i> <sub><i>F</i><sub>min</sub></sub>	minimum load of a sinusoidal wave in each cycle
<i>F</i> <sub>max</sub>	maximum load
<i>F</i> <sub>sp</sub>	splitting force
<i>G</i> <sub>F</sub>	specific fracture energy
<i>H</i> <sub>0</sub>	thickness of blades fixed on the bottom surface of the specimens
<i>K</i> <sub>Ic</sub>	fracture toughness

$K_{Ic}^c$	cohesive fracture toughness
$K_{Ic}^{ce}$	effective fracture toughness
$K_{Ic}^{ini}$	initial cracking toughness
$K_{Ic}^{un}$	unstable fracture toughness
$L$	specimen's length
$M_{max}$	bending moment due to the maximum load $F_{max}$ and self-weight
$N$	number of cycles
$R$	stress ratio
$R^2$	coefficient of determination
$S$	span length
$S_F$	applied stress during the load cycle
$S_M$	section modulus
$U$	= $x/a_c$
$W$	specimen's height
$W_{ef}$	specimen's effective height
$W_F$	work of fracture
$Y(\alpha)$	geometry function for the 3PB configuration

#### **Symbols – Latin alphabet lowercase letters**

$a, b$	material constants of Wöhler curve
$a_c$	equivalent elastic crack length
$a_e$	effective crack length
$a_0$	initial notch depth
$c$	coefficient corresponding with asymptote of approximation curve
$d$	midspan deflection
$d_{F_{max}}$	midspan deflection $d_{F_{max}}$ matching to the maximum load $F_{max}$
$d_i$	midspan deflection corresponding to the force $F_i$
$f_t$	tensile strength
$m, n$	coefficients corresponding to the time-dependent change of compressive strength
$q$	self-weight
$rf_c$	dimensionless relative compressive strength
$t$	specimen's age in days

#### **Symbols – Greek alphabet lowercase letters**

$\alpha$	relative crack length
$\alpha_c$	relative equivalent elastic crack length
$\alpha_e$	relative effective crack length
$\alpha_0$	relative depth of the initial notch
$\gamma$	crack inclination angle
$\sigma$	cohesive stress
$\sigma(CTOD_c)$	cohesive stress at the tip of an initial notch at the critical state